Modeling Radiative Transport and Heat Transfer in Multiphase Media

by

Bingjia Li

A dissertation submitted in partial fulfillment
of the requirements for the degree of
Doctor of Philosophy
(Mechanical Engineering)
in The University of Michigan
2025

Doctoral Committee:

Associate Professor Rohini Bala Chandran, Chair
Associate Professor Jesse Capecelatro
Associate Professor Xun Huan
Professor Xiaodong Sun

Bingjia Li
bingjia@umich.edu
ORCID iD: 0000 0002 8649 0068

© Bingjia Li 2025

To my father, mother, grandpa, and all my friends

To my grandma

ACKNOWLEDGEMENTS

I would first like to thank my advisor, Professor Rohini Bala Chandran. As a student who has been in Tree Lab for 7 years, I witness you manage the group from an early stage to the current 7 PhD students with multiple research achievements, just like a tree growing from a sapling to a towering tree with ripe fruits all over the branches. It is very inspiring to see you irrigating the tree with enthusiasm and responsibility. I have been enjoying this experience since my first arrival in the fall of 2018 as a master student. Thank you for helping me develop both professionally and personally.

I would also like to acknowledge my funding agencies, American Chemical Society Petroleum Research Fund (ACS PRF), National Science Foundation Faculty Early Career Development Program (NSF CAREER) and Department of Energy Office of Energy Efficiency and Renewable Energy (DOE-EERE).

I also want to thank my committee members, Professor Jesse Capecelatro, Xun Huan, and Xiaodong Sun. I appreciate the time and effort you all have spent as my committee.

I would like to thank all the members of the Tree Lab both past and present for making office a vivid and engaging work environment. Special thanks to current PhD students Zijie, Rachel, Rebecca, Fernando, and Areefa, as well as former lab members and PhD graduates Luisa, Bryan, Durga, Fangqi, and Mike. I enjoyed every moment of our lab outings to baseball games and small things like lab lunches and chats in the office. I wish you all have splendid futures! I would also appreciate all

the Master's and undergraduate students I've collaborated with: Aishiwarya, Theo, Brandon, Xingze, Yire, Sisir, Prathemesh.

Finally, I would like to acknowledge my family. Thank you to my parents, Jun and Shiai, my grandpa, Yingchao and my late grandma, Zhiping. I haven't seen you since my adventure landing on this country and I've been missing you all every day in these 7 years. And thank you to everyone else who has played a part in this journey that I did not have the chance to name.

TABLE OF CONTENTS

DEDICATION ii

ACKNOWLEDGEMENTS iii

LIST OF FIGURES ix

LIST OF TABLES xx

LIST OF APPENDICES xxii

LIST OF ABBREVIATIONS xxiii

LIST OF SYMBOLS xxiii

ABSTRACT xxvii

CHAPTER

I. Introduction 1

1.1 Motivation of Thesis 1
1.2 Radiative Transport in Static Particulate Media: Effects of Spatial Arrangements 3
1.2.1 Overview 3
1.2.2 Knowledge Gaps 6
1.2.3 Hypotheses & Research Objectives 7
1.3 Flow and Heat Transfer in Moving bed Heat Exchanger . . . 8
1.3.1 Overview 8
1.3.2 Knowledge Gaps 14
1.3.3 Hypotheses & Research Objectives 15
1.4 Thesis Outline 16

II. Radiative and Heat Transfer Models for Discrete Particles . 18

2.1 Monte-Carlo Ray Tracing Method 18

2.1.1 Collision-based Method 19
2.1.2 Path-length Method 23
2.2 Discrete Element Method 24
2.2.1 Flow Modeling 25
2.2.2 Heat Transfer Models 28

III. Effects of Spatial Correlations in Particulate Media on Dependent Scattering and Radiative Transport 48

3.1 Introduction 48
3.2 Theory & Modeling Approach 51
3.2.1 Generation of Packed Beds 53
3.2.2 Index of Cluster Sampling (*ICS*) 56
3.2.3 Monte Carlo Ray Tracing Simulations 57
3.2.4 Evaluation of Extinction Coefficient and Scale Factor 62
3.3 Results & Discussion 65
3.3.1 Quantifying Spatial Statistics of Particles with *ICS* 65
3.3.2 Effects of Solid Volume Fraction and Spatial Distribution on Radiative Transport 70
3.4 Limitations and Future Work 85
3.5 Conclusions 86

IV. Flow Modeling to Characterize Solid Volume Fractions in Gravity-Driven Particle Curtains 88

4.1 Introduction 88
4.2 Modeling methods 90
4.2.1 Single particle force balance 90
4.2.2 Discrete element modeling for particle tracking . . . 93
4.2.3 Transmittance dependence on particle reflectivities . 96
4.3 Results & Discussion 97
4.3.1 DEM simulations 97
4.3.2 Comparison of measurements and model predictions 101
4.3.3 Ray tracing and optical property dependence 102
4.4 Conclusions 105

V. Conductive and Radiative Heat Transfer Mechanisms Inform Nusselt Number Dependence on Solid Volume Fraction for Granular Flows 107

5.1 Introduction 107
5.2 Method 111
5.2.1 Modeling Domain 111
5.2.2 Discrete Element Modeling for Flow and Heat Transfer 114
5.2.3 Heat-transfer Coefficient and Nusselt Number . . . 117

5.2.4 Parametric Study in Plug Flow 118
5.3 Results & Discussion 119
5.3.1 Plug Flow: Effects of Solid Volume Fraction 119
5.3.2 Plug Flow: Coupled Effects of Parameters 120
5.3.3 Moving Beds: Effects of Mass Flow Rate 123
5.3.4 Overall and Radiative Nusselt Number 126
5.4 Conclusion 129

VI. Discrete Element Modeling for Dense Moving Bed Heat Exchanger Informs Comprehensive New Nusselt-Péclet Number Correlations 132

6.1 Introduction 132
6.2 Method 137
6.2.1 Modeling Domain 137
6.2.2 Discrete Element Modeling for Flow and Heat Transfer 138
6.2.3 Parametric Study 139
6.3 Results & Discussions 140
6.3.1 Effects of Geometric and Thermophysical Properties on Heat Transfer Coefficients 140
6.3.2 Comparison with Existing Correlations 149
6.3.3 New Péclet and Nusselt Number and their Correlation 152
6.4 Conclusion 158

VII. Conclusion and Future Work 161

7.1 Summary & Research Contributions 161
7.1.1 Radiative Transport in Static Particulate Media: Effects of Spatial Arrangements 161
7.1.2 Flow and Heat Transfer in Moving Bed Heat Exchangers 162
7.2 Limitations & Future Work 163
7.2.1 Radiative Transport in Static Particulate Media: Effects of Spatial Arrangements 163
7.2.2 Flow and Heat Transfer in Moving Bed Heat Exchanger 164

APPENDICES 166
A.1 Collision MCRT Simulation Validation 167
A.2 Validation for Radiative View Factor Correlations with Monte Carlo Ray Tracing Simulations 168
A.3 Sensitivity Study of Computational Cost and Performance Evaluation Related with Radiation Time Step 169
B.1 *ICS* Calculation Example 171
B.2 Transmittance versus Optical Thickness for Ordered Beds . . 172
B.3 Dependence of Particle Reflectivity on Transmittance 174

B.4 γ–*ICS* Fitting Results with cell size of 0.51 mm 176
B.5 Additional Results for Angular Distribution for Transmission, $p(\theta_t)$ 176
B.6 Additional Results for Scattering Phase Function 179
C.1 Experimental Setup for Particle Curtain Flow 182
C.2 Sensitivity of DEM results to particle size distributions 183
D.1 Comparison with Semi-empirical Correlation from Sullivan and Sabersky 185
D.2 Particle Size Effect Analysis 187
D.3 Curve-fitting Equations for the Correlation between Nusselt Number and Solid Volume Fraction 188
E.1 Temperature Profile to Verify Fully Thermal Development . . 190
E.2 The local profile for velocity 191
E.3 Effects of Particle Size on Solid Volume Fraction 192
E.4 Effects of Rolling Friction on Flow Rate, Solid Volume Fraction and Heat Transfer Coefficient 193
E.5 Comparison with Nusselt Number correlation Based on Effective Thermal Conductivity 194

BIBLIOGRAPHY 197

LIST OF FIGURES

Figure

1.1 Applications of multiphase media in multiple industrial processes, including spray of liquid fuel in combustion (adapted from Zhang et al.[5]), moving bed heat exchanger (obtained from Mehos et al.[6]), particle-based thermal energy storage system (obtained from NREL [9]) and solid-gas fluidized bed reactor (obtained from Guo et al.[11]). 2

1.2 (a) Scattering regime map for independent and dependent scattering established by Tien [31]; (b) Transmittance as a function of optical thickness under the effect of solid volume fraction for absorbing particles (ω=0.7) [20]. 5

1.3 (a) Plug flow model of a moving bed heat exchanger with ordered arrangement from Sullivan and Sabersky's work [43]; (b) Nusselt number as a function of modified Péclet number for all materials tested in Sullivan and Sabersky's work [43]; (c) Nusselt number as a function of inverse Graetz number for constant temperature boundary condition [65,67]. 13

2.1 Flowchart to lay out the approach and implementation of collision-based ray tracing simulations to compute radiative transport. Random numbers sampled from a uniform distribution of [0,1] are represented as R_i, where the subscript i refers to the variable for which the random number was generated. For example, R_x corresponds to a random number generated to sample for the x-location of the launch points. Overall, all the rays launched from the bottom surface were tracked until they either got absorbed by the particles or left the domain at the $z = 20$ mm plane. 20

2.2 (a) A schematic diagram of a line, originated from a point (x, y, z), intersect with a spherical object, located at (x_c, y_c, z_c) with a radius of r, at point (x_t, y_t, z_t); (b) A schematic diagram of determining the scattered orientation, $\mathbf{n}_r(\theta, \varphi)$, of an incident ray, $\mathbf{n}_i(\theta', \varphi')$, specularly reflected by a spherical object located at (x_c, y_c, z_c). 21

2.3 Flowchart to lay out the approach and implementation of path-length ray tracing simulations to compute radiative transport. Random numbers sampled from a uniform distribution of [0,1] are represented as R_i, where the subscript i refers to the variable for which the random number was generated. For example, R_x corresponds to a random number generated to sample for the x-location of the launch points. Overall, all the rays launched from the bottom surface were tracked until they either got absorbed by the particles or left the domain at the $z = 20$ mm plane. 23
2.4 Hertz-Mindlin contact Model obtained from Chen et al. [97]. 25
2.5 Solid-solid heat conduction model developed by Batchelor and O'Brien. Heat is conducted through the contact surface with radius, calculated as the effective radius from the contact area, $A_{ij,\mathrm{ss}}$. 29
2.6 Schematic of the solid-fluid-solid conduction for particle-particle and particle-wall contact. 31
2.7 Calculated radiative heat flux using iterative method for (a) an example of two particles under different temperatures ($T_1 = 1000$ K, $T_2 = 300$ K) in a fully reflective enclosure ($F_{12} = F_{21} = 1$), as a function of iterative step and compared with the matrix solver and Stefan-Boltzmann results for (b) uniform emissivities ($\epsilon_1 = 0.1$, $\epsilon_2 = 0.1$), and (c) differed emissivities ($\epsilon_1 = 0.2$, $\epsilon_2 = 0.01$). 41
2.8 Effect of emissivity ($\epsilon = 0.1$, 0.4, 0.7, 1.0) in (a) a suspended packed bed of 1,289 particles radiatively heated by surrounding walls using iterative method, matrix solver and Stefan-Boltzmann equations on (b) temporal development of the average particle temperature, and computational cost of (c) radiation calculation in one time step, and (d) the entire simulation in 300,000 time steps. 43
2.9 Cost evaluation for a (a) gravity-driven, moving packed bed model; (b) speedup performance as a function of the number of processors; and (c) computational cost as a function of the particle number for $\epsilon = 0.1$ and $\epsilon = 1.0$, with dashed curves representing extrapolations from incomplete simulations due to prohibitively high computational costs. 45

3.1 Modeling domain comprising of a packed bed with particles of diameter, $d_p = 0.25$ mm to quantify the spatial distributions of particles with a size of 20 mm × 20 mm × 20 mm (a,b) and to perform Monte Carlo ray tracing simulations with a size of 8 mm × 8 mm × 20 mm (c,d) for various spatial distributions and solid volume fractions of particles in the bed; (b,d) modeling domains for cluster beds with a single high-concentration or clustered region with a solid volume fraction, $\phi_{\text{s,cluster}} = 0.524$, present in the bottom left corner; cluster dimensions are dictated by Eq. (3.1). For the ray tracing simulations (c,d), the bottom launch surface ($z = 0$ mm) is modeled to be perfectly reflective, the side walls are periodic surfaces and the transmitted rays are counted at planes perpendicular the z-axis and along the direction of increasing optical thickness. Particles are assumed to be opaque and with a surface reflectivity, $\rho_p = 0.7$. 52

3.2 Effects of cell size on the index of cluster sampling, *ICS*, values for Poisson, random, ordered and cluster beds with cluster fractions, f_c = 0.2, 0.5, 0.8 and 0.99, for solid volume fractions of (a) $\phi_s = 0.05$, (b) $\phi_s = 0.2$, (c) $\phi_s = 0.5$; note that the y-axis scale in Fig. 3.2(c) is different from (a,b) for clarity in observing the trends. Modeling domain shown in Fig. 3.1(a,b) with a particle diameter of 0.25 mm was used for all these cases. 66

3.3 Transmittance, T, as a function of optical thickness, τ, for the Poisson, random, ordered and cluster beds with cluster fractions, f_c, of 0.2, 0.5, 0.8 and 0.99 for (a) $\phi_s = 0.05$, (b) $\phi_s = 0.2$ and (c) $\phi_s = 0.5$. The ray tracing modeling domain in Fig. 3.1(c,d) was used with a particle diameter, $d_p = 0.25$ mm and by assuming opaque, grey and specularly reflective surfaces with $\rho_p = 0.7$; $\sim 10^6$ rays were launched and traced for intersections with up to 78,000 particles to obtain these results. Transmittance was obtained at discrete values of optical thickness (solid circles) and the solid lines were drawn to guide the eye. Error bars were computed by averaging Monte Carlo ray tracing simulations over 10 trials for each spatial arrangement and solid volume fraction modeled. 69

3.4 Scale factor, γ, which is a ratio of effective extinction coefficient obtained from the ray tracing simulation to the one predicted by independent scattering theory (Eq. (3.14)) as a function of the *ICS* values for the Poisson, random, ordered and cluster beds with cluster fractions, f_c of 0.2, 0.5, 0.8 and 0.99. The solid line is the best-fit, cubic polynomial (Eq. (3.16)) obtained by excluding the data points for the ordered bed to correlate the effective extinction coefficient of the ensemble with the *ICS*, which is a spatial statistic that is dictated by the solid volume fraction and the spatial distribution of particles in an ensemble. 75

3.5 Probability density function for attenuation distance, $p(s)$, as a function of attenuation distance, s, for Poisson bed, random bed, ordered bed and cluster bed with cluster fractions of 0.2 and 0.99 with volume fraction fixed at (a) $\phi_s = 0.05$ and (b) $\phi_s = 0.50$. Solid lines represent $p(s)$, obtained from the collision MCRT simulations and the dashed lines represent the fitted path-length distribution, $p^*(s)$, obtained from Eqs. (3.12) and (3.13). Ray-tracing modeling domain shown in Fig. 3.1(c,d) with particle diameter of 0.25 mm and particle reflectivity of 0.7 was used to perform collision MCRT simulations. Path-length MCRT simulation used fitted parameters obtained in Table 3.4. The schematic in the legend depicts the attenuation distance, s, which is the distance a ray that is launched at the lower surface travels before being absorbed or reflected by a particle and used to obtain $p(s)$ as explained in Table 3.2. 78

3.6 Probability density function of transmitted angle for Poisson bed, random bed, ordered bed and cluster bed with cluster rate of 0.2 and 0.5 with volume fraction fixed at $\phi_s = 0.05$ and with radiative transmittance of (a) $T = 0.9$, (b) $T = 0.42$ and (c) $T = 0.1$. Ray-tracing modeling domain shown in Fig. 3.1(c,d) with particle diameter of 0.25 mm and particle reflectivity of 0.7 was used to perform collision MCRT simulations. The dashed line is the probability density function of launching angle at the lower surface. The schematic in the legend depicts the diffuse distribution of the launched rays (purple rays at $z = 0$) and the polar angle, θ_t, measured for a transmitted ray to obtain $p(\theta_t)$ as explained in Table 3.2. 80

3.7 Scattering phase function, $\Phi(\theta_i, \theta_s)$, based on incident, θ_i and scattered, θ_s, polar angles defined with respect to the global z-axis for ordered beds with solid volume fractions of (a) $\phi_s = 0.05$ and (b) $\phi_s = 0.5$. Ray-tracing modeling domain shown in Fig. 3.1(c,d) with particle diameter of 0.25 mm and particle reflectivity of 0.7 was used to obtain pairs of incident and scattered angle values based on the procedure explained in Table 3.2. Incident polar angles vary from 0°–90° with statistics obtained for $\Phi(\theta_i, \theta_s)$ with a bin size of 10°; individual colors in the color scheme represents θ_i belonging to angular intervals of [0°,10°),[10°,20°) up to [80°,90°]. $\Phi(\theta_i, \theta_s)$ for supplementary angles of θ_i will be equal and not shown. For a fixed range of θ_i values, represented by the individual colors, the x-axis indicates rays that are scattered into angular intervals for θ_s of [0°,10°),[10°,20°) up to [170°,180°]. 83

4.1 Flow model used in DEM simulations, including a detailed view of the discharge slot that accounts for the deformation in the manufactured hopper. 93

4.2 (a) Division of the flow chamber into subdomains for ray tracing simulations with (b) an exploded view of the subdomain and the corresponding boundary conditions for ray tracing simulations. . . . 97

4.3 Qualitative comparison of experimental (a,c) and simulated (b,d) curtain flow at a selected time instant. (a) and (b) show 1 mm particles, while (c) and (d) show 2 mm particles. Photos are generated by selecting a high-speed camera frame at steady state. 98
4.4 Sensitivity test of (a) mass flow rate and (b) solid volume fraction to particle-particle coefficient of static friction at $z = 0.1$ m; (c) solid volume fraction range for 1 mm and 2 mm particles with particle-particle frictional coefficient $\mu_{s,pp}$ ranging from 0 to 0.9. All baseline parameters are listed in Table 4.3. 99
4.5 Integrated comparison of experimental and modeling results for solid volume fraction as a function of height in a gravity-driven particle curtain for 1 and 2 mm particles. All plotted lines represent power law curve fits, intended to visually guide the connection between data. Thermopile and high-speed camera error bars are based on a 95% confidence interval in the transmittance measurements over four and six trials respectively at every z location. 100
4.6 Dependence of the relationship between transmittance and solid volume fraction on particle reflectivities based on ray tracing simulations (dotted lines, markers). For comparison, Beer's law (Eq. (1.2)) with (solid) and without (dashed) scale factor S_ϕ are included. 102
4.7 DEM results from Fig. 4.5 and experimental results rectified with a reflectivity-dependent scale factor, with the possible range of thermopile results given for particle reflectivities in the range $R_p \in [0, 0.99]$ indicated by the shaded regions. 105
5.1 Modeling domain for: (a) plug flows of particles in a rectangular channel with uniform particle velocities along the flow direction (Z-velocity), and with a Gaussian velocity distribution in the transverse direction (X- and Y-velocity) with a mean value of 0, $v_\mathrm{x}, v_\mathrm{y} \sim \mathcal{N}(\mu = 0, \sigma^2 = 1^2$ mm/s), to introduce physical contacts between particles, and (b) gravity-driven, dense, moving beds of particles in a rectangular channel that is fed by a hopper right above it. In both cases of flow configurations, cold particles enter from the top at 300 K and get heated by the two isothermal heating walls at a temperature of T_w (T_w is a variable parameter in the model and equals to 1000 K in this figure) and parallel to the X-Z plane. The particle insertion region and the heat-transfer region are highlighted in turquoise and black respectively. 112

5.2 Effects of solid volume fraction ($\phi_s = 0.07, 0.25, 0.43$) in the plug flow model at a constant mass flow rate ($\dot{m} = 1.59$ g/s), and correspondingly different Péclet number ($Pe_L = 660, 189, 109$) on (a) steady-state spatial distributions of particle temperatures at $t = 5$ s, (b) temporal evolution of average particle temperatures present inside the channel, (c) channel-averaged wall-to-particle heat-transfer coefficients, $\overline{h}_{wp}$, obtained from Eq. (5.1) with (d) the contributions from thermal radiation, solid-fluid-solid (sfs) and solid-solid (ss) conduction pathways. 119
5.3 Effects of particle emissivity, ϵ, and wall temperature, T_w, in the plug flow model ($\phi_s = 0.07, 0.25, 0.43$) at a constant mass flow rate ($\dot{m} = 1.59$ g/s), and correspondingly different Péclet number ($Pe_L = 660, 189, 109$) on (a,d) channel-averaged, wall-to-particle heat-transfer coefficient, $\overline{h}_{wp}$, (b,e) conductive and radiative heat-transfer coefficients, and (c,f) the percentage contribution of thermal radiation to overall heat transfer. 121
5.4 Coupled effects of particle diameter, d_p, and solid volume fraction, ϕ_s, in the plug flow model ($\phi_s = 0.07, 0.25, 0.43$) at a constant mass flow rate ($\dot{m} = 1.59$ g/s), and correspondingly different Péclet number ($Pe_L = 660, 189, 109$) on (a) channel-average, wall-to-particle heat-transfer coefficient, $\overline{h}_{wp}$, (b) conductive and radiative heat-transfer coefficients, and (c) the percentage contribution of thermal radiation to the overall heat transfer. 124
5.5 Effects of mass flow rate ($\dot{m} = 1.21, 3.42, 6.08$ g/s), and corresponding Péclet numbers ($Pe_L = 68, 184, 325$) in gravity-driven moving beds at a near-constant solid volume fraction ($\phi_s = 0.55$) on (a) steady-state spatial distributions of particle temperatures at $t = 5$ s, (b) temporal evolution of average particle temperatures present inside the channel, (c) channel-averaged wall-to-particle heat-transfer coefficient, $\overline{h}_{wp}$, with (d) contributions from thermal radiation, solid-fluid-solid (sfs) and solid-solid (ss) conduction pathways. 125
5.6 (a) Wall-to-Particle heat-transfer coefficient, $\overline{h}_{wp}$, (b) overall and (c) radiative Nusselt number as a function of solid volume fraction with results obtained from both plug flow and moving beds with alumina and mustard seeds. Alumina particles are modeled with a diameter of $d_p = 0.8$ mm with a modified Péclet number Pe_L^* of 72000, whereas mustard seeds have a diameter of $d_p = 2$ mm with a modified Péclet number Pe_L^* of 1200. The plug flow model data (hollow circles) is fitted and extrapolated to compare against the predictions obtained for the moving beds (filled circles). The best-fit curve is included as a guide to the eye, and it exhibits an exponential and logarithmic dependence of conductive and radiative heat transfer on the solid volume fraction respectively as shown in Eq. (D.1) and Eq. (D.2). . 126
6.1 Modeling domain for gravity-driven, dense, moving beds of particles in a rectangular channel that is fed by a hopper above. 138

6.2 Effects of particle thermal conductivity in gravity-driven moving beds with inlet particles at 1000 °C, particle diameter of $d_p = 0.3$ mm under an identical mass flow rate of $\dot{m}$= 2.27 g/s and a near-constant solid volume fraction ($\phi_s \approx 0.59$) on (a) steady-state spatial distributions of particle temperatures at $t = 10$ s ($k_s = 0.05$, 0.5, 5 W/m/K), (b) cross-sectional view of the particle temperature distribution at a location of $z = 0.045$–0.055 m of the moving beds (the cross-sectional view is notified by the black box in (a)), and (c) the average particle temperature profile along the x direction for thermal conductivity (k_s = 0.05, 0.5, 1, 2, 5 W/m/K) (d) channel-averaged, particle-to-wall heat-transfer coefficient as a function of the particle thermal conductivity contributed from thermal radiation, solid-fluid-solid (sfs) and solid-solid (ss) conduction pathways. 141

6.3 Effects of (a-c) channel length, L, and (d-f) channel width, W, on the (a,d) channel-averaged, particle-to-wall heat transfer coefficient, $\overline{h}_{\mathrm{pw}}$, as a function of mass flow rate; accompanied with (b,e) temperature and (c,f) solid volume fraction distribution, obtained from snapshots of particle positions after flows reaching steady state, in the gravity-driven moving beds with the (b,c) longest simulated channel (L = 0.5 m) at a near-constant mass flow rate ($\dot{m}$= 2.27±0.02 g/s) or (e,f) at a close mass flow rate ($\dot{m}$= 0.49±0.08 g/s), with all the rest of the parameters as the baseline values in Table 6.1. 143

6.4 Effects of particle diameter, d_p, on the (a) channel-averaged, particle-to-wall heat transfer coefficient, $\overline{h}_{\mathrm{pw}}$, as a function of mass flow rate, with values extrapolated (hollow circle) for higher mass flow rate ($\dot{m}$ > 2.28 g/s) and small particle sizes ($d_p \leq 0.4$ mm); accompanied with (b) temperature, (c) solid volume fraction distribution, and (d) the heat transfer coefficient for overall and radiative heat transfer components, as a function of particle diameter, in the gravity-driven moving beds at a near-constant mass flow rate ($\dot{m}$ = 2.27±0.01 g/s), with all the rest of the parameters as the baseline values in Table 6.1. 146

6.5 Effects of the particle-particle and particle-wall, static frictional coefficients on (a) mass flow rate, $\dot{m}$, (b) solid volume fraction, ϕ_s, and (c) particle-to-wall heat-transfer coefficient, $\overline{h}_{\mathrm{pw}}$, for a gravity-driven, moving bed, with the rest of parameters fixed as the baseline values in Table 6.1. The identical baseline results are underscored by red dots. The range of the tested static friction coefficient for particle-particle and particle-wall surfaces follows the physical interpretation that $\mu_{\mathrm{s,pp}} > \mu_{\mathrm{r,pp}} = 0.1$ and $\mu_{\mathrm{s,pw}} > \mu_{\mathrm{r,pw}} = 0.28$. 148

6.6 (a)(b) Particle-diameter-based Nusselt number, $\overline{Nu}_d$, as a function of the modified Péclet number, Pe_L^*, compared with Sullivan and Sabersky's correlation, and (c)(d) the hydraulic-diameter-based Nusselt number, $\overline{Nu}_{D_h}$, as a function of the inverse Graetz number, Gz^{-1}, compared with Muzychka's correlation for plane channel, for the simulation results with varied channel length, channel width, particle diameter and particle thermal conductivity (only one parameter of all data is varied while keeping other parameters as the values in Table 6.1). 150
6.7 The new Nusselt number, $\overline{Nu}_{\text{new}}$ with respect to the new Péclet number, $Pe_{\text{L,new}}$, including a dimensionless width to length ratio, W/L, with power of 2, a diameter to width ratio, d_p/W, a conductivity ratio, k_s/k_g, and a solid volume fraction with exponents obtained from nonlinear regression (Eq. (6.1)); the legend is shown as well. 154
6.8 Comparison of simulations data from this work with four sets of experimental data from other papers for particle-based heat exchangers under the proposed new Péclet number $Pe_{\text{L,new}}$ and new Nusselt number. A zoom in plot is included to show the detailed information. The fitting curve is $\overline{Nu}_{\text{new}} = 4.42 Pe_{\text{new}}^{0.3295}$. 155
A.1 Comparison of the transmittance result from Singh and Kaviany's data (dashed lines) with simulation code. Comparison of transmittance of Singh and Kaviany's data for perturbed random beds using collision-based ray tracing simulations for specularly reflecting opaque particles with reflectivity, $\rho_p = 0.7$ 168
A.2 The radiation model is validated by comparing Monte Carlo ray tracing simulations with our radiative view factor correlations in terms of the probability distribution of particle temperature ((a), (c)) and the probability distribution of net heat flux received by particles ((b), (d)); suspended particle beds are heated for 5 physical seconds at solid volume fractions of 0.02 ((a), (b)) and 0.43 ((c), (d)) respectively. 169
A.3 The computational cost for performing a simulation of plug flow model with $\phi_{\text{s}} = 0.07$ for 5 seconds, and the relative error for the average particle temperatures as an influence of radiation-to-flow time step ratio. 170
B.1 Two-dimensional (a) ordered, (b) Poissonian, (c) cluster example of quadrat method calculation in a surface of 8 mm × 8 mm with 64 particles with a diameter of 0.45 mm inside, and the area is uniformly divided into 16 quadrat with each size of 2 mm × 2 mm. The red lines indicate the divide of cells in domain. Mean value and variance of the frequency and the calculated ICS value are listed. 172
B.2 Transmittance, T, as a function of optical thickness, τ, for ordered bed at solid volume fraction ranging (a) ϕ_s = 0.05–0.35, and (b) ϕ_s = 0.35–0.50. 173

B.3 Transmittance, T, as a function of optical thickness, τ, for ordered bed at solid volume fraction (a) $\phi_s = 0.05$, and (b) $\phi_s = 0.50$. Fitting results of simple exponential and bi-exponential functions (Eqs. (3.12) and (3.13)) are presented with dashed-lines. 173
B.4 (a) Path-length ray tracing simulations for media of scattering albedo at $\omega = 0$, 0.7 and 0.99. A simple exponential function is plotted as a comparison with path-length results. (b) m value in Eq. (3.11) computed from path-length simulation as a function of particle reflectivity ρ_p and a fit curve obtained from Eq. (B.1). 175
B.5 Scale factor, γ, (ratio of effective extinction coefficient obtained from the ray tracing simulation to the one predicted by independent scattering theory) as a function of the *ICS* values for the Poisson, random, ordered and cluster beds with cluster fractions of 0.2, 0.5, 0.8 and 0.99. The solid and dashed lines are the best-fit, cubic polynomials obtained by excluding and including the data points for the ordered bed respectively. 177
B.6 Probability density function of transmitted angle for Poisson bed, random bed, ordered bed and cluster bed with cluster rate of 0.2 and 0.5 with volume fraction fixed at $\phi_s = 0.20$ and with radiative transmittance of (a) $T = 0.9$, (b) $T = 0.42$ and (c) $T = 0.1$. Ray-tracing modeling domain shown in Fig. 3.1(c,d) with particle diameter of 0.25 mm and particle reflectivity of 0.7 was used to perform collision MCRT simulations. The dashed line is the probability density function of launching angle at the lower surface. The schematic in the legend depicts the diffuse distribution of the launched rays (purple rays at $z = 0$) and the polar angle, θ_t, measured for a transmitted ray to obtain $p(\theta_t)$ as explained in Table 3.2. 178
B.7 Visualization of scattering in the ordered beds with solid volume fraction of $\phi_s = 0.05$ considering incident angle, (a) $\theta_i \in [0°, 10°)$, and (b) $\theta_i \in [40°, 50°]$. Incident, θ_i, and scattered, θ_s, polar angles are defined with respect to the global z-axis. The green arrow indicates the incident ray and the orange arrow indicates the scattered ray. . 180
B.8 Scattering phase function, $\Phi^*(\theta^*)$, based on the angle, θ^*, between incident and scattering ray for Poisson, random, ordered and cluster beds with solid volume fractions of (a) $\phi_s = 0.05$ and (b) $\phi_s = 0.5$. Same ray-tracing modeling domain shown in Fig. 3.1(c,d) with particle diameter of 0.25 mm and particle reflectivity of 0.7 was used to obtain the angle between incident and scattered rays. Angle θ^* vary from 0°–180° with statistics obtained for $\Phi^*(\theta^*)$ with a bin size of 10°. The x-axis indicates rays that are scattered with angular intervals for θ^* of [0°,10°),[10°,20°) up to [170°,180°]. 181
C.1 Lab-scale flow chamber for gravity-driven particle flow experiments. (a) Cross-sectional detail view of the hopper and the top slide gate. (b) Front view of flow chamber. (c) Side view of the flow chamber. . 182

C.2 DEM modeling results for solid volume fraction as a function of height for 1 mm and 2 mm particles with mono- and normally-dispersed size distributions. Plotted lines represent the power law curve fits to data points. In all cases, the monodisperse results show good agreement with the normally-dispersed results. 184
D.1 Nusselt number dependence on Péclet number based on the moving beds ($\phi_s \approx 0.55$) and the plug flow model ($\phi_s \approx 0.45$), and comparison with the semi-empirical correlation from Sullivan and Sabersky's work, where the particles flow through a 20 mm × 10 mm × 50.8 mm channel region with a heating plate in the length of 25.4 mm. . 186
D.2 (a) Schematic for the near-wall region or bulk region; (b)average estimated particle-particle and particle-wall contact area and (c) average wall-particle view factor for different particle diameter. 188
D.3 Coupled effects of particle diameter, d_p, and solid volume fraction, ϕ_s, in the plug flow model ($\phi_s = 0.07, 0.25, 0.43$) at a constant Péclet number of $Pe_L = 660$ on (a) channel-average, wall-to-particle heat-transfer coefficient, $\overline{h}_{wp}$, (b) conductive and radiative heat-transfer coefficients, and (c) the percentage contribution of thermal radiation to the overall heat transfer. 189
E.1 The non-dimensional temperature gradient along the flow direction, $\partial\theta/\partial z$, as a function of the normalized length, z/L, with average temperatures of particles obtained with a bin size of 20 mm along the z dimension in a channel with $L = 0.5$ m at a mass flow rate of 2.27 g/s. 191
E.2 The thermal entrance length, L_{th}, computed as the position that the $\partial\theta/\partial z < 0.3$, as a function of flow velocity, u, with the particle size varied from 0.4 mm to 0.6 mm; all results are obtained from snapshots that the moving bed flow achieving steady state. 192
E.3 In a moving bed flow with a channel length of L = 0.1 m and a mass flow rate of $\dot{m} = 2.27$ g/s, (a) the velocity profile obtained from snapshots of the DEM simulation at $t = 23$, 24, 25 s, which is already at a steady state, (b) the local velocity of particles as a function of the normalized length. The local velocity is obtained as the average velocity for particles within a bin size of 1 mm along the z direction. 193
E.4 The solid volume fraction averaged for particles in the entire channel and in the near-wall region, as a function of particle size, ranging from $d_p = 0.3$–0.8 mm, at a near-constant mass flow rate of $\dot{m} = 2.27$ ± 0.01 g/s. 194

E.5 Effects of the particle-particle and particle-wall, rolling frictional coefficients on (a) mass flow rate, $\dot{m}$, (b) solid volume fraction, ϕ_s, and (c) particle-to-wall heat-transfer coefficient, $\overline{h}_{\mathrm{pw}}$, for a gravity-driven, moving bed, with the rest of parameters fixed as the baseline values in Table 6.1. The identical baseline results are underscored by red dots. The range of the tested static friction coefficient for particle-particle and particle-wall surfaces follows the physical interpretation that $\mu_{\mathrm{r,pp}} < \mu_{\mathrm{s,pp}} = 0.6$ and $\mu_{\mathrm{r,pw}} < \mu_{\mathrm{s,pw}} = 0.3$. 195

E.6 (a)Particle-diameter-based Nusselt number, $\overline{Nu}_d$, as a function of the modified Péclet number, Pe_L^*, compared with Sullivan and Sabersky's correlation, and (b) the hydraulic-diameter-based Nusselt number, $\overline{Nu}_{D_h}$, as a function of the inverse Graetz number, Gz^{-1}, compared with Muzychka's correlation for plane channel, for the non-dimensional numbers calculated based on the effective thermal conductivity obtained from ZBS model. 196

LIST OF TABLES

Table

1.1	Scale factor correlations to correct fpr extinction coefficient Eq. (1.3), dependent on solid volume fraction from Kamiuto, Singh and Kaviany and Brewster.	6
1.2	Definitions of Péclet number, Graetz number and Nusselt number in literatures as dimensionless numbers relevant to heat transfer in particle flows.	10
1.3	Heat transfer coefficient or Nusselt number correlations in prior work	11
2.1	Particle-particle, F_{pp}, and particle-wall, F_{pw}, view factor correlations based on dimensionless distances, d^*, for different solid volume fraction ranging from 0.02 to 0.48.	35
2.2	The relative error comparing Monte Carlo ray tracing simulations and using our view factor correlations for different solid volume fractions.	37
3.1	Details of the types of spatial distributions of particles generated in the packed bed with schematics for their unit cells.	54
3.2	Description, significance, calculation details, and equations for various parameters computed from ray-tracing simulations to understand radiative transport in a packed bed of large and opaque particles.	60
3.3	Computed *ICS* values with a fixed cell size of 0.35 mm for the various spatial distributions and solid volume fractions considered for the packed beds.	68
3.4	Best-fit for the pre-exponential factor (p) and the scale factor, γ, for the Poisson, random (Eq. (3.12)), and the cluster beds (Eq. (3.13)) obtained from the transmittance versus optical thickness results via Monte Carlo ray tracing simulations (Fig. 3.3).	73
4.1	Relevant physical dimensions for measurement and modeling	92
4.2	Table of derived dimensions	92
4.3	Particle geometric and material properties used in DEM simulations	94
5.1	Mechanical and thermal properties of materials modeled in the DEM simulations — α-alumina and mustard seed.	115

5.2 Parameter exploration for the plug flow model (Fig. 5.1(a)) simulations with a fixed solids mass flow rate of $\dot{m} = 1.59$ g/s. For a fixed mass flow rate, differences in solid volume fraction are achieved by varying particle flow velocities resulting in different Péclet numbers. 118
6.1 Constant/fixed value of mechanical and thermal properties used in the DEM simulations. 139
6.2 Parameter exploration range used in the DEM simulations for moving bed. 140
6.3 Optimized multi-design parameters including length, velocity, width, particle size and conductivity simultaneously for the target heat transfer coefficient of 600 W/m^2/K. 157
B.1 Computed *ICS* values with a fixed cell size of 0.51 mm for the various spatial distributions and solid volume fractions considered for the packed beds. 178

LIST OF APPENDICES

Appendix

A. Chapter 2: Validations for Radiative and Heat Transfer Models for Discrete Particles 167

B. Chapter 3: Effects of Spatial Correlations in Particulate Media on Dependent Scattering and Radiative Transport 171

C. Chapter 4: Flow Modeling to Characterize Solid Volume Fractions in Gravity-Driven Particle Curtains 182

D. Chapter 5: Conductive and Radiative Heat Transfer Mechanisms Inform Nusselt Number Dependence on Solid Volume Fraction for Granular Flows 185

E. Chapter 6: Discrete Element Modeling for Dense Moving Bed Heat Exchanger Informs Comprehensive New Nusselt-Péclet Number Correlations 190

LIST OF ABBREVIATIONS

ARC advanced research computing

COP28 28th Climate Change Conference

CSP concentrating solar power

DEM discrete element method

HPC high-performance computing

ICS index of cluster sampling

LAMMPS large-scale atomic/molecular massively parallel simulator

LIGGGHTS LAMMPS improved for general granular and granular heat transfer simulations

MCRT Monte Carlo ray tracing

MPI message passing interface

RTE radiative transport equation

SVR support vector regression

TES thermal energy storage

LIST OF SYMBOLS

Greek Letters

α	thermal diffusivity
β	extinction coefficient
χ	experimental constant for thermal resistance
δ	Kronecker delta
δ_n	normal overlap displacement
ϵ	emissivity
γ	scale factor for extinction coefficient
γ_n	viscoelastic damping constant for normal contacts
γ_n	viscoelastic damping constant for tangential contacts
κ	absorption coefficient
λ	wavelength
μ	friction coefficient
ν	Poisson ratio
Ω	solid angle
ω	rotational velocity
Φ	scattering phase function
ϕ	volume fraction
ρ	density
σ	Stefan-Boltzmann constant
σ_s	scattering coefficient
τ	optical thickness
τ_r	torque due to rolling friction
θ	polar angle
φ	azimuthal angle

Latin Letters

$\dot{m}$	mass flow rate
$\dot{Q}$	heat rate
$\hat{\mathbf{s}}$	unit vector into a given direction
$\overline{X}$	mean value
$\mathbf{F}$	force
$\mathbf{g}$	gravity vector
$\mathbf{v}$	translational velocity
A	area
Ar	Archimedes number
C	clearance

c	interparticle distance
C_D	drag coefficient
c_p	thermal capacity
d	distance
D_{air}	air gap distance
D_h	hydraulic diameter
d_p	particle diameter
e	restitutional coefficient
F	view factor
f_c	cluster fraction
Fr	Froude number
G	shear modulus
G^*	reduced/effective shear modulus
Gz	Graetz number
h	heat transfer coefficient
I	radiative intensity
k	thermal conductivity
k_n	elastic constant for normal contacts
k_t	elastic constant for tangential contacts
L	length
m	mass
N	number
Nu	Nusselt number
$p(\theta_t)$	transmitted angle distribution function
$p(s)$	path-length distribution function
Pe_L	Peclet number
q	heat flux
R	thermal resistance
r	radius
R_θ, R_φ	random numbers of angle sampling
R_p	particle reflectivity
Re	Reynold number
S	scale factor
S^2	variance
St	Stokes number
T	transmittance, or temperature
t	time
u	flow velocity
W	width
x	particle size parameter
Y	Young's modulus
Y^*	reduced/effective Young's modulus

Superscripts & Subscripts

(n)	nth iteration
$*$	modified
b	blackbody
cond	conduction
eff	effective
ind	independent scattering assumption
max	maximum

min	minimum	s	solid phase
nw	near-wall	t	tangential component
n	normal component	w	wall
pw	particle-to-wall	c	center
p	particle	d	diameter based
rad	radiation	D_h	hydraulic diameter based
rt	ray-tracing	g	gas phase
sfs	solid-fluid-solid	L	Length based
ss	solid-solid	p	pre-exponential factor

ABSTRACT

Multiphase media involving solid particles and a gas phase have crucial applications, such as static packed beds of particles in chemical and nuclear reactors and flowing ceramic particles as heat transfer and thermal storage media. For applications involving high temperatures and/or systems where there are interactions between a radiation source (e.g, sunlight) and multiphase medium, radiative transport becomes important. The primary objectives of this thesis are to enhance the understanding of radiative transport and heat transfer behavior in both static multiphase media such as packed beds, and multiphase particular flows.

With an initial focus on static packed beds, the goal is to determine the influences of spatial arrangements of solid particles, in addition to size and solid volume fraction, on radiative transport. For large particles relative to characteristic wavelength, independent scattering theory is traditionally assumed to obtain effective radiative properties. However, there is limited knowledge on the influence of effects of spatial distributions of large particles on radiative transport. Monte Carlo ray tracing simulations are performed for packed beds of particles with varying spatial distributions and solid volume fractions. Model results demonstrate the dependency of radiative transport on the spatial distributions even for a fixed solid volume fraction and in developing correlations between radiative transmittance and a statistical index to quantify the spatial distributions.

For multiphase flows with solid particles, the primary focus of this dissertation is to develop coupled models for particle flow and heat transfer including radiation.

Discrete element method simulations are performed to track the motion of individual particles while accounting for multimode heat transfer, including conduction in solid and fluid phases, and radiation. An iterative approach compatible with the discrete element method simulations is implemented to parallelize radiative flux calculations, which reduces computational time by 98% for a flowing system with 100,000 particles. To isolate influences of flow regimes, channel-averaged heat transfer coefficients are obtained in isothermal channels with particle plug flows with solid volume fractions of 0.02–0.48 and a near-constant velocity. Results demonstrate that while the overall and conductive heat transfer coefficients increases with solid volume fraction because of more direct contacts between particles, the effectiveness of radiative heat transfer decreases due to the shading effects from neighboring particles. To further broaden applicability of model results, simulations are performed for gravity-driven, dense granular flows (solid volume fraction: 0.56–0.67) for selected combinations of varying channel geometries (length: 0.1–0.5 m, width: 5–8 mm), particle size (0.2–0.8 mm), and thermophysical properties of bulk conductivity (0.05–5 W/m/K) and static and rolling friction coefficients. These results are cast in the form of new Nusselt number correlations. Results demonstrate that with particle size increasing from 0.3 to 0.8 mm, the overall heat transfer coefficient decreases by 35% but the radiative heat transfer enhances by 3 times. Increasing particle-particle static friction decreases mass flow rate and solid volume fraction, reducing heat transfer performance. Notably, model-informed correlations are more adept in capturing the influences of a wide range of parameters and demonstrate a reasonable match with reported experimental data within a relative deviation of 25%.

The main contributions of this dissertation are to develop predictive modeling capabilities to couple particle flow and heat transfer including radiation to both provide mechanistic insights and quantitatively determine heat transfer performance for dense moving beds.

CHAPTER I

Introduction

1.1 Motivation of Thesis

The development and implementation of renewable energy technologies have become crucial for transitioning away from fossil-based energy sources in electricity production [1, 2]. To meet the 28th Climate Change Conference (COP28) target of achieving net-zero emissions by 2050 [3], it is imperative to enhance energy conversion efficiency and decarbonize processes. In this context, multiphase media, having the benefits of enhanced mixing, heat and mass transfer and reaction rates, emerge as a potential solution to optimize energy systems. Compared to traditional single-phase fluids, multiphase systems provide advantages in renewable energy technologies and gain interest in a wide range of areas in solar and nuclear energy, chemical catalysis, pneumatic conveying and combustion. Many applications that utilize the advantages of multiphase media are shown in Fig. 1.1. For example, in the gasification of municipal solid waste, the conversion into a solid-gas mixture can improve the waste reduction efficiency and reduce the green gas emission [4, 5]. In the field of renewable energy, solid particles are used as heat transfer media in the new generation concentrating solar power (CSP) plant to convert direct solar radiation into high-temperature thermal energy with higher efficiency than traditional single phase fluids [6, 7]. This is due to the ability of solid particles to withstand more elevated

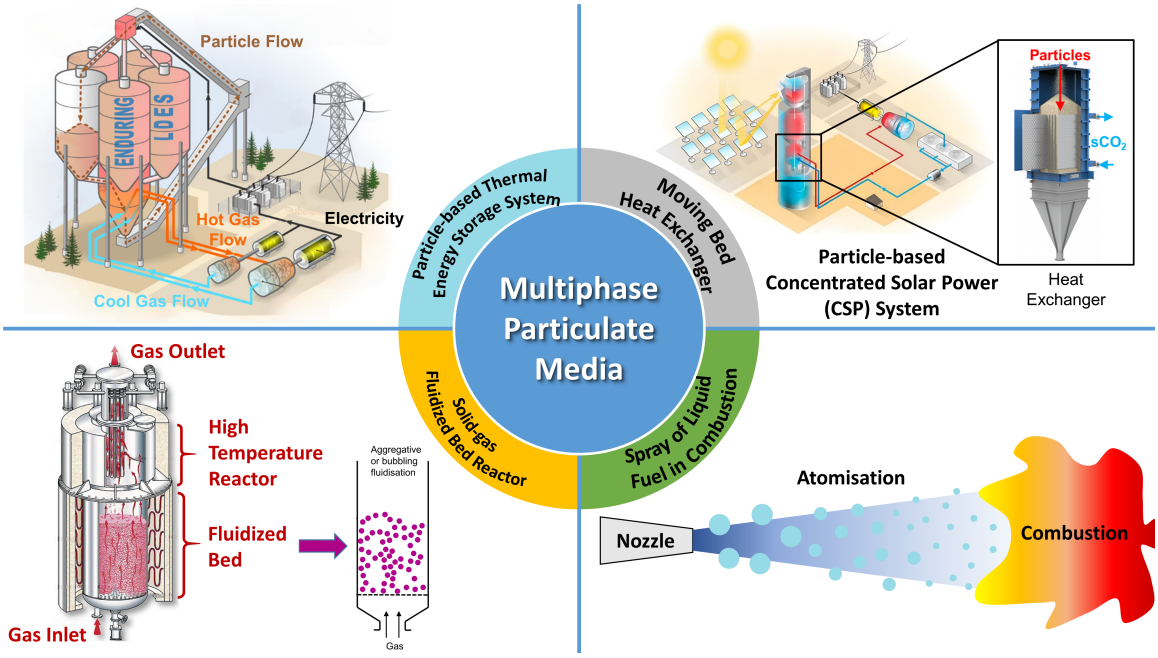


Figure 1.1: Applications of multiphase media in multiple industrial processes, including spray of liquid fuel in combustion (adapted from Zhang et al.[5]), moving bed heat exchanger (obtained from Mehos et al.[6]), particle-based thermal energy storage system (obtained from NREL [9]) and solid-gas fluidized bed reactor (obtained from Guo et al.[11]).

temperatures (> 700 °C), thereby optimizing thermal efficiency. Similarly, in thermal energy storage (TES) systems, solid particles are selected for their high energy density and stability, allowing to enhance energy efficiency and reduce the system size [8, 9]. Furthermore, in fluidized bed reactors, the usage of solid-liquid media enhances the mixture of two phase of reacting materials to improve heat transfer and chemical reaction of the system [10, 11]. These examples collectively demonstrate the significant impact of multiphase media in improving the efficiency and sustainability of energy and environmental systems.

However, the use of multiphase media in industries also poses challenges for engineers due to the complexity of such media. The interaction between different phase of materials lead to flow patterns that are difficult to predict and control. It is also more challenging to obtain the effective parameters, such as density, viscosity and conductivity for the multiphase medium. Additionally, these macroscopic properties

can change over time and results in heterogeneity of the medium. Moreover, with the increase of applying multiphase media in higher temperature environments, thermal radiation becomes inevitable and needs more understanding of its influence on multiphase media. This requires both (1) development of models for multiphase systems that account for radiative effects, and (2) more understanding of the characteristics of multiphase flow and its heat transfer behaviors.

Therefore, this dissertation is aimed at developing and improving radiative transport modeling in particulate media with a special focus on flowing particle systems, with applications to gravity-driven, particle curtain flows and packed moving bed flows.

1.2 Radiative Transport in Static Particulate Media: Effects of Spatial Arrangements

1.2.1 Overview

Radiative transport in particulate media is crucial in diverse fields, such as solar collector design, combustion processes optimization and heat transfer enhancement in nuclear reactors. Within particulate media, radiation interacts with particles through three primary mechanisms: emission, absorption and scattering [12–14]. These three phenomena are integrated in the radiative transport equation (RTE) [13, 15]. This fundamental equation describes the balance of radiative intensity, I, in thermal equilibrium, offering a quasi-steady representation of these complex interactions in particulate media (Eq. (1.1)), with all properties as functions of wavelength, λ.

$$\frac{dI_\lambda}{ds} = \hat{s} \cdot \nabla I_\lambda = \kappa_\lambda I_{b\lambda} - \beta_\lambda I_\lambda + \frac{\sigma_{s\lambda}}{4\pi} \int_{4\pi} I_\lambda(\hat{\mathbf{s}}_i)\Phi_\lambda(\hat{\mathbf{s}}_i, \hat{\mathbf{s}}) d\Omega_i \tag{1.1}$$

However, the radiative transport equation is not always the most practical tool for modeling radiative transport. The equation requires accurate prediction of the effective radiative properties, such as the extinction coefficient, β, and absorption coefficient, α, and the scattering phase function, $\Phi(s_i, \hat{s})$, where s is the geometric path length and $\hat{s}$ is the unit vector to a given direction. These properties can be dependent on multiple elements, such as temperature and wavelength. Besides, the high dimensionality of this integral-differential equation is computationally expensive to solve when the geometry is complex. Some methods to solve this RTE equation includes discrete ordinates method and spherical harmonics method [16]. However, the computational cost is still high and other simplified techniques, such as P_1-approximation, can be less agreed to experiments in various application [17]. Therefore, in many practical applications, the RTE equation is often simplified by considering the geometric configuration, such as assuming a one-dimensional framework, and the characteristics of the medium, such as non-scattering assumption. For instance, by constraining the medium to be one-dimensional, plane-parallel, isotropically scattering, and grey, the RTE equation can be approximated using the two-flux method [18].

For medium that is optically thin and homogeneous, the independent scattering theory, which assumes that scattering by one particle is unaffected by the presence of surrounding particles, is widely applied [19–32]. By employing this independent scattering theory, the transmittance of solar energy within a depth, W, can be calculated using Beer's Law [13, 33] in relation to parameters such as solid volume fraction, ϕ_s, and particle diameter, d_p (Eq. (1.2)).

$$T = \exp\left(-\beta W\right) = \exp\left(-\frac{3\phi_s}{2d_\mathrm{p}}W\right) \tag{1.2}$$

Beer's law is usually preferable to the RTE equation due to its simple form, making it applicable in many practical scenarios. This equation implies that both large particle

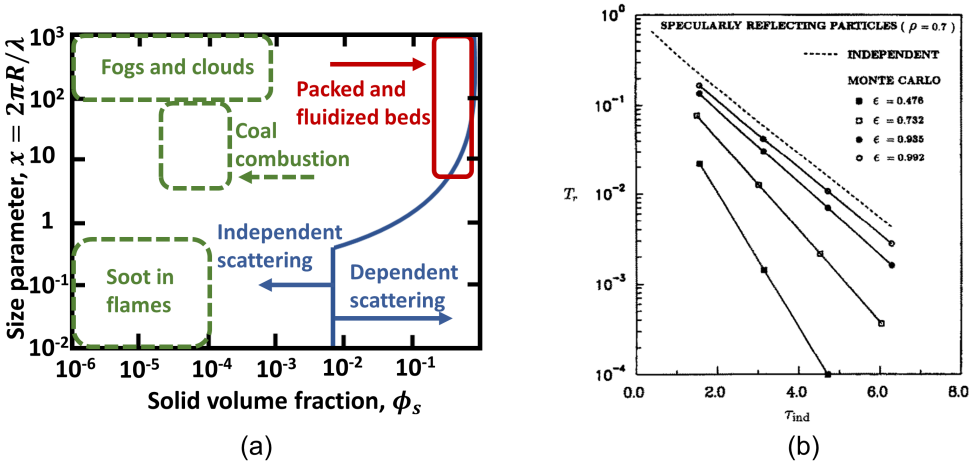


Figure 1.2: (a) Scattering regime map for independent and dependent scattering established by Tien [31]; (b) Transmittance as a function of optical thickness under the effect of solid volume fraction for absorbing particles (ω=0.7) [20].

size and low solid volume fraction would allow more rays to transmit through the media without attenuation. The validity of the independent scattering approximation in modeling radiative heat transfer is highly dependent on the particle volume fraction, ϕ_s, the size parameter, $x = \pi d_p/\lambda$, as established by Tien et al. [31, 34] (Fig. 1.2(a)). Coquard et al. further examined the boundary between dependent and independent scattering regime by performing ray-tracing simulations and concluded a large-sized packed bed with solid volume fraction lower than 5% is eligible to apply independent scattering theory [35].

In fact, due to the simplicity of Beer's law, deviation from this law can be used to evaluate the influence of dependent scattering on radiative transport. By retaining the straightforward form of Beer's law, the dependent scattering effects can be easily incorporated into a scale factor, defined as the ratio of extinction coefficient to that obtained assuming independent scattering (Eq. (1.3)).

$$\beta = S_{\phi}\beta_{\text{ind}} = S_{\phi}\frac{3\phi_s}{2d_{\text{p}}} \tag{1.3}$$

Table 1.1: Scale factor correlations to correct fpr extinction coefficient Eq. (1.3), dependent on solid volume fraction from Kamiuto, Singh and Kaviany and Brewster.

References	**Scale Factor Correlation**
Kamiuto[23]	$S_\phi = 1 + 1.5\phi_\mathrm{s} - 0.75\phi_\mathrm{s}^2, \phi_\mathrm{s} > 0.08$
Singh and Kaviany[20]	$S_\phi = 1 + 1.84\phi_\mathrm{s} - 3.15\phi_\mathrm{s}^2 + 7.20\phi_\mathrm{s}^3, \phi_\mathrm{s} < 0.7$
Brewster[31]	$S_\phi = 1/(1 - \phi_\mathrm{s})$

Kamiuto applied stochastic wave-mechanical theories to derive correlated radiative properties [23], such as the extinction coefficient and scattering albedo. The predicted transmittance achieves better alignment with experimental results from Chen and Churchill [36]. Singh and Kaviany employed Monte-Carlo ray tracing simulations to predict the transmittance of lights incident on particulate media with a solid volume fraction range of $\phi_s = 0.008 - 0.524$ (Fig. 1.2(b))[22]. Brewster proposed a simple model for the radiative properties of close-packed, large, opaque spheres [31], which agrees well with the findings of Singh and Kaviany [20]. All these investigations highlight a non-linear dependence of the scale factor on solid volume fraction as shown in Table 1.1. Because of the strong dependence of solid volume fraction on light attenuation, Beer's law has been widely applied in optical diagnostic to determine the concentration and polarization of the materials [37, 38].

Apart from solid volume fraction, researchers found other elements also influence dependent scattering in radiative transport. Randrianalisoa evaluated the radiative properties when the particulate media is heterogeneous [39]. Gusarov modified the RTE equation to incorporate inhomogeneity for two-phase particulate media [40]. Other researchers investigated the spectral dependence on radiative properties of specific materials, such as polyurethane foam [41] and ash deposits [42].

1.2.2 Knowledge Gaps

Despite significant advances in understanding radiative transport in particulate media, the influence of spatial distributions of particles is rarely addressed. Prior work

has utilized solid volume fraction in scale factors to account for dependent scattering effects. Usually, the influence of particle spatial distribution can be very limited for medium with low solid volume fraction that presents a rather random distribution. However, the detailed descriptions of the spatial arrangements of particles used in different researches are either omitted or indicate a distribution far from a random arrangement. These variations can lead to inconsistent forms of the scale factor correlations to account for dependent scattering. This gap highlights the necessity to apply statistical methods to quantify the spatial distribution of particles, which allows us to build connections with radiative transport.

1.2.3 Hypotheses & Research Objectives

Based on these knowledge gaps, this research makes the following hypothesizes:

1. The three-dimensional (3-D) spatial distribution of particles in particulate media, in addition to the solid volume fraction, significantly impacts non-point scattering effects and overall radiative transport.

2. Spatial correlations among particles influence radiative properties such as transmittance, extinction coefficient, and scattering phase function, leading to deviations from the independent scattering assumption.

To test these hypotheses, the objectives of this research include:

- Examining how different spatial distributions (Poisson, random, ordered, and clustered) and varying solid volume fractions ($\phi_s = 0.05$–0.5) affect radiative transport in particulate media.

- Developing and applying the Index of Cluster Sampling (ICS) to statistically quantify the spatial correlations of particles in packed beds.

- Performing Monte Carlo ray tracing (MCRT) simulations to analyze radiative transmittance, path-length distribution, angular distribution of transmitted

rays, and scattering phase function.

- Establishing a unified correlation to predict scale factors that accounts for dependent scattering, as a function of ICS and solid volume fraction.

1.3 Flow and Heat Transfer in Moving bed Heat Exchanger

1.3.1 Overview

Moving bed heat exchanger are increasingly playing a significant role in industrial energy conservation and solar energy utilization. Understanding the dynamics and heat transfer characteristics of the moving bed flow is crucial for enhancing the heat-to-electricity efficiency of CSP systems. Moving bed flow features a high solid volume fraction ($\phi_s > 0.5$) [43–46], implying frequent interactions between particles. To accurately capture the discrete behavior of moving particles, the Discrete Element Method (DEM) has become increasingly popular for modeling heat transfer in these flows [10, 46–64]. This method individually tracks solid particles within a Lagrangian framework for particle positions, linear and angular velocities, and temperatures. Although DEM is computationally demanding, it offers powerful insights by explicitly accounting for inter-particle mechanical and thermal interactions based on particle geometry and thermophysical properties, such as frictional coefficients and thermal conductivity.

The overall particle-wall heat transfer coefficient is a crucial parameter for designing and evaluating the performance of moving bed heat exchangers. It quantifies the efficiency of heat transfer between the channel walls and the particles, and is calculated based on the heat flux from the channel walls, q, the particle temperatures, T_{p}, and the wall temperatures, T_{w}, expressed by Eq. (1.4).

$$h_{\mathrm{pw}} = \frac{q}{T_{\mathrm{p}} - T_{\mathrm{w}}} \tag{1.4}$$

where h_{pw} can represent either a local or an average value over the entire length of the heat exchanger, $\overline{h}_{\mathrm{pw}}$, depending on the average particle temperature, $\overline{T}_{\mathrm{p}}$.

The heat transfer coefficient is typically affected by a range of parameters, notably the geometric dimensions of the system and the thermophysical properties of the materials involved. To generalize results and make it agnostic to geometry and test conditions, researchers often express these parameters as dimensionless numbers [43–45]. Table 1.2 presents several commonly used dimensionless numbers relevant to particle flows. The Péclet number, Pe_L^*, quantified the relative importance of convective flow effects compared to diffusive heat effects, dependent on factors such as flow velocity, u, characteristic length, L, and thermal diffusivity, $\alpha_p = k/\rho c_p$, where k, ρ and c_p are the effective thermal conductivity, density and heat capacity respectively. Sullivan and Sabersky developed a modified Péclet number, Pe_L^*, to account for fluid-phase thermal conductivity and particle diameter. The Graetz number, Gz, is inversely proportional to a characteristic length scale, typically the flow channel length, L, and describes the development of temperature profiles. A lower Graetz number suggests the flow is approaching a fully-developed state. The Nusselt number characterizes the ratio of total heat transfer to conductive heat transfer in a flow, and is calculated based on the overall particle-wall heat transfer coefficient, $\overline{h}_{pw}$, characteristic length, L and thermal diffusivity, α_p of the particle flow. Nusselt number can be defined differently based on the chosen characteristic length and the effective conductivity of the solid and fluid phase, which is different from the bulk conductivity of the solid phase, and can be obtained from empirical correlations and experimental testing [65, 66]. Existing Nusselt numbers in literature includes length-based, $\overline{Nu}_L$, hydraulic diameter based, $\overline{Nu}_{D_h}$, and particle size based, $\overline{Nu}_d$, Nusselt number.

In the study of dense, contact-dominated granular flows, significant research has focused on experimentally measuring the particle-wall heat transfer coefficient and developing semi-empirical or empirical dimensionless Nusselt number correlations.

Table 1.2: Definitions of Péclet number, Graetz number and Nusselt number in literatures as dimensionless numbers relevant to heat transfer in particle flows.

Dimensionless Number	**Expression**	**References**
Péclet Number	$Pe_L = \frac{uL}{\alpha_p}$	—
	$Pe_L^* = \left(\frac{uL}{\alpha_p}\right)\left(\frac{k}{k_g}\right)^2\left(\frac{d_p}{L}\right)^2$	[43–45]
Graetz Number	$Gz = \frac{Pe_{D_h} D_h}{L} = \frac{uD_h^2}{\alpha_p L}$	[67–70]
Nusselt Number	$\overline{Nu}_L = \frac{\overline{h}_{pw} L}{k}$	—
	$\overline{Nu}_d = \frac{\overline{h}_{pw} d_p}{k_g}$	[43–45]
	$\overline{Nu}_{D_h} = \frac{\overline{h}_{pw} D_h}{k}$	[67–70]

Table 1.3 summarizes the heat transfer coefficients or Nusselt number correlations established in previous studies.

Mickley and Fairbanks analytically derived the particle-to-wall heat transfer coefficient by considering packets of particles sweeping along the wall surface during short residence times [71]. The correlation was also experimentally tested for glass bead and microsphere particles. Sullivan and Sabersky constructively introduced a wall-particle thermal resistance term, χ, into an analytical plug flow model (Fig. 1.3(a)) [43]. By fitting their empirical measurements across various particle sizes, thermal conductivities, and channel lengths, they determine this wall-adjacent resistance term equal to 0.085. Their semi-empirical correlation showed excellent agreement with experimental data (Fig. 1.3(b)), emphasizing the importance of thermal resistance near the boundaries of heat exchangers — a phenomenon later termed as "near-wall effect". Subsequent researchers sought to incorporate this effect to refine their models. For instance, Denloye extended Mickley and Fairbanks' correlation by adding a contact resistance term [72], verified experimentally in a vertical particle flow setup, highlighting the impact of fluid phase thermal conductivity using Archimedes number, Ar. Other researchers have adapted Sullivan and Sabersky's correlation for different

Table 1.3: Heat transfer coefficient or Nusselt number correlations in prior work

Reference	**Correlation**	**Geometric Setup**	**Approach**	**Test Parameters**
Mickley and Fairbanks [71]	$h = \frac{2}{\sqrt{\pi}}\sqrt{\frac{uk\rho c_p}{L}}$	Vertical Rod	Analytical	$\phi_s = 0.60 - 0.65$ $d_p = 0.08$ mm $k_{\text{eff}} = 0.073 - 2.270$ W/m/K
Sullivan and Sabersky [43]	$\overline{Nu}_L = \left(\chi + \frac{\sqrt{\pi}}{2}\sqrt{\frac{1}{Pe_L^*}}\right)^{-1}$ $\chi = 0.085$	Vertical Plate	Analytical + Experimental	$u = 0.5 - 5$ cm/s $\phi_s = 0.60 - 0.65$ $d_p = 0.20 - 2.16$ mm $k_{\text{eff}} = 0.073 - 2.270$ W/m/K
Deloney and Botterill [72]	$\overline{Nu}_{d,\max} = 1.283A_r^{0.623}$ $A_r = gd_p(\rho_s - \rho_g)/\mu_s$	Vertical Rod	Analytical + Experimental	$d_p = 0.16 - 2.37$ mm $Ar = 10^3 - 10^6$
Patton and Sabersky [44]	$\overline{Nu}_d = \left(\chi + \frac{\sqrt{\pi}}{2}\sqrt{\frac{1}{Pe_L^*}}\left(1 + \beta\frac{Fr^*}{\sqrt{Pe_L^*}}\right)\right)^{-1}$ $\chi = 0.065$ $Fr^* = \left(\frac{u^2}{ghcos\theta}\right)\left(\frac{0.56}{\phi_s}\right)\left(\frac{d_p}{L}\right)\left(\frac{k_s}{k_g}\right)$	Inclined Plate	Analytical + Experimental	$d_p = 0.26, 2.94$ mm $k_{\text{eff}} = 0.21$ W/m/K
Colakyan [73]	$\overline{Nu}_d = 1.65\left(Pe_L\left(\frac{k}{k_g}\right)\left(\frac{d_p}{L}\right)\right)^{0.25}$	Horizontal Rod	Experimental	$u = 0.2 - 4$ cm/s $d_p = 0.27 - 2$ mm $k_{\text{s}} = 0.04 - 380$ W/m/K

Table 1.3: (continued) Heat transfer coefficient or Nusselt number correlations in prior work

Reference	**Correlation**	**Geometric Setup**	**Approach**	**Test Parameters**
Obuskovic and Colakyan [74]	$\overline{Nu}_d = 2.37(Pe_L^*)^{0.25}\left(\frac{k}{k_g}\right)^{0.3}\left(\frac{d_P}{L}\right)^{0.33}$	Horizontal Finned Tube	Experimental	$u = 0.1 - 2.5$ cm/s $\phi_s = 0.375 - 0.6$ $d_p = 0.11 - 1.6$ mm $k_{\text{s}} = 0.329, 0.8, 384$ W/m/K
Muzychka et al. [67]	$\overline{Nu}_{D_h} = \left(\left(\frac{1.128}{\sqrt{Gz^{-1}}}\right)^2 + (9.87)^2\right)^{1/2}$ for isothermal plane	Plane Channel	Analytical	
Wei et al. [75]	$\overline{Nu}_{D_h} = \left[\Sigma_{n=1}^{\infty}\frac{D_h Pe_{D_h}}{32n^4\pi^4 L}\left(\exp\left(-\frac{n^2\pi^2 L}{D_h Pe_{D_h}}\right) - 1\right) + \frac{R_{\text{nw}}}{R_p} + \frac{1}{12}\right]^{-1}$ $R_{\text{nw}} = \frac{d_p}{2k_{\text{nw,eff}}}$	Vertical Plate	Analytical + Numerical + Experimental	$\dot{m} = 15.1 - 37.2$ g/s $\phi_s = 0.506 - 0.525$ $d_p = 0.271, 0.364$ mm $k_{\text{eff}} = 0.12, 0.15$ W/m/K $T_p = 30 - 43$ °C
Adapa et al. [70]	$\overline{Nu}_{D_h} = \left[\Sigma_{n=1}^{\infty}\frac{D_h Pe_{D_h}}{32n^4\pi^4 L}\left(\exp\left(-\frac{16n^2\pi^2 L}{D_h Pe_{D_h}}\right) - 1\right) + \frac{R_{\text{nw}}}{R_p} + \frac{1}{12}\right]^{-1}$ $R_{\text{nw}} = \frac{D_{\text{air}}}{k_{\text{air}}}, \quad R_{\text{p}} = \frac{D_h}{4k_{\text{b,eff}}}$	Vertical Plate	Analytical + Experimental	$u = 0.5 - 1.5$ cm/s $\phi_s = 0.57 - 0.67$ $d_p = 0.28 - 0.96$ mm $k_{\text{eff}} = 0.21 - 0.64$ W/m/K $T_p = 300 - 650$ °C

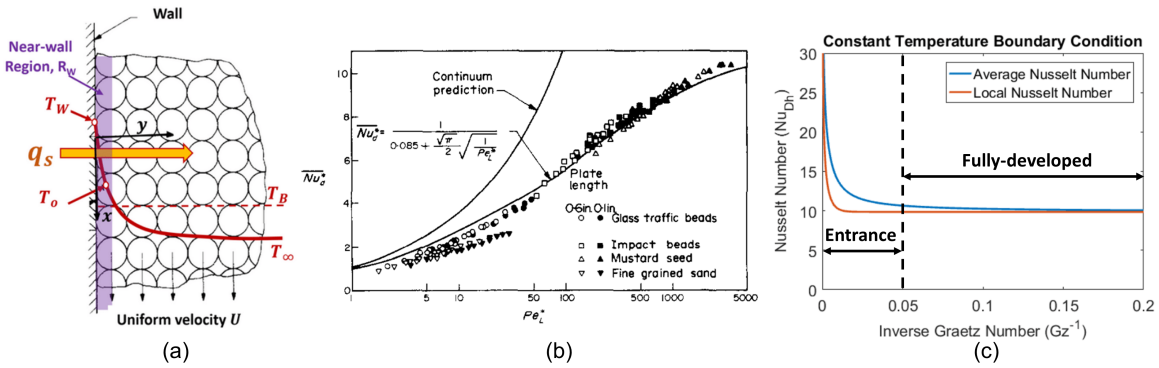


Figure 1.3: (a) Plug flow model of a moving bed heat exchanger with ordered arrangement from Sullivan and Sabersky's work [43]; (b) Nusselt number as a function of modified Péclet number for all materials tested in Sullivan and Sabersky's work [43]; (c) Nusselt number as a function of inverse Graetz number for constant temperature boundary condition [65,67].

heat exchanger configurations. Patton explored inclined chute flows, proposing an additional term for the plane's inclination angle [44]. Colakyan extended the model for a heating rod by incorporating a near-wall thermal resistance term [73]. Obuskovic applied a modified version to finned-tube moving bed setup [74].

Muzychka derived Graetz number correlations by developing analytical solutions for transient heat transfer in laminar pipe flow [67]. His work demonstrated that the local hydraulic diameter-based Nusselt number approaches a constant value once the inverse Graetz number is sufficiently large, indicating a fully developed thermal flow beyond a critical channel length (Fig. 1.3(c)). These Graetz number correlations serve as benchmarks and have been applied to transient heat transfer research in moving bed flows, with ongoing investigations into incorporating near-wall resistance terms to enhance accuracy for moving bed heat exchangers [68–70]. Recently, Wei et al. developed a 2D numerical model that includes effective bulk and near-wall conductivities [75]. A Nusselt number correlation was derived similar to Muzychka's work, with varied differential scheme applied between their work. Adapa et al. directly included a near-wall thermal resistance term into Muzychka's correlation and generated their Nusselt number correlation [70]. Although the Nusselt number correlations between

Wei and Adapa looks similar, their strategies to obtain their near-wall thermal resistance differs. Wei et al. rely on the analytical derivation from their model, while the near-wall resistance term from Adapa's work is obtained through an air gap distance, which is obtained from modulated photothermal radiometry (MPR) measurements in their experiments.

1.3.2 Knowledge Gaps

Compared to conduction [46, 51–53, 55–57, 76, 77] and fluid-phase convection [54, 78, 79], radiative heat transfer in solid-gas flows is less addressed, while it plays a crucial role in high-temperature applications. Traditionally, many assumptions are implemented to solve for heat flux and temperature profiles [46, 61–63, 80–82] due to limited development of radiation related modeling resources. The easiest way to account for radiative effects is to include it in the effective thermal conductivity correlations [80–85], which are only accurate under specific solid volume fraction, optical properties and packing structure. Monte Carlo ray tracing technique is generally considered to give accurate prediction on radiative behaviors. However, the computational cost of performing such simulations is very expensive for flowing systems, which limits these research to conduct one-way coupling between flow and heat transfer models [46, 61–63, 80], and only captures snapshots of particle positions for radiative modeling. Therefore, researchers divide the scenarios for dilute and dense flow, applying them with different assumptions. Some case-specific assumptions restrict to dense flows with black surfaces [46, 61, 63]. For dilute bed, two-fluid continuum models [86, 87] offer computational efficiency. However, determining effective radiative properties is challenging with numerous assumptions. This different treatment for dense and dilute flows leads to a gap in understanding the influence of solid volume fraction on the modes of heat transfer in granular flows.

The empirical and semi-empirical correlations presented in Table 1.3 are predom-

inantly based on the assumption of a continuum plug flow with near-wall resistance. These models are effective for moving bed systems with small particle sizes, where particle movement closely resembles that of continuous fluids. However, these models face limitations when particles are comparable in size to the characteristic dimensions of the heat exchanger, failing to adequately capture the discrete nature of particle flows. Despite the significant influence of solid volume fraction on heat transfer in moving bed heat exchangers, few advanced correlations explicitly incorporate this parameter, often treating it as merely a secondary factor affecting near-wall thermal resistance.

1.3.3 Hypotheses & Research Objectives

Based on these knowledge gaps, this research proposes the following hypotheses:

1. Heat transfer in granular flows will be strongly influenced by the solid volume fraction (ϕ_s) and particle size.

2. Solving the radiosity equation can be accelerated using parallelization techniques.

To test these hypotheses, the objectives of this research is to:

- Develop a multimode heat transfer model that couples DEM-based particle flow modeling with conductive and radiative heat transfer mechanisms.
- Create comprehensive heat transfer correlations that explicitly incorporate geometric and thermophysical parameters, including the solid volume fraction of the moving bed.
- Derive dimensionless Nusselt number dependencies on ϕ_s for conductive and radiative heat transfer.
- Develop a parallelization technique for solving radiosity equation that can be seamlessly integrated into existing DEM simulator.

1.4 Thesis Outline

This dissertation comprises one methodology chapter and four research chapters, each addressing distinct modeling investigations of particulate systems. Chapter 2 details the modeling techniques used in subsequent chapters. Chapters 3 and 4 focus on radiative transport in particulate media, whereas Chapters 5 and 6 explore the application of a DEM-based, radiation-coupled heat transfer solver to characterize particle flow and heat transfer.

Chapter 2 outlines the computational tools: (1) collision-based Monte Carlo ray tracing (MCRT), and path-length ray tracing techniques for tracking light emission, absorption and scattering in particulate media, used in Chapters 3 and 4; and (2) the Discrete Element Method (DEM) for modeling particle movement, collisions, and heat transfer, including existing solid-solid conduction, solid-fluid-solid conduction, and self-developed radiation models.

Chapter 3 is adapted from a publication in the *International Journal of Heat and Mass Transfer*. This chapter examines the influences of the three-dimensional spatial distributions and the solid volume fractions of particles on radiative transport. It uses the index of cluster sampling (ICS) and MCRT simulations to obtain radiative properties, revealing that radiative transmittance is significantly influenced by spatial distributions and leading to a generalized correlation.

Chapter 4 is primarily adapted from a publication in the journal *Solar Energy*. This study introduces a scale factor to account for particle surface reflectivity in a modified form of Beer's law for particle curtains. Solid volume fraction distribution, either obtained from DEM simulations or computed through transmittance measurements from a thermopile detector and a high-speed camera, demonstrated very similar trends of decreasing along the flow direction.

Chapter 5 is adapted from a publication in the journal *Powder Technology*. A plug flow model, along with a gravity-driven, moving bed model are developed to

illustrate heat transfer coefficient dependence on solid volume fraction. Key insights emerge regarding the interplay between flow physics, conduction, and radiation.

Chapter 6 is based on a manuscript submitted for publication. This chapter focuses on conducting parametric studies to explore the effects of particle characteristics and channel dimensions on heat transfer. This study develops universal dimensionless Nusselt and Péclet number correlations for multivariate influence.

Chapter 7 summarizes the research contributions and suggest future directions to further advance the modeling of radiative transport and heat transfer for particulate media.

CHAPTER II

Radiative and Heat Transfer Models for Discrete Particles

Parts of this chapter have been published by the author of this thesis:

- **Li, B., Bala Chandran, R., 2022. Effects of spatial correlations in particulate media on dependent scattering and radiative transport. International Journal of Heat and Mass Transfer 182, 121951.**
- **Li, B., Chen, Z., Bala Chandran, R., 2024. Conductive and radiative heat transfer mechanisms inform Nusselt number dependence on solid volume fraction for granular flows. Powder Technology 440, 119737.**

This chapter outlines the methodology utilized in this study, focusing on the Monte Carlo Ray Tracing (MCRT) method and the Discrete Element Method (DEM). The rationale for selecting these specific models is thoroughly examined. Additionally, a detailed description of the self-developed radiative heat transfer model is provided.

2.1 Monte-Carlo Ray Tracing Method

In particulate media, the radiative transport equation (RTE) (Eq. (1.1)) typically lacks exact, closed-form solutions, necessitating the use of numerical approaches for

most practical applications. Among these, the Monte Carlo Ray Tracing (MCRT) method stands out as a statistical technique that tracks a large number of rays through the geometry to simulate the emission, attenuation, and transmission events between rays and surfaces [88]. Due to its high accuracy in computing radiation interactions, the MCRT method is often employed as a benchmark for validating other radiation models [62].

2.1.1 Collision-based Method

In this study, an in-house code was developed in C++ and compiled using Microsoft Visual Studio Community 2019 to conduct collision-based MCRT simulations [15, 88]. The algorithm is illustrated in Fig. 2.1. Our investigation focuses on scenarios where particle size parameters are large ($\pi d_p/\lambda \gg 1$), typically exceeding 10, which is common in heat transfer and catalysis applications involving radiative transport [15, 89]. Under these conditions, the assumption of geometric optics is applicable for modeling radiation propagation. In the simulations, rays or energy bundles are diffusely launched from the base ($z = 0$ mm) of a rectangular box with dimensions 8 mm $\times$ 8 mm $\times$ 20 mm. For a diffuse and isotropic emitter, the polar angle, θ, and azimuthal angle, φ, of the emitted energy bundles are computed using random numbers, R_θ and R_φ, drawn from a uniform distribution over [0,1] according to Eq. (2.1) [88].

$$\begin{aligned} \theta &= \sin^{-1}\left(\sqrt{R_\theta}\right) \\ \varphi &= 2\pi R_\varphi \end{aligned} \tag{2.1}$$

Once launched, the intersection of rays with particles within the box, numbering up to 78,000 at the highest solid volume fraction modeled in our study, is determined by solving the line-sphere intersection equation given in Eq. (2.2), as depicted in Fig. 2.2(a).

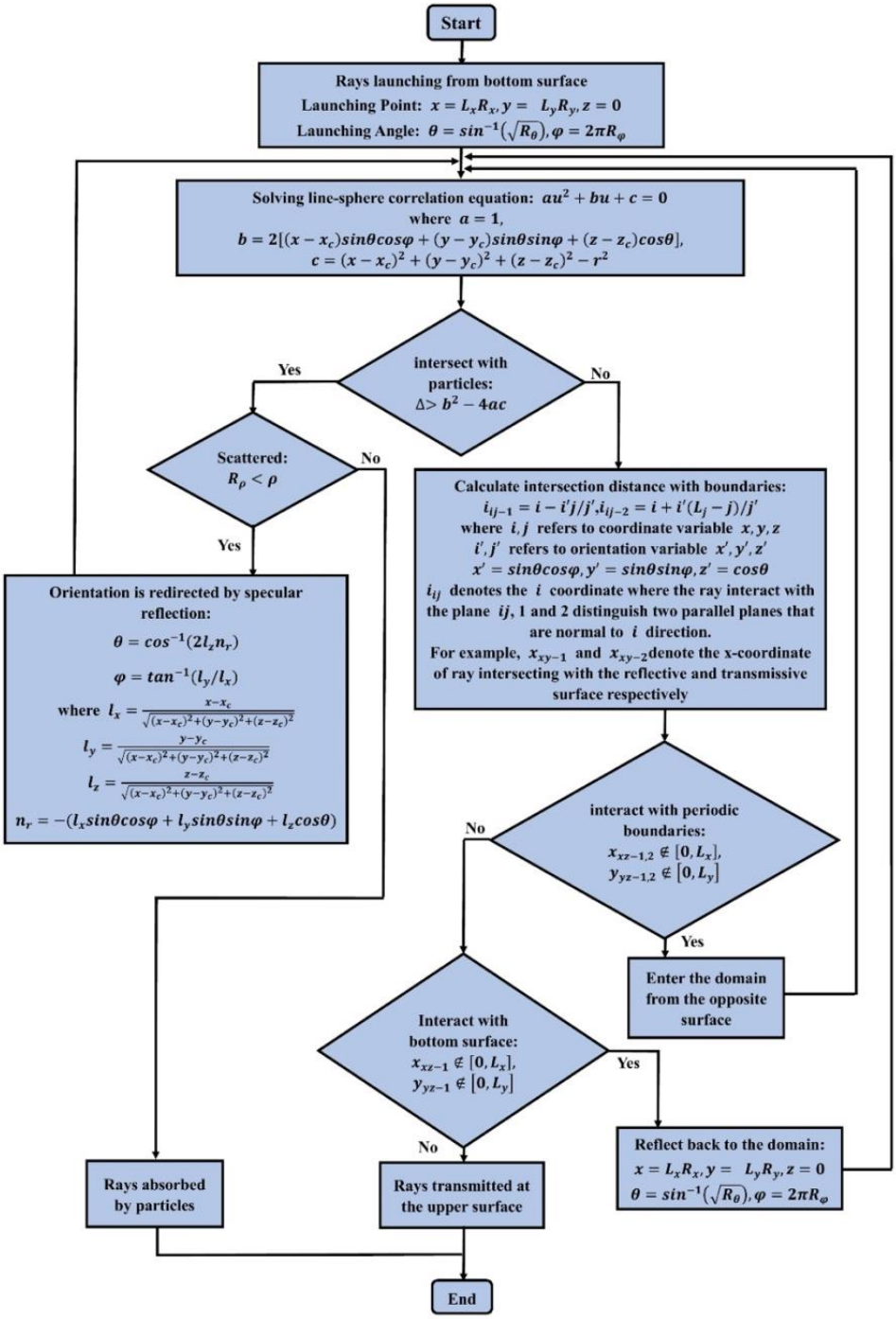


Figure 2.1: Flowchart to lay out the approach and implementation of collision-based ray tracing simulations to compute radiative transport. Random numbers sampled from a uniform distribution of [0,1] are represented as R_i, where the subscript i refers to the variable for which the random number was generated. For example, R_x corresponds to a random number generated to sample for the x-location of the launch points. Overall, all the rays launched from the bottom surface were tracked until they either got absorbed by the particles or left the domain at the $z = 20$ mm plane.

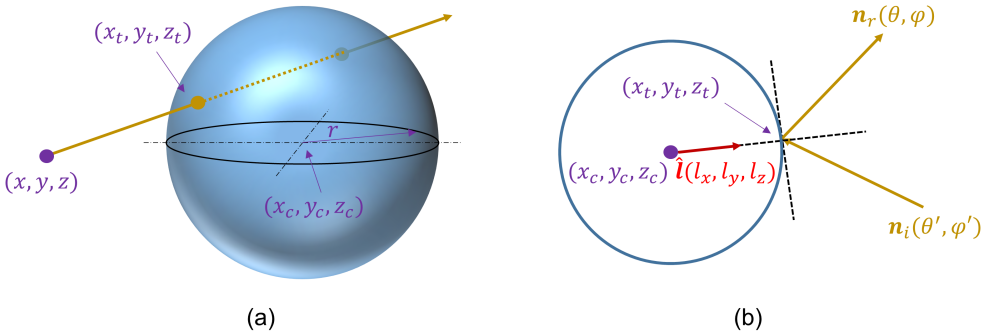


Figure 2.2: (a) A schematic diagram of a line, originated from a point (x, y, z), intersect with a spherical object, located at (x_c, y_c, z_c) with a radius of r, at point (x_t, y_t, z_t); (b) A schematic diagram of determining the scattered orientation, $\mathbf{n}_r(\theta, \varphi)$, of an incident ray, $\mathbf{n}_i(\theta', \varphi')$, specularly reflected by a spherical object located at (x_c, y_c, z_c).

$$au^2 + bu + c = 0 \tag{2.2}$$

where $a = 1$

$$b = 2\left((x - x_c)\sin\theta\cos\varphi + (y - y_c)\sin\theta\sin\varphi + (z - z_c)\cos\theta\right)$$

$$c = (x - x_c)^2 + (y - y_c)^2 + (z - z_c)^2 - r^2$$

The intersection point is calculated when Eq. (2.2) has real solutions (i.e., $b^2 - 4ac > 0$). The coordinates of the intersection point are given by Eq. (2.3).

$$\begin{cases} x_t = x + s_{min}\sin\theta\cos\varphi \\ y_t = y + s_{min}\sin\theta\sin\varphi \\ z_t = z + s_{min}\cos\theta \\ s = \dfrac{-b \pm \sqrt{b^2 - 4ac}}{2a} \end{cases} \tag{2.3}$$

where s_{min} is the minimum distance when iterating over all particles.

The particles in this study are assumed to be opaque and grey, implying that rays do not transmit through them and radiative properties are wavelength-independent. Rays interacting with particle surfaces are either absorbed or specularly reflected, governed by a constant particle reflectivity (scattering albedo), $\rho = 0.7$. A scattering

event is determined by comparing a random value, R_ρ, from a uniform distribution of [0,1], against the reflectivity value. Absorption occurs if $R_\rho \geq \rho$, terminating the ray's path, while specular reflection occurs if $R_\rho < \rho$, with the new direction calculated using Eq. (2.4) (Fig. 2.2(b)) [90].

$$\begin{gathered} \theta = \cos^{-1}(2l_x n_r) \\ \varphi = \tan^{-1}(l_y/l_x) \\ \begin{cases} l_x = \frac{x_t - x_c}{\sqrt{(x_t-x_c)^2+(y_t-y_c)^2+(z_t-z_c)^2}} \\ l_y = \frac{y_t - y_c}{\sqrt{(x_t-x_c)^2+(y_t-y_c)^2+(z_t-z_c)^2}} \\ l_z = \frac{z_t - z_c}{\sqrt{(x_t-x_c)^2+(y_t-y_c)^2+(z_t-z_c)^2}} \end{cases} \\ n_r = -(l_x \sin\theta\cos\varphi + l_y \sin\theta \sin\varphi + l_z \cos\theta) \end{gathered} \tag{2.4}$$

The boundary conditions of the rectangular box are defined as follows: The bottom surface, $z = 0$ mm, is diffuse and totally reflective to emulate a perfect launch surface, ensuring maximal launching conditions, whereas the top surface, $z = 20$ mm, is fully transmissive, allowing rays to leave the ray-tracing domain. Lateral surfaces, $x = 0$ mm, $x = 8$ mm, $y = 0$ mm, $y = 8$ mm, are treated as periodic boundaries, with rays exiting one side re-entering from the opposite side.

Since rays do not interfere with each other, ray generation and tracing are parallelized using Message Passing Interface (MPI), achieving near linear computational speedup with the number of processors utilized.

The collision-based MCRT simulations were validated by comparing the predictions for radiative transmittance predictions with published data from Singh and Kaviany [22]. Results matched within 0.1% and 20% relative error (Fig. A.1 in Appendix A.1) for the smallest (0.008) and the largest (0.52) solid volume fractions modeled respectively. The increasing deviation at the largest solid volume fraction is attributed to the disparities in the spatial distributions of the particles between our

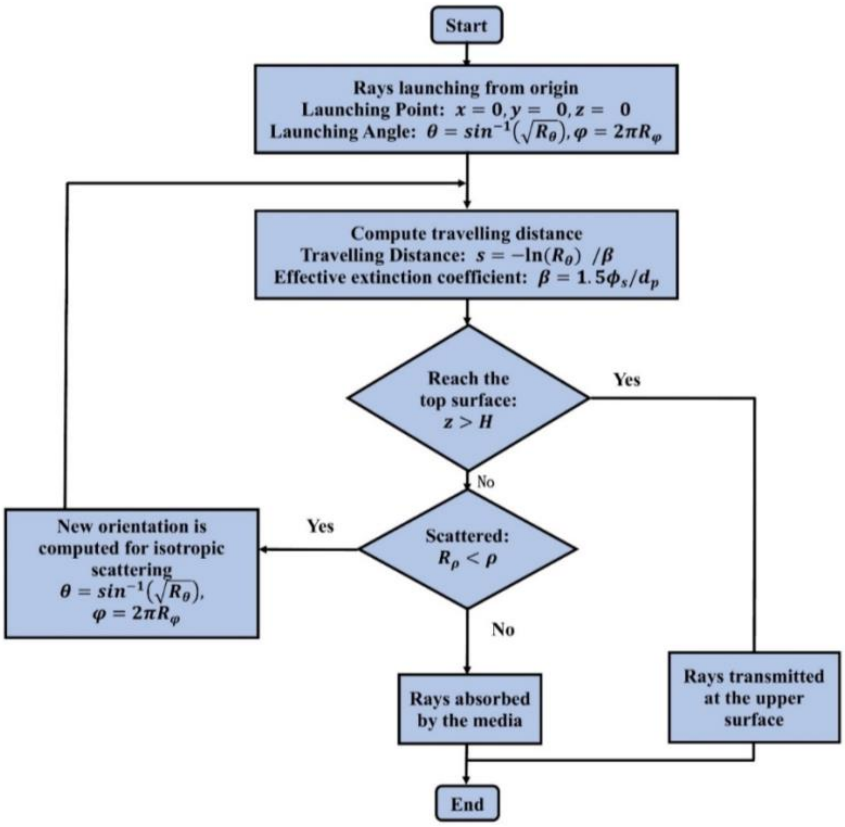


Figure 2.3: Flowchart to lay out the approach and implementation of path-length ray tracing simulations to compute radiative transport. Random numbers sampled from a uniform distribution of [0,1] are represented as R_i, where the subscript i refers to the variable for which the random number was generated. For example, R_x corresponds to a random number generated to sample for the x-location of the launch points. Overall, all the rays launched from the bottom surface were tracked until they either got absorbed by the particles or left the domain at the $z = 20$ mm plane.

models and those used by the authors.

2.1.2 Path-length Method

A path-length MCRT simulation was conducted to evaluate radiative transmittance predicted by independent scattering theory and to derive effective extinction coefficients from collision-based MCRT simulation results. The path-length approach models the packed bed of particles as a continuum. It traces the paths of numerous rays within the medium using effective radiative properties, including the extinction

coefficient, scattering albedo and scattering phase function. Unlike the collision-based MCRT simulations, which explicitly account for ray interactions with individual particles, the path-length MCRT method is computationally less intensive [91].

The path-length MCRT simulation was implemented using a MATLAB code, with the algorithm depicted in Fig. 2.1. In contrast to the collision-based method that tracks each individual emission, absorption and scattering event, the path-length approach monitors rays as they are gradually absorbed by the surface or medium. After being launched from the bottom surface ($z = 0$ mm), the travel distance between scattering events for each ray is determined using Eq. (2.5), which is derived from the Beer's law, with a reflection probability sampled from a uniform distribution in the range (0,1] [92].

$$s = -\frac{\ln(R_\alpha)}{\beta} = -\ln(R_\alpha)\frac{2d_p}{3\phi_s} \tag{2.5}$$

According to independent scattering theory, the extinction coefficient, β, is determined similar to Eq. (1.2). If a ray is scattered (i.e., $R_\rho < \rho$), its new direction is calculated under the assumption of isotropic scattering, as described by Eq. (2.1). All other ray-tracing behaviors, such as emission and transmission, are consistent with those used in the collision-based approach outlined in Sec. 2.1.1.

2.2 Discrete Element Method

The Discrete Element Method (DEM) is a numerical simulation technique well-suited for modeling particle systems, where interactions between neighboring particles are characterized as dynamic processes [60, 62, 93]. The particle positions and velocities are computed based on the Verlet algorithm [94], which is a numerical method to integrate Newton's equations of motion. The method advances the system's time evolution by employing a simple explicit finite difference scheme to compute new particle

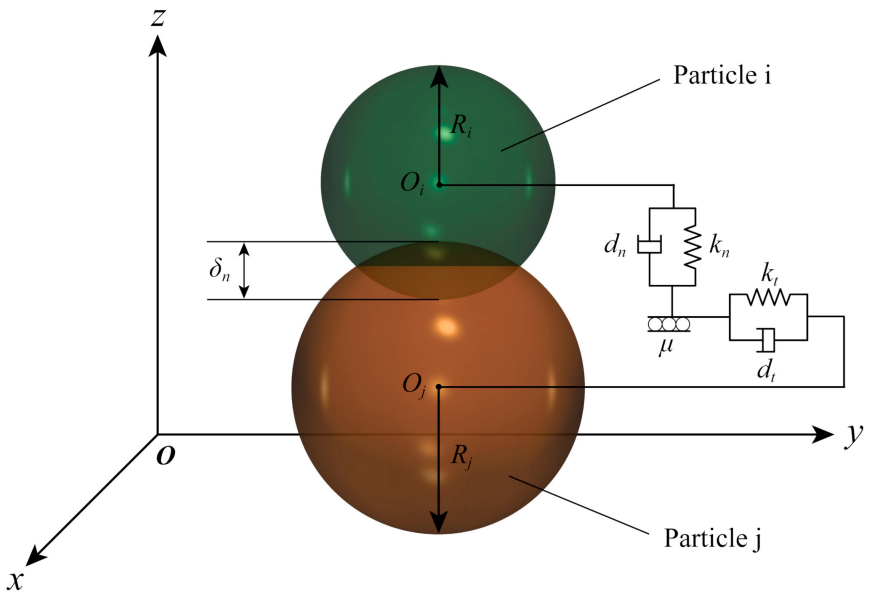


Figure 2.4: Hertz-Mindlin contact Model obtained from Chen et al. [97].

positions and velocities. In recent years, the DEM technique has gained popularity for exploring the heat transfer characteristics of particulate systems, as it offers detailed local and transient information on flow and heat transfer at the particle scale [60]. In this study, an open-source Discrete Element Method (DEM) software — LAMMPS Improved for General Granular and Granular Heat Transfer Simulations (LIGGGHTS), is used to track and update the positions, velocities, and temperatures of individual particles [95]. New functions of computing radiative heat transfer are implemented into the LIGGGHTS source code.

2.2.1 Flow Modeling

The Hertz-Mindlin model as described in Fig. 2.5 is applied to calculate the forces and moments based on the soft-sphere approach. This is a spring-dashpot model that allows for overlap in the normal and tangential directions between particles and between particles and wall surfaces [96, 97].

The translational and rotational motion of particle i in contact with particle j can

be determined by Eqs. (2.6) and (2.7),

$$m_i \frac{d\mathbf{v}_i}{dt} = \sum_{i=1}^{n} \left(\mathbf{F}_{\mathrm{n},ij} + \mathbf{F}_{\mathrm{t},ij} \right) + m_i \mathbf{g} \tag{2.6}$$

$$I_i \frac{d\omega_i}{dt} = \sum_{i=1}^{n} \left(\mathbf{R}_i \times \mathbf{F}_{\mathrm{t},ij} - \tau_{\mathrm{r},ij} \right) \tag{2.7}$$

where m_i, $\mathbf{v}_i$, $\mathbf{g}$, I_i and ω_i are the mass, translational velocity, gravity vector, moment of inertia and rotational velocity of particle i respectively. $\tau_{\mathrm{r},ij}$ is the torque due to rolling friction. $\mathbf{F}_{\mathrm{n},ij}$ and $\mathbf{F}_{\mathrm{t},ij}$ are the normal and tangential forces between particle i and its neighboring particle j, which can be determined by Eq. (2.8) and Eq. (2.9),

$$\mathbf{F}_{\mathrm{n},ij} = k_{\mathrm{n}} \delta \hat{\mathbf{n}}_{ij} - \gamma_{\mathrm{n}} v \hat{\mathbf{n}}_{ij} \tag{2.8}$$

$$\mathbf{F}_{\mathrm{t},ij} = k_{\mathrm{t}} \delta \hat{\mathbf{t}}_{ij} - \gamma_{\mathrm{t}} v \hat{\mathbf{t}}_{ij} \tag{2.9}$$

where k_{n} and k_{t} are the elastic constant for normal and tangential contact respectively. $\delta \hat{\mathbf{n}}_{ij}$ and $\delta \hat{\mathbf{t}}_{ij}$ are the overlap displacements for normal and tangential contacts. γ_{n} and γ_{t} are the viscoelastic damping constants for normal and tangential contact. According to the Coulomb friction limit, the tangential force is truncated to fulfill $\mathbf{F}_{\mathrm{t}} \leq \mu \mathbf{F}_{\mathrm{n}}$, where μ is the coefficient of particle-particle friction.

In this research, we adopt a nonlinear viscoelastic model, where the elastic constants for normal and tangential contacts depend on the normal overlap displacement, δ_{n}, as given in Eqs. (2.10–2.11). The viscoelastic damping constants are also a function of the overlap displacement as shown in Eqs. (2.12–2.13). This model is usually derived from the Hertzian theory of elastic contact and predicts particle collisions

more realistically than the linear viscoelastic model.

$$k_{\mathrm{n}} = \frac{4}{3} Y^* \sqrt{R^* \delta_{\mathrm{n}}} \tag{2.10}$$

$$k_{\mathrm{t}} = 8 G^* \sqrt{R^* \delta_{\mathrm{n}}} \tag{2.11}$$

$$\gamma_{\mathrm{n}} = -2\sqrt{\frac{5}{6}} \frac{\ln(e)}{\sqrt{\ln^2(e) + \pi^2}} \sqrt{2 m^* Y^* \sqrt{R^* \delta_{\mathrm{n}}}} \tag{2.12}$$

$$\gamma_{\mathrm{t}} = -2\sqrt{\frac{5}{6}} \frac{\ln(e)}{\sqrt{\ln^2(e) + \pi^2}} \sqrt{8 m^* G^* \sqrt{R^* \delta_{\mathrm{n}}}} \tag{2.13}$$

e is the coefficient of restitution, and Y^*, G^*, m^* and R^* are the reduced/effective Young's modulus, shear modulus, mass and particle radius respectively. These effective parameters can be calculated by Eqs. (2.14-2.17) when the Poisson ratio, ν, for particles in contact is provided.

$$\frac{1}{Y^*} = \frac{1 - \nu_i^2}{Y_i} + \frac{1 - \nu_j^2}{Y_j} \tag{2.14}$$

$$\frac{1}{G^*} = \frac{2(2 - \nu_i)(1 + \nu_i)}{Y_i} + \frac{2(2 - \nu_j)(1 + \nu_j)}{Y_j} \tag{2.15}$$

$$\frac{1}{m^*} = \frac{1}{m_i} + \frac{1}{m_j} \tag{2.16}$$

$$\frac{1}{R^*} = \frac{1}{R_i} + \frac{1}{R_j} \tag{2.17}$$

DEM simulations require the time step to be small enough to capture interparticle overlaps. The particle displacement within one time step should not exceed one particle diameter. This DEM time step is usually determined to be within 10% to 30% of the Rayleigh time step and no more than 10% of Hertz collision time [61, 62]. The Rayleigh time step and Hertz collision time step are given in Eq. (2.18) and Eq.

(2.19).

$$\Delta t_{\text{Rayleigh}} = \frac{\pi d_{\text{p}}}{2(0.8766 + 0.1631\nu)} \sqrt{\frac{2(1+\nu)\rho}{Y}} \tag{2.18}$$

$$\Delta t_{\text{Hertz}} = 2.87 \left(\frac{2m^2}{Y^2 v_{\max} d_{\text{p}}} \right)^{0.2} \tag{2.19}$$

2.2.2 Heat Transfer Models

In addition to position tracking, the temperature, T_j, of individual particles, j^{th} particle, is tracked with an energy-balance equation in Eq. (2.20); the rate of thermal energy stored in a particle, $m_j c_{p,j} \frac{dT_j}{dt}$, is balanced by the net rate of heat transfer between particles via conduction, $\dot{Q}_{ij,\text{cond}}$, and radiation, $\dot{Q}_{j,\text{rad}}$, from other particles and wall surfaces. For conductive heat transfer, Eq. (2.20) includes solid-solid, $\dot{Q}_{ij,\text{cond,ss}}$, and solid-fluid-solid conduction, $\dot{Q}_{ij,\text{cond,sfs}}$, pathways for inter-particle and particle-wall heat transfer. In Eq. (2.20), m_j and $c_{p,j}$ are the mass and mass-specific thermal capacity of the j^{th} particle respectively, and the i values ($i \neq j$) loop over other particles and wall surfaces, where N_{p} and N_{w} are the total number of particles and wall surfaces; $N_{\text{w}} = 2$ in this study, corresponding to the two heated walls. Particles are small enough that a uniform surface temperature, T_j, is assumed for all calculations.

$$m_j c_{p,j} \frac{dT_j}{dt} = \sum_{\substack{i=1 \\ i \neq j}}^{N_{\text{p}}+N_{\text{w}}} \left(\dot{Q}_{ij,\text{cond,ss}} + \dot{Q}_{ij,\text{cond,sfs}} \right) + \dot{Q}_{j,\text{rad}} \tag{2.20}$$

2.2.2.1 Solid-solid Conduction Model

Conductive heat transfer for solid-solid contacts, whether particle-particle or particle-wall, is an existing feature in LIGGGHTS (Eq. (2.21)). This flux formulation was

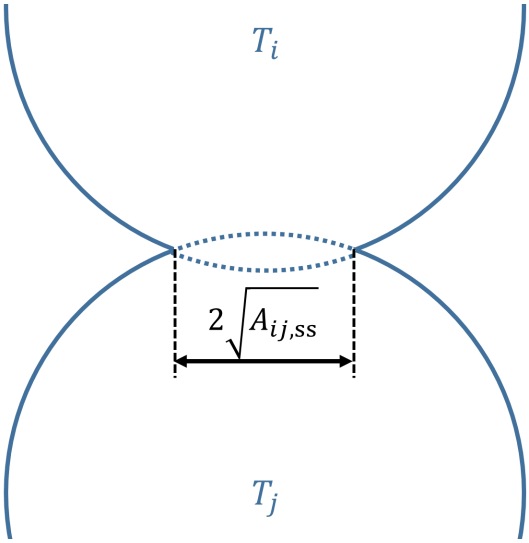


Figure 2.5: Solid-solid heat conduction model developed by Batchelor and O'Brien. Heat is conducted through the contact surface with radius, calculated as the effective radius from the contact area, $A_{ij,\mathrm{ss}}$.

first derived by Batchelor and O'Brien [76, 98],

$$\begin{aligned} \dot{Q}_{ij,\mathrm{cond,ss}} &= 2k_\mathrm{s}\sqrt{A_{ij,\mathrm{ss}}}(T_i - T_j)\left(\frac{Y}{Y^*}\right)^{\frac{1}{5}} \\ A_{ij,\mathrm{ss}} &= \frac{\pi}{4}(d_\mathrm{p} + d_{ij})(d_\mathrm{p} - d_{ij}) \end{aligned} \tag{2.21}$$

where $\dot{Q}_{ij,\mathrm{cond,ss}}$ is the conductive heat flux transferred to particle j from i neighboring particles, k_s is the thermal conductivity of particles, $A_{ij,\mathrm{ss}}$ is the area of overlap between the two objects in contact. This area is calculated using the inter-particle distance, d_{ij}, and particle size, d_p, according to Eq. (2.21), which is a simplified derivation for monodisperse particles [95]. Since the Young's modulus is artificially reduced to $Y = 5$ MPa for flow modeling, this simplification overestimates the area of overlap, $A_{ij,\mathrm{ss}}$, for heat transfer calculations. Therefore, a correction term $(Y/Y^*)^{1/5}$ is included, where Y and Y^* are the assumed values of 5 MPa for the flow simulation and the real material-specific Young's modulus set by the user respectively. The exponent of 1/5 in this correction corresponds to the Hertz contact model [98].

2.2.2.2 Solid-fluid-solid Conduction Model

The solid-fluid-solid conduction pathway, i.e., conduction through the stagnant interstitial air can be significant especially for the low solid volume fractions considered in this study [84]. Therefore, several techniques have been developed to account for this conduction pathway in DEM models [51, 54, 77]. In this study, the LIGGGHTS source code is modified to include the solid-fluid-solid conduction pathway, following the method proposed by Rong and Horio [51]. This method evaluates conductive resistance by assuming an annulus of fluid surrounding a spherical particle with a suggested thickness of $0.2d_{\mathrm{p}}$. Morris and Panala [52] extended this method to also evaluate conduction through the fluid present between the wall and individual particles, as depicted in Eq. (2.22).

$$\dot{Q}_{ij,\mathrm{cond,sfs}} = (T_i - T_j) \int_{r_{\mathrm{in}}}^{r_{\mathrm{out}}} \frac{2\pi k_{\mathrm{g}} r}{\max(l, s)} dr \tag{2.22}$$

where $\dot{Q}_{ij,\mathrm{cond,sfs}}$ is the conductive heat flux transferred from particle i to particle j through interstitial fluids, k_{g} is the thermal conductivity of the fluid phase, r is the radial position on a particle surface (Fig. 2.6), l is the normal distance from particle surface to either another particle surface or wall, which is a function of r. The lower and upper limits of the integral in Eq. (2.22), r_{in} and r_{out}, are respectively the smallest and the largest radial positions associated with the contacting annulus of the interstitial fluid present between particle-particle or particle-wall surfaces. The minimum conduction distance is dictated by the roughness of the particle, s, to prevent the integral from becoming singular in Eq. (2.22).

The solid-fluid-solid heat-transfer coefficient in Eq. (2.22) can be converted to a dimensionless variable by dividing by the fluid thermal conductivity and the particle radius, as shown in Eq. (2.23),

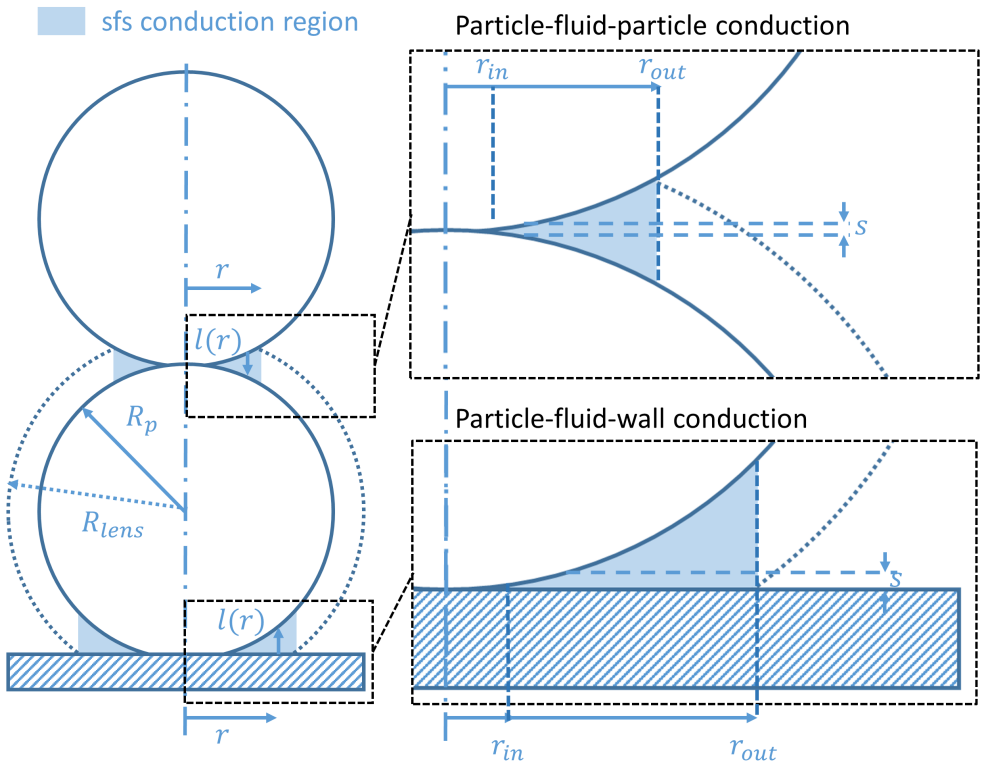


Figure 2.6: Schematic of the solid-fluid-solid conduction for particle-particle and particle-wall contact.

$$\hat{h}_{\text{cond,sfs}} = \frac{h_{\text{cond,sfs}}}{k_{\text{g}} R_{\text{p}}} = \int_{\hat{r}_{\text{in}}}^{\hat{r}_{\text{out}}} \frac{2\pi\hat{r}}{\max(\hat{l}, \hat{s})} d\hat{r} \tag{2.23}$$

where the non-dimensional variable denoted by hats, such as $\hat{l}$, $\hat{r}$, and $\hat{s}$ are the corresponding variables normalized by the particle radius. The result of the dimensionless solid-fluid-solid heat-transfer coefficient can be obtained from Eq. (2.24).

$$\hat{h}_{\text{cond,sfs}} = \begin{cases} \frac{\pi}{2\hat{s}}\left((1-\hat{\delta})^2 - A^2\right) \\ +\pi\left(B - A + (1-\hat{\delta})\ln\left(\frac{1-\hat{\delta}-B}{\hat{s}}\right)\right) & ,\hat{\delta} \geq 0 \\ 2\pi\left(\frac{\hat{r}_s^2}{2\hat{s}} + B - C\right) \\ +2\pi(1-\hat{\delta})\ln\left(\frac{1-\hat{\delta}-B}{1-\hat{\delta}-C}\right) & ,\hat{\delta} < 0 \end{cases} \tag{2.24}$$

Coefficients A, B, C in Eq. (2.24) are computed using Eq. (2.25),

$$\begin{aligned} A &= 1 - \hat{\delta} - \hat{s} \\ B &= \sqrt{1 - \hat{r}_{\text{out}}^2} \\ C &= \sqrt{1 - \hat{r}_{\text{s}}^2} \end{aligned} \tag{2.25}$$

where s is the minimum contact distance between surfaces. This value is varied for particle-particle and particle-wall contact. In this research, $\hat{R}_{\text{lens}}$ is fixed as 1.2. The particles are assumed to be smooth and thus s is comparable to the mean free path of gas molecules ($s_{\text{pw}} = 2s_{\text{pp}} = 2.75 \times 10^{-8}$ m). The effects of s on interstitial fluid conduction are elaborated by Morris et al. [52]. The lower bound of the integral $\hat{r}_{\text{s}}$ is the non-dimensional radial position that corresponds to where the particle to particle/wall surface distance equals to the minimum conduction distance ($\hat{l}(r_{\text{s}}) = \hat{s}$) (Fig. 2.6). The upper bound of the integral, $\hat{r}_{\text{out}}$, differs for particle-particle and

particle-wall contact. The calculations of these variables are given in Eq. (2.26),

$$\hat{r}_{\text{out,pp}} = \begin{cases} \hat{R}_{\text{lens}}\sqrt{1-\frac{(\hat{R}_{\text{lens}}^2+\hat{d}^2-1)^2}{4\hat{R}_{\text{lens}}^2\hat{d}}}, & \hat{d} > \sqrt{\hat{R}_{\text{lens}}^2-1} \\ 1, & \hat{d} \leq \sqrt{\hat{R}_{\text{lens}}^2-1} \end{cases}$$

$$\hat{r}_{\text{out,pw}} = \begin{cases} \sqrt{\hat{R}_{\text{lens}}^2-(1-\hat{\delta})^2}, & \hat{\delta} < 1-\sqrt{\hat{R}_{\text{lens}}^2-1} \\ 1, & \hat{\delta} \geq 1-\sqrt{\hat{R}_{\text{lens}}^2-1} \end{cases} \tag{2.26}$$

$$\hat{r}_{\text{s}} = \begin{cases} \sqrt{1-A^2}, & \hat{\delta} > -\hat{s} \\ 0, & \hat{\delta} \leq -\hat{s} \end{cases}$$

where $\hat{d}$ is the non-dimensional distance between two particle centers. $\hat{\delta}$ denotes the non-dimensional overlap distance for particle-wall contact and half the overlap distance for particle-particle contact respectively. $\hat{R}_{\text{lens}}$ is the non-dimensional radius of the fluid lens. The influence of $\hat{R}_{\text{lens}}$ on the conductive heat flux through interstitial fluid was also discussed by Morris et al. [54].

2.2.2.3 Radiation Model: Traditional Matrix Solver

To obtain the radiative heat transfer rate for individual particles, $\dot{Q}_{j,\text{rad}}$ in Eq. (2.20), a new function is implemented in the LIGGGHTS source code. All particles and walls are assumed to be grey and diffuse, and air assumed to be transparent to radiation. The net radiative flux leaving each particle surface can be obtained by considering a radiative energy balance with emitted and reflected components of thermal radiation as shown in Eq. (2.27),

$$\sum_{j=1}^{N_{\text{w}}+N_{\text{p}}} \left(\frac{\delta_{ij}}{\epsilon_j} - \left(\frac{1}{\epsilon_j} - 1 \right) \hat{F}_{ij} \right) q_j = \sum_{j=1}^{N_{\text{w}}+N_{\text{p}}} \left(\delta_{ij} - \hat{F}_{ij} \right) \sigma T_j^4 \tag{2.27}$$

where q_j is the net radiative heat flux and considered to be positive when it leaves the j^{th} surface, ϵ is the emissivity, δ_{ij} is the Kronecker delta, $\hat{F}_{ij}$ is the pairwise diffuse radiative view factor between i and j surfaces, and T_j is the temperature in Kelvin for the j^{th} surface. The radiative fluxes on all surfaces can be obtained by simultaneously solving the $N_\mathrm{w} + N_\mathrm{p}$ system of equations from Eq. (2.27), with the knowledge of surface temperatures and radiative properties. Because Eq. (2.27) assumes an enclosed system of surfaces, even if not all walls thermally interact with the particles, the calculated particle-wall view factors are consistent with an enclosure comprising 6 walls and only the view factors for the heating walls are used to update the temperature distribution. The rate of radiative heat transfer received by particle j is shown in Eq. (2.28),

$$\dot{Q}_{j,\mathrm{rad}} = -q_j A_{\mathrm{p},j} \tag{2.28}$$

where $A_{\mathrm{p},j}$ is the total surface area of j^{th} particle, which equals πd_p^2 and q_j is the net radiative heat flux obtained from Eq. (2.27). The negative sign is applied to transform the radiative flux emitted from the particle j to a positive radiative heat transfer rate entering particle j.

To fully couple heat transfer calculations with particle position tracking, reduced-order view factor correlations are developed based on multivariate linear regression models, as listed in Table 2.1. This makes the computations of pairwise view factors computationally tractable. Training data for these correlations is obtained from collision-based Monte Carlo ray tracing simulations as elaborated in Sec. 2.1.1, with 150–3600 particles ($\phi_s = 0.02 - 0.48$) randomly distributed in a rectangular box as later shown in Fig. 3.1. In a departure from our previous study that scanned neighboring particles, we capture the shading effects in an average sense to lower computational cost which are specific to the solid volume fraction. Specifically, Monte Carlo

Table 2.1: Particle-particle, F_{pp}, and particle-wall, F_{pw}, view factor correlations based on dimensionless distances, d^*, for different solid volume fraction ranging from 0.02 to 0.48.

Solid Volume Fraction, ϕ_{s}	**Particle-Particle View Factor Correlation**	**Particle-Wall View Factor Correlation**
0.02	$F_{\mathrm{pp}} = -1.1 \times 10^{-5} - \frac{0.0012}{d^*} + \frac{0.058}{d^{*2}} + \frac{0.016}{d^{*3}}$	$F_{\mathrm{pw}} = -0.11 + \frac{1.9}{d^*} - \frac{2.1}{d^{*2}} + \frac{0.92}{d^{*3}}$
0.07	$F_{\mathrm{pp}} = 2.6 \times 10^{-4} - \frac{0.0080}{d^*} + \frac{0.071}{d^{*2}} + \frac{0.011}{d^{*3}}$	$F_{\mathrm{pw}} = -0.074 + \frac{0.96}{d^*} - \frac{0.54}{d^{*2}} + \frac{0.092}{d^{*3}}$
0.15	$F_{\mathrm{pp}} = 7.2 \times 10^{-4} - \frac{0.015}{d^*} + \frac{0.072}{d^{*2}} + \frac{0.018}{d^{*3}}$	$F_{\mathrm{pw}} = -0.030 + \frac{0.23}{d^*} + \frac{0.76}{d^{*2}} - \frac{0.54}{d^{*3}}$
0.25	$F_{\mathrm{pp}} = 9.1 \times 10^{-4} - \frac{0.017}{d^*} + \frac{0.057}{d^{*2}} + \frac{0.036}{d^{*3}}$	$F_{\mathrm{pw}} = 0.018 - \frac{0.36}{d^*} + \frac{1.8}{d^{*2}} - \frac{1.1}{d^{*3}}$
0.31	$F_{\mathrm{pp}} = 7.9 \times 10^{-4} - \frac{0.013}{d^*} + \frac{0.034}{d^{*2}} + \frac{0.057}{d^{*3}}$	$F_{\mathrm{pw}} = 0.020 - \frac{0.34}{d^*} + \frac{1.4}{d^{*2}} - \frac{0.71}{d^{*3}}$
0.37	$F_{\mathrm{pp}} = 6.2 \times 10^{-4} - \frac{0.0091}{d^*} + \frac{0.012}{d^{*2}} + \frac{0.075}{d^{*3}}$	$F_{\mathrm{pw}} = 0.020 - \frac{0.32}{d^*} + \frac{1.2}{d^{*2}} - \frac{0.49}{d^{*3}}$
0.43	$F_{\mathrm{pp}} = 2.1 \times 10^{-5} - \frac{0.0010}{d^*} - \frac{0.025}{d^{*2}} + \frac{0.10}{d^{*3}}$	$F_{\mathrm{pw}} = 0.017 - \frac{0.28}{d^*} + \frac{0.93}{d^{*2}} - \frac{0.33}{d^{*3}}$
0.48	$F_{\mathrm{pp}} = 1.3 \times 10^{-5} + \frac{0.0030}{d^*} - \frac{0.044}{d^{*2}} + \frac{0.12}{d^{*3}}$	$F_{\mathrm{pw}} = 0.017 - \frac{0.24}{d^*} + \frac{0.65}{d^{*2}} - \frac{0.090}{d^{*3}}$

ray tracing simulations are performed on snapshots of particle positions obtained from plug flow models for $\phi_s \in [0.02, 0.48]$ at steady flow conditions that will be discussed in Sec. 5.2.1 (Fig. 5.1(a)). At least 10^6 rays are launched to attain convergence in the predicted view factors, with all particles treated as diffuse surfaces. Best-fit functions result in root mean square error values less than 7.56×10^{-4} and 0.042 for particle-particle and particle-wall view factors correspondingly for all solid volume fractions. Particle-particle and particle-wall view factors correlations, F_{pp} and F_{pw}, are polynomial functions dependent on dimensionless distance, d^*, which is respectively the inter-particle distance and the normal particle-wall distance, d, normalized by the particle diameter, d_p.

Predicted view factors should follow both the summation rule for a full enclosure $\left(\sum_{j=1}^{N_p+N_w} F_{ij} = 1\right)$ and the reciprocity rule ($A_i F_{ij} = A_j F_{ji}$) [99]. However, because we use correlations to obtain view factors (Table 2.1), there can be some numerical artifacts that fall short of satisfying these constraints. The summation rule is more strictly enforced to conserve net radiative energy in the enclosure through a normalization process (Eq. (2.29)).

$$\hat{F}_{ij} = \frac{F_{ij}}{\sum_{j=1}^{N_p+N_w} F_{ij}} \tag{2.29}$$

Each pairwise view factor, F_{ij}, is normalized by the summed view factors between particle i and all other j surfaces. While this normalization enforces summation, the reciprocity constraint is satisfied with the root mean square errors less than 2.39×10^{-4} for all solid volume fractions modeled. Additionally, comparisons are made for predicted particle temperatures and radiative heat fluxes using correlations in Table 2.1 with view factors directly obtained from Monte Carlo ray tracing simulations. For this validation case, particle positions are extracted from plug flow simulations after reaching steady-state flow for all the solid volume fractions in Table 2.1. The static

Table 2.2: The relative error comparing Monte Carlo ray tracing simulations and using our view factor correlations for different solid volume fractions.

Solid Volume Fraction, ϕ_s	**Average temperature after 0.01s**	**Average heat flux after 0.01s**	**Average temperature after 5s**	**Average heat flux after 5s**
0.02	0.027%	5.61%	2.37%	3.12%
0.07	0.022%	5.57%	2.63%	0.15%
0.15	0.0096%	3.63%	1.93%	2.95%
0.25	0.0050%	2.62%	1.15%	1.89%
0.31	0.0040%	2.48%	0.97%	1.75%
0.37	0.0030%	2.24%	0.76%	1.26%
0.43	0.0037%	3.09%	0.95%	1.89%
0.48	0.0006%	0.43%	0.19%	1.00%

particles are continually heated up by two heating walls (same in Fig. 5.1(a) in Sec. 5.2.1) for 5 seconds. Table 2.2 shows the percentage relative error for average particle temperature and heat flux after the 0.1 and 5 second. For all cases, the relative errors in temperature and heat fluxes are below 3% and 6%, demonstrating that the reduced-order models for the view factor correlations are effective. At any time step, relative errors in both the average temperature and the radiative heat flux mostly decreases with solid volume fraction. This is an artifact of the smaller mass in the low solid volume fraction which leads to larger temperatures, and larger accumulated differences between the two predictions. The errors in temperature accumulate with time, and are larger when computed at 5 s as compared to early times.

To further probe into the influences of the radiation modeling approach adopted, Fig. A.2 in Appendix A.2 reveals the comparisons in the probability distributions of temperatures and heat flux predicted by using view factor correlations as compared to applying direct Monte Carlo ray tracing for solid volume fraction of 0.02 and 0.43. While the distributions in temperature and radiative heat flux match reasonably well when using the view factor correlations as compared to performing ray tracing, it is challenging to exactly match the values, especially the minimums and maximums.

The computational cost for computing radiative fluxes remains large due to the

system of equations (Eq. (2.27)) that needs to be solved, which scales cubically with the number of particles, i.e., $\mathcal{O}({N_\mathrm{p}}^3)$. Therefore, we implement a *"radiation time-step"*, where view factor calculations (Table 2.1) and radiative fluxes (Eq. (2.27)) are updated less frequently than the particle positions. This approach is consistent with what has been done in prior work [61, 62]. From a sensitivity study, updating radiative fluxes after every 1000 time steps for particle flow/position calculations, i.e., $\Delta t_{\mathrm{rad}} = 1000\Delta t_{\mathrm{flow}}$, is found to be sufficiently accurate, while being computationally efficient. The relative error compared to DEM flow time step is within 0.06% for the average temperature of particles and the computational cost is cut down by 99.29%. More details about the computational cost and performance evaluation of radiation time step is provided in Appendix A.3. Additionally, computational cost is cut down further by restricting the radiative heat transfer calculations within only the heat-transfer region, while excluding the particle insertion and the hopper regions (Fig. 5.1) in Sec. 5.2.1.

2.2.2.4 Radiation Model: Iterative Solver

As previously discussed, the computational cost of solving this radiative heat exchange equation (Eq. (2.27)) rises monstrously as the number of particles increases. This is primary due to the view factor matrix term in Eq. (2.27), F_{ij}, which scales with the square of the number of particles ($\propto N_p^2$). Given that particle counts can easily exceed 10000 in a laboratory-scale particle heat exchanger, the resulting matrix is substantively gigantic. Consequently, many researchers focused on reducing the computational costs by either restricting the radiation effective region or simplifying the calculation process. For example, Cheng and Yu proposed a short-range model that only considers the radiation between neighboring particles [100]. Watkins et al. expanded the radiative effects from the heating walls to 2.5 layers of particles adjacent to the walls [46]. Gaviño et al. further extended the radiative effective

region to be 3.5 times of the particle size in a packed bed flow [63]. These models are restricted to be applicable for the particulate media to be densely packed ($\phi_s > 0.52$) where the shading effect between particles are very significant [101]. One of the simplest models for computing radiation incorporates radiative effects into the effective thermal conductivity. For example, Zehner-Bauer-Schlünder (ZBS) model incorporate the radiative effects into a parallel heat flux lines approach within a unit cell to obtain the effective thermal conductivity [65]. Wu et al. derived a correlation of the radiative effective thermal conductivity for a structured packed pebble bed [102]. These models are also only applicable for particulate media at high solid volume fractions and further assumes the packing structure of the particles. Johnson et al. implemented the radiative heat transfer into DEM-based simulator using Stefan-Boltzmann equation (Eq. (2.30)) [103]. This simplified model largely reduced the computational cost and complexity for computing radiation, but is only correct when particles can be considered as blackbodies ($\epsilon = 1$).

$$q_i = \epsilon_i \sum_{j=1}^{N} F_{ij} \sigma \left(T_i^4 - T_j^4 \right) \tag{2.30}$$

Many prior studies have also applied continuum methods, such as the spherical-harmonic method [104] or discrete ordinate method [105, 106], to compute radiation. These techniques requires to couple the DEM-based simulator with CFD approaches, which can largely add on computational cost. Moreover, converting discrete particles to continuum disobeys the discrete nature of solid particles and also is limited by the difficulty of obtaining effective properties of the medium. Ray tracing technique can also be implemented into DEM simulator to directly compute radiation. For example, Grobbel coupled Monte Carlo ray tracing (MCRT) into DEM simulator to compute radiation for neighboring particles in a solar receiver [62]. Though the development of parallelization techniques enable researchers to apply ray tracing technique for large

ensembles of particles, the computational cost of performing ray tracing for flowing particles is still prohibitible. Our previous work has implemented the general radiosity equation into LIGGGHTS to compute radiative heat transfer for flowing particles [107], which can be applicable for non-blackbody flowing particulate medium with broad solid volume fraction range ($\phi_s \in (0.02-0.65)$). Due to the high computational complexity of matrix manipulation when solving the radiosity equation, the modeling size, however, is limited to less than 40000 particles.

Parallelization techniques has been efficient for DEM-based simulations. Many existing DEM-based simulators apply spatial decomposition strategy to accelerate the simulations [95, 108]. The simulation domain is partitioned into multiple subdomains with each processor storing information for the subset of particles within it. This approach minimizes inter-processor communication by limiting data exchange to nearby particles, as particles only roam small distances within a single time step. However, the conventional matrix inversion for solving radiosity equation implemented in our previous work requires the particle information of the entire simulation domain. To parallelize this matrix solving process, frequent inter-processor communications with large-sized datasets are unavoidable but significantly decrease the parallelization efficiency. Therefore, in this study, we introduce an innovative iterative method for solving the radiosity equation (Eq. (2.27)). This approach demonstrates comparable accuracy to conventional matrix solvers while significantly reducing computational costs. Moreover, the iterative method can be seamlessly integrated into DEM software and benefits from acceleration through the Message Passing Interface (MPI) for parallel processing.

Eq. (2.31) presents the iterative approach for solving the radiative heat exchange equation.

$$q_i^{(n+1)} = \epsilon_i \sum_{j=1}^{N} F_{ij}\sigma(T_i^4 - T_j^4) + \epsilon_i \sum_{j=1}^{N} \left(\frac{1}{\epsilon_j} - 1\right) F_{ij} q_j^{(n)} \tag{2.31}$$

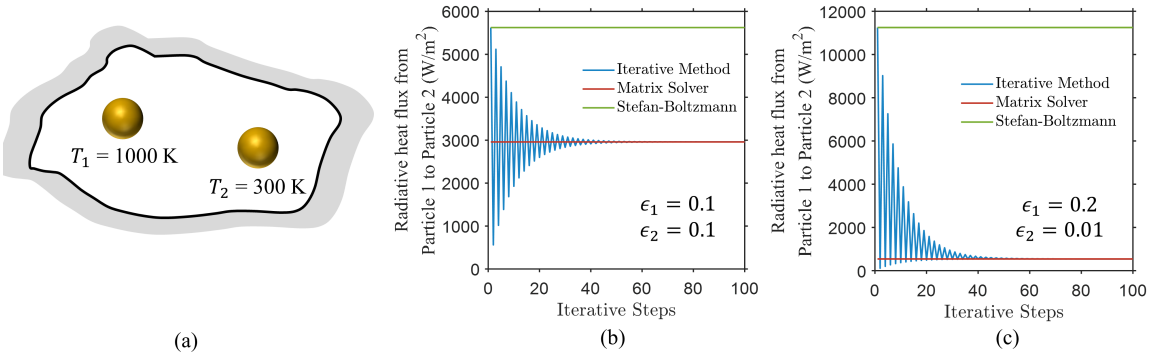


Figure 2.7: Calculated radiative heat flux using iterative method for (a) an example of two particles under different temperatures ($T_1 = 1000$ K, $T_2 = 300$ K) in a fully reflective enclosure ($F_{12} = F_{21} = 1$), as a function of iterative step and compared with the matrix solver and Stefan-Boltzmann results for (b) uniform emissivities ($\epsilon_1 = 0.1$, $\epsilon_2 = 0.1$), and (c) differed emissivities ($\epsilon_1 = 0.2$, $\epsilon_2 = 0.01$).

where $q_i^{(n)}$ is the radiative heat flux leaving the i^{th} surface during the n^{th} iteration, initially set to zero ($q_i^{(0)} = 0$). In the initial step ($n = 0$), the equation simplifies to the Stefan-Boltzmann equation (Eq. (2.30)). Beginning with the second iteration ($n \geq 1$), the radiative heat flux for the i^{th} surface, $q_i^{(n)}$, is updated based on the net emitted radiative energy across all surfaces. With sufficient iterations, the results converge to those obtained via the direct solution of the matrix equation (Eq. (2.27)). This convergence is achieved as the iterative process accounts for sequential radiative emission and reflection in the particulate media. Fig. 2.7 illustrates the iterative process using Matlab for a system of two spherical particles within a perfectly reflective enclosure, where the view factor between particles is unity ($F_{12} = F_{21} = 1$). With particle temperatures fixed at $T_1 = 1000$ K and $T_2 = 300$ K, the radiative heat flux is calculated using assigned emissivity values. For particles with identical emissivity of $\epsilon = 0.1$, convergence to the accurate value occurs after approximately 50 iterations (Fig. 2.7(b)). Notably, the flux calculated in the first step, standing for the result of solving Eq. (2.30) by assuming blackbody surfaces, deviates substantially from the correct value. Convergence is defined as achieving a relative error of less than 2 $\times$

10^{-6} between iterations, as expressed in Eq. (2.32).

$$\left| \frac{q^{(n+1)} - q^{(n)}}{q^{(n)}} \right| < 2 \times 10^{-6} \tag{2.32}$$

This error tolerance, which is maintained in the following discussion, ensures a relative error less than 0.1% compared to the actual value. Convergence remains robust even when particle emissivities differ, as depicted in Fig. 2.7(c). The rate of convergence is influenced by emissivity; higher emissivity results in faster convergence due to reduced reflective energy in each iteration. Similar to the matrix method, accurate convergence in the iterative approach relies on the correctness of the view factor matrix. In this study, the view factor matrix is determined by the view factor correlations under different solid volume fractions as described in Sec. 2.2.2.3.

Fig. 2.8 presents a validation case for a suspended bed. The setup consists of 1,289 particles, each with a diameter of 0.4 mm, within a rectangular box measuring 4 mm $\times$ 4 mm $\times$ 6 mm (L $\times$ W $\times$ H) as illustrated in Fig. 2.8(a). Initially at a uniform temperature of 300 K, these particles are heated by surrounding walls maintained at a constant temperature of 1000 K for a duration of 6 seconds. In this example, the particles remain stationary with only radiation between the particles and the walls to be considered. Both the particle bed generation and radiative heat transfer are conducted using LIGGGHTS, with implementations of both the matrix solver and the iterative method integrated into the source code. The simulation employs a time step of 2×10^{-5} seconds, resulting in a total of 300,000 steps in the simulation. Radiative heat flux is updated every 1,000 time steps as previously explained in Sec. 2.2.2.3 and view factor matrix is calculated using a collision-based Monte Carlo ray tracing simulations described in Sec. 2.1.1. Emissivity of both particles and walls is varied between 0.1 and 1.0. This validation case is particularly rigorous, as any error in each calculation step accumulates, providing a stringent test for the accuracy and

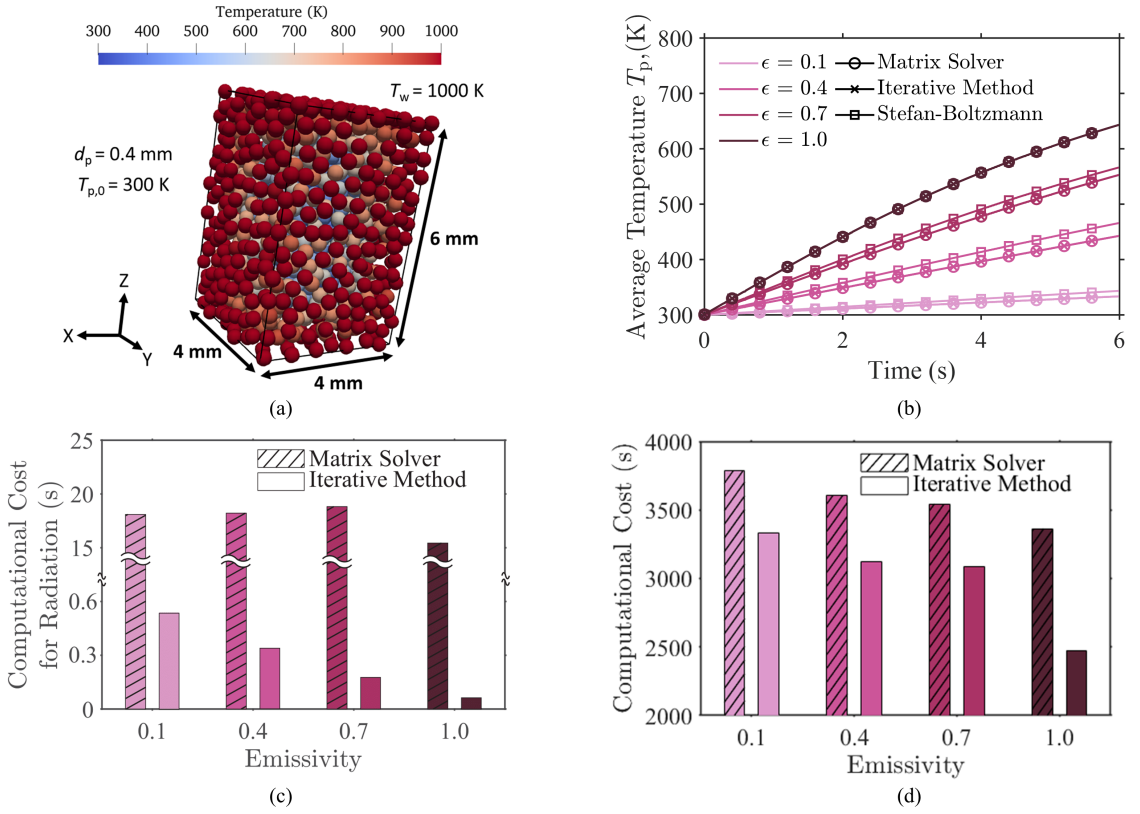


Figure 2.8: Effect of emissivity ($\epsilon = 0.1, 0.4, 0.7, 1.0$) in (a) a suspended packed bed of 1,289 particles radiatively heated by surrounding walls using iterative method, matrix solver and Stefan-Boltzmann equations on (b) temporal development of the average particle temperature, and computational cost of (c) radiation calculation in one time step, and (d) the entire simulation in 300,000 time steps.

reliability of the iterative method.

Fig. 2.8(b) demonstrates that, across simulations with various emissivities, the average particle temperature in the suspended bed remains consistent between the two radiative heat transfer computation methods. At the end of the simulations ($t = 6$ s), the relative error remains below 0.001%. On the contrary, the results computed from Stefan-Boltzmann equation have significant deviations from the real values for all non-blackbody results ($\epsilon \neq 1.0$), with a largest relative error of 3.2%. The computational cost per time step for calculating radiative heat flux is detailed in Fig. 2.8(c). Solving the matrix equations for a size of $1{,}492^2$ requires 15 – 19 seconds, whereas the iterative method completes the calculation in just 0.05 to 0.6 seconds, with costs increasing as emissivity decreases. This represents a 97% reduction in computational cost with the iterative method. Fig. 2.8(d) shows the overall computational cost for these simulations, revealing a reduction of 12 – 26%. This reduction is limited because, apart from the radiative heat transfer calculations, the simulations executes other functions in LIGGGHTS, which remain unchanged in this study. With the decrease of emissivity, the computational cost using the iterative method rises from 41 minutes to 55 minutes, reflecting more iteration steps.

One advantage of the iterative algorithm is its compatibility with MPI parallelization, which accelerates radiation calculations and integrates well with DEM software using spatial discretization techniques. Traditionally solving the radiative heat exchange equation (Eq. (2.27)) involves constructing a matrix that requires parameters from all particles, including particle positions, emissivities and temperatures, which are spread across different processors. One strategy is to share these parameters across all processors and construct the same matrix on each processor. However, this method compromises parallelization efficiency since matrix construction is the most computationally expensive part of the radiation calculation. Additionally, the cost of communicating large data sets between processors is extremely high, further

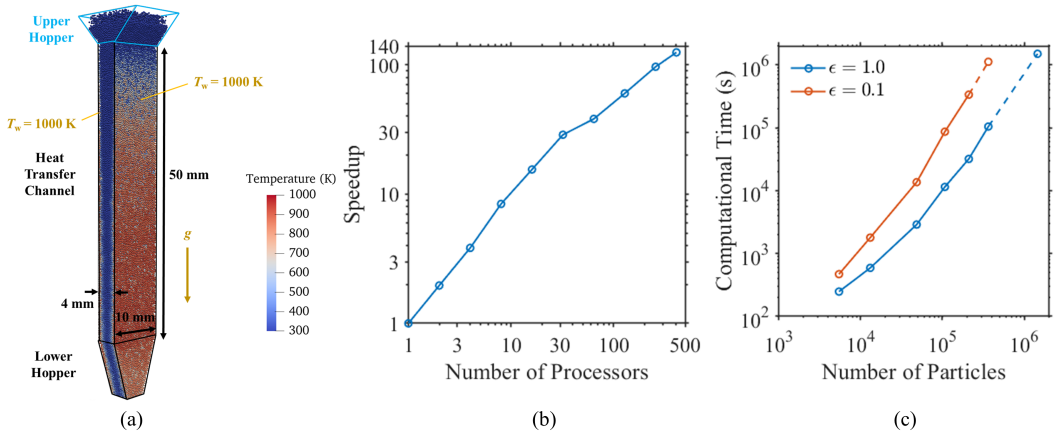


Figure 2.9: Cost evaluation for a (a) gravity-driven, moving packed bed model; (b) speedup performance as a function of the number of processors; and (c) computational cost as a function of the particle number for $\epsilon = 0.1$ and $\epsilon = 1.0$, with dashed curves representing extrapolations from incomplete simulations due to prohibitively high computational costs.

reducing efficiency. Furthermore, most advanced matrix solver take advantage of the special forms of the matrix (tri-diagonal or band-diagonal structures), which are not applicable here. In addition, building a gigantic matrix imposes a considerable memory burden on each processor, which becomes more severe as the particle number increases. The iterative method can largely alleviate these issues. Compared to the algorithm described in Eq. (2.31), the parallelized approach requires each processor to broadcast updated radiative heat fluxes for local particles during each iteration. Although communication between processors is more frequent, the size of the data exchanged is limited, adding minimal computational cost. Moreover, each processor only construct a few rows of the view factor matrix relevant to its local particles, significantly reducing memory requirements.

Fig. 2.9 illustrates the performance of the MPI-accelerated iterative method for simulating a gravity-driven moving bed model using LIGGGHTS. In this model, particles initially at 300 K are introduced at the upper hopper and move under gravity into a vertical channel measuring 10 mm $\times$ 4 mm $\times$ 50 mm (L $\times$ W $\times$ H), as depicted in Fig. 2.9(a). As the particles travel through the channel, they absorb heat from

the two heating walls maintained at a constant temperature of 1,000 K. The model incorporates both conductive (solid-solid and solid-fluid-solid pathways) and radiative heat transfer, as detailed in Sec. 2.2.2.1 and 2.2.2.2. The lower hopper regulates the mass flow rate, and together with the upper hopper, ensures a high solid volume fraction in the channel. The simulation lasts for 5 physical seconds, corresponding to 500,000 time steps, with radiative heat transfer calculations performed every 1,000 steps. For particles with a diameter of $d_p = 0.3$ mm, approximately 0.1 million particles reside in the channel region participating in heat transfer.

Fig. 2.9(b) shows the speedup of the simulations as a function of processors used for parallelization, defined in Eq. (2.33),

$$\text{Speedup} = \frac{t_{\text{serial}}}{t_{\text{parallel}}} \tag{2.33}$$

where t_{serial} and t_{parallel} are the computational time of simulations running using 1 processor and multiple processors respectively. Conducted on the Great Lakes platform, a high-performance computing (HPC) Linux-based cluster from Advanced Research Computing (ARC) at the University of Michigan, the MPI-accelerated iterative method demonstrates enhanced efficiency for radiation calculations in DEM software. Maximum performance is achieved with 408 processors, resulting in computations 124 times faster than serial processing.

By varying particle size within the channel, the number of particles in the model can be adjusted. Fig. 2.9(c) shows the computational cost relative to the number of particles, with a constant parallelization of 64 processors. The computational cost increases significantly with more particles due to the vast amount of information exchanged between processors for radiation computation and particle interactions. Additionally, the computational cost escalates when particle emissivity is lower, leading to more iterations in the radiation calculations. This indicates that the current iter-

ative method for computing radiative heat transfer remains limited by the high cost of frequent inter-processor communication. To cope with that, future investigations can focus on including a radiation cutoff distance that restricts the communication between processors within neighboring ones. At least for moving bed with high solid volume fractions, the import of cutoff distance has already shown great improvement for reducing computational cost [63].

CHAPTER III

Effects of Spatial Correlations in Particulate Media on Dependent Scattering and Radiative Transport

This chapter has been published by the author of this thesis:

- **Li, B., Bala Chandran, R., 2022. Effects of spatial correlations in particulate media on dependent scattering and radiative transport. International Journal of Heat and Mass Transfer 182, 121951.**

3.1 Introduction

Radiative transport in multiphase particulate media such as fixed beds of particles [19–24, 31, 32], reticulate foams and fibrous materials [25–30], granular and fluidized flows [43, 109] plays a crucial role in heat transfer for solar and nuclear energy, additive manufacturing, combustion and catalysis applications. Radiative transport in such media can be modeled by taking into account emission, absorption and scattering events [13, 110]. To model these phenomena, effective (or volumetric) radiative properties, including the extinction and absorption coefficients and the scattering phase functions, and their dependence on the individual particle/material properties, such as the optical properties — reflectance or emittance, and the medium morphology

are required. In prior work, independent scattering is a common assumption that has been used to obtain effective radiative properties of static and multiphase particulate media [19–32, 109]. This study focuses on investigating the role of the spatial distributions of particles on the applicability of the assumption of independent scattering theory for a packed bed of large and opaque particles.

When considering particulate media with characteristic length scales, L, that are much larger than the wavelengths of interest, λ ($L \gg \lambda$), the impacts of near-field effects such as interference and diffraction of scattered electromagnetic waves, will not be significant [111]. For such media, the independent scattering assumption neglects the effects of non-point scattering, which arises due to the interactions of scattered radiation from one particle with the neighboring particles [24, 112]. Therefore, effective radiative properties for the ensemble can be deduced from Mie theory calculations for a single spherical particle [12]. Tien and colleagues empirically identified three non-dimensionless parameters—(1) the size parameter, $\pi d_p/\lambda$, which compares the circumference of the particle to the characteristic radiation wavelength; (2) solid volume fraction of the particles; and (3) the ratio of the average clearance, C between the particles to the wavelength (C/λ), to classify the independent and dependent scattering regimes for radiative transport in participating media [113–115]. While these criteria are widely used in practice, deviation from independent scattering has been demonstrated even when the suggested criteria were satisfied [22, 23, 31]. For example, Singh and Kaviany established significant deviations between direct simulation results obtained via ray-tracing and the predictions from independent scattering theory for packed beds of large particles even when the solid volume fractions were as low as 6.5% [22].

To account for the effects of non-point scattering, scale factors have been predicted using models and measurements [22, 23, 31]. These scale factors determine the ratio of the extinction coefficient that accounts for dependent scattering effects, to that

obtained assuming independent scattering. For large and opaque particles, scale factors have been shown to only depend on the solid volume fraction. All these investigations point to a non-linear dependence of the scale factor on the solid volume fraction, and the more recent investigations predict more-or-less similar scale factors for a fixed solid volume fraction. However, these studies did not consider the role of spatial distributions of particles on radiative transport. In this study, we hypothesize that the three dimensional (3-D) spatial distribution of the particles will also impact non-point scattering effects and the overall radiative transport, in addition to the solid volume fraction. For particulate media with small size parameters, for example in paints and coatings, prior studies have discussed the role of the spatial point-statistics on the opacity and scattering strength of the media [116–118]. The necessity to account for the effects of spatial correlations and inhomogeneities in particulate media have been previously discussed for applications ranging from complex porous media [119–121] to atmospheric radiation physics [122], and to computer graphics [123, 124]. Yet, the effects of spatial distributions of large particles on radiative transport has not been rigorously examined. Furthermore, there is a lack of knowledge on computational approaches to independently control the spatial distributions and solid volume fraction of particles in a packed bed. This knowledge will be essential to better characterize radiative transport in multiphase flows with solid particles, where the flow field can influence the spatial distribution of the particles. For example, localized clusters of particles may be present for fluidized beds when the Stokes number, $St \sim 1$, where the Stokes number compares the momentum response time of the particles to the flow response time [125]. When these timescales are comparable, particles can centrifuge out and follow a trajectory towards regions of low vorticity resulting in clustering [126]. Spatial inhomogeneities in particle concentrations are also observed in granular flows–bubbling occurs with vibration and shaking of granular flows [127], and clustering has been observed in sheared granular flows [128]. Therefore, there is a

need to develop improved assessments of how dependent scattering can be influenced by the spatial distributions of particles.

Motivated by these knowledge gaps, the primary objective of this study is to develop a comprehensive modeling framework to quantify the influences of the spatial distributions or spatial correlations and solid volume fractions on radiative transport in a packed bed of large particles. Specifically, we develop and apply Monte Carlo ray tracing simulations to simulate radiation-particle interactions in numerically/computationally generated packed beds. Compared to prior work, our study reports on three major advancements—(1) modeling techniques have been developed to control and independently vary the spatial statistics and the solid volume fractions of particles in packed beds; (2) an index of cluster sampling has been introduced as a relevant statistical metric to quantify the three-dimensional distribution of the particles, which quantifies the spatial correlations present in the medium; and (3) unified scaling parameters are obtained as a function of, both, the spatial distributions of the particles and the solid volume fraction to account for the non-point (dependent) scattering effects for large and opaque particles. Direct ray tracing simulations are used to predict radiative transport properties, including the extinction coefficient, probability density function for extinction, and the scattering phase function. Evaluating these properties not only provides an enhanced understanding of the impacts of spatial distribution of large particles on radiative transport, but also provide inputs for more advanced stochastic models, e.g., generalized radiative transport equation to predict radiative transport in complex particulate media [121, 124].

3.2 Theory & Modeling Approach

The modeling domain is a packed bed with spherical particles of a fixed diameter with a range of solid volume fractions and various three-dimensional spatial distributions (Fig. 3.1). Cubic packed beds were modeled to quantify statistically the spatial

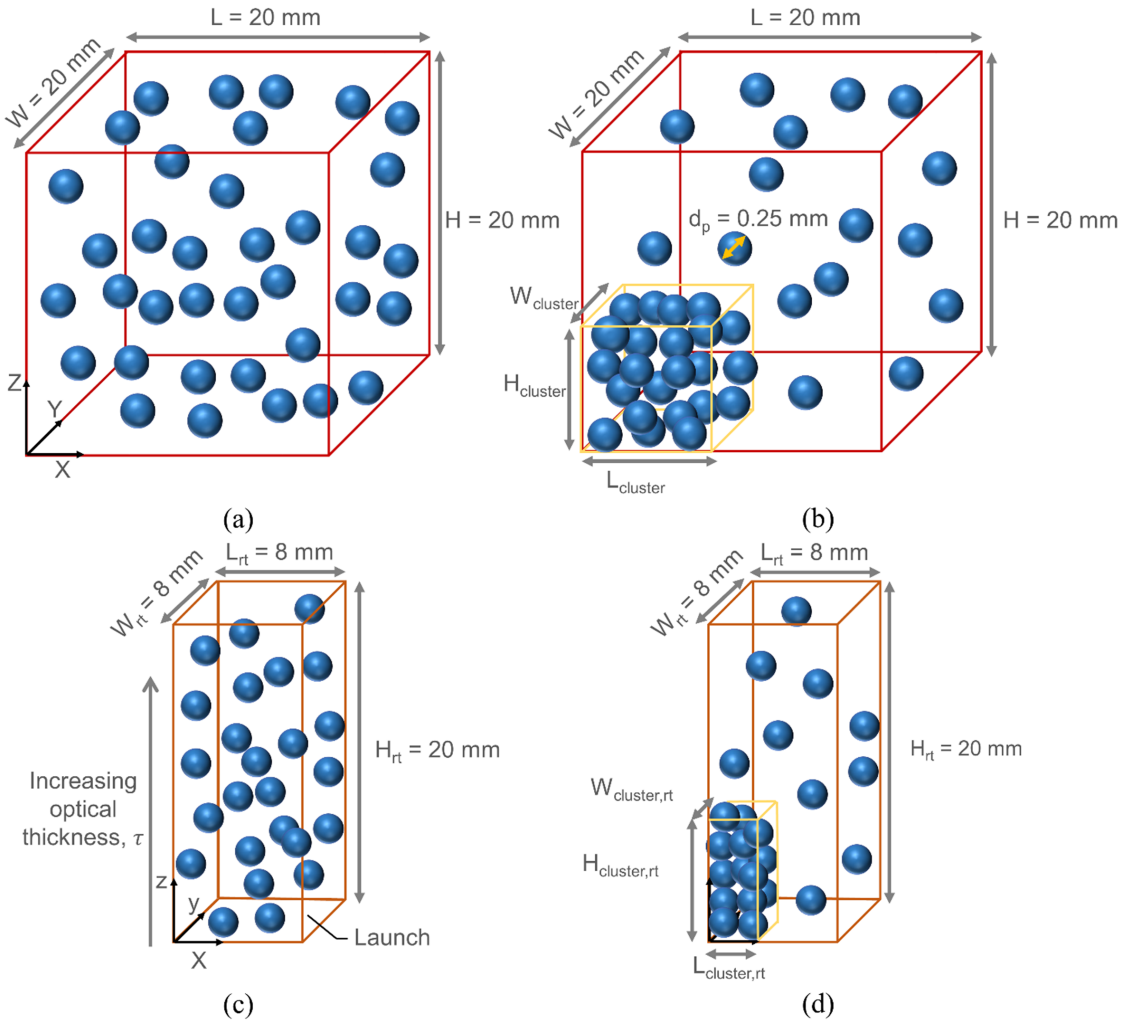


Figure 3.1: Modeling domain comprising of a packed bed with particles of diameter, $d_p = 0.25$ mm to quantify the spatial distributions of particles with a size of 20 mm $\times$ 20 mm $\times$ 20 mm (a,b) and to perform Monte Carlo ray tracing simulations with a size of 8 mm $\times$ 8 mm $\times$ 20 mm (c,d) for various spatial distributions and solid volume fractions of particles in the bed; (b,d) modeling domains for cluster beds with a single high-concentration or clustered region with a solid volume fraction, $\phi_{\text{s,cluster}} = 0.524$, present in the bottom left corner; cluster dimensions are dictated by Eq. (3.1). For the ray tracing simulations (c,d), the bottom launch surface ($z = 0$ mm) is modeled to be perfectly reflective, the side walls are periodic surfaces and the transmitted rays are counted at planes perpendicular the z-axis and along the direction of increasing optical thickness. Particles are assumed to be opaque and with a surface reflectivity, $\rho_p = 0.7$.

distributions of the particles, and a smaller domain (Fig. 3.1(b)) was used to perform the ray-tracing simulations to reduce computational costs. The method to generate different spatial distributions of the bed is first described. Subsequently, the approach to obtain an index of cluster sampling (ICS) to quantify the three-dimensional distributions of the particles in the bed is discussed. Then, the collision-based Monte Carlo ray tracing (MCRT) approach used to determine the radiative transport behavior is presented. Finally, statistical techniques to compute the effective extinction coefficient and scale factors from the MCRT simulations and to correlate scale factors with the ICS values are discussed.

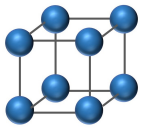
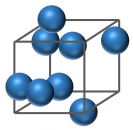
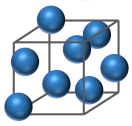
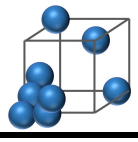
3.2.1 Generation of Packed Beds

Packed beds with spheres of a fixed diameter, $d_p = 0.25$ mm, were generated inside a cube of size 20 mm (which is $80d_p$), for solid volume fractions, ϕ_s, varying between 0.05–0.5. Four different spatial distributions of the particles — Poisson, random, ordered, and clustered distributions of particles were considered (Table 3.1). Except for the random bed, in-house codes were developed in C++ to obtain the desired the particle distributions. The solid volume fraction, ϕ_s, is defined as the ratio of the volume occupied by all particle and the volume of the domain,

$$\phi_s = \frac{N_{p.i}\pi d_p^3}{6L_iW_iH_i} \tag{3.1}$$

where, $N_{p,i}$ is the number of particles, and L_i,W_i,H_i are the length, width and height for i = bed or the ray tracing (rt) domain. To maintain consistency in this definition across all spatial arrangements, we ignore the effects of particle overlaps on resultant changes to ϕ_s and the optical thickness (Eq. (3.1)). Particle overlaps are a factor of concern only for the Poisson beds, and can result in up to a 15% deduction in the actual volume occupied by the particles. While particle centers are ensured to be

Table 3.1: Details of the types of spatial distributions of particles generated in the packed bed with schematics for their unit cells.

Bed Type	Description of Bed Generation	Unit Cell
Poisson	Particle centers were randomly sampled from a uniform distribution of points within the box; overlap of particles was allowed	
Random	Particle centers were randomly sampled from a uniform distribution without allowing for overlap between particles	
Ordered	Simple cubic packing of particles with the interparticle spacing given by Eq. (3.2)	
Clustered	Single clustered region with a solid volume fraction of 0.524; outside of the clustered region the solid volume fraction is lower; no particle overlap was allowed	

fully inside the modeling domain, its surface can intersect with the domain boundaries resulting in a portion of the particle volume being outside the boundary.

A *Poisson bed* was generated by randomly sampling for particle centers from a uniform distribution bounded by the dimensions of the bed. Particles were placed in the bed, spatially unhindered by the presence of other particles, therefore allowing for overlaps between particle surfaces. Even though the Poisson bed with overlapping spherical surfaces is physically unrealistic, it provides us a useful framework to compare the other spatial distributions against a completely random (*Poisson*) distribution of particles [129]. For the largest solid volume fraction, particle overlaps result in a near doubling of the average distance between particle pairs as compared to the random bed, which has no overlaps (8.4 mm versus 4.2 mm).

The *random bed* was generated using an open-source code, LIGGGHTS [95], specifying the desired domain size and the solid volume fraction by modifying an existing input script (*packing*). In this technique, smaller sized particles that are 0.15 mm in diameter, were first deposited. The number of particles were retained to be the

same as that required to attain the desired solid volume fraction with a particle size of 0.25 mm. Then, the diameters of all particles were increased to a size of 0.25 mm with the same coordinates for the particle centers. When the particle size becomes larger, it leads to overlapping volumes. Therefore, a soft-sphere model in LIGGGHTS was applied to compute the forces exerted by the overlapping particles in order to dynamically relax their positions over a period of time ($>$ 5 seconds of simulation time). This process causes the overlapping particles to move away from one another within the modeling domain.

The *ordered bed* was created by placing particle centers in a simple cubic arrangement, with the interparticle distance, c_{ordered}, determined as a function of the particle size and solid volume fraction (Eq. (3.2))

$$c_{\text{ordered}} = \left(\frac{\pi d_p^3}{6\phi_s}\right)^{\frac{1}{3}} \tag{3.2}$$

Clustered beds were generated assuming the presence of a single high solid volume fraction region, i.e., a cluster, with $\phi_{\text{s,cluster}} = 0.52$, at the bottom left corner of the modeling domain (Fig. 3.1(c)). The size of the clustered region, $a_{\text{cluster},i}$, depends on: (a) the solid volume fraction of the packed bed, ϕ_s, (b) the cluster fraction, f_c, which quantifies the ratio of the number of particles in the clustered region to the total number of particles; f_c ranged from 0.2 to 0.99 in our simulations, and (c) the dimensions of the packed bed or the ray-tracing domain, a_i. This dependency is shown in Eq. (3.3),

$$a_{\text{cluster},i} = a_i \left(\frac{\phi_s f_c}{\phi_{\text{s,cluster}}}\right)^{\frac{1}{3}}; \quad i = \text{bed}, \text{rt} \tag{3.3}$$

where, $a_{\text{cluster},i}$ is the length/width/height of the clustered region and a_i is the corresponding length-scale for i = bed or the ray tracing (rt) domain. For a fixed solid volume fraction in the bed, higher cluster fractions lead to a larger size of the clustered

region. For example, consider a packed bed with a solid volume fraction of $\phi_s = 0.05$, and a cluster fraction of $f_c = 0.99$. For a length of the bed of $a_{\text{bed}} = L_{\text{bed}} = 20$ mm, the length of the clustered region is $a_{\text{cluster,bed}} = 9.1$ mm. For the ray tracing models, the same length becomes $a_{\text{cluster,rt}} = 3.64$ mm because the length of the ray tracing domain is smaller with $L_{\text{rt}} = 8$ mm. To generate the clustered beds, the 20 mm-sized modeling domain was divided into smaller cells with their size equal to the particle diameter. Every cell inside the clustered region contains one particle each, such that the cluster has a solid volume fraction of 0.52. Outside the clustered region, particles were placed randomly inside the smaller cells to attain the desired ϕ_s for the bed. The probability of deposition was computed as the ratio of the number of particles to be deposited to the number of vacant cells outside the clustered region. For every vacant cell, random numbers were generated using a uniform distribution, between 0 and 1, and compared against this probability of deposition. If the generated number is less than the deposition probability, then the cell is filled with a particle and vice-versa, after which, the deposition probability gets updated.

3.2.2 Index of Cluster Sampling (*ICS*)

A quadrat-based, statistical sampling technique was modified and adapted for a three-dimensional (3-D) domain to quantify the index of cluster sampling (*ICS*) for the various spatial distributions of particles considered [130–132]. The *ICS* is representative of the extent of deviation of the spatial distributions of the particles from a Poisson distribution. To compute *ICS*, the 20 mm-sized modeling domain was divided into an integer number of smaller cells (Fig. 3.1). The frequency distribution for the number of particles present in each cell was used to determine,

$$ICS = \frac{S^2}{\overline{X}} - 1 \tag{3.4}$$

where, $\overline{X}$ is the mean and S^2 is the variance for the frequency distribution. Particles are treated as point locations centered inside the cells. Therefore, particle surfaces intersecting the boundary does not impact *ICS* quantification.

A Poissonian process with particle centers randomly distributed will ideally result in $ICS = 0$, i.e., spatially uncorrelated positions of the particles. Spatial ordering results in $ICS < 0$, i.e., negative spatial correlations, because of smaller cell-to-cell variance in the number of particles per cell as compared to the mean. Clustering of particles results in $ICS > 0$, i.e., positive spatial correlation, due to the increase of the variance in the cell-to-cell distribution of the particles. Therefore, relative to the Poisson bed, smaller *ICS* values are indicative of spatial ordering and the larger *ICS* values point towards clustering. As an example, *ICS* calculations for a 2-D domain with Poisson, ordered, and clustered distributions are presented in Appendix B.1.

The *ICS* values were found to be sensitive to the size of the cells used to obtain the frequency distributions. When the cell size was smaller as compared to the particle size, cluster detection becomes a challenge. On the other hand, when the cell size was larger than the particle size, the statistics to obtain frequency distributions were negatively impacted and detecting ordering in the spatial distributions becomes more difficult. Sec. 3.3.1 presents detailed analyses of these tradeoffs to guide the selection of cell sizes.

3.2.3 Monte Carlo Ray Tracing Simulations

The developed collision-based Monte Carlo ray tracing model (MCRT) has been detailed in Sec. 2.1.1. In this approach, a statistically large number of rays were launched and tracked for interactions with individual particles present in the modeling domain based. Physics-informed probability density functions were used to launch rays from a surface and track their interactions with the particles and the boundaries. To reduce the computational intensity of tracking intersections of a large number of

rays ($> 10^5$) with a large number of particles ($<$ 490,000 particles), a smaller domain of size of 8 mm $\times$ 8 mm $\times$ 20 mm was selected with 78,000 particles for the highest solid volume fraction modeled. Particles were generated within these smaller domains in the exact same manner as described in Sec. 3.2.1 and therefore, the *ICS* values predicted from the 20-mm sized beds are also applicable for these smaller domains used for ray tracing. We have consistently scaled the dimensions of the domains used in *ICS* calculations and for performing MCRT simulations (Fig. 3.1). The particle size, the solid volume fraction, and the ratio of the domain size to the cluster size in cluster beds (Eq. (3.3)), were kept constant for both modeling domains. The reason to include two different domain sizes is because *ICS* calculations benefits from having a larger domain to provide more reliable statistics, whereas the smaller domain size reduces the computational intensity for MCRT simulations. Simulations confirm that the MCRT simulations in the smaller domain sizes yields the same results as the larger domain used for *ICS* calculations while saving 90% of the computational time.

Optical thickness, τ, is the dimensionless distance within the participating medium (Eq. (3.5)), defined based on the extinction coefficient, β_{ind}, determined by the independent scattering theory for an ensemble of large and opaque spheres [22], and the physical depth, z,

$$\tau = \underbrace{\left(\frac{3\phi_s}{2d_p}\right)}_{\beta_{\text{ind}}} z \tag{3.5}$$

Optical thickness increases when the solid volume fraction or the depth into medium increases, or, when the particle size decreases, or, due to all these effects occurring simultaneously. Therefore, for a fixed value of ϕ_s and d_p, the depth into the medium increases when τ increases. However, when τ is fixed for media with the same particle size, d_p, the depth into the medium, z and the solid volume fractions are inversely related. The extinction coefficient obtained from independent scattering

theory, β_{ind}, varies from 300 m^{-1} to 3000 m^{-1} for a fixed particle size of 0.25 mm and the range of solid volume fractions considered in this study. The ray-tracing domain height was fixed at 20 mm, which yielded a maximum optical thickness of 6 for the lowest ϕ_s modeled. For optical thicknesses larger than 6, more than 10^6 rays were required to get reliable statistics for the transmitted rays, which made these simulations more computationally intensive. Therefore, the maximum optical thickness was fixed at 6 for our study.

The flowchart in Fig. 2.1 further describes the procedure of the collision-based MCRT simulations adopted to: (a) statistically sample for the points of launch, ray directions, and to determine absorption/scattering events in the domain; (b) criteria used to detect intersection of the rays with the particles, and (c) the mathematical implementation of the various boundary conditions. Simulations were used to compute the transmittance, probability density functions for attenuation distance and the angle of transmission, and the scattering phase function. Table 3.2 provides a description and approach to compute these metrics.

Path-length MCRT simulations was performed to evaluate radiative transmittance as predicted by independent scattering theory and to deduce effective extinction coefficients from the collision MCRT simulation results. The developed algorithm has been detailed in Sec. 2.1.2.

The collision-based and path-length MCRT simulations were performed on an Intel®Core$^{\text{TM}}$ i9-9900 CPU (3.1 GHz, 32 GB) and took up to 2.5 hours of wall clock time for the largest solid volume fraction modeled for the collision-based MCRT simulations. Convergence for the ray tracing simulations was ensured that the radiative transmittance changed by less than 0.5% with any further increase in the number of rays launched. Furthermore, for every solid volume fraction and spatial distribution of the particles that was modeled, radiative transmittance was averaged over 10 trials such that the standard deviation was within 5% of the mean value at any optical

Table 3.2: Description, significance, calculation details, and equations for various parameters computed from ray-tracing simulations to understand radiative transport in a packed bed of large and opaque particles.

Computed Metric, *symbol*	**Description & Significance**	**Calculations & Equations**
Transmittance, T	Ratio of the number of rays leaving a surface to the total number of rays launched from the bottom surface. Transmittance computed as a function of optical thickness helps determine the rate of attenuation of incident radiation via absorption and scattering in the medium.	$$T(\tau) = \frac{N_{\text{transmitted}}(\tau)}{N_{\text{launch}}} \quad (3.6)$$
Path-length distribution function, or the probability density function for attenuation, $p(s)$	The area under this curve corresponds to the probability that a ray launched from the bottom surface gets absorbed or reflected before traveling the distance specified by the independent axis. This probability density function for attenuation can be directly used as an input in stochastic simulations to determine the distances before which an extinction event occurs in the bed.	Distance traveled by every ray launched was recorded prior to the ray being either absorbed or reflected by the particle. The probability density was computed by, $$p(s) = \frac{N(s)}{N_{\text{attenuated}} \cdot \Delta s} \quad (3.7)$$ where Δs is the range over which the attenuated number of rays are counted, ($\Delta s = 0.01 d_p$), $N_{\text{attenuated}}$ is the total number of rays attenuated by particles and $N(s)$ is the number of rays attenuated within the distance range of (s,$s + \Delta s$).

Table 3.2: (continued) Description, significance, calculation details, and equations for various parameters computed from ray-tracing simulations to understand radiative transport in a packed bed of large and opaque particles.

Computed Metric, *symbol*	**Description & Significance**	**Calculations & Equations**
Angular distribution for transmission, or the probability density function for the transmitted angles, $p(\theta_t)$	Area under this curve represents the probability that a transmitted ray at a fixed optical thickness has a polar angle (measured with respect to the z-axis) that is less than the value specified by the independent axis. This probability density function physically informs the directionality of the transmitted radiation and how spatial arrangement of particles can influence this behavior.	Polar angles were recorded for the transmitted rays at a specified optical thickness τ. Probability density for transmitted angles, $$p(\theta_t) = \frac{N(\theta_t)}{N_{\text{transmitted}} \cdot \Delta\theta_t} \quad (3.8)$$ where $\Delta\theta_t$ is the transmitted polar angle range size ($\Delta\theta_t = 2^\circ$), $N_{\text{transmitted}}$ is the total number of transmitted rays, and $N(\theta_t)$ is the number of rays transmitted within the angle range of (θ_t,$\theta_t + \Delta\theta_t$).
Scattering phase function, $\Phi(\theta_i, \theta_s)$	The scattering phase function represents the probability that a ray with an incident angle, θ_i, is scattered to angle θ_s (both angles are measured with respect to the z-axis) such that, the integral of the scattering phase function over all solid angles yields 4π. Scattering phase function predictions from our model can be used to directly determine the direction of the scattered ray for a given incident angle in stochastic simulations that consider the packed bed as an effective medium.	Rays were randomly launched from the void space in the packed bed with incident angles sampled from $\theta_i = \cos^{-1}(1 - 2R_\theta)$, by considering an isotropic medium. The number of rays incident within (θ_i,$\theta_i + \Delta\theta_i$), N_i, and the number of rays scattered within (θ_s,$\theta_s + \Delta\theta_s$), N_s, were recorded to obtain the scattering phase function. $\Delta\theta_i, \Delta\theta_s = 10^\circ$. Because the medium is isotropic, the phase function was obtained only as a function of the polar angle, θ. $$\int_0^\pi (\theta_i, \theta_s) \sin\theta_i d\theta_i d\phi = 4\pi \quad (3.9)$$ $$\Phi(\theta_i, \theta_s) = \frac{N_s}{N_i}\left(\frac{4\pi}{2\pi \sin\theta_i \Delta\theta_i}\right) \quad (3.10)$$

thickness. For all other metrics in Table 3.2, the same averaging procedure led to even smaller deviations and therefore are not shown in the results.

3.2.4 Evaluation of Extinction Coefficient and Scale Factor

For diffuse illumination, the governing relationship between the radiative transmittance and the effective extinction coefficient of a radiatively participating medium is not a simple exponential dependence as in the case of the Beer-Bouger-Lambert's law, which can be applied to determine radiative transmittance of normal irradiation in a purely absorbing medium [18, 133]. Therefore, we derived a generalized exponential relationship (Eq. (3.11)),

$$T = p \exp(-m\beta z) \tag{3.11}$$

where, p is the pre-exponential factor that dictates the probability with which rays can traverse the domain and $p \approx 1$ for all beds other than cluster beds; β is the effective extinction coefficient of the medium; and m value is dictated by the scattering albedo of the medium (or equivalently the modeled specular reflectivity of large particles). This equation form was informed by performing path-length MCRT simulations on a 1-D, homogeneous and isotropically scattering radiatively participating medium combined with knowledge of closed-form solutions based on the two-flux approximation for the radiative transport equation (see Sec. B.3) [15, 18]. We observed that for the specific case of specular particle reflectivity, $\rho_p = 0.7$, which translates to a scattering albedo value of $\omega = 0.7$, the value of m is very close to 1. Therefore, the average relative error between computing transmittance by applying a simple exponential function (Eq. (3.12)), and performing the path length MCRT simulations is

less than 10% (for optical thicknesses, $\tau^* = \beta z$, less than 6).

$$T = p \exp(-\beta z) \tag{3.12}$$

For any other particle reflectivity or scattering albedo values, the approximation in Eq. (3.12) can lead to significant errors (Figure B.4 in Appendix B.3). Section B.3 provides more details on these calculations and derivations that inform the non-linear dependence of the factor m on ω ($m \propto \sqrt{1-\omega}$). Because all our simulations assumed a fixed particle reflectivity of 0.7 and using Eq. (3.12) leads to small errors, and this equation form is used with p and β as two fitting parameters.

For the Poisson and random beds, Eq. (3.12) was applied to determine p and β from the transmittance results obtained from direct, collision MCRT simulations. For the cluster beds, Eq. (3.13) was used with an additional exponential term that is included to account for the inhomogeneities in the particle concentrations due to the presence of clusters,

$$T = p \exp\left(-\beta z\right) + (1-p) \exp\left(-\beta_2 z\right) \tag{3.13}$$

In Eq. (3.13), the first and the second terms represent the attenuation of radiative intensity outside and inside the clustered region of the bed respectively; the pre-exponential factors, p and $1-p$, are the probabilities with which the rays traverse the respective regions; β is the effective extinction coefficient outside the clustered region. Because the solid volume fraction and the spatial arrangement of particles is fixed in the clustered region, the extinction coefficient, β_2, will be a fixed value that is independent of f_c and ϕ_s. The best-fit value for β_2 was determined from a range of 3000 m^{-1}–5100 m^{-1}, which included the baseline value of $\beta_{\mathrm{cluster}} = 3000 m^{-1}$. This baseline value is the extinction coefficient obtained from independent scattering theory for the cluster solid volume fraction, $\phi_{\mathrm{s,cluster}} = 0.5$. As will be discussed, for the

perfectly negatively correlated spatial positions of the particles in an ordered bed, it is challenging to deduce an effective extinction coefficient that can be rationalized from a physics standpoint. Best-fit coefficients for p, β and β_2 were obtained using non-linear regression with the constraint that the coefficient of determination, $R^2 > 0.95$. To perform this regression, 7 pairs of T versus z data points (obtained from the collision MCRT simulations), were used for each spatial arrangement of the particles. The applicability of the fitted values of p and β (from Eqs. (3.12) and (3.13)) is further confirmed by a good match between the path-length distribution functions obtained from collision and path-length MCRT simulations (will be shown in Fig. 3.5), wherein the latter used the fitted values for p and β as inputs to determine the statistics of attenuation events in the participating medium.

The scale factor, γ, compares the effective extinction coefficient obtained from the ray tracing simulations, Eqs. (3.12) and (3.13), to that predicted by independent scattering theory (Eq. (3.5)),

$$\gamma = \frac{\beta}{\beta_{\text{ind}}} \tag{3.14}$$

The particle reflectivity (or equivalently the scattering albedo) modeled will affect the transmittance at any optical thickness and the m value in Eq. (3.11), i.e., the rate of change of transmittance with optical thickness (Fig. B.4 in Appendix B.3). However, the fitted value for β from the $m = 1$ scenario will still be applicable, as it only depends on the solid volume fraction, particle size and the spatial distribution of the particles. Therefore, the scale factors obtained from this approach will be applicable for any specular particle reflectivity other than the modeled value of 0.7. The strength of the correlations between the scale factor, γ, and (a) the *ICS* and (b) the ϕ_s value, was assessed with the Spearman's test [134]. A Spearman's correlation coefficient of either 1 or -1 between two random variables indicates a perfect mono-

tonic correlation, while a value of 0 implies that the variables are independent of each other.

The curve fitting tool (*cftool*) in Matlab R2020a, with default settings, was used to perform all the data-fitting with appropriately chosen constraints for target residuals and the coefficient of determination, R^2. The fitting equations and the regression models were modified as per need. For example, an exponential fitting function and non-linear regression was used for Eqs. (3.12) and (3.13), whereas a polynomial fitting and linear regression was used to model the dependence of the scale factor, γ, on the *ICS*.

3.3 Results & Discussion

First, we report on the computed *ICS* values for the various spatial arrangements and solid volume fractions of particles in a packed bed. Next, the effects of spatial correlations and the solid volume fractions on the radiative transmittance is discussed. The effective extinction coefficients and their correlations with the computed *ICS* values are discussed. Finally, the implications of the spatial correlations of the particles on other radiative properties, including the probability density functions for the attenuation distance and the angle of transmission, and the scattering phase function are presented.

3.3.1 Quantifying Spatial Statistics of Particles with *ICS*

Fig. 3.2 shows that, even for a fixed spatial arrangement of particles and a fixed solid volume fraction, the *ICS* values are strongly impacted by the cell size used to determine the frequency distributions (Eq. (3.4)). An optimal cell size was selected such that the predicted *ICS* values are: (1) very close to 0 for the Poisson bed; (2) less than 0 for the ordered beds; and (3) larger in magnitude for the clustered beds as compared to the Poisson and the ordered beds.

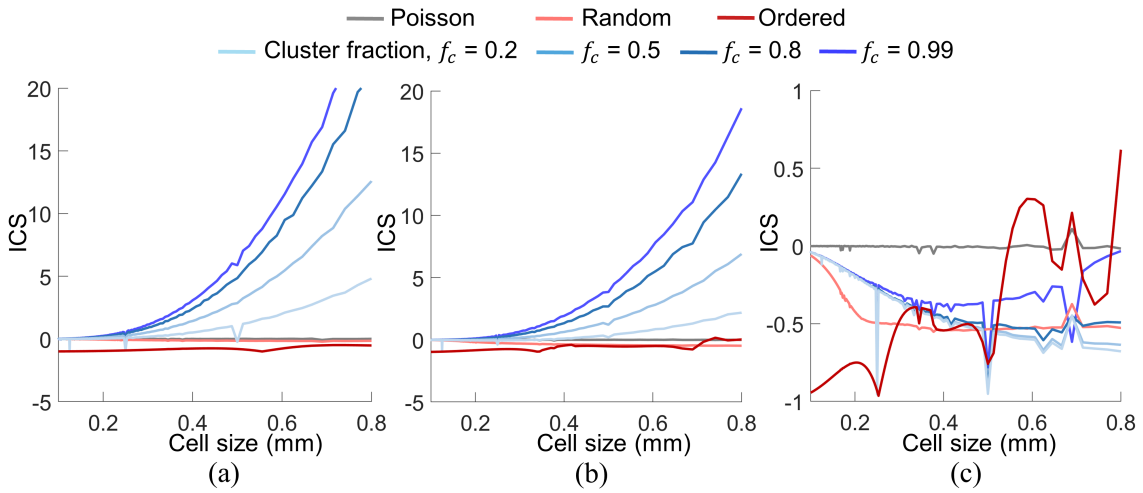


Figure 3.2: Effects of cell size on the index of cluster sampling, *ICS*, values for Poisson, random, ordered and cluster beds with cluster fractions, $f_c = 0.2$, 0.5, 0.8 and 0.99, for solid volume fractions of (a) $\phi_s = 0.05$, (b) $\phi_s = 0.2$, (c) $\phi_s = 0.5$; note that the y-axis scale in Fig. 3.2(c) is different from (a,b) for clarity in observing the trends. Modeling domain shown in Fig. 3.1(a,b) with a particle diameter of 0.25 mm was used for all these cases.

Fig. 3.2 confirms that for all cell sizes and solid volume fractions, the *ICS* values for the Poisson bed are within 0.4% of the ideal value of 0. For the random beds at a fixed volume fraction, the *ICS* values closely approach 0 for the small cell sizes and decreases as the cell size increases. This trend is because with the larger cell size, the number of particles inside each cell increases, which results in a larger mean value, $\overline{X}$, in Eq. (3.4). However, the cell-to-cell variation in the number of particles doesn't change significantly with cell size, because both the number of particles and the mean value increases with cell size. Thus, the *ICS* decreases with increase in cell size for random beds. For the ordered beds, the *ICS* is -1, i.e., perfectly negatively correlated spatial positions of the particles, only when the cell sizes are integer multiples of the interparticle spacing, a_{ordered} (Eq. (3.2)). In this instance, all the cells comprise of the same number of particles, resulting in an *ICS* of -1. For cell sizes that are non-integer multiple of a_{ordered}, $S^2 > 0$ and therefore, $-1 < ICS < 0$. Depending upon the solid volume fraction, when the cell size is large (e.g., cell size larger than 0.7 mm and

0.51 mm for $\phi_s = 0.2$ and 0.5 respectively), *ICS* values for the ordered beds change more drastically with small changes in cell size and even tend towards positive values. Beyond a certain cell size, instead of having the same number of particles in all the cells, the number of particles in any cell alternates between different values (resulting in an oscillatory trend), which results in $S^2 > 0$ and thereby making $ICS > -1$. For the clustered beds at a fixed solid volume fraction, *ICS* increases with increasing cell size because of the increasing differences in the number of particles present inside and outside the cluster region. For cell sizes smaller than 0.25 mm, *ICS* values for the cluster bed are within 5% of the random bed at the same solid volume fraction. From these results, it is inferred that the smaller cell sizes (< 0.51 mm) are better to capture spatial ordering of the particles, whereas larger cell sizes (> 0.25 mm) can improve cluster detection. Mathematically, the upper limit for a cell size of 0.51 is twice the inter-particle spacing for a simple cubic packing of the particles in the ordered beds with $\phi_s = 0.5$ (from Eq. (3.2)). Several cell sizes between the two limits ($0.25 \text{ mm} < a_{\text{cell}} < 0.51$ mm) were selected to obtain correlations between *ICS* and the scale factors. As will be discussed, a cell size of 0.35 mm yield the best fit for correlating *ICS* and the scale factors.

Table 3.3 lists *ICS* values determined with a fixed cell size of 0.35 mm; Table B.1 in Appendix B.4 shows the same results for a cell size of 0.51 mm. At any value of ϕ_s, the *ICS* values are close to 0 for the Poisson beds, largest for the clustered beds, and are bounded by the lower limit of -1 for the random and the ordered beds. For the ordered beds, *ICS* values generally becomes larger, from -0.8 to -0.4, for a fixed cell size and as the solid volume fraction increases due to the increasing variation in the number of particles present in each cell. For the random beds, *ICS* is less than 0 at any solid volume fraction, which indicates relatively greater spatial ordering as compared to the Poisson beds. The *ICS* values become more negative as the solid volume fraction increases for the random beds because of the increased constraints in

Table 3.3: Computed *ICS* values with a fixed cell size of 0.35 mm for the various spatial distributions and solid volume fractions considered for the packed beds.

Solid Volume Fraction	**Poisson**	**Random**	**Ordered**	**Cluster beds with varying cluster fraction**			
				$f_c = 0.2$	$f_c = 0.5$	$f_c = 0.8$	$f_c = 0.99$
0.05	−0.0006	−0.11	−0.81	0.33	0.92	1.57	1.97
0.1	0.0042	−0.21	−0.75	0.22	0.72	1.31	1.73
0.15	−0.0022	−0.28	−0.82	0.12	0.56	1.09	1.47
0.2	0.0008	−0.34	−0.83	0.015	0.35	0.82	1.21
0.25	−0.0021	−0.39	−0.63	−0.081	0.19	0.60	0.95
0.3	−0.0089	−0.43	−0.48	−0.16	0.035	0.36	0.68
0.35	−0.0028	−0.46	−0.42	−0.24	−0.10	0.13	0.43
0.4	−0.0010	−0.48	−0.39	−0.31	−0.24	−0.085	0.18
0.45	0.0006	−0.50	−0.39	−0.37	−0.34	−0.27	−0.099
0.5	−0.0091	−0.53	−0.40	−0.42	−0.42	−0.41	−0.35

the positions of the particles increases, which results in more spatial ordering. The influence of the solid volume fraction on *ICS* is most pronounced for the clustered beds. For example, in a clustered bed with a cluster fraction, $f_c = 0.99$, *ICS* rapidly decreases from 1.97 to −0.35 as ϕ_s increases from 0.05 to 0.5. The spatial arrangement of particles outside the clustered region approaches the distribution inside as the ϕ_s increases, which increases the tendency for spatial ordering and therefore lowers the *ICS* values. For a fixed ϕ_s value, *ICS* value monotonically increases with the cluster fraction, as the number density of particles within the clustered region increases. Even though the *ICS* attains negative values for cluster beds with high solid volume fraction ($\phi_s \geq 0.3$), these values are still comparatively larger than those for the ordered beds at the same ϕ_s.

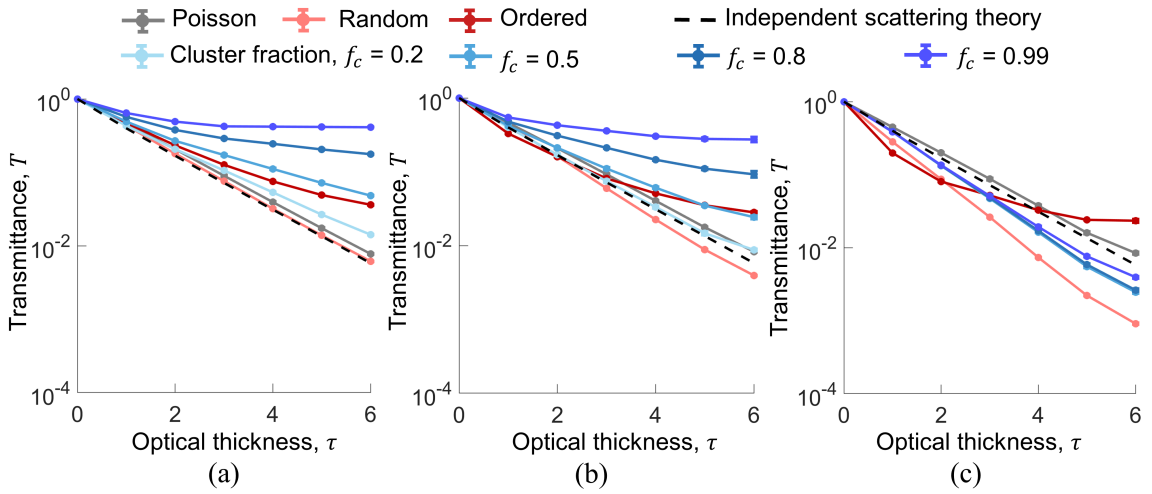


Figure 3.3: Transmittance, T, as a function of optical thickness, τ, for the Poisson, random, ordered and cluster beds with cluster fractions, f_c, of 0.2, 0.5, 0.8 and 0.99 for (a) $\phi_s = 0.05$, (b) $\phi_s = 0.2$ and (c) $\phi_s = 0.5$. The ray tracing modeling domain in Fig. 3.1(c,d) was used with a particle diameter, $d_p = 0.25$ mm and by assuming opaque, grey and specularly reflective surfaces with $\rho_p = 0.7$; $\sim 10^6$ rays were launched and traced for intersections with up to 78,000 particles to obtain these results. Transmittance was obtained at discrete values of optical thickness (solid circles) and the solid lines were drawn to guide the eye. Error bars were computed by averaging Monte Carlo ray tracing simulations over 10 trials for each spatial arrangement and solid volume fraction modeled.

3.3.2 Effects of Solid Volume Fraction and Spatial Distribution on Radiative Transport

3.3.2.1 Radiative transmittance

Fig. 3.3 shows the modeling predictions for radiative transmittance (mean and standard deviation) as a function of optical thickness for all the spatial distributions and selected solid volume fraction of 0.05, 0.2 and 0.5. Transmittance exponentially decreases with optical thickness for all the beds with extinction rates that are dictated, both, by the spatial arrangement of the particles and the solid volume fractions. For the Poisson bed, the transmittance at any optical thickness is within 16% of independent scattering theory predictions. Therefore, when the particle positions are spatially uncorrelated, as in the case of a Poisson bed, independent scattering theory is a reasonable assumption. To maintain consistency in comparison of different spatial distributions, these calculations preclude any deductions in ϕ_s due to particle overlaps for the Poisson bed; this factor only becomes significant for $\phi_s > 0.35$. If this effect were taken into consideration, transmittance at any optical thickness will be lower than the prediction in Fig. 3.3 for the Poisson bed.

At any solid volume fraction and for small optical thicknesses ($\tau \leq 1$), the transmittance is smaller for the random and the ordered beds as compared to the Poisson beds because of the presence of overlapping particles in the latter, which decreases the attenuation of radiative intensity. However, for the larger optical thicknesses, the ordered bed has a relatively larger transmittance compared to the Poisson and the random beds because of more direct view-paths for the transmission of rays. For $\phi_s \leq 0.2$, clustering of particles leads to larger transmittance as compared to all the other spatial distributions (Fig. 3.3(a) and Fig. 3.3(b)). The presence of clusters increases the direct view paths for the transmission plane from the launch plane, which increases even further as the cluster fraction increases. However, for $\phi_s = 0.5$, even

for the largest cluster fraction, $f_c = 0.99$, transmittance for the clustered beds is lower than the Poisson (for all τ) and the ordered (for $\tau > 3$) beds (Fig. 3.3(c)). For this case, there is an increased number density of particles even outside the clustered region, which obstructs the rays and therefore lowers transmittance to a larger extent as compared to the Poisson and the ordered beds. For the same case, transmittance for the cluster bed is comparatively larger than the random bed because of the presence of fewer particles outside the clustered region.

If independent scattering theory is a valid assumption, transmittance at a fixed optical thickness, τ, (defined based on β_{ind} in Eq. (3.5) will be invariant with ϕ_s, indicating that the extinction coefficient of the ensemble proportionally increases with ϕ_s. However, this behavior is observed only for the Poisson bed (Fig. 3.3). For the ordered beds, there is a marginal decrease in the transmittance when ϕ_s increases from 0.05 to 0.35 because of the decrease in the fraction of directly transmitted rays. For larger solid volume fraction, $\phi_s > 0.35$, transmittance at a fixed τ value, does not change with further increase in ϕ_s (Fig. B.2 in Appendix B.2). This trend is attributed to the linear increase in the rate of attenuation with respect to the solid volume fraction, which is already accounted for in the optical thickness (Eq. (3.5)). In comparison with the ordered bed, the random and the clustered beds exhibit a more dramatic decrease in the transmittance with increasing ϕ_s even at a fixed τ value. This outcome is due to the non-negligible effects of dependent scattering, and the extinction coefficient exhibits an increasingly non-linear dependence on the number of particles present per unit volume as the ϕ_s increases. Whereas the deviation of transmittance from independent scattering theory becomes smaller with increase in solid volume fraction for the cluster beds, the opposite trend is observed for the random beds. In a cluster bed, the spatial distribution of particles inside and outside the clustered region approach each other (also captured by the decreasing *ICS* values in Table 3.3) as ϕ_s increases, which causes transmittance to decrease and approach

values obtained for the Poisson bed (Fig. 3.3). In contrast, particles in a random bed deviate from a Poisson distribution by larger amounts as ϕ_s increases, which amounts to the larger deviations in transmittance from independent scattering theory. Overall, these results reinforce prior finding from Singh and Kaviany with respect to deviations from independent scattering even for small solid volume fractions [22], but also highlights the differences caused by spatial distributions of the particles even at the same solid volume fraction.

3.3.2.2 Scale factor dependence on the spatial statistics

Table 3.4 shows best-fit values for the scale factor, γ (Eq. (3.14)), and the pre-exponential factor, p, for all spatial distributions other than the ordered bed. These coefficients were determined from the average transmittance values presented in the data shown in Fig. 3.3 and using Eqs. (3.12) and (3.13). For the Poisson bed, the scale factor is approximately constant at 0.79 ± 0.02, and changes very minimally with respect to the solid volume fraction because the effective extinction coefficient, scales proportional to ϕ_s. For the random beds, the scale factor monotonically decreases as the ϕ_s increases. The pre-exponential factor, p, is mostly constant and invariant with ϕ_s (1 ± 0.001) for the Poisson and the random beds (Eq. (3.12)), indicating that the probability of rays interacting with the particles is independent of the distance traveled by the rays within the bed for random distributions of particles. For the cluster beds, transmittance is obtained as a function of two attenuation coefficient, β and β_2 (Eq. (3.13)), corresponding to the two regions of low and high concentration of particles. The regression models resulted in a best-fit value of $\beta_2 = 3900$ m^{-1} for the high-concentration/clustered region (Eq. (3.13)), which is somewhat close to the baseline value of 3000 m^{-1} based on independent scattering, but closer to the fitted value of 3750 m^{-1} obtained for the random bed with a solid volume fraction of 0.5 (Table 3.4). This value for β_2 remains constant at all solid volume fractions for the

Table 3.4: Best-fit for the pre-exponential factor (p) and the scale factor, γ, for the Poisson, random (Eq. (3.12)), and the cluster beds (Eq. (3.13)) obtained from the transmittance versus optical thickness results via Monte Carlo ray tracing simulations (Fig. 3.3).

Solid Volume Fraction	**Poisson bed**		**Random bed**		**Cluster bed**							
					$f_c = 0.2$		$f_c = 0.5$		$f_c = 0.8$		$f_c = 0.99$	
	p	γ	p	γ	p	γ	p	γ	p	γ	p	γ
0.05	1.00	0.79	1.00	0.85	0.60	0.59	0.55	0.41	0.52	0.19	0.50	0.04
0.10	1.00	0.88	1.01	0.86	0.65	0.67	0.55	0.45	0.48	0.20	0.44	0.07
0.15	1.00	0.80	1.01	0.88	0.70	0.72	0.57	0.51	0.47	0.26	0.41	0.06
0.20	1.00	0.78	1.01	0.89	0.74	0.78	0.59	0.58	0.48	0.31	0.41	0.10
0.25	1.00	0.80	1.02	0.95	0.79	0.84	0.63	0.70	0.51	0.40	0.44	0.19
0.30	1.00	0.80	1.02	1.00	0.83	0.85	0.68	0.77	0.56	0.51	0.50	0.27
0.35	1.00	0.78	1.02	1.06	0.88	0.92	0.74	0.82	0.64	0.70	0.58	0.48
0.40	1.00	0.80	1.02	1.10	0.92	0.96	0.82	0.90	0.73	0.81	0.69	0.62
0.45	1.00	0.77	1.03	1.16	0.96	0.96	0.90	0.94	0.85	0.92	0.83	0.84
0.50	1.00	0.79	1.04	1.25	1.00	0.98	1.00	0.98	1.00	0.98	1.00	0.99

cluster beds. Outside the clustered region, the β value, and therefore the scale factor, γ, in Table 3.4, increases with increasing solid volume fraction and decreasing cluster fraction. An increase in β with solid volume fraction is attributed to the increase in attenuation of rays outside the clustered region. However, β and γ decrease with an increase in the cluster fraction because a larger proportion of the particles are present in the clustered region, which increases the concentration of void spaces outside. Eq. (3.15) shows that the pre-exponential factor, p, follows the same trend as the scale factor with respect to the solid volume fraction and the cluster fraction.

$$p = 0.82 - 0.50 f_c - 0.85\phi_s + 0.11 f_c^2 + 0.28 f_c \phi_s + 3.1\phi_s^2 \tag{3.15}$$

For the ordered beds, a bi-exponential function yielded the best fit (R^2 value of 1.00) for the simulated transmittance data (Fig. B.5 in Appendix B.4). A simple exponential function, as in Eq. (3.12), yielded an R^2 of 0.99, but resulted in substantial deviations, up to 95% for transmittance at large optical thicknesses ($\tau > 2$). Even though a bi-exponential dependence of transmittance on optical thickness yielded a good fit, this functional dependence cannot be explained using the underlying physics. Despite the computed *ICS* values, which are in the range of **-0.81—0.39** for the ordered beds, theoretically an *ICS* value of -1 is expected for all the ordered beds with optimal choice of the cell size, irrespective of its solid volume fraction (Fig. 3.2). Together, these factors pose limitations to: (a) deduce an effective extinction coefficient, β, and (b) correlate this coefficient to *ICS* for ordered beds with perfectly negative spatial correlations of the particles.

The Spearman's test was applied to test for the strength of the correlation of γ values (Table 3.4) with (a) *ICS* (Table 3.3) and (b) ϕ_s values, for all spatial distributions other than the ordered beds.

Spearman's correlation coefficients of -0.99 and 0.58 were obtained between γ and

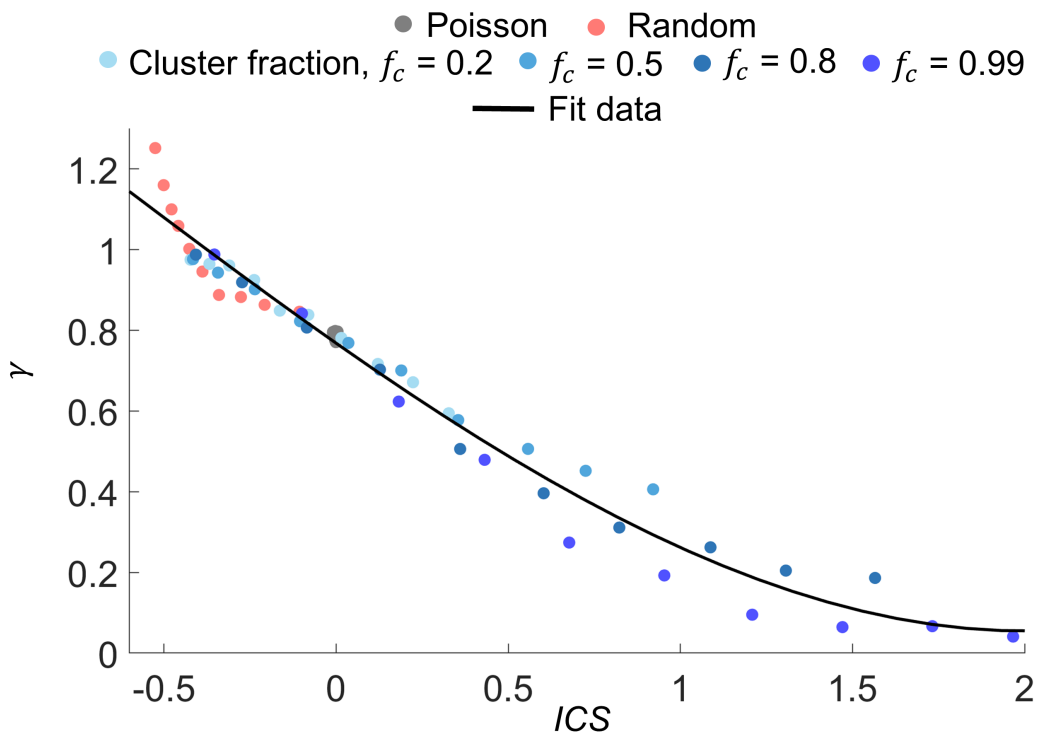


Figure 3.4: Scale factor, γ, which is a ratio of effective extinction coefficient obtained from the ray tracing simulation to the one predicted by independent scattering theory (Eq. (3.14)) as a function of the *ICS* values for the Poisson, random, ordered and cluster beds with cluster fractions, f_c of 0.2, 0.5, 0.8 and 0.99. The solid line is the best-fit, cubic polynomial (Eq. (3.16)) obtained by excluding the data points for the ordered bed to correlate the effective extinction coefficient of the ensemble with the *ICS*, which is a spatial statistic that is dictated by the solid volume fraction and the spatial distribution of particles in an ensemble.

ICS, and γ and ϕ_s respectively, which indicates that the scale factor is more strongly correlated to the *ICS* as compared to the ϕ_s values. Fig. 3.4 shows scale factors as a function of *ICS* values for all the spatial arrangements and solid volume fractions; a cell size of 0.35 mm was applied for these calculations. In general, the scale factor decreases with increasing *ICS* values because radiative transmittance increases as the spatial positions of the particles becomes increasingly more positively correlated. For spatially uncorrelated particles in the Poisson bed, *ICS* is very close to 0 (Table 3.3) and corresponding value of γ remains constant at 0.79 $\pm$ 0.01. For the random beds, the scale factor increases steeply as the *ICS* values become more negative with

increased constraints in the spatial locations of the particles when the solid volume fraction becomes larger (Table 3.3). The residuals and fitting errors are relatively larger (by 10%) for the larger solid volume fractions (ICS values of -0.53 to -0.48 for $\phi_s = 0.4$–0.5), as compared to the smaller solid volume fraction (ICS values of -0.46 to -0.11 for $\phi_s < 0.4$). This difference in the quality of fitting is in part due to the challenge of generating random distributions of particles that minimize for overlaps for the larger solid volume fractions ($\phi_s > 0.4$). For the cluster beds, the scale factor decreases as the ICS value ranges from -0.42 to 1.97 depending upon the solid volume fraction and the cluster fraction (Table 3.3). For ICS values in the range of -0.42 to 0, the clustered and the random arrangements of the particles are grouped close to each other because the cluster beds have similar spatial arrangement of particles, both, inside and outside the clustered region regardless of different cluster fractions when $\phi_s > 0.4$. Therefore, both the random and the clustered beds start to exhibit more ordering effects resulting in overlapping ICS values when the solid volume fraction is large.

The scale factors can be correlated to the ICS values by a cubic polynomial given by Eq. (3.16) and represented as the solid black line in Fig. 3.4,

$$\gamma = 0.029(ICS)^3 + 0.063(ICS)^2 - 0.60(ICS) + 0.77 \tag{3.16}$$

Eq. (3.16) fits the data with an R^2 of 0.97 and a maximum residual value of 6.1% for the random beds. This correlation is able to correct for the dependent scattering effects due to both the spatial arrangements of the particles and the solid volume fraction, as compared to the prior literature, which reported a cubic dependence fo the scale factor as only a function of the solid volume fraction [20, 23, 24, 32].

To probe the sensitivity of the cell size on the γ–ICS correlations, the above analyses was also repeated for a cell size of 0.51 mm, i.e., $a_{\text{cell}} \approx 2d_p$ (Table B.1 in

Appendix B.4). The quality of the fit function is not as good for $a_{\text{cell}} = 0.51$ mm as compared to $a_{\text{cell}} = 0.35$ mm. The fitting errors increase (R^2 value decreases to 0.92 from 0.97) mostly due to the large residuals obtained for the high solid volume fraction random beds, $\phi_s > 0.4$. Even though the strength of the correlations are different with the chosen cell sizes, the cubic polynomial dependence is preserved.

3.3.2.3 Path-length distribution

Fig. 3.5 presents the path-length distribution functions, $p(s)$, obtained from the collision MCRT simulations (solid lines) and as explained in Table 3.2, as a function of the attenuation distance, s. For all spatial distributions other than the ordered beds, Fig. 3.5 also depicts the fitted path-length distribution function (dashed lines), $p^*(s)$,

$$p^*(s) = -\frac{d}{ds}\left(T(s)\right) \tag{3.17}$$

where $T(s)$ is obtained with Eqs. (3.12) and (3.13) using parameters from Table 3.4. Results in Fig. 3.5 are shown only for the smallest and largest solid volume fractions; for the sake of brevity we only include cluster fractions of 0.2 and 0.99 in Fig. 3.5. Except for the ordered beds, all the other spatial arrangements exhibit exponential dependence of $p(s)$ on the attenuation distance. The fitted functions are within 10% of predictions from direct MCRT simulations, for attenuation distances larger than 2.8 mm and 2 mm for $\phi_s = 0.05$ and 0.5 respectively. However, for the smaller attenuation distances, the fit function overestimates the probability densities, by up to 40% for the cluster beds ($f_c = 0.99$). These differences are attributed to the local particle concentration variations near the bottom launch surface and its effects on radiative transport. While these variations are intrinsically accounted for in the direct/collision MCRT simulations, the fit function, $p^*(s)$, models an *effective*

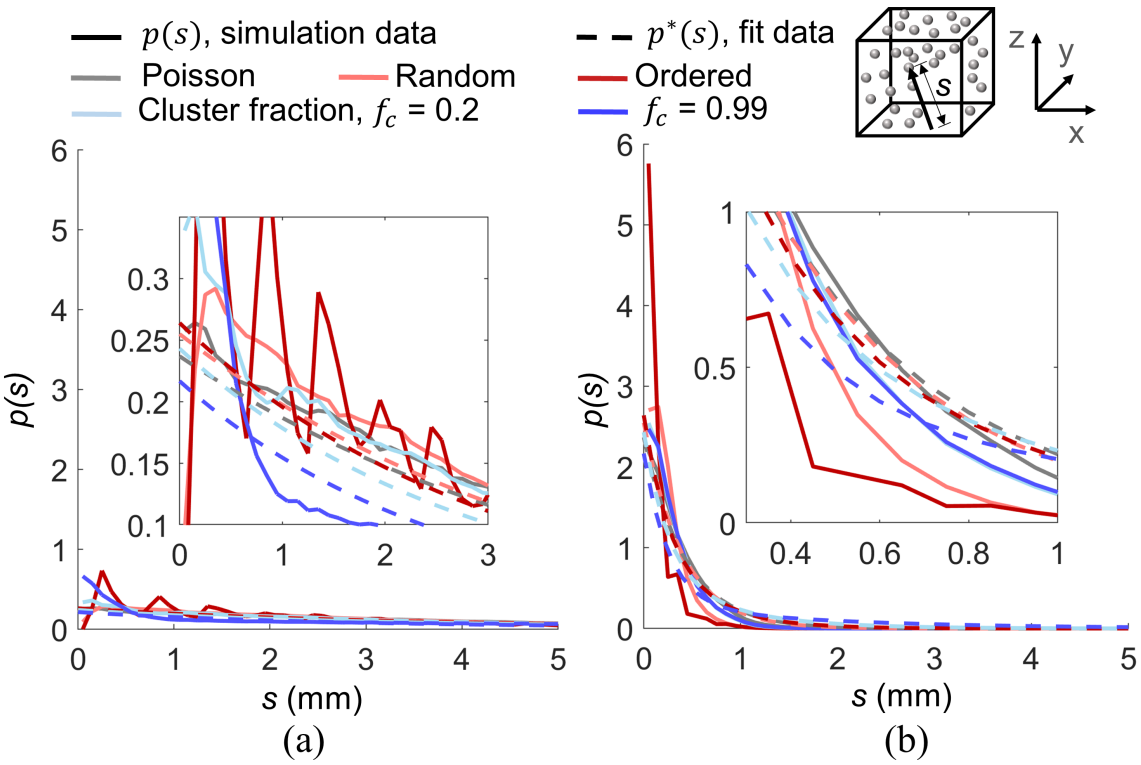


Figure 3.5: Probability density function for attenuation distance, $p(s)$, as a function of attenuation distance, s, for Poisson bed, random bed, ordered bed and cluster bed with cluster fractions of 0.2 and 0.99 with volume fraction fixed at (a) $\phi_s = 0.05$ and (b) $\phi_s = 0.50$. Solid lines represent $p(s)$, obtained from the collision MCRT simulations and the dashed lines represent the fitted path-length distribution, $p^*(s)$, obtained from Eqs. (3.12) and (3.13). Ray-tracing modeling domain shown in Fig. 3.1(c,d) with particle diameter of 0.25 mm and particle reflectivity of 0.7 was used to perform collision MCRT simulations. Path-length MCRT simulation used fitted parameters obtained in Table 3.4. The schematic in the legend depicts the attenuation distance, s, which is the distance a ray that is launched at the lower surface travels before being absorbed or reflected by a particle and used to obtain $p(s)$ as explained in Table 3.2.

extinction coefficient by treating the discrete particles as a continuum resulting in the largest disparities close to a boundary.

At any solid volume fraction, the probability density functions for the Poisson and the random beds are comparable to each other, except at low attenuation distances, where the interparticle spacing for the random bed is larger than that of the Poisson bed (Fig. 3.5). This results in relatively larger $p(s)$ for the random beds as compared to the Poisson bed. In contrast, for small attenuation distances, $p(s)$, is larger for the cluster beds, and increases even further with cluster fraction, as compared to the Poisson bed. This trend is because the cluster region with a large solid volume fraction ($\phi_{\mathrm{s,cluster}} = 0.52$) is located at the bottom left corner of the domain (Fig. 3.1),which increases the attenuation probabilities of the rays launched from the bottom surface. The ordered beds exhibit the most unique features with evident oscillations between local minima and maxima in its $p(s)$ profiles. This effect is due to the discrete nature of absorption and scattering events in an ordered bed as compared to the other spatial arrangements, the latter results in a more statistically continuous occurrence of the same events. The local maxima (peaks) are representative of rays being attenuated at discrete particle layers present at a fixed depth in the bed, i.e., at a fixed s value. The local minima (troughs) result from the lack of absorption or scattering in the void space in between particle layers. For the case of $\phi_s = 0.5$, the probability density functions are similar for all the spatial distributions because the rays are more likely to be attenuated within a short distance for all spatial arrangements of the particles.

3.3.2.4 Angular distribution for transmission, $p(\theta_t)$

Simulation results were also used to probe the influences of the spatial distributions on the directional nature of radiation scattering events that leads to transmission of rays by the ensemble. Fig. 3.6 compares the probability density functions for transmission, $p(\theta_t)$, obtained from Table 3.2, for the different spatial distributions of

the particles at a fixed solid volume fraction of $\phi_s = 0.05$ and by considering cases of low, moderate and high transmittance of $T = 0.1$, 0.42 and 0.9 respectively. Varying the transmittance is physically equivalent to changing the thicknesses of the packed bed for a fixed solid volume fraction and a packing arrangement. A solid volume fraction of 0.05 was selected so that enough statistics ($> 10^5$ rays) is available to generate $p(\theta_t)$, especially when considering $T = 0.1$.

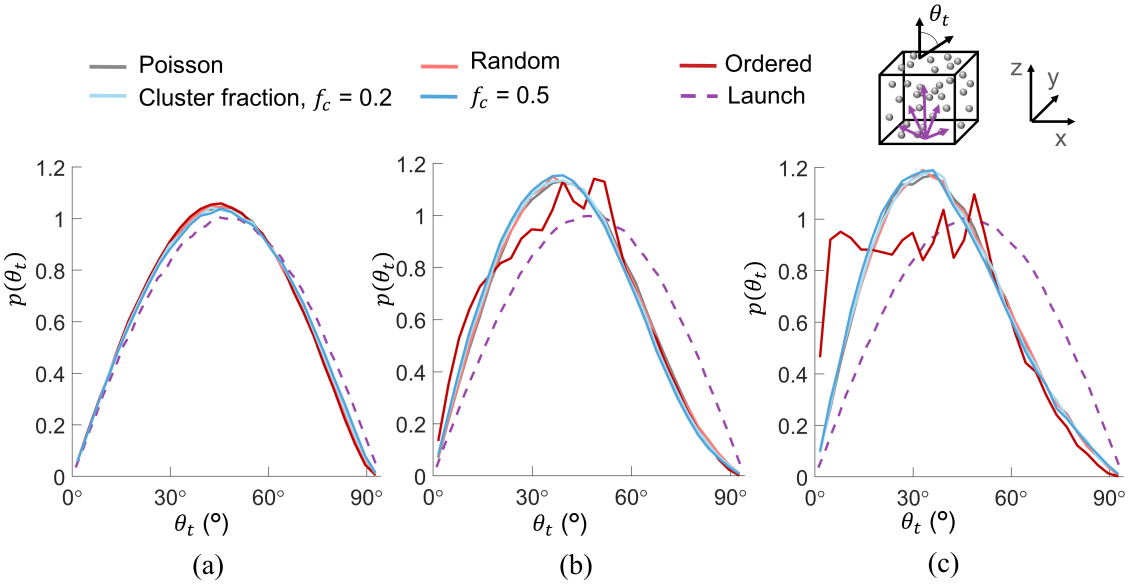


Figure 3.6: Probability density function of transmitted angle for Poisson bed, random bed, ordered bed and cluster bed with cluster rate of 0.2 and 0.5 with volume fraction fixed at $\phi_s = 0.05$ and with radiative transmittance of (a) $T = 0.9$, (b) $T = 0.42$ and (c) $T = 0.1$. Ray-tracing modeling domain shown in Fig. 3.1(c,d) with particle diameter of 0.25 mm and particle reflectivity of 0.7 was used to perform collision MCRT simulations. The dashed line is the probability density function of launching angle at the lower surface. The schematic in the legend depicts the diffuse distribution of the launched rays (purple rays at $z = 0$) and the polar angle, θ_t, measured for a transmitted ray to obtain $p(\theta_t)$ as explained in Table 3.2.

We first consider the trends for the angular distribution of the transmitted rays for all beds other than the ordered bed. In all these cases, the angular distribution of the transmitted rays largely matches the diffuse nature of the rays launched from the bottom surface, i.e., $p(\theta_t) \approx \sin(2\theta_t)$, at all transmittance values. For low and mod-

erate transmittance ($T = 0.1$ and 0.42), the peak probability density for transmitted rays occurs at 30°. At smaller transmittance, relatively more rays undergo multiple scattering events before getting transmitted, as compared to the larger transmittance cases. After many scattering events, it is observed that the transmitted rays are more likely to have smaller polar angles. Therefore, the peak θ_t value is smaller as compared to the launch distribution. When the transmittance increases to 0.9 (Fig. 3.6(a)), the peak value for θ_t shifts closer to 45° and starts to resemble closely the diffuse angular distribution of the launched rays. This is because relatively more rays can get directly transmitted from the launch surface.

For the ordered beds, not only is the $p(\theta_t)$ different as compared to the other beds, but it's also significantly influenced by the transmittance. For a low transmittance of 0.1 (Fig. 3.6(c)), the ordered bed exhibits multiple local minima and maxima in the $p(\theta_t)$ profile, similar to that observed for $p(s)$ (Fig. 3.5), because of scattering (and therefore transmission) events occurring at discrete layers of particles in the ordered packing of the ensemble. The local maxima occurs whenever rays get transmitted (either directly or after multiple scattering events) while traveling through the gaps between neighboring particles. Compared to the other spatial distributions, there is a distinctly higher probability density for transmitted rays with $\theta_t \approx 10°$. This is attributed to directly transmitted rays through the clear view paths between discrete layers of particles. As the transmittance increases, the ordered bed $p(\theta_t)$ approaches the statistics obtained for the other beds and that of the launched rays because of the transmission plane being very close to the launch surface (within 3.1 mm and 0.55 mm respectively for $T = 0.42$ and 0.9 respectively). A similar analysis was performed for a higher solid volume fraction of 0.2 and the effects of the spatial distributions on the trends for $p(\theta_t)$ were comparable to the results obtained in Fig. 3.6 (Fig. B.6 in Appendix B.5).

3.3.2.5 Scattering phase function, $\Phi(\theta_i, \theta_s)$

Fig. 3.7 shows the computed scattering phase functions for the ordered beds at the smallest and the largest solid volume fraction modeled. In Fig. 3.7, the polar angles for incident and the scattered rays are measured with respect to the global z-axis, where an incident angle of 0° is parallel to the z-axis, whereas an incident/scattered angle of 90° will be perpendicular to the z-axis (Fig. 3.7); forward scattering of rays along the direction of the launched rays occurs when $\theta_s \leq 90°$ and back-scattering for $\theta_s > 90°$. For all spatial arrangements of the particles other than the ordered bed, isotropic scattering, i.e., $\Phi(\theta_i, \theta_s) \approx 1$ with equal probability of scattering in all directions, was predicted at all solid volume fractions (not shown). This outcome of isotropic scattering for the Poisson, random and the clustered beds is justifiable because specular reflection is modeled where the ray intersects the particle surface. In the limiting case of a single particle, specular surface reflections will lead to a scattering phase function of 1. The same behavior is also observed for the ensemble because of the isotropic nature of all the beds modeled (including the ordered beds), where there is no difference in the arrangement of the particles with respect to x-, y-, or$z$-axis. Therefore, rays launched from the void space of the bed intersects at different points on the surfaces of the particles that are randomly distributed throughout the volume of the bed, which, overall, contributes to isotropic scattering by the ensemble.

Fig. 3.7 shows that ordered beds exhibit anisotropic scattering, where the scattering phase function is dependent on the incident and the scattered angles and is also influenced by the solid volume fraction. This trend is largely because of scattering events occurring on a selected subset of points on the particle surfaces for the ordered bed, as compared to a more random distribution of ray-particle intersection points for all the other spatial distributions. For the sake of brevity, scattering phase functions are only shown for incident angles, $\theta_i \in [0°, 90°]$, because the phase functions are the

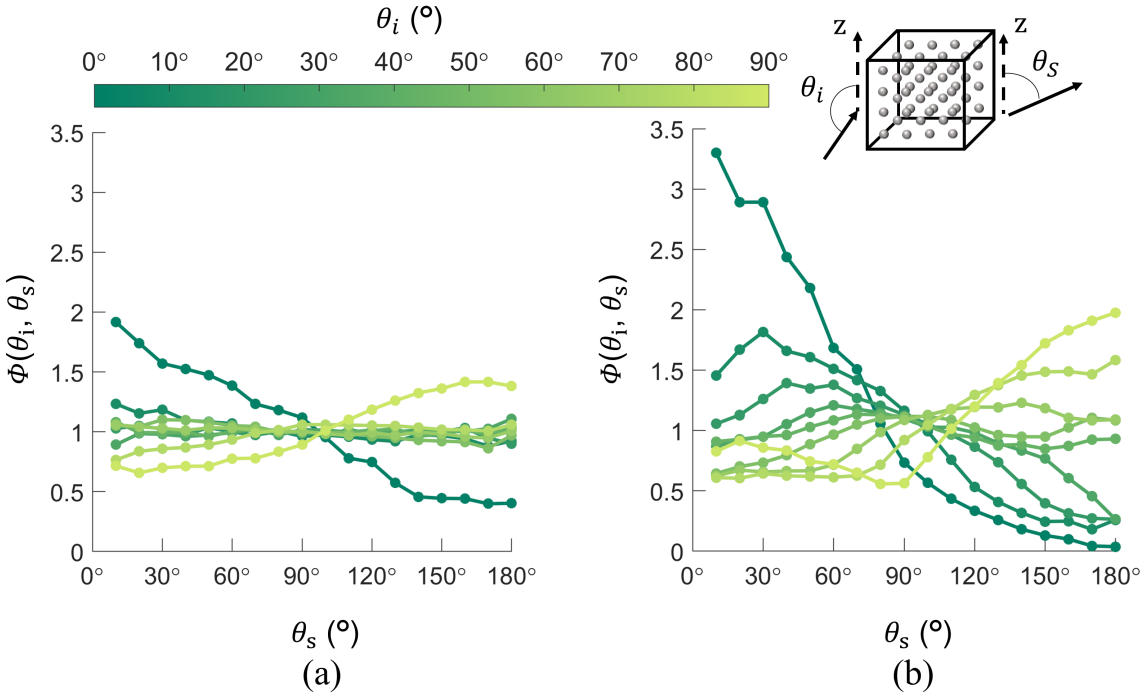


Figure 3.7: Scattering phase function, $\Phi(\theta_i, \theta_s)$, based on incident, θ_i and scattered, θ_s, polar angles defined with respect to the global z-axis for ordered beds with solid volume fractions of (a) $\phi_s = 0.05$ and (b) $\phi_s = 0.5$. Ray-tracing modeling domain shown in Fig. 3.1(c,d) with particle diameter of 0.25 mm and particle reflectivity of 0.7 was used to obtain pairs of incident and scattered angle values based on the procedure explained in Table 3.2. Incident polar angles vary from 0°–90° with statistics obtained for $\Phi(\theta_i, \theta_s)$ with a bin size of 10°; individual colors in the color scheme represents θ_i belonging to angular intervals of [0°,10°),[10°,20°) up to [80°,90°]. $\Phi(\theta_i, \theta_s)$ for supplementary angles of θ_i will be equal and not shown. For a fixed range of θ_i values, represented by the individual colors, the x-axis indicates rays that are scattered into angular intervals for θ_s of [0°,10°),[10°,20°) up to [170°,180°].

same for the supplementary incident angles (Eq. (3.18)) volume fraction.

$$\Phi(\theta_i, \theta_s) = \Phi(180^\circ - \theta_i, \theta_s) \tag{3.18}$$

The scattering phase functions are equal for supplementary incident angles because of the symmetry in the ordered beds generated, i.e., the ensemble of particles appears the same for incident angles of, both, θ_i and $180^\circ - \theta_i$. For the case of the low solid volume fraction (Fig. 3.7(a)), largest anisotropy in scattering is observed for incident angles that are either closely parallel or antiparallel (i.e., $\theta_i \in [0^\circ, 10^\circ]$ and $[170^\circ, 180^\circ]$, or, when nearly perpendicular ($\theta_i \in [80^\circ, 100^\circ]$) to the z-axis. For incident rays with $\theta_i \in [0^\circ, 10^\circ]$ and $\theta_i \in [170^\circ, 180^\circ]$, a relatively larger fraction of forward scattering is observed with $\theta_s < 90^\circ$. For these incident angles, the incident rays are more likely to be intercepted at points on the surface of the particle where the local incident angle (i.e., the angle subtended by the incident ray with the line vector connecting the center of the particle and the point of intersection) is very close to or only a little less than 90°. Specular reflections at these points of intersection will lead to the polar angles of the scattered rays being more concentrated in the range of $[0^\circ, 90^\circ]$. The opposite trend is observed for incident rays with $\theta_i \in [80^\circ, 100^\circ]$, wherein, a relatively larger fraction of rays is likely to be back scattered with $\theta_s > 90^\circ$. Detailed visualizations of the rays corresponding to the incident angles, which lead to substantial anisotropy in $\Phi(\theta_i, \theta_s)$ are shown in Fig. B.7 in Appendix B.6. With increase in the solid volume fraction, the extent of anisotropy between forward and backward scattering with respect to the different incident angles becomes even larger (Fig. 3.7(b)). For example, when $\phi_s = 0.5$, incident angles in the range of $[0^\circ, 30^\circ]$ and $[150^\circ, 180^\circ]$ result in a relatively larger fraction of forward scattered rays, as compared to when $\phi_s = 0.05$. This is because the interparticle distance between particles increases with volume fraction ϕ_s, which results in a larger fraction of incident rays to intersect on

particle surfaces with local incident angles close to 90°. The same reason contributes to relatively more backward scattering for incident angles of $[60°, 120°]$ in the case of $\phi_s = 0.5$. Fig. B.8 in Appendix B.6 shows results for the scattering phase function in terms of the angle between the incident and the scattered directions. These results also indicate increase in anisotropy for the ordered bed with increase in solid volume fraction.

3.4 Limitations and Future Work

This work relied on using the *ICS* to quantify the spatial statistics of particle distributions and concentrations. However, this metric is highly sensitive to the cell size and requires a large domain size relative to the cell size to obtain reliable statistics. The first factor is also the reason why the predicted *ICS* values for random and ordered beds are somewhat indistinguishable, and that the *ICS* values for the ordered beds are not always equal to -1. Therefore, the cell size needs to be carefully optimized and selected for *ICS* quantification in any application. In this work, we determined an optimal cell size of $1.5d_p$ based on the goodness of fits obtained for γ–*ICS* correlations. In general, we recommend choosing cells sizes (relative to the particle size) that are large enough to detect clusters and small enough to get reliable statistics (at least $>$ 100 cells for *ICS* quantification). Even though, this study included clustered particles, only a single cluster was modeled, and this cluster solid volume fraction was fixed at 0.52. An extension of this framework to include multiple clusters and cluster solid volume fractions is outside the scope of this work, but will be considered in future research. Finally, the proposed approach to evaluate scale factors as a function of the *ICS* is not operative for an ordered arrangement of particles. Therefore, future work will explore the use of γ–*ICS* correlations in multiphase flows with solid particles and further probe radiative transport in ordered distributions of particles.

3.5 Conclusions

We present a comprehensive investigation of the role of spatial distributions and solid volume fractions on radiative transport in particulate media with large size parameters. Compared to prior literature, our study uniquely quantifies how three-dimensional spatial distributions of particles, in addition to the solid volume fraction, affects dependent or non-point scattering in participating media with large size parameters. Two main modeling innovations were introduced in this work: (a) a rigorous framework was developed to control the spatial arrangements and solid volume fractions of particles; and (b) radiation-particle interactions in all spatial arrangements were evaluated against the fully random Poisson distribution to contextualize results. For the first time, we have predicted scale factors, which compare the extinction coefficients with and without dependent scattering, as a function of spatial correlations in particulate media.

Packed beds of particles with varying spatial distributions–Poisson, random, ordered (simple cubic ordering), and cluster, and solid volume fraction (0.05–0.5), were computationally generated. Spatial point statistics was quantified using an index of cluster sampling (ICS). Collision-based Monte Carlo ray tracing simulations were performed to evaluate radiative transport. Model results highlight that even at a fixed solid volume fraction, the spatial distributions of particles can have a significant impact on the radiative transmittance and therefore the extinction coefficients and scale factors for packed beds. Even for the lowest solid volume fraction modeled ($\phi_s = 0.05$), substantial deviations from independent scattering theory were observed in spatially correlated media (i.e., ordered and cluster beds of particles); deviations of up to 84% and 99% respectively from independent scattering theory predictions. Our study reveals that the scale factors are strongly correlated to the ICS values, which are influenced by, both, the three-dimensional distributions and the solid volume fraction of particles. Scale factors were determined for all spatial distributions

other than the ordered beds. The ordered beds exhibited a more distinct radiative transport behavior as compared to all the other spatial distributions. This outcome is attributed to the more discrete nature of radiation-particle interactions in ordered beds. While the path-length distribution was largely exponential for all other spatial distributions, the ordered bed exhibited discrete peaks and troughs. Similarly, the angular distribution of the transmitted rays for the ordered bed had multiple peaks and differed markedly from the diffuse distribution of the rays launched. Finally, while all the other spatial distributions exhibited isotropic scattering, ordered beds resulted in anisotropic scattering, the extend of which increased with the solid volume fraction.

On the whole, the scale factor γ–ICS correlations developed in this work present a far more agile and a computationally efficient approach determine effective radiative properties while accounting for dependent scattering effects, as compared to direct ray tracing. These correlations are expected to especially be useful when modeling radiation in multiphase flows with solid particles.

CHAPTER IV

Flow Modeling to Characterize Solid Volume Fractions in Gravity-Driven Particle Curtains

This chapter has been adapted from a manuscript published by the author of this thesis:

- **Rulko, T.A., Li, B., Surhigh, B., Mayer, J.M., Bala Chandran, R., 2023. Optical measurements and flow modeling to characterize solid volume fractions in gravity-driven particle curtains. Solar Energy 264, 111989.**

4.1 Introduction

The next generation of concentrated solar power (CSP) plants promises improved efficiency and lower cost, partly through the use of solid ceramic particles as a medium to capture, transfer, and store heat in place of molten salts. Gas–solid multiphase flows, including fluidized beds, moving packed beds, and gravity-driven particle curtains, marry the advantages of high thermal capacity and thermal conductivities in solids with enhanced mass, momentum, and heat transfer rates by achieving fluid-like behavior, making them ideal for heat transfer and thermal energy storage applica-

tions [135–137]. This study focuses on modeling to validate the solid volume fractions (equivalently solids concentration) distribution to experimental measurements in a gravity-driven flow of particles.

Traditionally, the flowing particles are treated as a continuum, assigned with effective/bulk parameters different from fluids. This approach is criticized for failing to describe the discrete nature of moving particles, especially it can hardly evaluate the influence of multiple particle parameters, including restitution and friction coefficients. Therefore, the Discrete Element Method (DEM), a Lagrangian approach that tracks individual particles, was developed to copy with this challenge [138]. Recent improvements in computer hardware and parallelization strategies allow researchers to apply DEM technique to model industrial systems.

DEM modeling has been validated as a well-established tool to solve engineering problems [139, 140]. For instance, DEM technology has been successfully used to model the powder transport in screw conveyor [141] and rotating paddle wheels [142]. It helped designers determine the optimal feeding mass flow rate that gives the best product quality. Coupled with computational fluid dynamics (CFD) module, DEM technology can treat more complex systems, such as chemically reacting systems. For example, Peters examined the iron ore reduction in blast furnaces [143]. Gao et al. studied the pyrolysis of cubic biomass particles in a fixed-bed reactor [144]. Mahiques et al. simulated the calcination of limestone in shaft kilns and the combustion of municipal waste on grate firing systems [145].

Motivated by these factors, this study applies DEM modeling in a gravity-driven flow of millimeter-sized ceramic particles to validate the solid volume fraction distribution measured in experiments. To deduce a solid volume fraction from the measured transmittance, prior work has extensively applied the Beer-Bougert-Lambert law (henceforth referred to as Beer's law), which is only applicable for homogeneous and purely absorbing media with normal illumination [146]. Good agreements are ob-

served between the experimental measurements and the DEM simulations. A unique contribution from this study is that these assumptions were tested with ray tracing simulations, informing the governing relationships between measured transmittance, optical properties of the particles, and the solid volume fraction. Two elements: (a) discharge slot width, and (b) friction coefficient are adjusted to validate the mass flow rate and the solid volume fraction.

4.2 Modeling methods

The solid volume fraction, ϕ_s, is expected to decrease as a function of vertical height through the channel, z. This dependence is quantified with two modeling approaches. In a relatively simplistic calculation, a force balance was performed for a single particle combined with empirical correlations for particle discharge rates from the hopper. In another model, multi-particle position tracking was performed using discrete element modeling.

4.2.1 Single particle force balance

Balancing the gravitational and drag forces in 1D, a reasonable approximation for the spatial variation of ϕ with z is obtained. The ordinary differential equation (ODE) in Eq. (4.1) governs the net acceleration of the particle, with the initial condition given in Eq. (4.2):

$$\frac{dv_p}{dt} = g - \frac{0.5\rho_{\text{air}} C_D A_p v_p^2}{m_p} \tag{4.1}$$

$$v_p(t=0) = v_{p0} \tag{4.2}$$

where v_{p0} is the initial particle velocity as it exits the hopper, ρ_{air} is the air density, A_p is the cross-sectional area of one particle, m_p is its mass, and C_D is the drag coefficient

for a sphere. The latter is obtained from the empirical correlation reported by [147]:

$$C_D = \frac{24}{\mathrm{Re}} + \frac{2.6\left(\frac{\mathrm{Re}}{5.0}\right)}{1+\left(\frac{\mathrm{Re}}{5.0}\right)^{1.52}} + \frac{0.411\left(\frac{\mathrm{Re}}{2.63\times10^5}\right)^{-7.94}}{1+\left(\frac{\mathrm{Re}}{2.63\times10^5}\right)^{-8.00}} + \frac{0.25\left(\frac{\mathrm{Re}}{10^6}\right)}{1+\left(\frac{\mathrm{Re}}{10^6}\right)} \tag{4.3}$$

where the Reynolds number is defined based on the particle size, $\mathrm{Re} = \rho_{\mathrm{air}} v_p d_p / \mu$, and ranges from $\mathcal{O}(10^1)$ to $\mathcal{O}(10^2)$. Note that μ is the dynamic viscosity of air. By conservation of mass and for a steady flow rate, $\dot{m}$, through the channel, the solid volume fraction is inversely proportional to particle velocity, v_p:

$$\phi_s = \frac{\dot{m}}{\rho_p \, A \, v_p} \tag{4.4}$$

where ρ_p is the bulk particle density and A is the curtain cross-sectional area, defined by the depth and width of the flow channel.

The initial velocity as the particle exits the hopper is obtained by adapting the empirical Rose–Tanaka–Beverloo–Nedderman (R–T–B–N) correlation for hoppers with rectangular openings [148]:

$$v_{p0} = 0.74\sqrt{g D^*_{sH}} \tag{4.5}$$

where D^*_{sH} is the hydraulic diameter. The discharge slot area and perimeter, A^*_s and P^*_s, respectively, used to calculate hydraulic diameter (Tables 4.1, 4.2) are corrected for an empty zone near the slot edge, which has been observed empirically [149]. This correction is applied by subtracting $k^* d_p$ from each slot dimension, where $k^* = 1.15$ is a constant. For clarity, the physical dimensions are described in Table 4.1, while areas and other derived dimensions are described in Table 4.2. The R–T–B–N correlation is most accurate for particle diameters greater than 0.4 mm, below which drag effects become important, and where at least 6 particles fit across the width of the hopper

opening [149].

Table 4.1: Relevant physical dimensions for measurement and modeling

Symbol	Description
$d_p = 1.23$ or 2.18 mm	Particle diameter
$W = 9.58$ mm	Flow chamber width
$L = 150$ mm	Flow chamber length
$H = 500$ mm	Flow chamber height
$\overline{W}_s = 5.93$ mm	Discharge slot width (average)
$W_{s,c} = 5.73$ mm	Discharge slot width (at center)

Table 4.2: Table of derived dimensions

Symbol	Description
$W_s^* = \overline{W}_s - k^* d_p$	Modified discharge slot width
$L^* = L - k^* d_p$	Modified discharge slot length
$A_p = \pi d_p^2/4$	Cross-sectional particle area
$A = LW$	Curtain cross-sectional area
$A_s = L\overline{W}_s$	Discharge slot area at hopper exit
$A_s^* = L^* W_s^*$	Modified discharge slot area
$P_s^* = 2L^* + 2W_s^*$	Modified discharge slot perimeter
$D_{sH}^* = 4A_s^*/P_s^*$	Modified hydraulic diameter

Finally, the steady-state mass flow rate referenced in Eq. (4.4) is governed by the rate of discharge of particles from the hopper, which is obtained from the initial velocity estimated using the R–T–B–N correlation in Eq. (4.5) and the definition of mass flow rate:

$$\dot{m} = \rho_p \phi_0 A_s^* v_{p0} \tag{4.6}$$

where ϕ_0 is the initial solid volume fraction of particles in the hopper. Assuming an initial random packing of monodisperse spheres in the hopper, ϕ_0 is set equal to 0.625 [150]. The set of algebraic equations given in Eqs. (4.3)–(4.6) is solved along with the ODE in Eq. (4.1) to determine ϕ as a function of position, z.

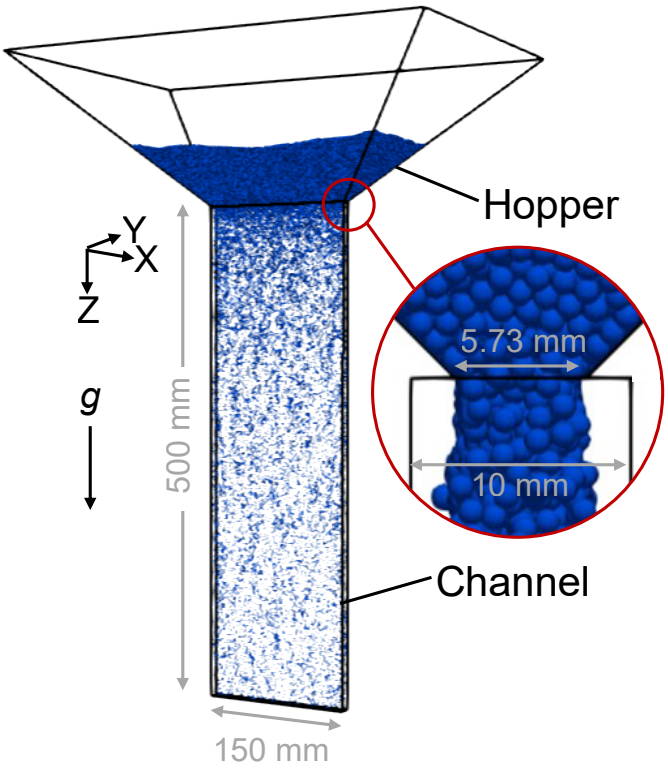


Figure 4.1: Flow model used in DEM simulations, including a detailed view of the discharge slot that accounts for the deformation in the manufactured hopper.

4.2.2 Discrete element modeling for particle tracking

To perform multi-particle position tracking, LIGGGHTS [151], an open-source software to perform discrete element modeling (DEM), is used. The modeling domain (Fig. 4.1) is a hopper-channel geometry based on the experimental flow chamber (Fig. C.1) in T.A. Rulko et al. [152]. The dimensions of the discharge slot are selected based on the geometry as manufactured; deformations in the manufactured hopper are non-uniform and greater in the center where the transmittance is measured. This leads to a modeled slot width, $W_{s,c}$ of 5.73 mm (Fig. 4.1 inset, Table 4.1). This choice results in the overall slot area being smaller than the manufactured slot area, while the width at the center matches the manufactured flow chamber.

In this DEM simulation, particle-particle and particle-wall collisions are computed

based on the Hertzian theory. The DEM time step is set to 2×10^{-5} s, following the criteria in Sec. 2.2.1. The effect of drag on particle flow was found to be negligible due to the short residence time of particles in the channel and the low viscosity of air. This was further confirmed by comparisons of analytical models with and without drag. The parameters implemented in this DEM model are reported in Table 4.3. Neither the particle-particle nor particle-wall rolling friction forces are modeled since their influences are expected to be negligible for the flow configuration investigated in this study [153].

Table 4.3: Particle geometric and material properties used in DEM simulations

Parameter	Value
Particle density ρ (kg/m^3)	2760.5
Particle diameter d_p (mm)	1.23, 2.18
Young's modulus E (MPa)	5.00
Poisson's ratio υ	0.17
Coeff. of restitution, particle-particle ϵ_p	0.45
Coeff. of restitution, particle-wall ϵ_w	0.45
Coeff. of static friction, particle-particle $\mu_{s,pp}$	0.36
Coeff. of static friction, particle-wall $\mu_{s,pw}$	0.1

The particles modeled in the DEM simulations are assumed to be spherical and monodisperse with an average diameter and particle density obtained from measurements. DEM simulations show that the influence of a polydisperse distribution on flow is negligible; comparable results are obtained with a monodisperse distribution with an average particle size obtained from the experimentally measured size distribution (Sec. C.2). While particle shape can significantly influence flow behavior [154], image analyses of particle samples show high sphericity and validate the choice of modeling particles as spheres. Additionally, particle surface roughness can influence friction and restitution coefficients, and therefore sensitivity of predictions to the friction coefficient is evaluated.

It is expected that DEM simulation results will be influenced by input values

chosen for various model parameters, including the friction and restitution coefficients (Table 4.3) [153]. Therefore, baseline values are selected rationally and sensitivity analyses is performed for specifically the particle-particle and particle-wall friction coefficients. An unrealistically small Young's modulus of $E = 5$ MPa was used for the particle force calculations, where the permitted range is 5 MPa to 1 GPa in LIGGGHTS [151]. This artificial reduction in Young's modulus has been applied in prior work and has been shown to have negligible influence on the flow behavior [155]. While particle-wall static friction has negligible influence on the flow behavior, the particle-particle friction coefficient has a significant effect on both the mass flow rate and the solid volume fraction distribution. Particle-particle friction coefficients in the range of 0 to 0.9 are modeled, which includes the values 0.5 to 0.72 reported in the literature for commercially available Carbobead HSP and CP ceramic particles for CSP applications [156, 157]. A nominal restitution coefficient of 0.45 is assumed with the expectation that its influence on dilute particle curtain flows will be minimal. This is further supported by predictions that show less than 8% deviation in mass flow rates for a wide range of restitution coefficients ($\epsilon_p \in (0.05\text{–}0.85)$) in a more contact-driven flow of particles inside a hopper [153]. Rolling friction is neglected as its effects on dilute, particle curtain flows are expected to be insignificant.

To initialize the DEM calculations, 1.5 kg of particles are inserted in the hopper and given $\sim$5 seconds to settle. Then, the particles are released into the channel until the hopper is empty. To obtain the solid volume fraction, ϕ, a few snapshots of the positions of particles in the channel are extracted from the simulations. The channel region is divided into 20 bins and the number of particles inside each bin, $N_{p,b}$, is counted. This bin height is selected to be much larger than the particle size ($H_b = 25\text{mm} \approx 12\text{–}25d_p$). The spatially-averaged solid volume fraction is computed

with Eq. (4.7):

$$\phi_b = \frac{N_{p,b}\frac{\pi}{6}d_p^3}{LWH_b} \tag{4.7}$$

The approach of obtaining solid volume fraction from DEM simulations differs from the experimental techniques, which transform a measured transmittance to a solid volume fraction.

4.2.3 Transmittance dependence on particle reflectivities

Snapshots of particle positions from the DEM simulations are directly input to collision-based Monte Carlo ray tracing models to calculate transmittance for various particle reflectivities, R_p ranging from 0 (purely absorbing/black) to 0.99 (highly reflective). These results inform how measured transmittance can be converted to a solid volume fraction and its dependence on particle reflectivity. The flow channel is vertically divided into ten subdomains with a size of 10 mm $\times$ 150 mm $\times$ 50 mm subdomains (Fig. 4.2(a)). In each subdomain, 10^6 rays are launched parallel to the y-axis (normal to the x-z plane), as shown in Fig. 4.2(b). Rays are considered transmitted when they reach the opposite side of the channel from where they were launched. Surfaces normal to the z-axis are periodic boundaries, and the surfaces normal to the x-axis are purely absorbing walls.

Transmittance simulations require inputs for the reflectivity of the particles. The model treats particle reflectivity as a variable parameter, but reasonable estimates using experimental measurements are also obtained. Even though the total reflectivity of the porcelain particles is dependent on the spectrum of the light source, estimates for this value are made by measuring the spectral reflectivity of packed beds of the porcelain particles in a UV–Vis spectrophotometer (Shimadzu UV-2600). The particle beds exhibit reflectivity values between 0.5 and 0.6 throughout the visible

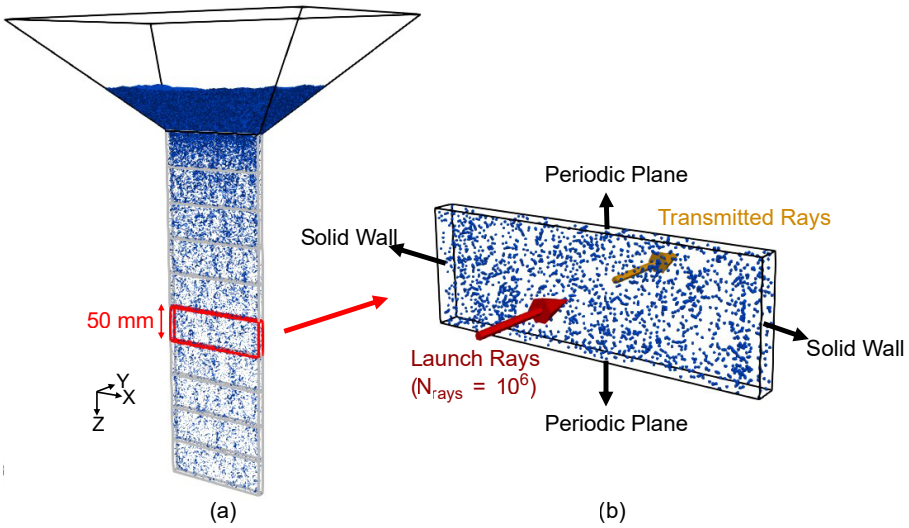


Figure 4.2: (a) Division of the flow chamber into subdomains for ray tracing simulations with (b) an exploded view of the subdomain and the corresponding boundary conditions for ray tracing simulations.

spectrum, which includes most of the energy emitted by the light source. However, the reflectance measured for the bed of particles is expected to underestimate the reflectivity of individual particle surfaces because of multiple light scattering events within the bed.

4.3 Results & Discussion

4.3.1 DEM simulations

Fig. 4.3 shows a qualitative comparison of DEM simulations with snapshots of particle positions captured by the high-speed camera at steady state. Apart from the slight non-uniformity in the experimental results due to a manufacturing defect, these images qualitatively match well with the predicted spatial distribution and the corresponding local solid volume fractions of particles. This lends further credibility to this approach and parameter selection for the DEM simulations. Models predict mass flow rates of 0.206 kg/s and 0.137 kg/s for 1 mm and 2 mm particles, respectively, which is within 10.43% and 14.37% of the experimentally measured values,

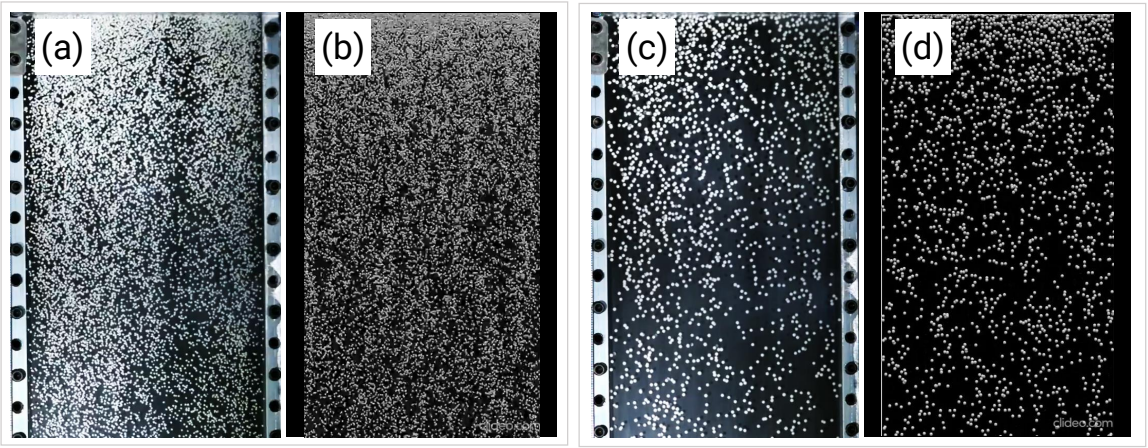


Figure 4.3: Qualitative comparison of experimental (a,c) and simulated (b,d) curtain flow at a selected time instant. (a) and (b) show 1 mm particles, while (c) and (d) show 2 mm particles. Photos are generated by selecting a high-speed camera frame at steady state.

respectively. This deviation is attributed to the manufacturing irregularities in the width of the discharge slot, which cause the modeled overall slot area (which in turn governs the flow rate), to differ from the experimental overall slot area. This is because the modeled geometry uses the center slot width, W_s (Table 4.1). If instead the average slot width, $\overline{W}_s$, is used, a significantly improved prediction within 5% of measurements is observed. All DEM model results for solid volume fractions hereafter are however obtained considering the center slot width to better match the geometry where thermopile transmittance measurements are obtained.

Sensitivity analysis of the predicted mass flow rate and solid volume fraction to the particle-particle coefficient of static friction was performed to calibrate the DEM model to experiments. Fig. 4.4 shows the results of this analysis, where the solid volume fraction is measured at a representative location near the top of the channel ($z = 0.1$ m). The tested coefficients of static friction ranged from 0 to 0.9, and steady-state values are shown in Fig. 4.4. Both the mass flow rate and solid volume fraction decrease more steeply initially when $\mu_{s,pp}$ increases from 0 to 0.5. At $\mu_{s,pp} = 0.5$, the mass flow rate is $\sim$50% lower than at $\mu_{s,pp} = 0$. For further increases in the friction

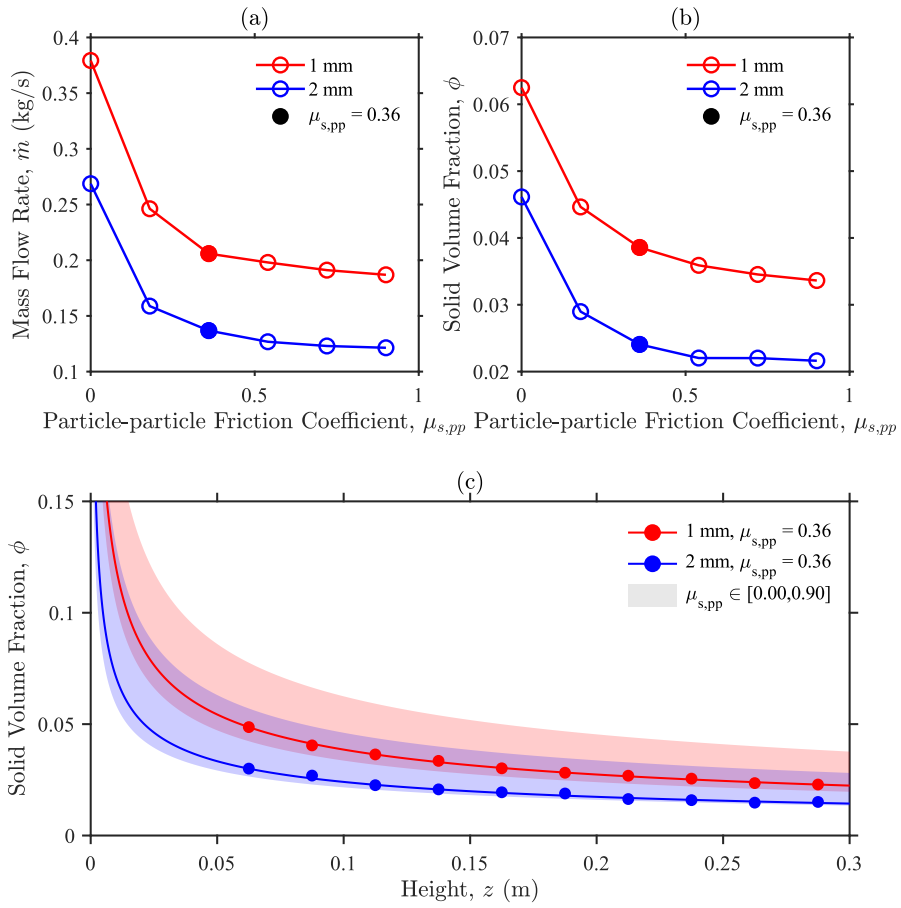


Figure 4.4: Sensitivity test of (a) mass flow rate and (b) solid volume fraction to particle-particle coefficient of static friction at $z = 0.1$ m; (c) solid volume fraction range for 1 mm and 2 mm particles with particle-particle frictional coefficient $\mu_{s,pp}$ ranging from 0 to 0.9. All baseline parameters are listed in Table 4.3.

coefficient, the mass flow rate and solid volume fraction converge asymptotically to a value. With increasing friction coefficient, particles entering the channel lose more momentum through more intensive inter-particle interactions and thus decrease the mass flow rate. Particles spread out along the flow direction under gravity and then are less affected by friction. Friction, as a damping effect against gravity, indicates a lower acceleration rate for rough particles compared to smooth particles. Hence, the velocities for high-friction particles would increase slower and are prone to have lower

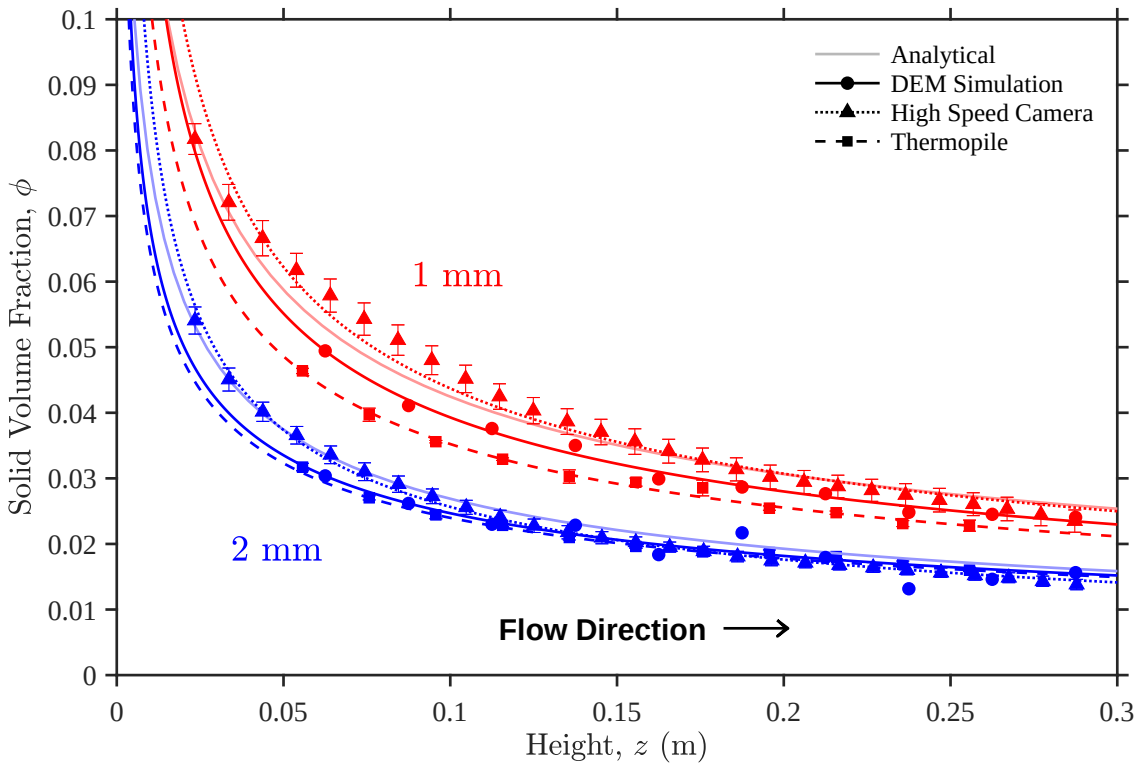


Figure 4.5: Integrated comparison of experimental and modeling results for solid volume fraction as a function of height in a gravity-driven particle curtain for 1 and 2 mm particles. All plotted lines represent power law curve fits, intended to visually guide the connection between data. Thermopile and high-speed camera error bars are based on a 95% confidence interval in the transmittance measurements over four and six trials respectively at every z location.

solid volume fractions. However, the decreasing trend levels off after $\mu_{s,pp} = 0.5$. For particle curtain flows with relatively insignificant inter-particle contacts, most particles are already subject to small tangential forces compared to the normal forces. Therefore, increases in the static friction coefficient beyond a threshold value lead to fewer sliding events and have diminishing effects on the flow behavior. In summary, both the mass flow rate and solid volume fraction are most sensitive to the particle-particle frictional coefficient when it is lower than 0.5; beyond this value, they are less sensitive to this parameter.

From the sensitivity study, $\mu_{s,pp} = 0.36$ was selected as the best value to draw com-

parisons between model predictions and experimental evaluations. From the range of values examined, this friction coefficient minimized error for both mass flow rate and for the estimated range of solid volume fractions from the thermopile measurements. Additionally, the same value of $\mu_{s,pp} = 0.36$ led to a good match between predictions and measurements for both particle sizes tested. Even though this best-fit value is reasonably close to the reported data (0.5–0.72) for commercial proppants considered for CSP applications [156, 157], the porcelain particles investigated in this study are different from these in chemical composition and surface finish. Therefore, a direct comparison of this value against literature data is non-trivial.

4.3.2 Comparison of measurements and model predictions

Fig. 4.5 shows a comparison of the solid volume fractions obtained from the different measurement in T.A. Rulko et al. [152] and modeling techniques. Note that for the experimental methods, solid volume fraction was calculated from raw transmittance by finding the roots of the nonlinear system. All methods predict similar trends of decreasing solid volume fraction along the flow direction and a reduction in the solid volume fraction with an increase in particle size. For all datasets, the solid volume fraction is lower for the larger particle size at all heights, z, which is consistent with the lower flow rates measured for the larger particles; from Eq. (4.4), it is expected that ϕ_s is proportional to $\dot{m}$. For any particle size, the solid volume fraction decreases following a power-law relationship along the flow direction as particles spread out due to gravitational acceleration.

Compared to the thermopile measurements and the DEM simulations, predictions from the single-particle model and the processed images from the high-speed camera overestimate ϕ, especially for the 1 mm particles. The R–T–B–N correlation using Eqs. (4.4) and (4.5) matches measured mass flow rates within 1.2% and 9.4%, respectively, for the 1 mm and 2 mm particles. The larger error for the 2 mm particles

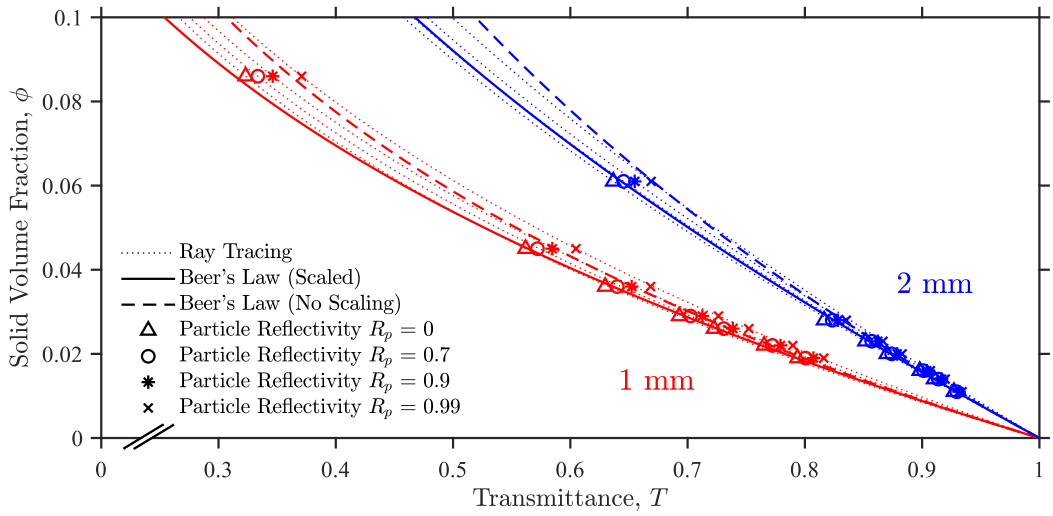


Figure 4.6: Dependence of the relationship between transmittance and solid volume fraction on particle reflectivities based on ray tracing simulations (dotted lines, markers). For comparison, Beer's law (Eq. (1.2)) with (solid) and without (dashed) scale factor S_ϕ are included.

is attributed to the increase in the particle size relative to the hopper discharge slot width, which lowers the accuracy/effectiveness of the R–T–B–N correlation [149]. The overprediction of ϕ from this model is primarily because it precludes the effects of inter-particle interactions in the force calculations and does not account for manufacturing defects and tolerances. Finally, the DEM results match experimental measurements to within 12%. However, these results are specific to chosen model parameters, especially the coefficient of static friction (Table 4.3).

Overall, the comparisons in Fig. 4.5 reveal that there is reasonable convergence in the estimated solid volume fractions across different techniques.

4.3.3 Ray tracing and optical property dependence

To probe the effects of particle reflectivity, R_p, on the relationship between transmittance and solid volume fraction, Monte Carlo ray tracing simulations were performed. These are direct simulations that track intersections of rays with particles present at locations obtained from snapshots in the DEM model and hence dependent

scattering effects are intrinsically factored in these calculations. Results are presented in Fig. 4.6 and are compared with predictions obtained from Beer's law equations with and without dependent scattering effects. These results reveal that as the particle reflectivity increases, the solid volume fraction to yield a fixed transmittance also increases. Therefore, when the measured transmittance from the thermopile is used to obtain a solid volume fraction, particle reflectivity plays an important role, especially when the measured transmittance is small.

The difference between independent and dependent scattering is more pronounced when transmittance decreases and the corresponding solid volume fraction increases. The comparison between the unscaled Beer's law (dashed line) and the ray tracing results (dotted line) reveals a larger difference for the 2 mm particles than the 1 mm ones. This dependence may arise as a consequence of the small ratio between the channel width and the particle diameter, which causes the spatial Poisson distribution assumed by Beer's law to be unrealized. Furthermore, the solid volume fraction at a given transmittance changes with R_p because of scattering due to reflections in the particle curtain; Beer's law does not account for this effect. Indeed, for highly reflective particles, Beer's law with dependent scattering effects, Table 1.1, underestimates the solid volume fraction at a given transmittance.

The results generated from Monte Carlo ray tracing simulations (Fig. 4.6) are applied to obtain a new, reflectivity-dependent scale factor, S_R in Eq. (4.8), applied alongside S_ϕ in Table 1.1, to relate transmittance and solid volume fraction:

$$S_R = 0.13\sqrt{1 - R_p} + 0.87 \tag{4.8}$$

The dependence of the reflectivity scale factor on the particle reflectivity (Eq. (4.8)) is obtained by using the ray tracing datasets with the MATLAB *curve fitting toolbox*, yielding good quality fits ($R^2 = 0.99$). The square root dependence of transmittance

with $1 - R_p$ is consistent with closed-form solutions obtained for transmittance in one-dimensional participating media [158]. For perfectly absorbing particles, S_R has a limiting value of 1 which leads to the traditional Beer's law expression in Eq. (1.2).

Combined, a modified, closed-form expression (Eq. (4.9)) is proposed to relate transmittance and solid volume fraction in particle-flow measurements that accounts for dependent scattering effects as well as particle reflectivities with a collimated incident light source:

$$T = \exp(-S_\phi S_R \underbrace{\beta_{\text{ind}} W}_{\tau_W}) \tag{4.9}$$

Solid volume fractions derived from the thermopile measurements by applying the modified Beer's law expression (Eq. (4.9)) are presented in Fig. 4.7. The shaded region represents the variation in the estimated solid volume fraction for a range of particle reflectivities, $R_p \in [0, 0.99]$. The area of this region is larger for the smaller particle size due to the increased likelihood of light scattering/reflections with a larger ratio of the channel width to particle size. The relationship in Eq. (4.9) between transmittance and solid volume fraction is equally applicable for any particle size, curtain thickness, or optical properties.

The solid volume fractions calculated from the thermopile measurements using the new scale factor give exceptional agreement with the DEM results (within 5%) when assuming $R_p = 0.67$, based on the measured reflectance of a bed of porcelain particles. The best-fit values for R_p will change based on the assumption of diffuse/specular reflections on the particle surface; this study assumed diffuse reflections. This underscores the benefits of applying an improved radiative transport expression with the knowledge of particle optical properties to convert measured transmittance to a solid volume fraction.

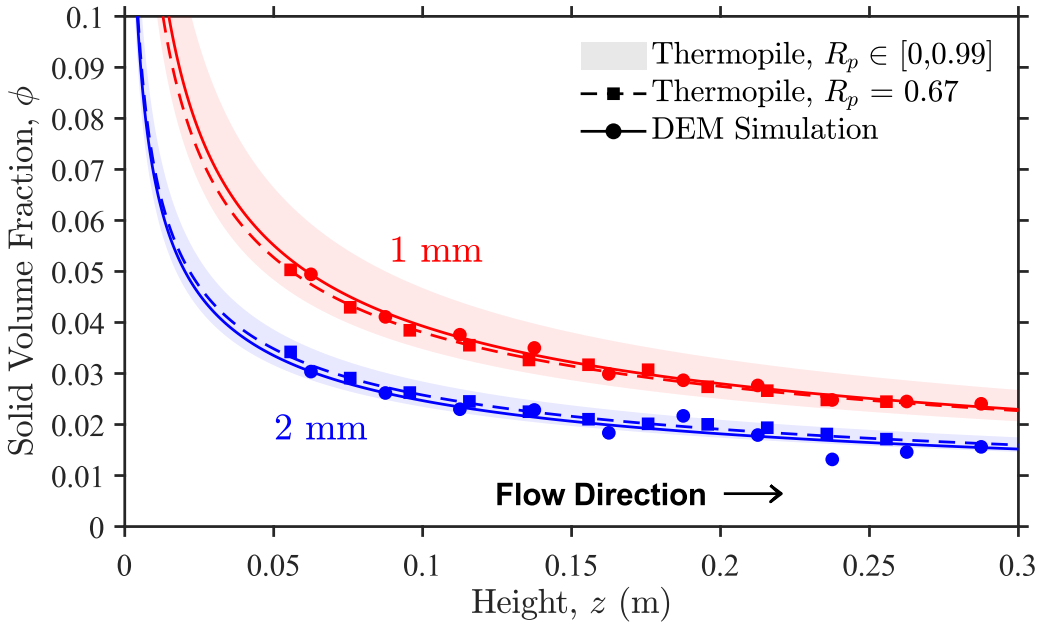


Figure 4.7: DEM results from Fig. 4.5 and experimental results rectified with a reflectivity-dependent scale factor, with the possible range of thermopile results given for particle reflectivities in the range $R_p \in [0, 0.99]$ indicated by the shaded regions.

4.4 Conclusions

This study successfully demonstrates very good agreement between models, both analytical and particle tracking, with experimental data. All methods show that the solid volume fraction decreases along the flow direction following a power-law relationship and that the dip is larger for the 1 mm particles than the 2 mm ones. Qualitatively, snapshots of the flow captured in DEM simulations and by the high-speed camera show very similar flow profiles. Sensitivity analyses performed on the DEM model show a significant influence of the particle-particle static friction coefficient on both the mass flow rate and the predicted solid volume fraction distributions. The measured steady flow rates of 0.230 and 0.160 kg/s for the 1 and 2 mm particles, respectively, match those found with empirical correlations and DEM simulations within 10%.

Distinct from the DEM simulations that directly calculate solid volume fractions,

the thermopile and high-speed imaging techniques rely on transforming the measured transmittance to a solid volume fraction. Ray tracing simulations inform the development of a new, effective, and simple closed-form expression to relate transmittance, solid volume fraction, and additionally, particle reflectivity. This leads to a much closer match of within 5% between the thermopile estimations and DEM simulations for solid volume fractions for both particle sizes tested.

On the whole, DEM simulations are a reliable approach to characterize the solid volume fraction distribution in particle flows.

CHAPTER V

Conductive and Radiative Heat Transfer Mechanisms Inform Nusselt Number Dependence on Solid Volume Fraction for Granular Flows

This chapter has been published by the author of this thesis:

- **Li, B., Chen, Z., Bala Chandran, R., 2024. Conductive and radiative heat transfer mechanisms inform Nusselt number dependence on solid volume fraction for granular flows. Powder Technology 440, 119737.**

5.1 Introduction

Multiphase media involving solid particles find crucial applications as heat-transfer and heat-storage media in concentrated solar power plants [159–164], nuclear fuels in pebble bed reactors [47, 48, 83, 165, 166] and reactive media in fluidized bed chemical reactors [10, 167–171]. When solid particles flow in "fluid-like" manner, heat and mass transfer are enhanced with the added benefits of relatively larger thermal conductivity and thermal capacity of solid compared to gases. While much prior work has focused on assessing flow behavior, either in the absence of heat transfer [47, 49, 50, 171, 172]

or has investigated coupled flow with conductive/convective heat transfer [10, 43–45, 51–57, 75, 76, 80, 164, 169, 170, 173], this study focuses on coupling flow and heat transfer, including conduction and radiation, for granular flows. This is significant as thermal radiation becomes a dominant mode of heat transfer at elevated temperatures (> 873 K).

To model the flow behavior of the solids, the Discrete Element Method (DEM) has been extensively applied [10, 46–64, 76, 84, 164, 172]. In this method, the solid particles are individually tracked in a Lagrangian framework for position, linear and angular velocity, and temperature. While this approach is computationally intensive, it provides powerful capabilities to explicitly account for inter-particle mechanical and thermal interactions, as dictated by particle geometry and thermophysical material properties, including frictional coefficient and thermal conductivity [57–59]. In addition to flow physics modeling, there is growing interest to apply DEM techniques to also predict heat transfer behavior [46, 51–64, 76, 77, 84]. Compared to conduction [46, 51–53, 55–59, 76, 77] and fluid-phase convection [54, 78, 79], studies that perform radiative heat transfer modeling are far more limited for multiphase flows with solid particles.

For dense, contact-dominated granular flows, seminal work was performed by Sullivan and Sabersky to establish a semi-empirical Nusselt number correlation [43]. This was obtained from analytical models and by performing experiments with glass, sand, and mustard seed at low temperatures, where radiative heat transfer was not significant. These correlations informed the dependence of the heat-transfer coefficients on the Péclet number, and additionally underscored the influences of near-wall thermal resistance. The near-wall resistance was deduced to be a function of the particle size, packing fraction in the near-wall region and the relative thermal conductivity of the solid phase compared to the gas phase [44–46, 80, 81, 173]. While conduction through the solid phase is the most crucial for dense flows and more generally when

the conductivity of the solid phase is much larger than that of the fluid-phase [55–57], conduction through the fluid phase is also shown to be important, especially, in the near-wall region and for dilute flows [51, 53, 77].

For applications involving dense flows at high temperatures, radiative heat transfer has been modeled with many case-specific assumptions [46, 61–63, 80–82]. In a majority of prior studies, radiation is modeled using effective thermal conductivity correlations [80–85] or applying one-way coupling between flow and heat transfer models, where particle positions at snapshots of time are extracted to obtain heat fluxes and temperature distributions [46, 61–63, 80]. Additionally, in many of these studies, assumptions have been made in the radiative flux calculations that make them strictly only applicable for black surfaces [46, 61, 63] or preclude the influences of long-range radiative exchanges between walls and particles [63]. Watkins et al. applied a 1-D semi-analytical model for dense, gravity-driven flows of particles, similar to that developed by Sullivan and Sabersky, to determine effective thermal conductivity correlations that especially resolve near-wall thermal resistances [43, 46]. DEM modeling was performed to only quantify flow characteristics to determine packing fraction and obtain statistics to track particle-wall contacts in the near-wall region. While radiative heat transfer was considered, it was only factored in the particle-wall view factors within 3 particle diameters, and by assuming black surfaces. Therefore, many simplifications made in this study make it strictly only applicable for dense flows (solid volume fraction, $\phi_s \sim 0.6$). Distinct from the above studies, Johnson et al. [61] and Qi et al. [84] have developed coupled flow and heat transfer DEM models for moderate-to-dense gravity-driven ($\phi_s = 0.25$–0.64) and rotary ($\phi_s = 0.1$–0.37) granular flows respectively by applying view factor correlations to obtain radiative heat fluxes. While the former study demonstrated the significance of radiative heat transfer for heat exchanger applications, the approach for radiative flux calculations was strictly only applicable for dense flows and black surfaces. The latter study show-

cased that radiation contributed 14–16% of the total heat transfer in rotary flows with biomass particles, even with a maximum operating temperature of 840 K. However, the effects of particle-wall and long-range particle-particle radiative heat transfer were not considered. Overall, many existing model formulations suffer from the limitations of either not fully coupling particle flow with heat transfer including radiative transport and/or using modeling assumptions that are strictly only applicable for dense granular flows with black surfaces (i.e., emissivity equals 1).

For more dilute flows, radiation has been modeled using Monte Carlo ray tracing techniques, which is most commonly applied without any direct coupling to the flow behavior. These techniques use standalone, snapshots of particle positions to obtain effective radiative properties of a cloud of particles [87, 174, 175], or couple with two-fluid continuum models for the solid and fluid phases [81, 85, 176]. While the two-fluid modeling methods are computationally efficient, they pose challenges in the determination of effective transport properties, including for radiation, as many flow-regime and materials-specific assumptions are made. Braham et al. developed a fully coupled Monte Carlo ray tracing to obtain transmittance with DEM particle flow models for fluidized-beds of photocatalysis [86]. More recently, Chen et al. have integrated Monte Carlo ray tracing calculations for radiative fluxes with particles-in-cells flow modeling for solar receiver applications [87]. However, these studies were restricted to dilute flows with solid volume fractions less than 0.1. Therefore, there are gaps in understanding how the solid volume fraction influences both the extent and the relative contributions of the different modes of heat transfer in granular flows. Whereas solid-phase conduction is expected to be significant for dense flows ($\phi_s > 0.5$) [44–46, 81, 82], fluid-phase convection becomes dominant in fluidized beds ($\phi_s < 0.1$) [10, 168, 177], and radiative heat transfer in the solids becomes critical at high temperatures [46, 178], especially for more dilute flows ($\phi_s < 0.1$).

Motivated by the identified knowledge gaps and limitations in modeling tech-

niques, this study develops and applies particle-tracking models that fully couple flow physics with conductive and radiative heat transfer in granular flows. Models are used to determine *wall-to-particle* heat-transfer coefficients for plug flows of particles with near-uniform velocities along the flow direction, and gravity-driven moving beds of particles. Compared to the dense moving beds regime, the plug flow modeling domain provides independent control of solid volume fraction. Parametric explorations are therefore performed in the plug flow model to determine the influences of particle size, operating wall temperatures, and relevant thermophysical properties at fixed solid volume fractions. To enhance the applicability of model predictions of heat-transfer coefficients, dimensionless Nusselt numbers are additionally evaluated. Key advancements propelled by this study compared to prior work includes: (a) development of a fully coupled flow and heat transfer model including thermal radiation for a range of solid volume fractions ranging from 0.02–0.55, (b) implementation of a more versatile radiative flux calculation approach using the net radiosity method to be applicable for both grey and black surfaces, (c) transformation of model-specific results for heat-transfer coefficients to more universally applicable Nusselt numbers, revealing their dependencies on solid volume fractions for the first time.

5.2 Method

5.2.1 Modeling Domain

Two different particle flow models are developed — (a) a homogeneous suspension flow of particles, referred to as plug flow hereafter, with uniform velocities of particles along the flow direction, and (b) gravity-driven, dense, moving beds of particles, referred to as moving beds (Fig. 5.1). Plug flows have practical applications in pneumatic flows of solids suspended in a gas phase, where they are likely operative in dilute flow regimes ($\phi_s < 0.1$) [179] with large velocities. A key objective to consider

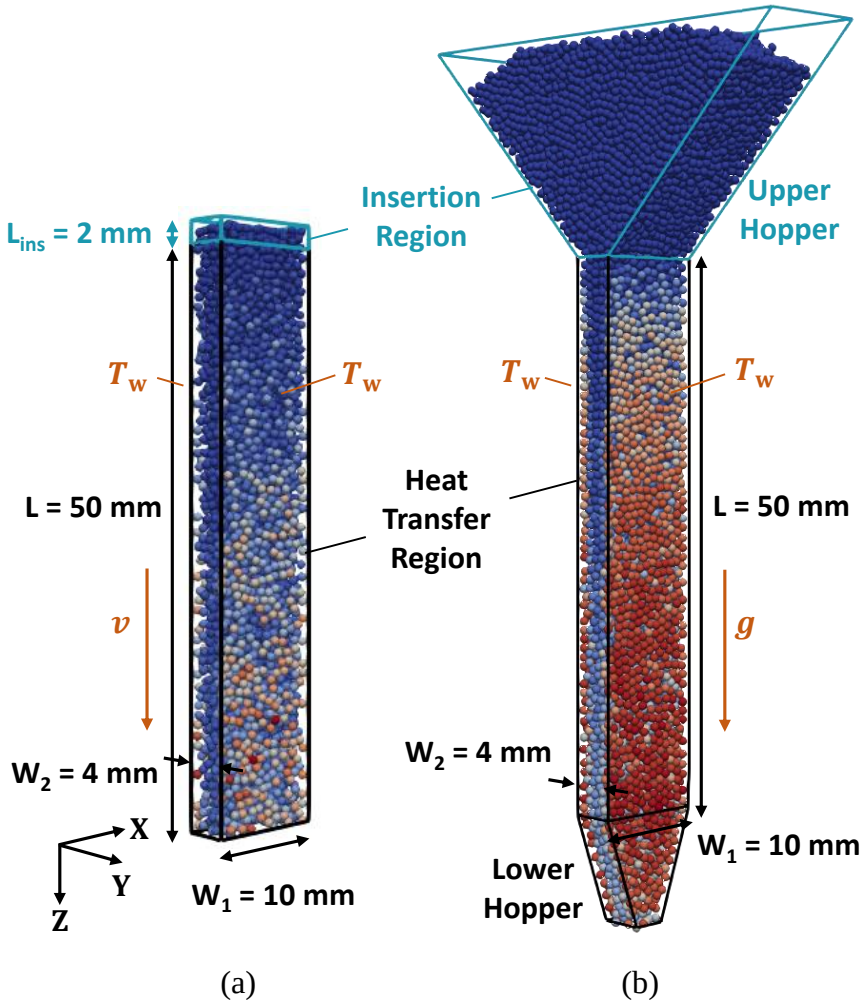


Figure 5.1: Modeling domain for: (a) plug flows of particles in a rectangular channel with uniform particle velocities along the flow direction (Z-velocity), and with a Gaussian velocity distribution in the transverse direction (X- and Y-velocity) with a mean value of 0, $v_x, v_y \sim \mathcal{N}(\mu = 0, \sigma^2 = 1^2$ mm/s), to introduce physical contacts between particles, and (b) gravity-driven, dense, moving beds of particles in a rectangular channel that is fed by a hopper right above it. In both cases of flow configurations, cold particles enter from the top at 300 K and get heated by the two isothermal heating walls at a temperature of T_w (T_w is a variable parameter in the model and equals to 1000 K in this figure) and parallel to the X-Z plane. The particle insertion region and the heat-transfer region are highlighted in turquoise and black respectively.

the plug flow model in this study is to isolate the influences of solid volume fraction on multimode heat transfer for a range of dilute-to-dense solid volume fractions ($0.02 < \phi_s < 0.48$). In contrast, we lack independent control of the solid volume fraction for the domain that considers gravity-driven, moving beds of particles. These flows are intrinsically dense with large solid volume fractions ($\phi_s > 0.5$), and are considered because of their practical applications as particle-based heat-exchangers in concentrated solar power plants [80] and in chemical looping reactors [177].

For the sake of simplicity, and to retain the focus on the inter-particle and particle-wall interactions for force calculations, momentum and energy transport is not modeled in the fluid-phase in all our calculations. This is a reasonable choice because, even for the smallest particle diameter modeled, the Stokes number is much larger than 1 ($\mathcal{O}(100)$), and indicative of particle flow being unaffected by the fluid phase. Even though fluid-phase convective heat transfer is not modeled, the solid-fluid-solid conduction pathway is taken into account (Sec. 2.2.2.2).

Fig. 5.1(a) shows the plug flow modeling domain. Cold particles are introduced at 300 K in the insertion region (10 mm $\times$ 4 mm $\times$ 2 mm), and subsequently flow into the heat-transfer region (10 mm $\times$ 4 mm $\times$ 50 mm), where particle-particle and particle-wall heat transfer interactions are modeled. Spherical particles with uniform size are continuously introduced with constant velocity in the streamwise direction (Z-direction). In the transverse direction (X and Y directions), a Gaussian velocity profile is modeled to induce inter-particle collisions and contacts, similar to what is expected in moving beds [180]. In this Gaussian distribution, the mean velocity is 0 and the standard deviation is fixed at 1 mm/s, which is within 5% of the streamwise velocities modeled (Fig. 5.1(a)). The magnitude of the inlet velocity and the number of particles that inserted at each time step are varied to control the mass flow rate of the particles. To achieve desired solid volume fraction, the particle insertion frequency is additionally manipulated to yield dilute-to-dense flows with $0.02 < \phi_s < 0.48$. For

the most dense plug flow model, the maximum number of particles in the domain is about 3600. The two side walls of the heat-transfer region are modeled as isothermal plates at varying temperatures of $T_{\mathrm{w}} = 700$, 1000, and 1300 K. The other two lateral walls are treated to be adiabatic.

Fig. 5.1(b) shows the modeling domain for the gravity-driven, moving beds, which includes two hoppers above and below the channel. Particles are first inserted and collected in the upper, feed hopper up to a height of 20 mm, without any discharge to the channel below, to maintain high solid volume fractions of particles when flowing into the channel. The lower hopper has a height of 10 mm with outlet sizes adjusted based on the desired flow rates for the solids — 2 × 4 mm, 3 × 4 mm and 4 × 4 mm for 1.21, 3.42, and 6.08 g/s respectively. For all these cases, a total mass of 14.5 g alumina particles is loaded into the hopper, translating to a maximum of 13,700 particles in the entire domain; while for mustard seeds, nearly 11,000 particles with a total mass of 33.1 g are loaded instead. Similar to the plug flow modeling domain (Fig. 5.1(a)), the flow channel is heated by two isothermal walls at set temperatures and cold particles enter from hopper into the channel; the flow channel and the heat-transfer region are of exactly the same dimensions in both modeling domains.

5.2.2 Discrete Element Modeling for Flow and Heat Transfer

An open-source Discrete Element Method (DEM) software — LAMMPS Improved for General Granular and Granular Heat Transfer Simulations (LIGGGHTS), is used to track and update the positions, velocities, and temperatures of individual particles [95]. For both the plug flow and moving beds, the modeling approach is the same for heat-transfer calculations as described in Sec. 2.2.

The Hertz-Mindlin model is applied to calculate the forces and moments based on the soft-sphere approach. To update the positions, the DEM time step is 5×10^{-6} s for $d_{\mathrm{p}} = 0.4$ mm and 1×10^{-5} s for larger particle sizes. These time steps are chosen

Table 5.1: Mechanical and thermal properties of materials modeled in the DEM simulations — α-alumina and mustard seed.

Properties, Symbol	**α-Alumina**	**Mustard Seed**	**Unit**
Particle diameter, d_{p}	0.8	2.0	mm
Density, ρ	3984	729	kg/m^3
Specific heat capacity, c_p	755	1980	J/kg/K
Thermal conductivity, k_{s}	33	0.156	W/m/K
Thermal diffusivity, α	1.1×10^{-5}	1.0×10^{-7}	m^2/s
Real Young's modulus, Y^*	414		GPa
DEM Young's modulus, Y	5		MPa
Static friction coefficient, μ_{s}	0.4		
Restitution coefficient, e	0.45		
Poisson's ratio, ν	0.23		

based on the Rayleigh time step and Hertz collision time step as depicted in Sec. 2.2.1.

Particle mechanical and thermal properties are modeled based on sintered α-alumina (Table 5.1), which is a ceramic material. Thus, it can withstand high temperature and is selected for this study as comprehensive data is available for all its thermophysical properties [181, 182]. For the sake of simplicity, all thermophysical properties are modeled to be constant and temperature-independent. The Young's modulus used for the flow simulation is reduced to 5 MPa compared to the reported value of 414 GPa for α-alumina, as it is the lowest permitted value in LIGGGHTS [95]. Though unrealistic, this artificial reduction on Young's modulus has been shown to have negligible impact on the flow physics, and is a commonly adopted approach to save computational cost [62, 183, 184]. This outcome is confirmed by performing sensitivity analysis in our own work [152]. Static friction is modeled for solid surfaces, while rolling friction is assumed to be 0 for simplicity. Even though the absolute magnitude of the predicted heat-transfer coefficients are expected to change when rolling friction is taken into account, it is anticipated that the influences of pertinent parameters (particle size, solid volume fraction, Péclet number) on heat transfer will

not change. For instance, in the case of plug flow, the effect of including rolling friction is rather minimal because of very few inter-particle collisions. Therefore, for this case, the predicted average particle temperatures and the wall-to-particle heat-transfer coefficients deviate by less than 10% when a rolling friction coefficient of 0.18 (consistent with property values reported in [66] for alumina-rich composite ceramics) is modeled. In the case of the dense, moving beds of particles, this deviation becomes larger; for fixed dimensions of the lower hopper adding on rolling friction decreases the average particle velocities, steady-state mass flow rate, and solid volume fraction in the channel, making overall wall-to-particle heat transfer less effective.

Mustard seed, a material with low thermal conductivity (Table 5.1), is also modeled in this study with the same geometric modeling setup and particle size as the work from Sullivan and Sabersky [43]. Due to the different material properties and modeling length, the Péclet numbers are 6000 and 176 for mustard seed and alumina particles respectively, and the modified Péclet numbers, Pe^*_{L}, is 1200 for mustard seed as compared to 72000 for alumina (Eq. (5.3)). The additional modeling for mustard seed aims to facilitate model validation with the reported Nusselt number correlations for moving beds with mustard seed. Fig. D.1 in Appendix D.1 shows a comparison for Nusselt number without radiation between the reported correlation and our models: plug flow model with $\phi_{\mathrm{s}} = 0.45$ and moving beds model with approximately $\phi_{\mathrm{s}} = 0.55$. The comparisons indicate the reported correlation is generally applicable for more densely packed flows of particle in a solid volume fraction range between $\phi_{\mathrm{s}} = 0.45 - 0.55$, and again reinforces the sensitivity for conductive heat transfer to the solid volume fraction. In practice, the friction coefficients (static and rolling) modeled will be material-specific, and could be different for alumina and mustard seeds. However, in the absence of specific data, and for the sake of making controlled comparisons between the two materials, we assume these properties to be exactly the same for both materials.

5.2.3 Heat-transfer Coefficient and Nusselt Number

Model predictions for conductive, $\dot{Q}_{j,\text{cond}}$, (Eqs. (2.21)-(2.22)) and radiative heat transfer rates, $\dot{Q}_{j,\text{rad}}$, (Eq. (2.28)) on individual particle are used to obtain the channel-averaged (over the flow length) wall-to-particle heat-transfer coefficient, $\overline{h}_{\text{wp}}$, using Eq. (5.1),

$$\overline{h}_{\text{wp}} = \frac{\sum_{j=1}^{N_\text{p}} (\dot{Q}_{j,\text{cond}} + \dot{Q}_{j,\text{rad}})}{\left(T_\text{w} - \overline{T}_\text{p}\right) 2A_\text{w}} \tag{5.1}$$

where $\overline{T}_\text{p}$ is the number-averaged temperature of all particles within the channel ($\overline{T}_\text{p} = \sum_j^{N_\text{p}} T_{\text{p},j}/N_\text{p}$), $\dot{Q}_{j,\text{cond}}$ is the net conductive heat transfer rate for the j^{th} particle ($\dot{Q}_{j,\text{cond}} = \sum_i^{\text{contacts}} \dot{Q}_{ij,\text{cond}}$), and $\dot{Q}_{j,\text{rad}}$ is the net radiative heat transfer rate, A_p and A_w are the particle surface area and the wall area. At steady-state, the numerator in Eq. (5.1) is equal to the rate of sensible thermal energy transferred to the particles ($\dot{m} c_p \left(T_\text{out} - T_\text{in}\right)$).

To further generalize the results and make it agnostic to geometry and test conditions, a dimensionless channel-averaged, particle-size dependent, Nusselt number is obtained in Eq. (5.2), where k_g is the conductivity of air (0.026 W/m/K), and d_p is the particle diameter.

$$\overline{Nu}_\text{d} = \frac{\overline{h}_{\text{wp}} d_\text{p}}{k_\text{g}} \tag{5.2}$$

In prior work by Sullivan and Sabersky [43], this Nusselt number has been demonstrated to be correlated with a modified particle-size-based Péclet number, Pe^*_L, which can be calculated from a length-based Péclet number, Pe_L, (Eq. (5.3)).

$$Pe^*_\text{d} = Pe_\text{L} \left(\frac{k_\text{s}}{k_\text{g}}\right)^2 \left(\frac{d_\text{p}}{L}\right)^2 = \left(\frac{vL}{\alpha}\right) \left(\frac{k_\text{s}}{k_\text{g}}\right)^2 \left(\frac{d_\text{p}}{L}\right)^2 \tag{5.3}$$

In Eq. (5.3), v is the average particle velocity of the moving-particle flow, L is the

Table 5.2: Parameter exploration for the plug flow model (Fig. 5.1(a)) simulations with a fixed solids mass flow rate of $\dot{m} = 1.59$ g/s. For a fixed mass flow rate, differences in solid volume fraction are achieved by varying particle flow velocities resulting in different Péclet numbers.

Parameters	**Value***
Solid Volume Fraction (Péclet number), ϕ_s (Pe_L)	**0.07 (660), 0.25 (189), 0.43 (109)**
Particle size, d_p (mm)	0.4, **0.8**, 1.0
Wall Temperature, T_w (K)	700, **1000**, 1300
Emissivity, ϵ	0.1, 0.4, 0.7, **1.0**

*The values in bold are baseline parameters that are held constant when other parameters are varied.

characteristic length of the flow channel along the flow direction, which is the height of the channel in this study ($L = 50$ mm as shown in Fig. 5.1), α is the thermal diffusivity of the particle (obtained as $k_s/\rho c_p$), k_s and k_g are the thermal conductivity of the solid-phase and fluid-phase respectively. Pe_L physically represents a comparison of the time scale for heat diffusion between the flowing particles as compared to the residence time of particles in the channel.

5.2.4 Parametric Study in Plug Flow

The plug flow model provides a computationally tractable, canonical framework to explore the influences of various physical parameters on the heat transfer behavior (Table 5.2). Specifically, we consider different: (a) solid volume fractions, ϕ_s, and particle sizes, d_p, to investigate effects of morphology and flow regimes, the solid volume fractions are achieved by varying particle flow velocities and therefore Péclet numbers, Pe_L; (b) wall temperatures, T_w, to capture influences of different heating conditions; and (c) thermophysical material properties including a range of particle emissivity, ϵ, and thermal conductivity, k_s. For simplicity, the thermophysical properties for particles and walls are identical. Baseline values and parameter ranges explored in this study are shown in Table 5.2.

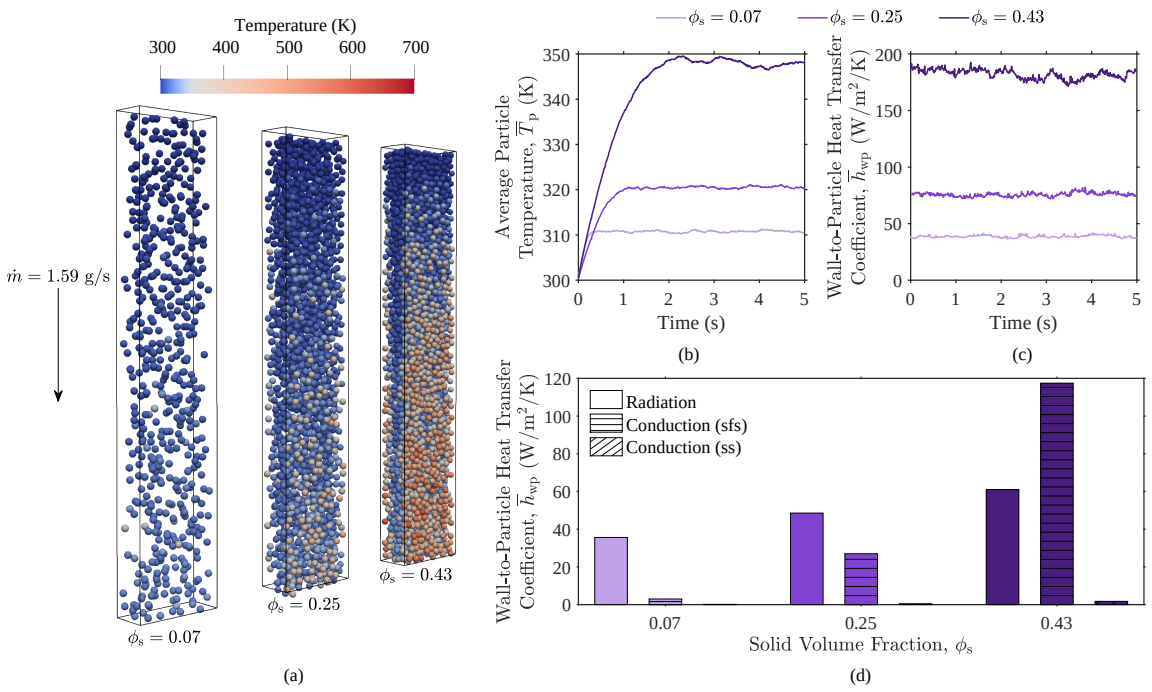


Figure 5.2: Effects of solid volume fraction ($\phi_s = 0.07, 0.25, 0.43$) in the plug flow model at a constant mass flow rate ($\dot{m} = 1.59$ g/s), and correspondingly different Péclet number ($Pe_L = 660, 189, 109$) on (a) steady-state spatial distributions of particle temperatures at $t = 5$ s, (b) temporal evolution of average particle temperatures present inside the channel, (c) channel-averaged wall-to-particle heat-transfer coefficients, $\overline{h}_{wp}$, obtained from Eq. (5.1) with (d) the contributions from thermal radiation, solid-fluid-solid (sfs) and solid-solid (ss) conduction pathways.

5.3 Results & Discussion

5.3.1 Plug Flow: Effects of Solid Volume Fraction

Fig. 5.2(a) reveals the steady-state ($t = 5$ s) spatial temperature profiles for the plug flow model with three different solid volume fractions ($\phi_s = 0.07, 0.25, 0.43$) at a fixed mass flow rate of 1.59 g/s; all other parameters are fixed at baseline conditions (Table 5.2). With this constraint, the particle flow velocity and equivalently the Péclet number decreases ($Pe_L = 660 - 109$), while the residence time increases ($t_R = 1.19 - 1.92$ s) with solid volume fraction. The average particle temperature within the channel (Fig. 5.2(a), (b)), and the wall-to-particle heat-transfer coefficient,

$\overline{h}_{\mathrm{wp}}$, (Fig. 5.2(c)) increase with solid volume fraction. This increase is mainly due to the improved solid-fluid-solid conduction pathways, which additionally benefits from the increase in residence time (decrease in Pe_{L}). While the Sullivan-Sabersky correlation [43] predicts an increase in heat transfer with Pe_{L} for dense moving beds at a fixed solid volume fraction, our results reveal more pronounced benefits of improved conduction with the increase in solid volume fraction even at the cost of a smaller Pe_{L}. Fig. 5.2(d) further reveals the contributions from conduction and radiation to the heat-transfer coefficient. While the relative contribution from radiation is the largest for the most dilute flow modeled with $\phi_{\mathrm{s}} = 0.07$, conduction dominates when $\phi_s = 0.43$. As the flow becomes more dense, there are less open spaces for particles to radiatively view each other and the heated walls, i.e., particles shade each other and radiative transport effectiveness diminishes. Within the different conduction pathways, conduction through the interstitial fluid, $\dot{Q}_{ij,\mathrm{cond,sfs}}$, (Eq. (2.22)) dominates while the conduction between only solid contacts, $\dot{Q}_{ij,\mathrm{cond,ss}}$, (Eq. (2.21)) is minimal even when $\phi_{\mathrm{s}} = 0.43$. This is because the plug flows with a homogeneous suspension of particles have very minimal inter-particle contacts, whereas, the interstitial fluid is always present. Therefore, solid-fluid-solid conduction surface area is larger than the solid-solid contact area. These results underscore the importance of considering conduction through the interstitial fluids for granular flows, and reinforces inferences from prior work [51, 53, 84].

5.3.2 Plug Flow: Coupled Effects of Parameters

Fig. 5.3 shows the effects of particle emissivity and wall temperature, and Fig. 5.4 shows the influence of particle size on the heat transfer performance. In all these cases, three different solid volume fractions are still considered for a fixed mass flow rate of $\dot{m} = 1.59$ g/s. While the differences in the Péclet number still influence the absolute value for the predicted heat-transfer coefficients, it does not alter the trends

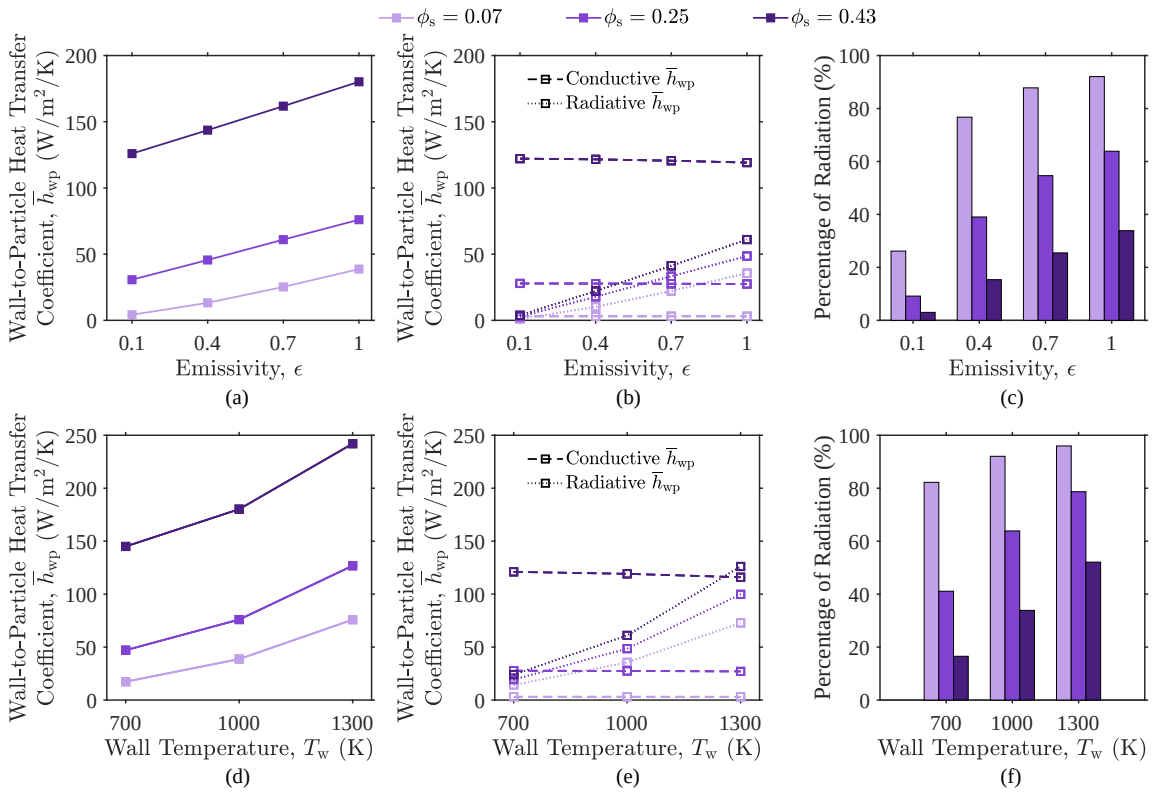


Figure 5.3: Effects of particle emissivity, ϵ, and wall temperature, T_w, in the plug flow model ($\phi_s = 0.07, 0.25, 0.43$) at a constant mass flow rate ($\dot{m} = 1.59$ g/s), and correspondingly different Péclet number ($Pe_L = 660, 189, 109$) on (a,d) channel-averaged, wall-to-particle heat-transfer coefficient, $\overline{h}_{wp}$, (b,e) conductive and radiative heat-transfer coefficients, and (c,f) the percentage contribution of thermal radiation to overall heat transfer.

in Fig. 5.3-5.4.

The wall-to-particle heat-transfer coefficient, $\overline{h}_{wp}$ (Fig. 5.3(a)) and the contribution from radiation (Fig. 5.3(c)) largely linearly increases with emissivity. Even though the radiative fluxes are obtained by solving a system of equations. (Eqs. (2.27–2.29)), the resulting linearity between heat-transfer coefficient and particle emissivity is indicative of the granular flow behaving effectively like a plane-parallel slab of particles viewing the wall surfaces. A very minimial indirect effect of the interplay between radiation and conduction is captured in our model, where the conductive heat transfer diminishes marginally with the increase in emissivity (Fig. 5.3(b)), especially for the denser flows modeled ($\phi_s = 0.25$, 0.43). This is because as radiative

transport improves, the average temperature difference between the solid surfaces becomes smaller, which lowers conductive heat transfer.

Similar to the effect of emissivity, increasing wall temperature enhances the wall-to-particle heat-transfer coefficient (Fig. 5.3(d)) due to stronger radiative heat transfer (Fig. 5.3(e), (f)). The cubic dependence for the heat-transfer coefficient on wall temperature ($\overline{h}_{\mathrm{wp}} \propto T_{\mathrm{w}}^3$) is consistent with the expected trends for radiative heat-transfer coefficient and stems from the thermal emission increasing proportional to T_{w}^4 [12].

Fig. 5.4 shows the influence of particle size on the heat-transfer behavior. Consistent with our prior results (Fig. 5.2), the wall-to-particle heat-transfer coefficient still increases with solid volume fraction for any fixed particle size and mass flow rate, despite the decreasing Péclet number. For all solid volume fractions ($\phi_{\mathrm{s}} = 0.07, 0.25, 0.43$), heat-transfer coefficients decrease as the particle size increases (Fig. 5.4(a)), and this trend is largely dominated by conduction (solid-fluid-solid and solid-solid pathways) worsening with increasing particle size. Fig. 5.4(b) shows the contributions of conductive and radiative heat transfer coefficients. The conductive heat transfer coefficients decrease with particle size and increase with solid volume fraction. This is dictated by the changes in total surface area of the particles per unit volume of the heated channel, which scales proportional to $\phi_{\mathrm{s}}/d_{\mathrm{p}}$. This is further verified by approximately estimating the contact surface area in the bulk and near-wall regions (Appendix D.2). Compared to conductive heat-transfer coefficient, particle size doesn't as significantly influence the radiative heat-transfer coefficient, particularly for the high solid volume fractions, $\phi_{\mathrm{s}} = 0.25, 0.43$. This is attributed to the competing influences of particle size on the specific surface area and the shading effect between particles and the heated wall surfaces. For the dense flows ($\phi_{\mathrm{s}} = 0.25$, 0.43), the shading effect plays a more dominant role than for the dilute flow. Therefore, in these two cases, despite the decrease in the particle specific surface area with particle

size, the radiative heat transfer improves, resulting in a small, but net increase in the radiative heat-transfer coefficient in Fig. 5.4(b). In contrast, for the case with the smallest solid volume fraction modeled, shading effects are not that pronounced, and therefore radiative heat transfer decreases with particle size due to smaller specific area for heat exchange. The average wall-particle radiative view factor determines how effectively the heated wall surface radiates to the particles, and it follows similar trends with particle size, which reinforces the competing effects at play (Appendix D.2). Fig. 5.4(c) shows that with increasing particle size, the fractional contribution of radiation to overall heat transfer increases, which is consistent with the expected reduction in shading effects and in conduction contribution. Shading by neighboring particles plays a more dominant role for the dense flows, and therefore the relative changes in the percentage contribution of radiation with particle size is more prominent in this case. Even though the results in Fig. 5.4 are presented for a fixed mass flow rate, the trends with respect to particle size look similar when these calculations are performed for the same Pe_{L} as presented in Fig. D.3, but with varying mass flow rates across different solid volume fractions.

5.3.3 Moving Beds: Effects of Mass Flow Rate

Fig. 5.5 shows the effects of mass flow rate in the gravity-driven moving beds (Fig. 5.1(b)). Three different opening sizes are modeled for the lower hopper with outlet velocities, $v_{\mathrm{z}} = 1.36, 3.88, 7.00$ cm/s, and corresponding Péclet numbers, $Pe_{\mathrm{L}} = 68, 184, 325$, leading to mass flow rates of $\dot{m} = 1.21, 3.42, 6.08$ g/s respectively (all these mass flow rates differ from what is used for the plug flow calculations in Table 5.1). In contrast to the plug flow model, the solid volume fraction of particles within the channel mostly remains constant at 0.55 ± 0.005, both along the flow direction and with changing mass flow rates. For the slower mass flow rates (i.e., low Pe_{L} values), the residence time is larger, which improves conductive heat transfer. This leads to

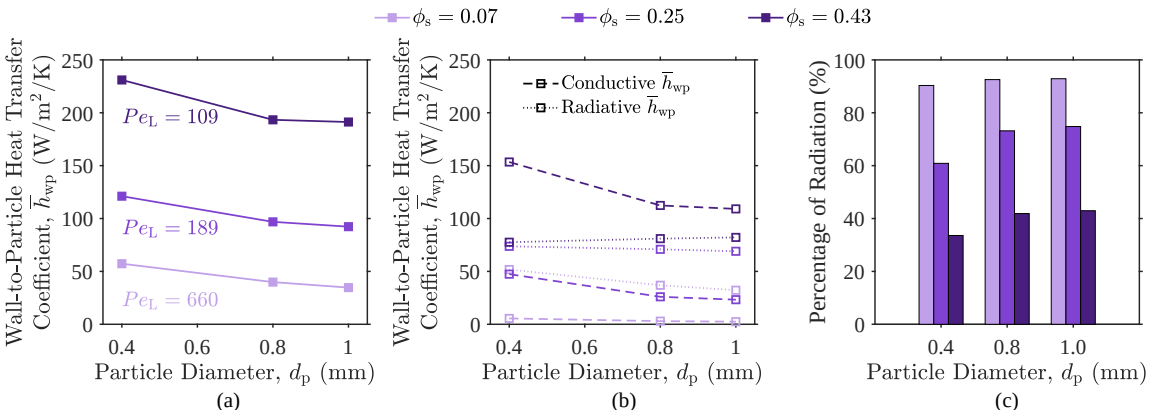


Figure 5.4: Coupled effects of particle diameter, d_p, and solid volume fraction, ϕ_s, in the plug flow model ($\phi_s = 0.07, 0.25, 0.43$) at a constant mass flow rate ($\dot{m} = 1.59$ g/s), and correspondingly different Péclet number ($Pe_L = 660, 189, 109$) on (a) channel-average, wall-to-particle heat-transfer coefficient, $\overline{h}_{wp}$, (b) conductive and radiative heat-transfer coefficients, and (c) the percentage contribution of thermal radiation to the overall heat transfer.

more spatially uniform temperature profiles (Fig. 5.5(a)), and correspondingly larger average particle temperatures (Fig. 5.5(b)). As expected, time to attain steady-state increases as the mass flow rate and Péclet number decreases. While the wall-particle heat-transfer coefficient is initially ($t < 0.1$ s) larger for the slower mass flow rate (smaller Pe_L), the trend switches to increase with mass flow rate as the flow approaches steady-state (Fig. 5.5(c)). This is because the increase in the total heat flux advected by the solids outcompetes the reduction in the temperature difference between the wall and the particles inside the channel (Eq. (5.1)). For equivalent channel length, particle size, and similar mass flow rate ($\dot{m} = 3.42$ g/s), the wall-to-particle heat-transfer coefficient, $\overline{h}_{wp}$, predicted for the moving beds with $\phi_s = 0.55$ is at least 5 times larger than that obtained for the plug flow modeled with $\phi_s = 0.43$. This reveals the outsized influence of the solid volume fraction on the heat transfer behavior. As will be discussed subsequently in Sec. 5.3.4, this dependency on the solid volume fraction is further exaggerated due to the large conductivity of alumina ($k_s = 33$ W/m/K). While the overall heat-transfer coefficient changes with respect

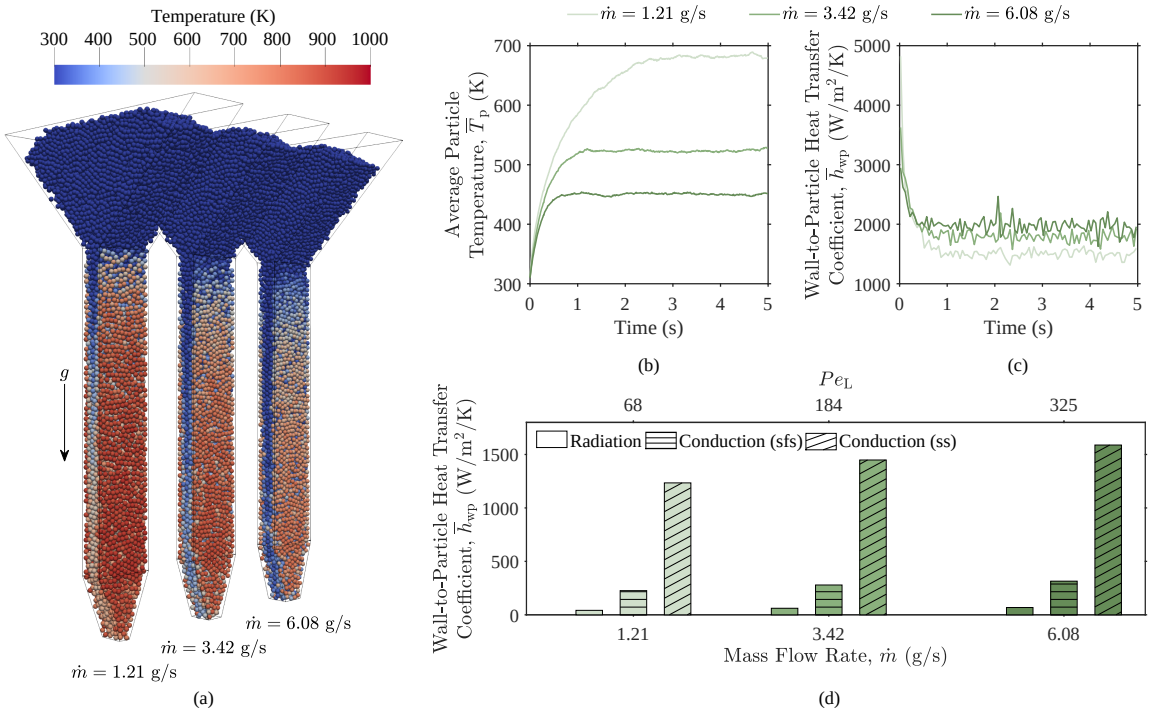


Figure 5.5: Effects of mass flow rate ($\dot{m} = 1.21, 3.42, 6.08$ g/s), and corresponding Péclet numbers ($Pe_L = 68, 184, 325$) in gravity-driven moving beds at a near-constant solid volume fraction ($\phi_s = 0.55$) on (a) steady-state spatial distributions of particle temperatures at $t = 5$ s, (b) temporal evolution of average particle temperatures present inside the channel, (c) channel-averaged wall-to-particle heat-transfer coefficient, $\overline{h}_{wp}$, with (d) contributions from thermal radiation, solid-fluid-solid (sfs) and solid-solid (ss) conduction pathways.

to the mass flow rate, the contributions from the different modes remain the same as the solid volume fraction is not changing (Fig. 5.5(d)). All three cases are dominated by solid-solid conduction because of the dense solid packing of $\phi_s = 0.55$, followed by solid-fluid-solid conduction and then radiation. Radiation contributes to at most 4% of the overall heat transfer in this flow regime with the heated walls at 1000 K, and by treating both the particle and wall surfaces to be optically black, i.e., $\epsilon = 1$. From the trends obtained in the plug flow results (Fig. 5.2), we project that this contribution will linearly increase with particle emissivity, and increase significantly as the wall surfaces get hotter.

5.3.4 Overall and Radiative Nusselt Number

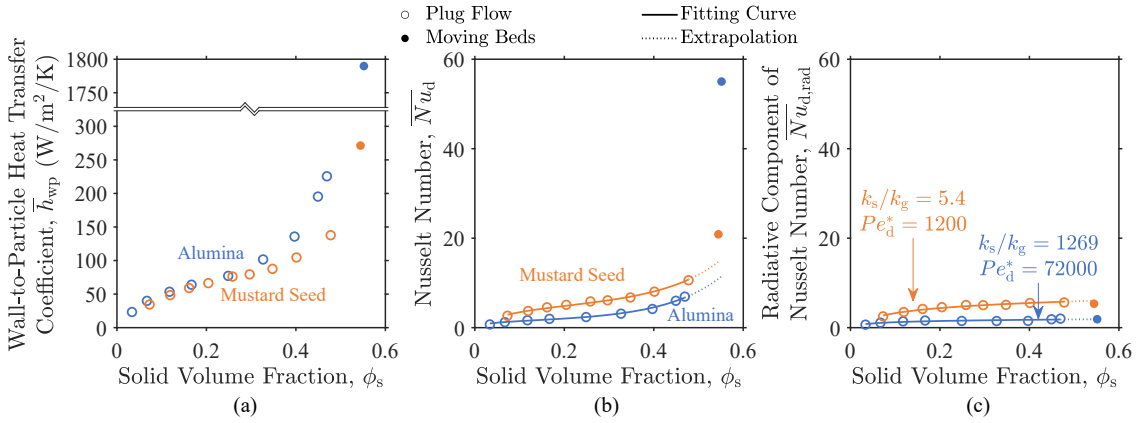


Figure 5.6: (a) Wall-to-Particle heat-transfer coefficient, $\overline{h}_{wp}$, (b) overall and (c) radiative Nusselt number as a function of solid volume fraction with results obtained from both plug flow and moving beds with alumina and mustard seeds. Alumina particles are modeled with a diameter of $d_p = 0.8$ mm with a modified Péclet number Pe_L^* of 72000, whereas mustard seeds have a diameter of $d_p = 2$ mm with a modified Péclet number Pe_L^* of 1200. The plug flow model data (hollow circles) is fitted and extrapolated to compare against the predictions obtained for the moving beds (filled circles). The best-fit curve is included as a guide to the eye, and it exhibits an exponential and logarithmic dependence of conductive and radiative heat transfer on the solid volume fraction respectively as shown in Eq. (D.1) and Eq. (D.2).

To generalize our predictions beyond model-specific inputs used in this study, channel-average, wall-to-particle heat-transfer coefficient (Fig. 5.6 (a)) and dimensionless Nusselt numbers (Fig. 5.6 (b) and (c)) are obtained. The overall and radiative component of Nusselt number, $\overline{Nu}_d$ (Eq. (5.2)) and $\overline{Nu}_{d,rad}$, are obtained as a function of solid volume fraction from steady-state plug flow and moving beds models respectively (Fig. 5.1). In this figure, we report Pe_L^* instead of Pe_L to enable comparisons against the reported Nusselt number data by Sullivan and Sabersky [43]. The particle size, the flow channel dimensions, and therefore the Péclet numbers are different for the models with alumina and mustard seed (Table 5.1 and Fig. D.1 in Appendix D.1). Therefore, Pe_L^* (Eq. (5.3)) values are different — 72000 and 1200 respectively — for alumina and mustard seed; in Fig. 5.6 this is fixed for both plug

flow and moving beds with respect to solid volume fraction.

Predictions from plug flow and moving beds models in Fig. 5.6(a) for both alumina and mustard seed demonstrate that the wall-to-particle heat-transfer coefficient significantly changes and non-linearly increases with solid volume fraction. At any solid volume fraction, the heat-transfer coefficient for mustard seeds is smaller than alumina due to the combined influences from its larger particle size, larger Péclet number (Pe_{L}), and its significantly smaller thermal conductivity. This difference is most dramatic for moving beds, with heat-transfer coefficients of 270 and 1800 $\mathrm{W/m^2/K}$ for mustard seeds and alumina respectively. Fig. 5.4(a) illustrated that the overall heat-transfer coefficient decreases with particle size at a fixed Péclet number, Pe_{L}. While the heat-transfer coefficient for moving beds is predicted to increase with Pe_{L} in Fig. 5.5, for flows with larger Pe_{L} values, it has been experimentally demonstrated to decrease to some extent with Pe_{L}, as indicative from Sullivan and Sabersky's correlation [43] and following work from Patton et al. and Natarajan et al. [44, 45]. Additionally, a higher thermal conductivity improves the conductive heat transfer significantly, especially for flows with high solid volume fraction.

Fig. 5.6(b) depicts the dimensionless overall Nusselt number from the predicted heat-transfer coefficients (Eq. (5.2)) in Fig. 5.6(a), scaled with the appropriate size of the particles modeled for the two materials. Similar to the heat-transfer coefficients, for both materials, the Nusselt number also increases non-linearly with solid volume fraction, and more significantly in the high solid volume fraction range; it more than doubles from 2.4 to 6.7 for alumina, and 5.5 to 10.6 for mustard seeds for plug flows with $\phi_{\mathrm{s}} = 0.25$–0.48. The sensitivity of the overall Nusselt number to the solid volume fraction is most evident in the more than 6-fold increase from the plug flow model with $\phi_{\mathrm{s}} = 0.48$ to the moving beds model with $\phi_{\mathrm{s}} = 0.55$ for alumina particles. This effect is driven by substantial enhancements of conductive heat transfer, which contributes to more than 96% of the overall heat transfer. Compared to alumina, while there is

still an increase in the overall Nusselt number for mustard seed, this effect is subdued dictated by its low thermal conductivity — $\overline{Nu}_{\mathrm{d}}$ increases from 10.6 in the plug flow model with $\phi_{\mathrm{s}} = 0.48$ to 20.9 in the moving beds with $\phi_{\mathrm{s}} = 0.55$. Therefore, the dependence of the overall Nusselt number on the solid volume fraction is amplified for solids with large thermal conductivity.

Unlike heat-transfer coefficients, which are always larger for alumina as compared to mustard seed, the Nusselt number switches trends between plug flow and moving beds. This is due to the compounded effects of particle size being included in the Nusselt number (Eq. (5.2)). For equivalent heat-transfer coefficients, and identical thermal conductivity from the gas phase, the larger size modeled for the mustard seed as compared to alumina ($d_{\mathrm{p,\ mustard}} = 2.5 d_{\mathrm{p,alumina}}$) will result in a larger Nusselt number. However, Fig. 5.6(a) shows that while the heat-transfer coefficients of mustard seed and alumina do not differ by more than a factor of 2 in the plug flow regime, they are nearly order-of-magnitude larger for alumina in the moving bed regime. Consequently, the Nusselt number is larger for mustard seed compared to alumina in plug flow regime, but smaller in the moving bed regime.

An implication of our findings regarding heat-transfer coefficients and Nusselt number is that the measured thermal performance of components that especially involve dense flows of solids, e.g., moving bed heat exchangers for particle-based concentrated solar power applications [80, 81, 164], will be highly sensitive to even small changes in the solid volume fraction. And therefore, experimental characterization of the solid volume fraction in such systems will be critical in addition to temperature measurements. Consistent with these findings, the extrapolation of the overall Nusselt number, $\overline{Nu}_{\mathrm{d}}$, (elaborated in Appendix D.3) from plug flow to the gravity-driven, moving beds are more successful for the low conductivity mustard seed as compared to the high conductivity alumina. To better quantify this dependence, future work should consider Nusselt number predictions as a function of the thermal conductivity

ratio (k_s/k_g), especially for the dense flows ($\phi_s > 0.48$).

In contrast to the overall Nusselt number, Fig. 5.6(c) shows that the radiative Nusselt number increases only initially for ϕ_s in the range of 0.02 to 0.25, after which it levels off at near-constant values of 5.3 and 2.0 respectively for mustard seed and alumina. This is explained by the competing influences from an increase in the number of particles being radiatively heated by the walls with a reduction in the open spaces between particles for radiative transport. The radiative Nusselt number is nearly offset by the differences in the particle size, i.e., $\overline{Nu}_{d,rad}$ for mustard seed is ≈2.6 times larger than that for alumina, which is approximately the ratio of the particle sizes modeled for these materials. This is because particle size and the modified Péclet number do not significantly impact radiative transport. Therefore, even though the overall heat-transfer coefficient changes subject to the material modeled, the radiative heat-transfer coefficient mostly remains the same. Moreover, the extrapolated predictions from plug flow model for the radiative Nusselt number matches well with the predicted value for the gravity-driven moving beds as radiative heat transfer is barely altered in this range of solid volume fraction. This is suggestive of a simplified plug flow model being an adequate canonical framework to capture radiative heat transfer behavior in moving beds.

5.4 Conclusion

Our study develops a comprehensive, multimode heat transfer model for granular flows with applications for concentrated solar and high-temperature thermal energy technologies. Notable highlights include: (a) the full coupling of particle flow, conductive, and radiative heat transfer for a wide range of solid volume fractions (0.02–0.55), (b) the development and application of a rigorous, yet computationally tractable method to predict radiative fluxes in discrete particle models, and (c) parametric explorations of the effects of solid volume fraction, particle size, heating

conditions, and thermophysical properties on the heat transfer performance.

Models are developed and applied for a plug flow of particles with a constant streamline/flow velocity, and a gravity-driven, dense, moving beds of particles. The plug flow model is selected as a canonical framework to independently control of solid volume fraction over a wide range (0.02–0.48), and to perform parametric explorations to predict wall-to-particle heat-transfer coefficients. Plug flow model results reveal significant influences of solid volume fraction on wall-to-particle heat-transfer coefficients. For a fixed mass flow rate of the solids, while radiative transport diminishes, conduction improves with the increase in solid volume fraction; relative contribution of radiation decreases from 92% to 34% when the solid volume fraction increases from 0.07 to 0.43. Driven by the enhancements to radiation, the overall heat-transfer coefficient linearly increases with particle emissivity, and exhibits a cubic dependence on the wall temperature. Interplay between the different modes are observed with the stronger radiation resulting from improved particle emissivity or larger wall temperature, and also leads to a minor reduction in the conductive heat-transfer coefficient. Opposing effects of particle size are predicted on conduction and radiation, depending on the solid volume fraction in the plug flow regime. While conductive heat transfer is only dictated by the specific surface area available for heat exchange, which is enhanced by smaller particle sizes, radiative transport is also affected by shading effects from neighboring particles, which starts to play a dominant role for larger solid volume fractions. Therefore, for the denser plug flows of $\phi_s = 0.25$ and 0.43, the radiative heat-transfer coefficient slightly increases, but monontonically decreases for $\phi_s = 0.07$, with particle size. As a consequence, the overall (conduction + radiation) wall-to-particle heat-transfer coefficient decreases by only 17% for the former, whereas it is reduced by 39% for the latter when particle diameter increases from 0.4 mm to 1 mm.

Wall-to-particle heat-transfer coefficient predictions from plug flow and moving

beds are transformed and generalized to obtain channel-averaged Nusselt numbers with radiation effects included. These predictions demonstrate the substantial influence of solid volume fraction on heat-transfer coefficients and the corresponding Nusselt number. Specifically, heat-transfer coefficients (and equivalently the Nusselt number) are enhanced by factors of 4 and 10 for mustard seed and alumina respectively when the solid volume fraction increases from 0.02 to 0.48. The improvements in the heat-transfer performance is especially more dramatic in the dense flow regime — the heat-transfer coefficients more than sixfold even for a relatively small, 15% increase in the solid volume fraction from 0.48 to 0.55 for the high-conductivity alumina particles. This amplified effect of the solid volume fraction on the thermal performance is because of the dominance of conductive heat transfer for dense flow-regimes. While it is challenging to directly extrapolate the Nusselt number from the plug flow to the moving beds for the high-conductivity alumina particles, this extrapolation becomes more reasonable for the low-conductivity mustard seed. For predicting the radiative Nusselt number, the extrapolation from plug flow to moving beds is more reasonable, and independent of the material thermal conductivity.

On the whole, this study develops powerful modeling capabilities based on open-source software to understand and predict the interplay of conductive and radiative heat transfer mechanisms for dilute-to-dense granular flows. Model predictions are further interpreted to provide important insights to guide design and operation for many different multiphase flows, including dilute particle-curtain flows, pneumatic flow with suspensions of particles and dense moving beds.

CHAPTER VI

Discrete Element Modeling for Dense Moving Bed Heat Exchanger Informs Comprehensive New Nusselt-Péclet Number Correlations

Adapted from a manuscript under preparation:

- **Chen, Z., Li, B., Bala Chandran, R., 2024. DEM Modeling for Dense Moving Bed Heat Exchanger Informs Comprehensive New Nusselt–Péclet Number Correlations.**

6.1 Introduction

Dense moving beds of inert or reactive particles have many applications including particle-based heat exchangers [164, 185–188], additive manufacturing [189–191] and thermochemical reactors [192–196]. In concentrated solar power plants, a heat-transfer fluid collects the high-quality heat incident from sunlight in a solar receiver, and transfers it to the working fluid of a power cycle (e.g., steam in Rankine cycles) [197, 198]. Changing the heat transfer medium from traditional options including liquids such as molten salts and oils, and gases such as high-pressure, high-temperature

steam and air, to ceramic solid particles [6, 164], enables operation at high temperatures exceeding 873 K. This can in turn operate higher-temperature thermodynamic power cycles such as the sCO_2 based Brayton cycle with larger thermodynamic efficiencies. Ceramic particles tend to have larger thermal conductivity (k_s = 4.5–6.5 W/m/K) as compared to air or gaseous fluids, but, dependent on material composition, it may not be as conductive as molten nitrate salts [199]. Therefore, in particle-based heat exchangers, overall heat transfer coefficients are limited on the order of 100–300 W/m^2/K. In contrast, heat exchangers with molten nitrate salts report overall heat transfer coefficients as high as 300–900 W/m^2/K. Broadly, this limitation of wall-to-particle heat transfer in dense-bed heat exchanger systems has inspired recent work to understand and improve their performance through both model predictions and experimental measurements. The objective of our study is to apply discrete element modeling to understand the dependencies of geometric and thermophysical properties on the heat transfer performance of dense moving bed flows and identify the possible pathway to enhance the heat transfer coefficients for particle-based heat exchanger.

Extensive prior works have been done to obtain semi-empirical and empirical correlations for particle-wall heat transfer in dense moving beds. In our recent study [107], we discussed the state-of-the-art in continuum and discrete particle flow modeling techniques. Whether model-based predictions or experimental measurements, prior work has more extensively focused on low-to-moderate temperature dense granular flows, where effects of radiation are not significant or at best subdued [43, 75]. Even though radiative effects were included in our own prior work, we considered very few parameter combinations, which precludes broad applicability of these predictions [107]. Even though continuum-model based Nusselt number correlations are powerful to traverse a wide range of parameters including Péclet number and geometric parameters, they are based on this central theme of continuum fluid flow. These cor-

relations still don't fully capture the case of even dense granular flows, where a plug flow assumption is reasonable. Therefore, in this study we use our developed discrete element modeling methods [107], and scale up the code to explore a wide range of parameters–specifically we quantify the effects of channel length, width, particle size, thermal conductivity and solid volume fraction.

Mickley and Fairbanks [71] derived an analytical solution for the particle-to-wall heat transfer coefficient based on a continuum model involving packets of particles sweeping along a wall surface for a short residence time. However, the particles are assumed to be homogeneous and have uniform thermal properties. Sullivan and Sabersky [43] built further on this framework to obtain a more generalized Nusselt number correlation, which additionally included a thermal resistance in the near wall region. This resistance was determined based on best-fit values based on experimental measurements performed in a hopper-channel system with varying particle sizes (0.2–2 mm), different thermal conductivities, and channel lengths. However, all these measurements were obtained at a low temperature range (23–34 °C). This correlation is based on an analytical plug flow model using dimensionless Péclet number, which characterizes the rate of flow effects to heat diffuse effects. This continuum-model based correlation from Sullivan and Sabersky has been extended to other flow configurations. Several research groups conducted experiments for an inclined chute flow and deduced smaller contact resistance values between the walls and the particles [44, 200, 201]. This suggests a thinner air gap in inclined particle flow channels, likely due to increased residence time for the particles. Patton et al. [44] further proposed an additional term to account for the influence of the plane's incline angle. In seeking a physical interpretation for near-wall thermal resistance, Natarajan and Hunt [45, 202] proposed a kinetic theory to describe the flow and heat transfer for particles densely moving in a vertical channel. Comparing with experimental measurements, they found that the heat transfer coefficient/Nusselt number decreases slightly and

levels off beyond a modified Péclet number of 600 and explained this as increasing flow velocity (Péclet number) decreases the solid volume fraction in the near-wall region, thereby lowering the Nusselt number. The development of these Péclet number based correlations identify the significance of near-wall effect on granular flow heat transfer and find good agreement with experimental measurements. Though researchers have underscored the importance of solid volume fraction in heat transfer, few analyses quantify its sensitivity.

Besides Péclet number, the Graetz number has gained popularity in quantifying heat transfer behaviors in particle moving beds. Unlike the Péclet number, the Graetz number incorporates the effect of both channel length and width, offering a more comprehensive characterization of the channel geometry. Muzychka et al. [67] derived the analytical solutions for transient heat transfer in laminar pipe flow. The Graetz number correlation served as benchmarks and has been subsequently applied to transient heat transfer research in moving bed flows. Following researchers found the benefit of applying this correlation to particle flows. Watkins and Gould [68] examined the Muzychka's Graetz number correlation for vertical pipe flow and found a 15% overestimation from their experimental measurements, attributed to the discrete nature of particles. Ho and Albrecht [203] applied these solutions to a densely packed moving bed in a particle-to-sCO_2 heat exchanger to find optimal geometry design. Recently, many researchers have attempted to adapt these continuum fluid-flow heat transfer correlations for plug flow profiles. For instance, Wei et al. [75] followed Muzychka's analytical derivation and achieved a semi-empirical Nusselt number correlation through fitting their 2D model that includes effective bulk and near-wall regions conductivity. However, the particle temperature tested in their experiment is no more than 43 °C. Adapa et al. also modified Graetz number correlation by incorporating an effective thermal conductivity which was translated from an effective air gap distance between the heating wall and the moving bed; their results aligned within the

error margins of their experimental data. Generally, Graetz number correlation offers a better understanding of the influence of geometric parameters, especially informing the status of a fully developed flow. However, the discrete nature of the moving bed flow of particles is not captured when particle diameter is varied.

Although researchers have leveraged the modeling techniques to obtain the empirical correlations, these are primarily limited to analytical model based on continuum flow. For the recent decade, discrete element method (DEM) has gained attention for moving particle-bed heat transfer modeling. This modeling approach tracks individual particles and is generally considered to capture the discrete nature of moving particles more accurately. Through discrete element modeling (DEM) of particle distribution in a vertical channel, Watkins developed an analytical expression for the effective thermal conductivity in the near-wall region [46]. Johnson, Guo and Qi [61, 81, 84] calculated the heat transfer coefficients from their 3D DEM simulations for flowing particles but not translated the non-dimensional Nusselt number or Graetz numbers. Our previous work [107] related the Nusselt number with the effect of operating temperature, particle size, solid volume fraction and particle materials properties. However, state-of-the-art heat transfer correlations for moving beds typically incorporate only one or two of these key parameters, rather than all of them. The comprehensive Nusselt number correlation including the effect of operating, geometrical and thermal parameters altogether is still missing in the community. More importantly, although solid volume fraction is considered an essential factor, it is only often reflected in the near-wall effective thermal conductivity instead of overall correlation.

Motivated by these factors, the objective of this work is to apply discrete particle flow and heat transfer models to predict the thermal performance of dense moving beds of particles over a wide range of materials, design and operating parameters. Specifically, we consider an extensive range for channel length (0.1–0.5 m), channel

width (5–8 mm), particle thermal conductivity (0.05–5 W/m/K), particle size (0.2–0.8 mm) and solid volume fraction (0.54–0.66). Model predictions are used to inform new heat-transfer correlations, which now additionally include the direct effect of solid volume fraction compared to reported Nusselt correlations in prior work. Additionally, we benchmark and compare an extensive set of experimental data against predictions from our new correlation to validate it. Most importantly, we use and interpret these correlations to provide strategic pathways for design, operation and material options to achieve at least a doubling of the state-of-the-art moving bed heat exchanger performance from 300 to 600 $W/m^2/K$.

6.2 Method

6.2.1 Modeling Domain

Fig. 6.1 shows the modeling domain of the gravity-driven, densely moving bed. This model includes one vertical rectangular heat transfer channel at a standard size of 5 mm $\times$ 5 mm $\times$ 500 mm and two hoppers: one hopper above with a height of 20 mm is used as a region to insert particles (d_p = 0.3 mm at a standard case) and then feed into the rectangular channel. This feeding hopper ensures a high solid volume fraction above 0.5 in the channel region. The other hopper below the channel is the outlet hopper with a height of 10 mm. By adjusting the outlet size of the hopper, we can control the mass flow rate of the granular flow ranging from 0.17 to 3.62 g/s. In a standard case, the entire model would accommodate nearly 114,000 ceramic particles (with an equivalent mass of 4.4 g) and at least 90% of the particles locate in the channel region. Particles are initially inserted into the upper hopper at a constant temperature of 1,000 K. These particles would flow into the heat transfer channel region in the steamwise direction (z-direction) under gravity. In the traverse direction (x- and y-direction), these particles lose heat to the four isothermal walls

at a constant temperature of 300 K through heat conduction and radiation.

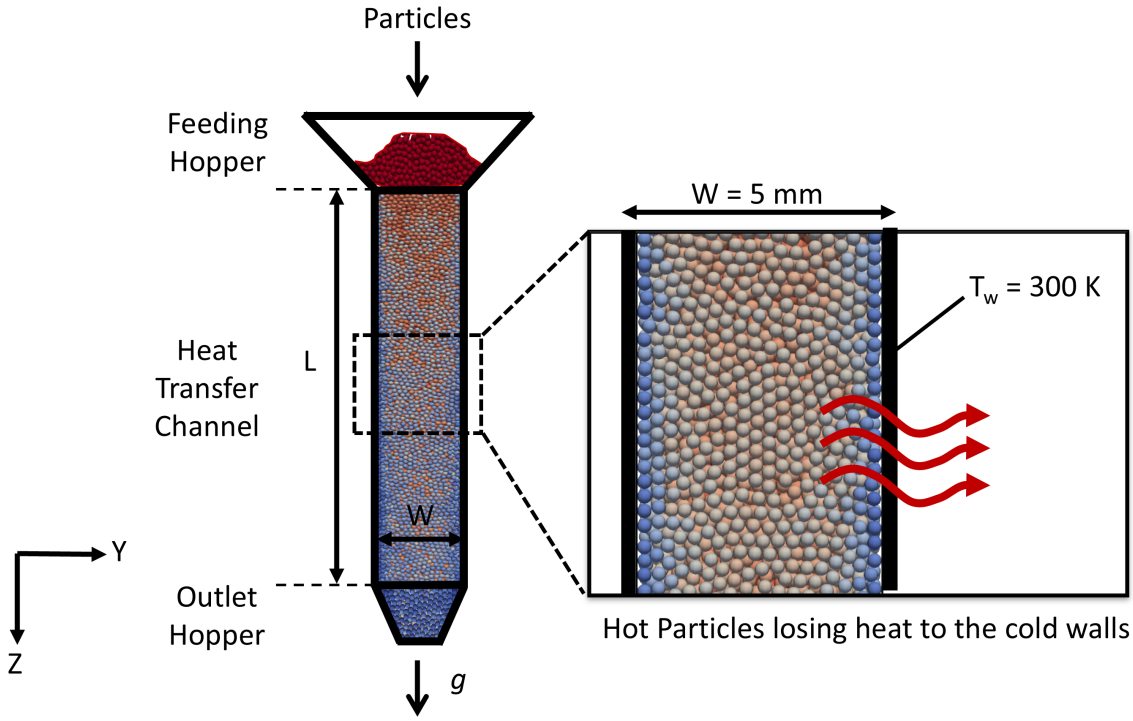


Figure 6.1: Modeling domain for gravity-driven, dense, moving beds of particles in a rectangular channel that is fed by a hopper above.

6.2.2 Discrete Element Modeling for Flow and Heat Transfer

The particle position, velocity and temperature are tracked using the DEM simulator, LIGGGHTS [95], as mentioned in previous chapters. The conduction and radiation model have been elaborated in Sec. 2.2.2.1, 2.2.2.2 and 2.2.2.4 respectively. A DEM time step of 5×10^{-6} s for $d_p = 0.2$ mm and 1×10^{-5} s for other larger particle sizes is applied according to the suggestion given in Sec. 2.2.1.

The mechanical and thermal properties set in the DEM modeling are listed in Table 6.1, which are based on porcelain beads as particles and stainless steel as channel surfaces. Both the ceramic particles and the steel surfaces can withstand high temperature and is selected for this study as comprehensive data with available thermophysical properties. For the sake of simplicity, all thermophysical properties

Table 6.1: Constant/fixed value of mechanical and thermal properties used in the DEM simulations.

Properties, symbol	**Value**	**Unit**
Particle Density, ρ_p	2760	kg/m^3
Particle specific heat capacity, $c_{p,p}$	1200	J/kg/K
Wall specific heat capacity, $c_{p,w}$	500	
Wall thermal conductivity, k_w	23	
Particle real Young's modulus, Y_p^*	215	GPa
Wall real Young's modulus, Y_w^*	190	
Particle/Wall DEM Young's modulus, Y	5	MPa
Particle Poisson's ratio, ν_p	0.3	
Wall Poisson's ratio, ν_w	0.27	
Particle-particle restitution coefficient, e_{pp}	0.77	
Particle-wall restitution coefficient, e_{pw}	0.44	
Particle emissivity, ϵ_p	1	
Wall emissivity, ϵ_w	1	

are modeled to be constant and temperature-independent. The Young's modulus used for the flow simulation is reduced to 5 MPa compared to the reported value of 215 GPa for ceramic materials, as it is the lowest permitted value in LIGGGHTS. Though unrealistic, this artificial reduction in Young's modulus has been shown to negligibly impact flow physics and is a common approach to reduce computational cost. The emissivities for both particles and wall surfaces are assumed to be 1 as the largest possible value. Later in Sec. 6.3.1 our results show that the contribution from radiation is very minimal at certain conditions and this overestimation of the emissivity would make negligible impact on the heat transfer.

6.2.3 Parametric Study

To generalize a comprehensive correlation for moving bed flow heat transfer, we specifically consider the following parameters: (a) Channel length, L, width, W, and particle diameter, d_p, to investigate of the geometric parameter of the flow regimes; (b) Thermophysical property such as thermal conductivity of particle, k_p; and (c) Solid volume fraction of the moving bed, ϕ_s, by varying the frictional coefficients in-

Table 6.2: Parameter exploration range used in the DEM simulations for moving bed.

Parameters	**Range**	**Unit**
Particle size, d_p	0.2, **0.3**, 0.4, 0.6, 0.8	mm
Particle thermal conductivity, k_s	0.05, **0.5**, 1, 2, 5	W/m/K
Channel length, L	**0.1**, 0.2, 0.5	m
Channel width, W	**5**, 6, 8	mm
Particle-particle, static frictional coefficient, $\mu_{s,pp}$	0.12, 0.15, 0.18, 0.2, 0.3, **0.6**, 0.9	
Particle-wall, static frictional coefficient, $\mu_{s,pw}$	**0.3**, 0.4, 0.5, 0.7, 0.9	
Particle-particle, rolling frictional coefficient, $\mu_{r,pp}$	**0.1**, 0.3, 0.6	
Particle-wall, rolling frictional coefficient, $\mu_{r,pw}$	0.1, 0.15, 0.2, **0.28**, 0.3	
Moving bed outlet velocity, u	0.51 – 7.02	cm/s
Solid volume fraction, ϕ_s	0.56 – 0.66	

*The values in bold are baseline parameters that are held constant when other parameters are varied.

cluding the static and rolling, particle-particle and particle-wall frictional coefficients. Baseline values are given in Table 6.1 and the parameter ranges explored in this study are shown in Table 6.2.

6.3 Results & Discussions

6.3.1 Effects of Geometric and Thermophysical Properties on Heat Transfer Coefficients

Fig. 6.2 demonstrates that the bulk particle thermal conductivity strongly affects the overall particle-to-wall heat transfer coefficients for the dense moving beds of particles. Five different particle thermal conductivities, $k_s = 0.05, 0.5, 1, 2, 5$ W/m/K, are modeled for a fixed mass flow rate of $\dot{m} = 2.27$ g/s and an outlet velocity of $u_{\text{outlet}} = 5.55$ cm/s. At this mass flow rate, and for a channel length of 0.1 m, the factor that limits the overall heat transfer is both near-wall conduction, and bulk advection due to the flowing particles, and is subsequently discussed in Fig. 6.3. The steady-state

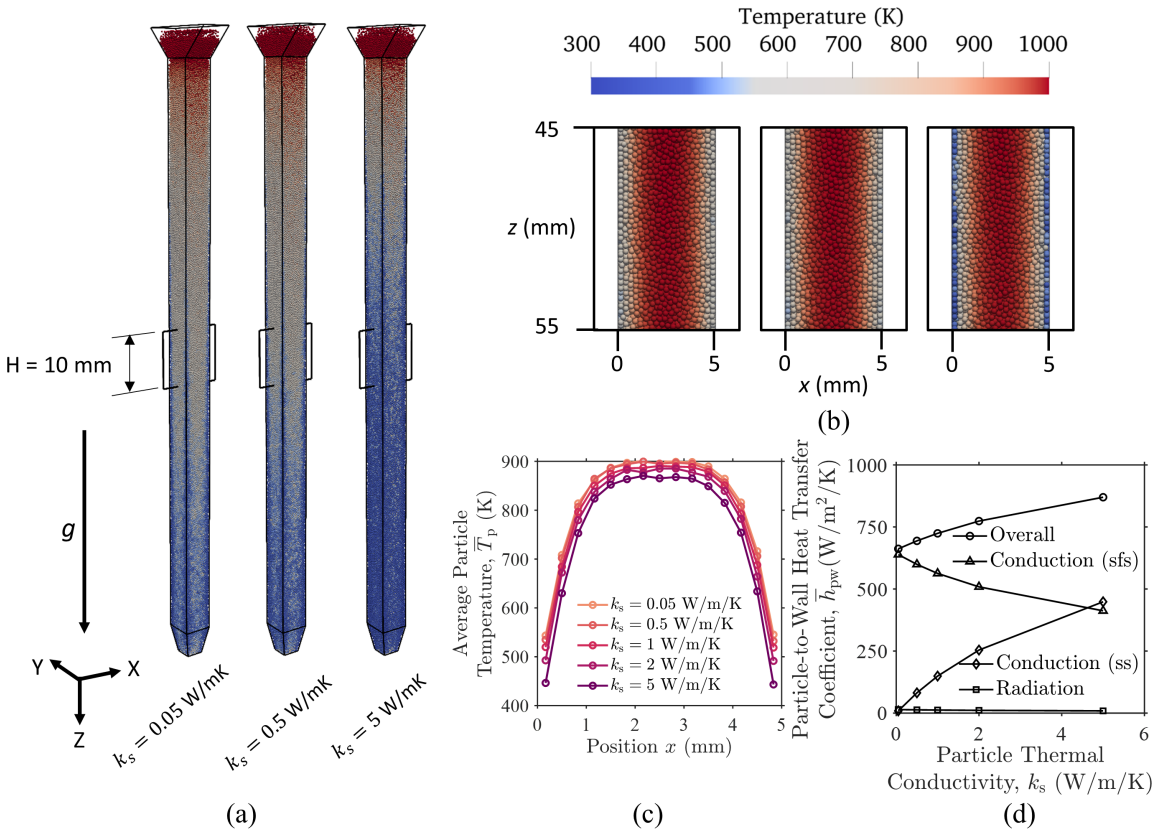


Figure 6.2: Effects of particle thermal conductivity in gravity-driven moving beds with inlet particles at 1000 °C, particle diameter of d_p = 0.3 mm under an identical mass flow rate of $\dot{m}$= 2.27 g/s and a near-constant solid volume fraction ($\phi_s \approx 0.59$) on (a) steady-state spatial distributions of particle temperatures at t = 10 s (k_s = 0.05, 0.5, 5 W/m/K), (b) cross-sectional view of the particle temperature distribution at a location of z = 0.045–0.055 m of the moving beds (the cross-sectional view is notified by the black box in (a)), and (c) the average particle temperature profile along the x direction for thermal conductivity (k_s = 0.05, 0.5, 1, 2, 5 W/m/K) (d) channel-averaged, particle-to-wall heat-transfer coefficient as a function of the particle thermal conductivity contributed from thermal radiation, solid-fluid-solid (sfs) and solid-solid (ss) conduction pathways.

particle temperature distribution (Fig. 6.2(a)) reveals that particles cool along the streamwise direction of the moving bed, with higher thermal conductivity enhancing this cooling effect and lower particle temperatures at the outlet to 419, 408 and 360 °C respectively for $k_s = 0.05$, 0.5 and 5 W/m/K. Particles adjacent to the isothermal walls ($T_w = 300$ K) cool down more significantly, relative to the particles present in the core of the channel, due to the larger contact area and the relatively large wall thermal conductivity modeled assuming steel walls ($k_w = 23$ W/m/K). To illustrate temperature gradients from the walls to the center of the channel, Fig. 6.2(b) shows spatial temperature profiles of particles over a 1 cm region at channel depths between $z = 45$ and 55 mm. Particles adjacent to the walls are cooled down to 446 K for k_s = 5 W/m/K, compared to 543 K and 534 K for $k_s = 0.05$ W/m/K and ks = 0.5 W/m/K respectively due to the non-linear dependence of the rate of wall-to-particle heat transfer on the bulk thermal conductivity of the particles. The temperature gradient is obtained in Fig. 6.2(c) by averaging the particle temperatures along the entire length and depth of the channel, within a bin size of 0.33 × 5 × 100 mm; the resolution along the x-direction is comparable to the particle diameter (0.3 mm). With increasing conductivity, both the bulk and the near-wall particle temperature decreases, with a more significant reduction near the walls.

Fig. 6.2(d) shows that the overall heat transfer coefficient increases with particle thermal conductivity as expected. Heat transfer in the moving bed is primarily dominated by conduction (97.86%) largely due to the high solid volume fraction modeled for these cases ($\phi_s \approx 0.59$). As particle thermal conductivity increases from 0.05 to 5 W/m/K, the particle-to-wall heat transfer coefficient from solid-solid conduction rises 50-fold from 9 W/m^2/K, and correspondingly the heat transfer coefficient from solid-fluid-solid conduction decreases. This is because the solid-solid conductive heat fluxes are enhanced by the particle thermal conductivity, whereas the solid-fluid-solid conductive fluxes is independent of the particle thermal conductivity. And the tem-

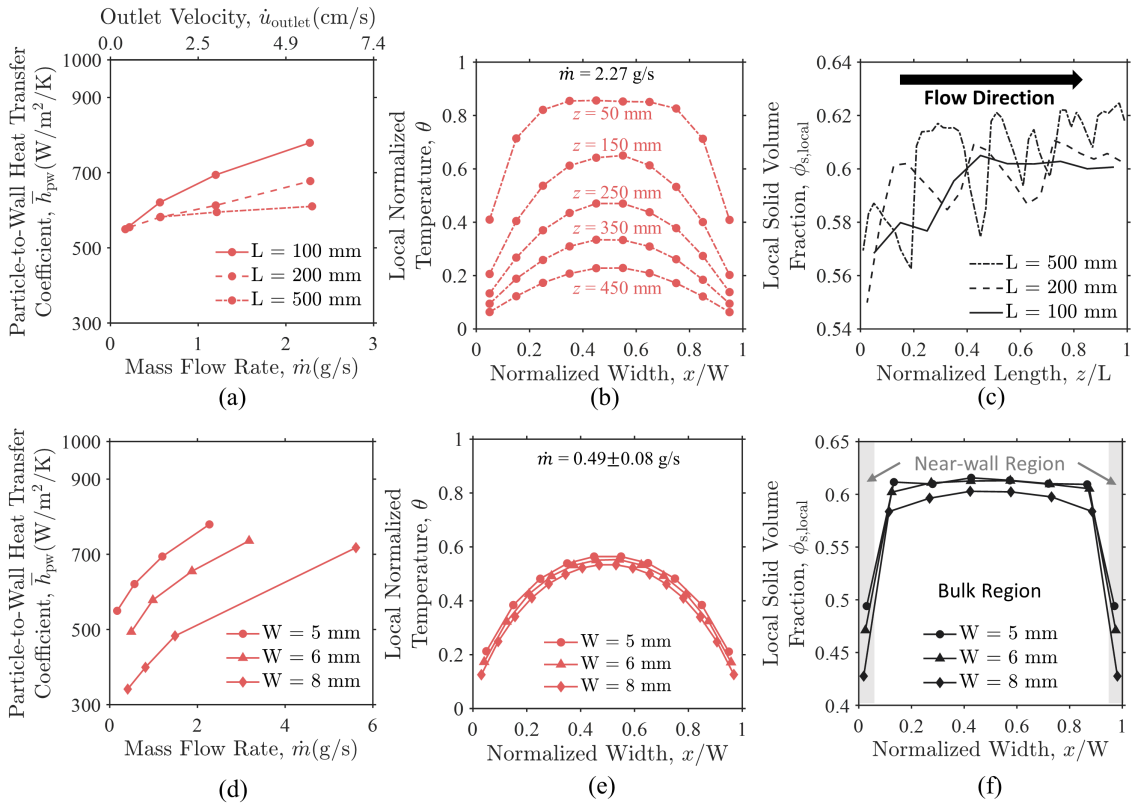


Figure 6.3: Effects of (a-c) channel length, L, and (d-f) channel width, W, on the (a,d) channel-averaged, particle-to-wall heat transfer coefficient, $\overline{h}_{pw}$, as a function of mass flow rate; accompanied with (b,e) temperature and (c,f) solid volume fraction distribution, obtained from snapshots of particle positions after flows reaching steady state, in the gravity-driven moving beds with the (b,c) longest simulated channel (L = 0.5 m) at a near-constant mass flow rate ($\dot{m}$= 2.27±0.02 g/s) or (e,f) at a close mass flow rate ($\dot{m}$= 0.49±0.08 g/s), with all the rest of the parameters as the baseline values in Table 6.1.

perature gradient between the particles and the walls is largely reduced with stronger solid-solid conductive heat transfer, which further weakens the solid-fluid-solid conductive heat transfer due to the interplay between two heat transfer modes. Even though the contribution of radiation to the overall heat transfer is small (= 2.14%) for the specific case modeled in Fig. 6.2, this is highly sensitive to the particle thermal conductivity and the size, in particular. This will be discussed in more details in Fig. 6.4(d).

Fig. 6.3 shows the influences of heat exchanger geometric parameters, including

channel length, L, and channel width, W, on the particle-to-wall heat transfer. The channel-averaged, overall heat transfer coefficient, $\overline{h}_{\mathrm{pw}}$, diverges with the increase of mass flow rate for three different channel lengths at $L = 100$, 200 and 500 mm (Fig. 6.3(a)). This is because the flow would be fully developed when the channel is long and the flow rate is low, according to the definition of Graetz number. When the flow is fully developed, the heat transfer coefficient would only be slightly affected by the varying of mass flow rate. Fig. 6.3(b) demonstrates the temperature gradient developing along the flow direction for the longest channel tested ($L = 500$ mm), where the local particle temperature is obtained by averaging the particle temperatures within a small bin of 0.5 mm $\times$ 5 mm $\times$ 5 mm. Fig. 6.3(b) demonstrates the normalized temperature profile developing along the flow direction for the longest channel tested ($L = 500$ mm) with mass flow rate of 2.27 g/s, where the local particle temperature is obtained by averaging the particle temperatures within a small bin of 0.5 mm $\times$ 5 mm $\times$ 5 mm at 5 selected height. The relative variation of the temperature profile is slowly decelerated along the flow direction, indicating the flow approaches fully thermal development. This can be verified by the non-dimensional temperature gradient plot as shown in Fig. E.1 in Appendix E.1. Fig. 6.3(c) demonstrates the solid volume fraction distribution for three different channel lengths, obtained from snapshots of particle distributions after the flows reaching steady state. The increase in solid volume fraction is due to the increased settling of particles along the flow direction for moving beds. It is to be noted that the trends predicted in the model could be exacerbated by the soft-sphere assumption as compared to experimental data. For the same reason, the overall averaged solid volume fraction is higher for longer channel length due to larger total mass in the channel. The oscillations in the data are related to the statistical nature of the motion of particles, where dictated by frictional and gravitational effects. Appendix E.2 shows select stagnation zones that correlate with reductions in the solid volume fraction at select snapshots of time. Fig.

6.3(d) illustrates how the particle-to-wall heat transfer coefficient dependence on the mass flow rate for various channel widths. Expectedly, larger channel widths lead to a smaller heat transfer coefficient due to the increased conductive resistance at all mass flow rates. To explain this better, the temperature and solid volume fraction profiles are obtained by averaging the temperature and solid volume fraction values within 0.5 mm-sized bins divided along the width, x direction (Fig. 6.3(e)(f)). The selected mass flow rates are within the range of $\dot{m} = 0.49 \pm 0.08$ g/s. Fig. 6.3(e) shows that the local normalized temperature, θ, with narrower width is consistently higher than the ones with wider width across the normalized width direction. Fig. 6.3(f) depicts a significantly low solid volume fraction in the near-wall region ($\phi_{\mathrm{s,nw}} \in (0.42–0.5)$), defined as the domain within a distance of one particle diameter from the wall boundaries, compared to the bulk area ($\phi_{\mathrm{s,bulk}} \in (0.57–0.61)$). The presence of this near-wall region has been extensively discussed in prior research [43, 70]. Considering the near-wall region is mainly dependent on the particle size, solid volume fraction distribution is not affected by the varying of channel widths. The differences of temperature and solid volume fraction profiles for various channel widths are mainly due to the difference of mass flow rates ($\Delta\dot{m}$ up to 27.3%), where larger width has lower selected mass flow rate. Unfortunately it is challenging to independently control the mass flow rate across different channel widths. Ideally, the profiles of the solid volume fraction distribution for different widths would be more identical. Based on the discussion of results of varying lengths and widths, the influence of geometric parameters generally follows the predictions of treating the discrete particles as a continuum.

Fig. 6.4 shows the combined influence of particle material properties on the particle-to-wall heat transfer, including the particle size, d_p, and particle thermal conductivity, k_s. The heat transfer coefficient increases with decreasing particle size due to the increased surface area per unit volume for inter-particle and particle-wall conduction (Fig. 6.4(a)). Maintaining a constantly high solid volume fraction for

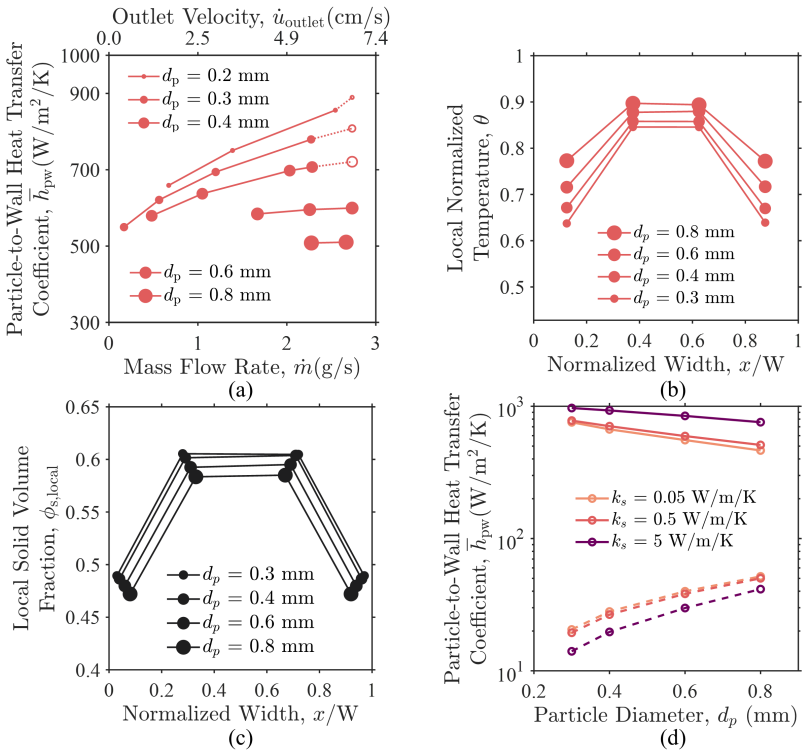


Figure 6.4: Effects of particle diameter, d_p, on the (a) channel-averaged, particle-to-wall heat transfer coefficient, $\overline{h}_{\text{pw}}$, as a function of mass flow rate, with values extrapolated (hollow circle) for higher mass flow rate ($\dot{m} > 2.28$ g/s) and small particle sizes ($d_p \leq 0.4$ mm); accompanied with (b) temperature, (c) solid volume fraction distribution, and (d) the heat transfer coefficient for overall and radiative heat transfer components, as a function of particle diameter, in the gravity-driven moving beds at a near-constant mass flow rate ($\dot{m} = 2.27 \pm 0.01$ g/s), with all the rest of the parameters as the baseline values in Table 6.1.

moving bed flows is challenging at high flow rates, especially for smaller particle size. Therefore, in order to evaluate the effects of particle size across wider mass flow rate range, the heat transfer coefficients for small particle sizes ($d_p \leq 0.4$ mm) are extrapolated to get results at higher mass flow rate ($\dot{m} > 2.28$ g/s) using the new Péclet number and Nusselt number correlations obtained in this work Sec. 6.3.3.

In addition, the near-wall effect for larger particles is more significant due to the enlarged near-wall region. The decrease of the solid volume fraction in both near-wall and bulk region (Fig. 6.4(c)) results in reduced heat transfer between larger

particles and the walls (Fig. 6.4(b)). Fig. E.4 in Appendix E.3 shows the overall averaged solid volume fractions under varied particle sizes, which presents consistent trends with local solid volume fraction in Fig. 6.4(c). Though large particle size is a disadvantage for heat transfer in moving bed flows, it improves the radiative heat transfer significantly (Fig. 6.4(d)). For a fixed thermal conductivity of 0.5 W/m/K, the overall heat transfer coefficient reduced by 34.5% when increasing particle size from 0.3 mm to 0.8 mm, while the radiative heat transfer coefficient increased by 2.6 times, and the relative contribution from radiation elevated from 2.49% to 9.82%. The radiative contribution is more significant with the decrease of particle thermal conductivity, consistent with the findings in Fig. 6.2(d). This indicates that radiation is no longer negligible when particle size is at least above 0.6 mm (contributing at least 5% of the overall heat transfer) in a moving bed flow. These datasets also point to the need for informed discretion on when to factor in radiative heat transfer for dense moving beds of particles. For large particle size ($d_p \geq 0.6$ mm), radiation makes up at least 5% of the overall heat transfer, and therefore should be considered. However, the computational cost of including for radiation is extremely high even with parallelization (39–52% more computational time), especially for models with longer ($L > 0.1$ m) and wider ($W > 5$ mm) channels. Therefore, the baseline conditions of k_s = 0.5 W/m/K and $d_p = 0.3$ mm is considered where radiation isn't expected to play a significant role ($< 2.5\%$ contribution) for the sake of computational tractability.

Our previous discussion has focused on a fully packed flow with a relatively constant solid volume fraction of $\phi_s = 0.59$ ($\pm$ 0.019) averaged over the entire length of the channel when the particle size wasn't too large. However, this solid volume fraction changes depending on the modeled frictional coefficients, especially the static particle-particle and particle-wall friction coefficient, with all other parameters held fixed. While the static particle-particle friction coefficient was varied from $\mu_{\mathrm{s,pp}}$ = 0.1–0.9, we model a more restricted variation in the static particle-wall friction $\mu_{\mathrm{s,pw}}$

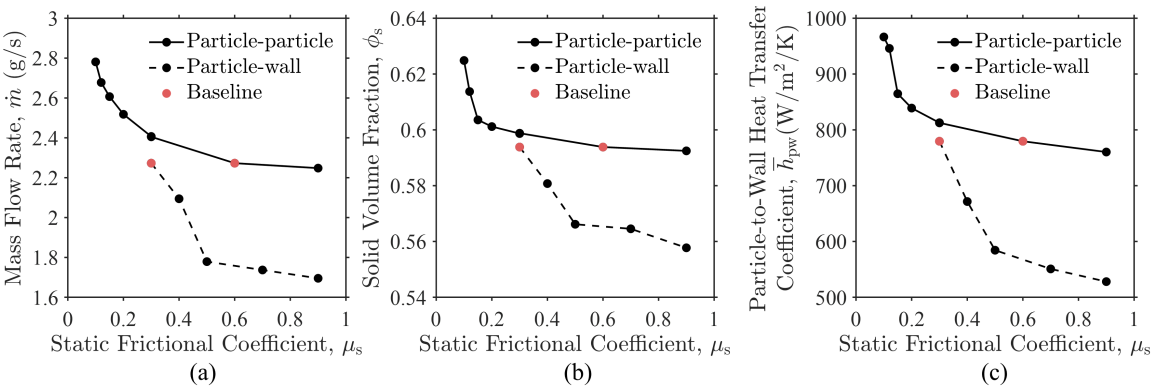


Figure 6.5: Effects of the particle-particle and particle-wall, static frictional coefficients on (a) mass flow rate, $\dot{m}$, (b) solid volume fraction, ϕ_s, and (c) particle-to-wall heat-transfer coefficient, $\overline{h}_{\rm pw}$, for a gravity-driven, moving bed, with the rest of parameters fixed as the baseline values in Table 6.1. The identical baseline results are underscored by red dots. The range of the tested static friction coefficient for particle-particle and particle-wall surfaces follows the physical interpretation that $\mu_{\rm s,pp} > \mu_{\rm r,pp} = 0.1$ and $\mu_{\rm s,pw} > \mu_{\rm r,pw} = 0.28$.

= 0.3–0.9. This range is dictated by the constraint of rolling friction coefficient being less than the static counterpart, i.e., $\mu_{\rm r} < \mu_{\rm s}$.

As shown in Fig. 6.5, even though solid volume fractions change by less than 5% when the particle-particle friction coefficient changes from 0.62 to 0.59, this results in more than 21.3% change in the heat transfer coefficient. This is because the heat transfer coefficient is significantly sensitive to the small changes in solid volume fraction under the conduction-dominated heat transfer. Similar trends are observed with the particle-wall friction coefficients with dramatic reductions in the heat transfer coefficients with decrease in ϕ_s from 0.59 to 0.56 for the baseline calculation.

Compared to the static friction coefficient, the rolling friction coefficient for both particle-particle and particle-wall plays a much less significant role in these simulations because the relative rolling between particles and walls is very rare in a vertical channel. More details can be found in Appendix E.4 for rolling particle-particle friction coefficients varied from 0.1 to 0.59 (ensuring $\mu_{\rm r,pp} < \mu_{\rm s,pp} = 0.6$) and the rolling particle-wall friction coefficients varied from 0.1 to 0.28 (ensuring $\mu_{\rm r,pw} < \mu_{\rm s,pw}$

$= 0.3$).

6.3.2 Comparison with Existing Correlations

Fig. 6.6 transforms the predicted particle-to-wall heat transfer coefficients obtained from 39 distinct simulations in Fig. 6.2–6.4 in the form of two commonly used Nusselt number correlations in the community: (1) the Nusselt number based on particle size ($\overline{Nu}_d$) versus the modified Péclet number (Pe_L^*) established by Sullivan and Sabersky (Fig. 6.5(a)), and (2) the Nusselt number based on the hydraulic diameter ($\overline{Nu}_{D_h}$) versus the inverse Graetz number (Gz). Instead of using the effective thermal conductivity of the solid-fluid (particle-air) medium, the intrinsic particle thermal conductivity, k_s, is used in these correlations. This is the way to avoid making any continuum/effective medium assumptions for granular flow. Fig. 6.5(a) shows that our simulation predictions consistently result in larger $\overline{h}_{\text{pw}}$ and therefore larger $\overline{Nu}_d$ (up to 350% relative deviation) for all cases modeled as compared to using the Sullivan-Sabersky correlation for equivalent Pe_L^*. In part, this is attributed to our simulations being performed with rather dense beds with ϕ_s of 0.58–0.60, as compared to the reported range of 0.37–0.41 in their experimental measurements. As we've demonstrated in our prior work [107] and in Fig. 6.5, the solid volume fraction has a sizeable impact on the heat transfer coefficients. To probe if any discrepancy arises due to the choice of us using the bulk conductivity of the solid particle in obtaining Pe_L^* and $\overline{Nu}_d$, Fig. E.6 in the Appendix E.5 shows the same comparisons made based on using an effective medium conductivity obtained from the ZBS model. However, the deviation from the Sullivan-Sabersky correlation is still significant (up to 280% deviation). These trends demonstrate that the influence of solid volume fraction always exist under the choice of using bulk versus an effective conductivity.

The data for different channel lengths (7 datasets obtained with 3 different lengths) collapses reasonably well in Fig. 6.3(a). This is because the inverse dependence

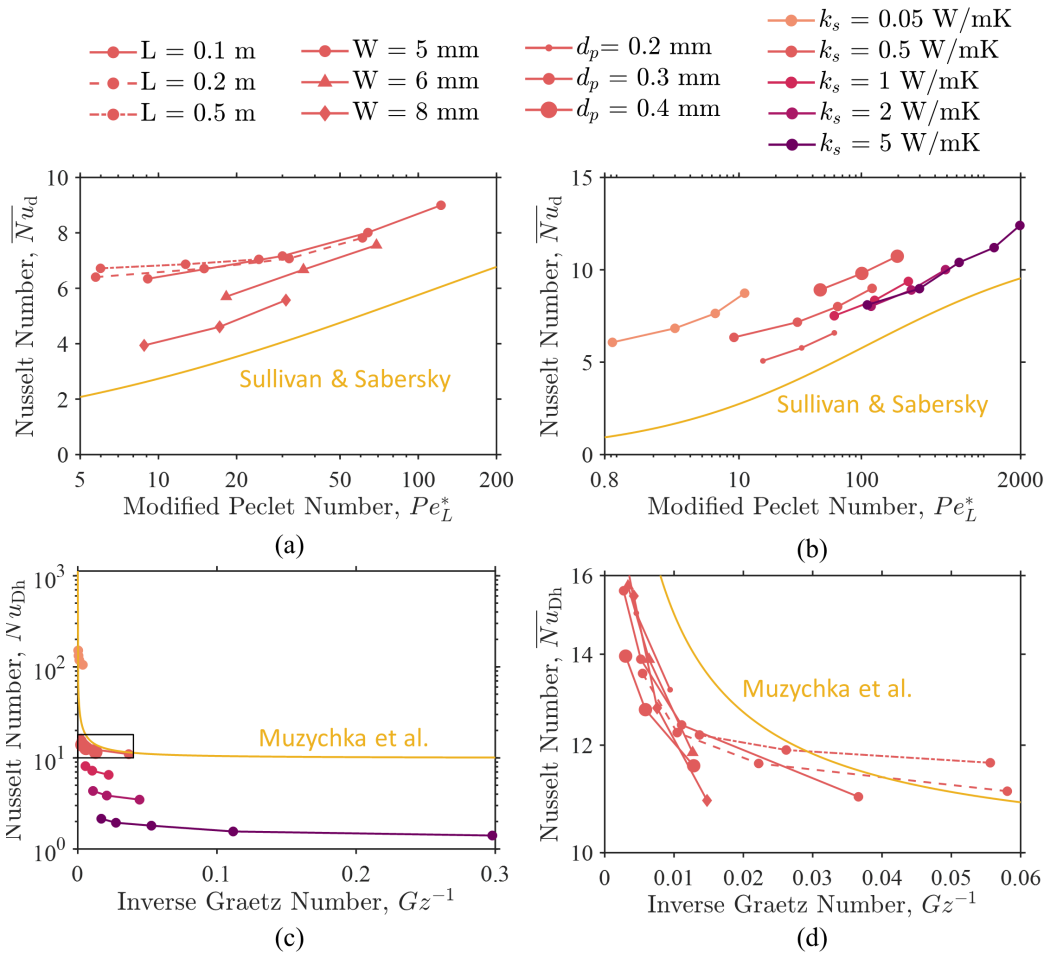


Figure 6.6: (a)(b) Particle-diameter-based Nusselt number, $\overline{Nu}_d$, as a function of the modified Péclet number, Pe_L^*, compared with Sullivan and Sabersky's correlation, and (c)(d) the hydraulic-diameter-based Nusselt number, $\overline{Nu}_{D_h}$, as a function of the inverse Graetz number, Gz^{-1}, compared with Muzychka's correlation for plane channel, for the simulation results with varied channel length, channel width, particle diameter and particle thermal conductivity (only one parameter of all data is varied while keeping other parameters as the values in Table 6.1).

of the channel-averaged particle-to-wall heat transfer coefficient on length is physically reasonable. Although particle size and thermal conductivity are included in both non-dimensional numbers, these datasets do not collapse as effectively, indicating more non-linear effects of these parameters, and a need for improved non-dimensionalization. The near-wall thermal resistance (χ parameter) is assumed to be linearly proportional to particle diameter and inversely related to thermal conductivity based on a semi-empirical solution by Sullivan and Sabersky, where these dependencies are further investigated in following researchers to capture the effective conductivity better for discrete particles [43] and the influence of radiation potentially. Because the channel width isn't incorporated in the Sullivan-Sabersky correlation, the 6 datasets obtained by varying the widths appear distinct where larger channel width results in smaller $\overline{Nu}_d$ values. This is because $\overline{Nu}_d$ is solely affected by the heat transfer coefficients and therefore sustains a similar trend in Fig. 6.3(b).

Fig. 6.6(c) shows that, the correlation proposed by Muzychka et al. [67] performs well to capture the dependencies of both channel length and width, suggesting that the continuum solution is effective to capture dependencies of geometric parameters in terms of dictating the thermal entrance length and the boundary layer. Since particle size is neither included in the hydraulic diameter based Nusselt number and the Graetz number, the datasets for various particle sizes do not collapse well (deviation up to 40.9%). This deviation is smaller for the particle size range between 0.2 mm and 0.4 mm (deviation up to 18.5%). This is because larger particle size ($d_p > 0.4$ mm) has a more significant impact on the solid volume fraction and heat transfer for the flowing particles, as depicted in Fig. 6.4(d) and Fig. E.4. This underscores the discrepancy between the continuous fluids and the discrete particles for heat exchange. The more distinct deviation of particle size in Fig. 6.6(a) is enlarged by particle size ($\propto d_p^2$) in the form of the modified Péclet number. Similar to Fig. 6.6(b), the datasets in Fig. 6.6(c) don't collapse very well mainly for the different thermal conductivities modeled, but

the correlation predictions and our model predictions match well within 15% deviation for $k_s = 0.5$ W/m/K. This is consistent with the findings from Ho and Albrecht [203], and also additionally by Watkins and Gould's measurements [68] as the conductivity used is 0.2–0.6 W/m/K. However, Muzychka's correlation shows significant deviation for other collected thermal conductivities. This is mostly because the correlation was derived from a continuum model for traditional fluids, whereas the near-wall effect for particle flow largely reduced the heat transfer coefficients and results in significant overestimation of $\overline{Nu}_{D_h}$ for the correlation. This finding indicates that, unlike traditional fluids, the discrete nature of particles requires considering thermal conductivity in a different manner. Overall, these two correlations can only predict either length or width dependence using W^2L^{-1}, but not for particle size, conductivity and solid volume fraction.

6.3.3 New Péclet and Nusselt Number and their Correlation

In addition to the data presented in Fig. 6.2–6.6, extensive DEM simulations were conducted to systematically investigate a broader parameter space including variations in width, length, conductivity, particle size and solid volume fraction, as well as non-baseline combinations of these parameters. Based on the conclusion drawn from Fig. 6.6, attempts to project multivariate parameter data onto two existing state-of-art correlations yield widely scattered results without discernible trends. To address this limitation, this study introduces an approach to directly incorporate width and length dependencies from the Graetz number correlation, and more importantly expand the functional forms to explicitly account for the effects of particle diameter,

particle conductivity and solid volume fraction.

$$
\begin{aligned}
Pe_{\text{new}} &= Pe_L \left(\frac{W}{L}\right)^2 \left(\frac{k_s}{k_g}\right)^{c_1} \left(\frac{d_p}{W}\right)^{c_2} \phi_s^{c_3} \\
Nu_{\text{new}} &= Nu_L \left(\frac{W}{L}\right) \left(\frac{k_s}{k_g}\right)^{c_4} \left(\frac{d_p}{W}\right)^{c_5} \phi_s^{c_6}
\end{aligned}
\tag{6.1}
$$

The proposed formulation, as shown in Eq. (6.1), defines the new Péclet number as a product of the original Pe_L with four dimensionless parameters — width-to-length ratio, the particle-to-gas conductivity ratio, the particle-size-to-width ratio and the solid volume fraction. The scaling exponents for these parameters are constrained as: a fixed value of 2 for the first term, and variables c_1, c_2, c_3 for the subsequent terms, determined through an optimized support vector machine regression (SVR) framework with physical constraints. An analogous formulation is developed for the new Nusselt number, and the corresponding exponent is a fixed value of 1 for the leading term and variables c_4, c_5, c_6 for the remaining parameters. The optimization procedure initializes all six exponents at unity and constrains them within the physically meaningful bounds of [0, 5] to ensure solution robustness.

Fig. 6.7 presents the relationship between the newly defined Nusselt number and Péclet number derived from our multivariate DEM simulation data. The dataset comprises 135 distinct cases encompassing systematic variations in: three channel lengths (0.1, 0.2. 0.5), four channel widths (5, 6, 8, 10), six particle diameters (0.2, 0.3, 0.4, 0.6, 0.8, 1.0) and seven thermal conductivities (0.05, 0.1, 0.2, 0.5, 1, 2, 5). The new Péclet number and the new Nusselt number are dictated by the exponents obtained from the nonlinear SVR regression optimization. Fig. 6.6 demonstrates the performance of SVR with employing different regularization parameters – box constraint of 0.5, 1.2, 1.5. The model with the weak regularization (box constraint = 0.5) failed to find optimal exponent values, yielding poor data collapse with an R^2 value of 0.73204 while maintaining exponents near their initial values of unity. En-

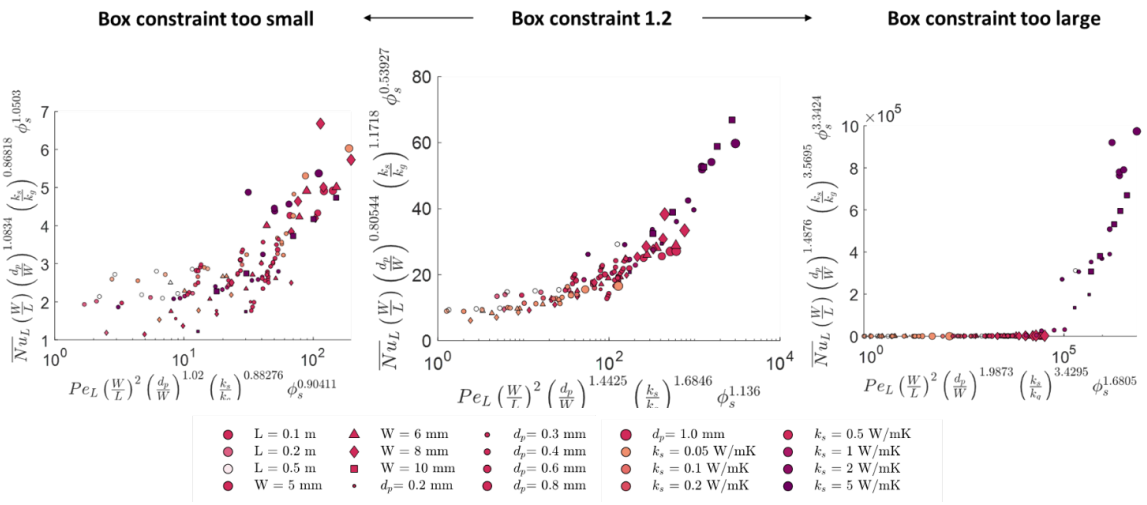


Figure 6.7: The new Nusselt number, $\overline{Nu}_{\text{new}}$ with respect to the new Péclet number, $Pe_{\text{L,new}}$, including a dimensionless width to length ratio, W/L, with power of 2, a diameter to width ratio, d_p/W, a conductivity ratio, k_s/k_g, and a solid volume fraction with exponents obtained from nonlinear regression (Eq. (6.1)); the legend is shown as well.

hanced regularization (box constraint = 1.2) significantly improved the data collapse, achieving an R^2 value of 0.904 with optimized exponents: $c_1 = 1.442$, $c_2 = 1.685$, $c_3 = 1.136$ for Péclet number and $c_4 = 0.805$, $c_5 = 1.172$, and $c_6 = 0.539$ for Nusselt number. Further increasing the box constraint to 1.5 marginally improved the fit ($R^2 = 0.9253$), but produced unrealistically large dimensionless numbers due to exponent overfitting. Alternative linear and nonlinear regression methods were explored but they did not surpass the R^2 value of nonlinear SVR optimization or produce Nusselt numbers within an acceptable range without overfitting.

Therefore, the optimal scaling exponents for the modified Péclet number and Nusselt number are selected based on a box constraint of 1.2, representing an optimal balance between data correlation quality and prevention of overfitting. As displayed in Fig. 6.8, the new dimensionless number demonstrates satisfactory performance, with majority of data exhibiting a consistent trend. Both dimensionless numbers exhibit strong positive correlation with increasing width-to-length ratio, particle-size-to-width ratio, and solid volume fraction, following their respective power-law

relationships. The conductivity ratio plays the most significant role in enhancing the new Péclet number and Nusselt number with $c_2 = 1.685$ and $c_5 = 1.172$. This dominant effect is visually apparent in the clear left-to-right color gradient corresponding to increasing conductivity values.

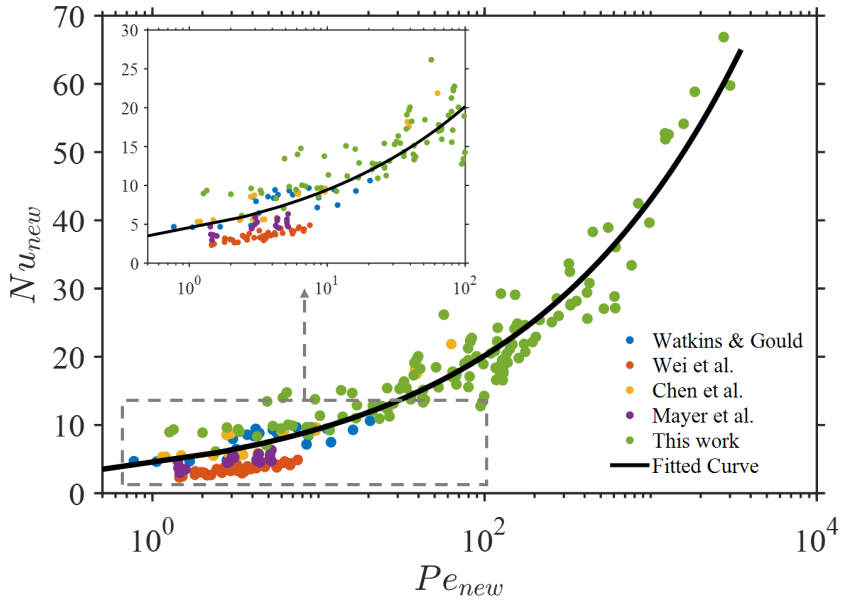


Figure 6.8: Comparison of simulations data from this work with four sets of experimental data from other papers for particle-based heat exchangers under the proposed new Péclet number $Pe_{\mathrm{L,new}}$ and new Nusselt number. A zoom in plot is included to show the detailed information. The fitting curve is $\overline{Nu}_{\mathrm{new}} = 4.42 Pe_{\mathrm{new}}^{0.3295}$.

To validate the proposed dimensionless numbers based on DEM simulations, Fig. 6.8 compares our simulated data with four experimental studies of moving bed particle flows [68, 70, 75, 204], which were conducted under different geometric configurations and particle properties. Overall, the range of new Péclet number for our data is larger than majority of experimental data since we explore a broader parameters space, particular in shorter channel length ($L = 0.1$ m) and relatively higher flow velocities (0.5–9 cm/s). Despite the extended coverage, both experimental and simulated data points exhibit a consistent trend when plotted using the new Péclet and Nusselt numbers, even though the experimental data were excluded from the regres-

sion training. The unified correlation is generated based on the new Péclet number and Nusselt number as $\overline{Nu}_{\text{new}} = 4.42Pe_{\text{new}}^{0.3295}$ with a R^2 value of 0.904. The new Nusselt numbers of our data are slightly larger than the experimental measurements, where most of their solid volume fractions of granular flows are lower than our simulated results. Although the dependence of solid volume fraction has been included, deviation for large solid volume fractions still have some impact. Among the four experimental groups, Chen et al. and Watkins et al. have better alignment with our new dimensionless numbers with an R^2 value of 0.8596 and 0.7660, respectively. Compared to them, Mayer et al. and Wei. et al. have smaller new Nusselt numbers for most of their data. This is potentially due to the degraded performance of heat exchangers and the low operating temperatures and temperature differences as mentioned in their work separately. The root mean square error (RMSE) for this work is larger than that of all the experimental datasets, because our dataset covers a much larger range of new Nusselt numbers up to 70, and all the experimental datasets only cover up to about 20.

To further test the robustness of the proposed correlations, additional simulation were performed for unexplored parameters both within the range (for example, $k_s = 0.6$), and extending beyond the range (for example, $k_s = 6$). Although these data were not included in the training process, they show good alignment with proposed correlations. This new Péclet and Nusselt number correlation can be used to provide design insights for enhancing a particle-based heat exchanger with a design case. The optimized parameters are calculated using the correlations by varying one for each time while fixing all the other parameters to be the baseline value shown in Table 6.1. For velocity, length and particle size, they are feasible to be changed to reach a higher heat transfer coefficient. For width, conductivity and solid volume fraction, they either reach an unreasonable number or optimized values can not be obtained under the constraint of current correlations. Therefore, to double the heat transfer

Table 6.3: Optimized multi-design parameters including length, velocity, width, particle size and conductivity simultaneously for the target heat transfer coefficient of 600 W/m^2/K.

Length L (m)	**Velocity u (m/s)**	**Width W (m)**	**Particle diameter d_p (m)**	**Conductivity k_s (W/m/K)**
0.3023	0.0616	0.0037	0.0005	4.3729
0.3024	0.0604	0.0270	0.0005	4.3438
0.3029	0.0441	0.0015	0.0004	4.7331
0.3199	0.0720	0.0015	0.0005	2.4367
0.3201	0.0928	0.0016	0.0007	2.6922
0.3427	0.0867	0.0015	0.0005	1.1548
0.4363	0.0454	0.0072	0.0002	3.4394
0.4513	0.0984	0.0179	0.0005	3.4956
0.4805	0.0875	0.0055	0.0004	3.4000
0.9737	0.0619	0.0337	0.0001	4.1598

coefficient from 300 to 600 W/m^2/K, either increase the velocity from 1.042 to 8.546 cm/s, or decrease the length from 0.5 to 0.06 m or decrease the particle size from 0.3 mm to 0.0368 mm as shown in Table 6.3. These are extreme conditions since only one parameter are optimized each time. If multiple parameters are optimized simultaneously, the heat transfer coefficient can be improved in without such big changes for each of parameters.

Overall, the new Péclet and Nusselt number correlation is versatile to offer quick estimation and prediction for moving-bed particle heat exchanger with the combined effects of Width, W, length, L, particle size, d_p, thermal conductivity, k_s, and solid volume fraction, ϕ_s, considered. Additionally, this could be a standardized matrix to make comparison between different experimental setups. This correlation is based on the closed form equation, offering rapid heat transfer estimation with convoluted geometric and thermophysical properties design for a moving bed heat exchanger.

6.4 Conclusion

Our study presents a comprehensive investigation of the effects of multivariate parameters on the flow dynamics and heat transfer of moving bed flow of particles. Compared to prior literature, we additionally include the effects of solid volume fraction directly into our new developed, modified Nusselt-Péclet correlation. Notable highlights include: (a) investigating heat transfer in dense moving bed flows using discrete element method (DEM), capturing the discrete nature of particle dynamics and heat transfer mechanisms, including conduction and radiation, (b) exploring a wide range of geometric and thermophysical parameters, including channel length, width, particle size, thermal conductivity and solid volume fraction, providing insights into their individual and combined effects on heat transfer performance, and (c) designing a novel dimensionless correlation, incorporating geometric ratios, particle properties and solid volume fraction, which provides a unified framework for predicting heat transfer in moving bed systems.

Models are developed and applied for a gravity-driven, dense, moving beds of particles to perform parametric explorations to predict particle-to-wall heat transfer coefficients. Under a same mass flow rate, increasing the channel length diminishes the overall heat transfer coefficient between walls and particles, allowing the moving bed flow to achieve fully thermal development. For the longest channel modeled in this study ($L = 0.5$ m), the solid volume fraction distribution indicates an periodically increasing trend along the flow direction, due to the increased compression from the total mass of particles and the complex inter-particle collision and friction effects. These results underscore the discrete nature of the particle flow and disclose the limitation of applying continuum based models. Increasing channel width also lowers the particle-to-wall heat transfer coefficient due to the decrease of the area to volume ratio for heat transfer to occur. Consistent with our previous research that radiation has a minimal effect on the overall heat transfer in the dense moving bed

flow, this study finds the contribution of radiative heat transfer is with 2.5%, for the particle thermal conductivity varying from 0.05 to 5 W/m/K, with a particle size of 0.3 mm. However, it is noticeable that the radiative effect is no longer negligible when the particle diameter is large. For instance, the contribution from radiation mechanism increases to nearly 10% when the particle size increases to 0.8 mm. Solid volume fraction is a parameter that has been considered significant in heat transfer for moving bed flow but insufficiently investigated. In this study, a broad range of solid volume fraction ($\phi_s = 0.54$–0.63) is applied to moving bed modeling by adjusting the input friction coefficients in DEM simulator. The results presents the sensitivity of the tested solid volume fraction range on the overall heat transfer coefficient, which varies from 790 to 980 W/m^2/K. A collection of 39 distinct datasets with different parameters of length, width, particle size and thermal conductivity are transformed to compare with the Nusselt number and Graetz number correlation, that is mostly commonly used by the community. The comparison shows the merits and limits of the state-of-the-art correlations and requires researchers to improve the scaling for some parameters, especially for thermal conductivity, particle size and solid volume fraction. Based on these investigation and more extensive DEM simulations, our study generated a modified non-dimensional Nusselt and Péclet number, along with a correlation between them through a support vector regression optimization approach. The quality of the correlation is validated by comparing with experimental data from prior work. Except for data measured under rather low temperatures, our correlation shows good alignment with experimental results. The results suggest pathways to enhance heat exchanger performance, such as optimizing particle size, flow velocity, and channel geometry, with potential to double heat transfer coefficients from 300 to 600 W/m^2/K under specific conditions.

On the whole, this research develops a comprehensive heat transfer correlations to incorporate multivariate effects from geometric setup and particle thermophysical

properties. Model predictions are further interpreted to provide strategic pathways for design, operation and material selections to achieve optimal heat transfer performance.

CHAPTER VII

Conclusion and Future Work

This dissertation focuses on radiative transport in particulate media and heat transfer in moving bed of particles. The investigations presented in this dissertation are processed through modeling approaches. The results of these simulations aim at demonstrating the characteristics of the static and dynamic multiphase systems operating under high temperatures. Consequently, key contributions of this work include (1) the development of a generalized expression to correlate quantified spatial arrangement of particles to radiative behaviors in particulate medium, and (2) disclosing the conductive and radiative heat transfer behaviors in particle flows under the influence of multiple geometrical and thermophysical properties, respectively.

7.1 Summary & Research Contributions

7.1.1 Radiative Transport in Static Particulate Media: Effects of Spatial Arrangements

Despite the significance of solid volume fraction for dependent scattering in particulate media, the influence of spatial distributions of the particles has not been investigated. In Chapter 3, we examine the influences of the three-dimensional spatial distributions and the solid volume fraction of particles on radiative transport, and quantify the resulting deviations from the independent scattering assumption.

Compared to prior studies, a contribution of this work is applying an index of cluster sampling–a spatial statistical approach previously used in geology and biology, to quantify the 3-D spatial distribution of particles. Results reveal that the radiative transmittance and the extinction coefficient are strongly influenced by the spatial distributions of the particles, in addition to the solid volume fraction. For the first time, we have developed a generalized correlation that predicts scale factors as a function of the index of cluster sampling, which is dictated by the spatial distributions and the solid volume fractions of the particles. Overall, this study provides a computationally efficient approach to determine effective radiative properties while accounting for dependent scattering effects, and are expected to be applicable in multiphase flows with solid particles.

7.1.2 Flow and Heat Transfer in Moving Bed Heat Exchangers

In solar receiver, particle flows form as a curtain with decreasing dilute concentration, capturing heat from concentrated solar energy. Chapter 4 presents the flow regime of a particle curtain flow using DEM simulations. Calibrated by identifying the coefficient of static friction between particles, simulation results for both particle diameters of 1 mm and 2 mm gave equivalent mass flow rates and decreasing solid volume fraction distributions to the experimental results, which are obtained through a thermopile detector and a high-speed camera. A key outcome of the research is the derivation of a new scale factor dependent on particle reflectivity, which leads to significantly improved agreement between experimental and simulated results. This provides a simple, closed-form equation to transform measured transmittance to a solid volume fraction while accounting for particle reflectivities.

Moving bed flow can be found in particle-based heat exchangers, playing an important role in energy and catalysis applications. In Chapter 2, a comprehensive discrete particle tracking flow model is fully coupled with conductive and radiative heat

transfer. A plug flow model and a gravity-driven dense moving bed model are used in Chapter 5 to systematically investigate the interdependent of flow regime dependent parameters and thermophysical particles properties. To generalize and broaden the applicability of our results, a dimensionless Nusselt number is calculated to evaluate its thermal performance, and its dependence on solid volume fraction (0.02 – 0.55) is established. These results reveal the high sensitivity of the overall Nusselt number to even small changes in solid volume fraction in the dense flow regime, particularly for high-conductivity alumina particles. In contrast, the radiative Nusselt number only gradually changes and asymptotically approaches a limit for large solid volume fractions.

7.2 Limitations & Future Work

7.2.1 Radiative Transport in Static Particulate Media: Effects of Spatial Arrangements

In Chapter 3, the optimal cell size for calculating *ICS* values is selected under a uniform and fixed size of 0.25 mm. In practical applications, ensembles of particles always have a size distribution. It is necessary to evaluate the influence of size distribution on the selection of the optimal cell size in future, to help broaden the application of our generalized radiation-spatial correlation. Ordered beds with perfectly negative correlations in the spatial positions of the particles exhibit a more discrete interaction of radiation with the ensemble as compared to the other spatial distributions. This phenomenon can differ for other types of unit packing, such as body-centered cubic and hexagonal close packing. Future investigations can be evaluating the scattering effects on these different ordered packing structures (e.g., quantify extinction coefficients for each structure). The current generated correlation is solely bridging the radiative transmittance and the particle spatial distributions. Future work will focus

on extending the correlation to link other radiative heat transfer properties, such as absorption, extinction, scattering coefficients, with spatial arrangements of particulate media. Several thermal conductivity correlations are successfully applied in the CSP community. However, these correlations rely on many assumptions and empirical parameters. For example, the ZBS model treats the radiation thermal conductivity based on a cubic particle arrangement assumption. In future, our research can derive correction factors to accurately fill the gap between the cubic ordered packing and a more realistic packing structure to improve the radiation thermal conductivity correlations.

7.2.2 Flow and Heat Transfer in Moving Bed Heat Exchanger

The DEM modeling tool used in Chapters 5 and 6 to study the flow and heat transfer behavior has limitations. Due to the implementation of solid-fluid-solid conduction and radiation solvers, the computational cost increases significantly with the number of particles modeled. This restricts the maximum number of particles for radiation-included DEM modeling to be within 1 million, which is not enough to directly model a lab-scale moving bed flow experiment and requires assumptions to reduce the modeling domain as described in Chapters 5 and 6. Future work is necessary to improve the computational efficiency, especially for radiative heat computing. The computational overhead for computing radiation using iterative method can be reduced by restricting the parallel communication within neighboring particles. An alternative method would be applying GPU acceleration techniques for more efficient parallelization.

In Chapter 5, the plug flow and the moving bed model has difficulties to cover the solid volume fraction range between $\phi_s = 0.48$–0.55. Therefore, the amplification for solids with large thermal conductivity of the dependence of the Nusselt number on solid volume fraction is lack of investigation. Future work is needed to collect

data within this range by applying different contact models for the plug flow to decrease the frictional effect on the flow velocity. The newly generated Nusselt-Péclet number correlation in Chapter 6 is obtained by assuming thermal conductivity to be temperature independent. Future investigations are required to evaluate the prediction variation of this correlation due to temperature dependence. In Chapters 5 and 6, opposing effects of particle size are predicted on conduction and radiation, depending on the solid volume fraction in the plug flow regime. Future investigations could include modeling particle flows with bi-distribution. Small-sized particles can improve the conductive heat transfer through elevated solid volume fraction and reduced near-wall region thickness, while large-sized particles can increase the radiative heat transfer when operating at high temperatures.

APPENDICES

APPENDIX A

Chapter 2: Validations for Radiative and Heat Transfer Models for Discrete Particles

A.1 Collision MCRT Simulation Validation

The collision MCRT simulation code was validated by comparing with the published data from Singh and Kaviany [22]. To perform this validation, packed beds are generated by introducing random perturbations to particle centers in a simple cubic packing unit cells as detailed by Singh and Kaviany [22]. Transmittance is obtained for four different solid volume fractions with a particle reflectivity of 0.7. Model results for transmittance match with Singh and Kaviany's data within 0.1%, 1.1%, 9.4% and 19.9% for solid volume fraction of 0.008, 0.065, 0.268 and 0.524 at the optical thickness of 3.146.

The setting of the bed structure is duplicated except that the bottom surface is denoted as reflective one where rays interacting with it will pass through and be counted as reflective rays. It appears to be a perturbed random bed where random perturbations are introduced to the centers of particles. The particulate media is considered more reflective and the reflectivity of the particles were set to be $\rho_p = 0.7$.

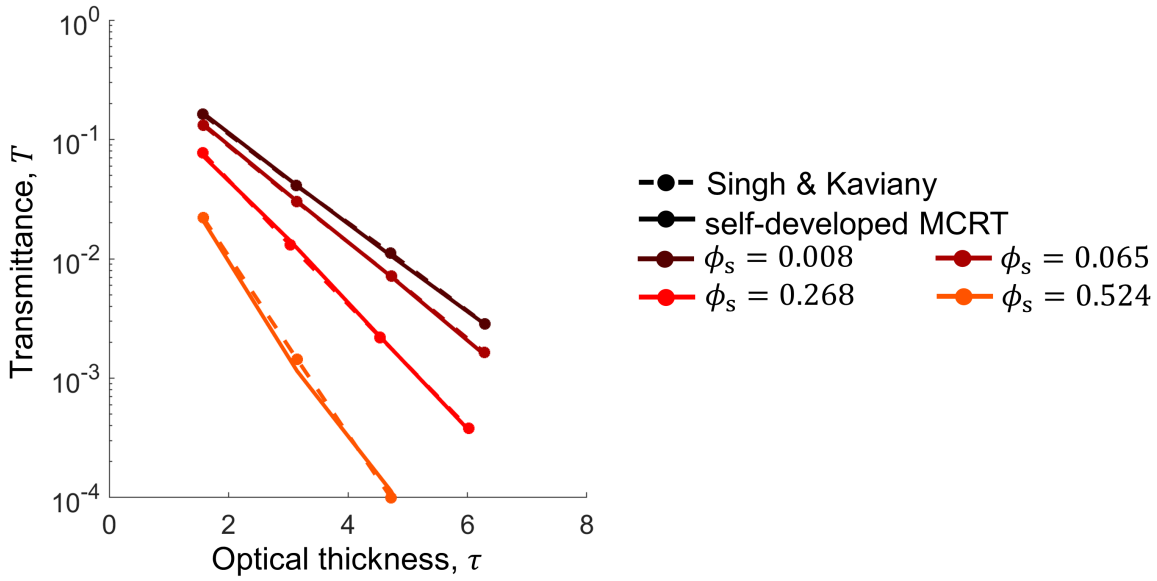


Figure A.1: Comparison of the transmittance result from Singh and Kaviany's data (dashed lines) with simulation code. Comparison of transmittance of Singh and Kaviany's data for perturbed random beds using collision-based ray tracing simulations for specularly reflecting opaque particles with reflectivity, $\rho_p = 0.7$

Four solid volume fractions are selected ranging from $\phi_s = 0.008$ to $\phi_s = 0.524$. By running the Monte Carlo ray tracing simulation using the self-developed code, a validation comparison is given in Fig. A.1.

A.2 Validation for Radiative View Factor Correlations with Monte Carlo Ray Tracing Simulations

Fig. A.2 shows the validation for radiation model by comparing Monte Carlo ray tracing simulation with our radiative view factor correlations for the snapshot of plug flow model after reaching steady-state. The distribution for particle temperature and heat flux for bed with solid volume fraction of 0.02 and 0.43 is shown in (a), (b) and (c), (d).

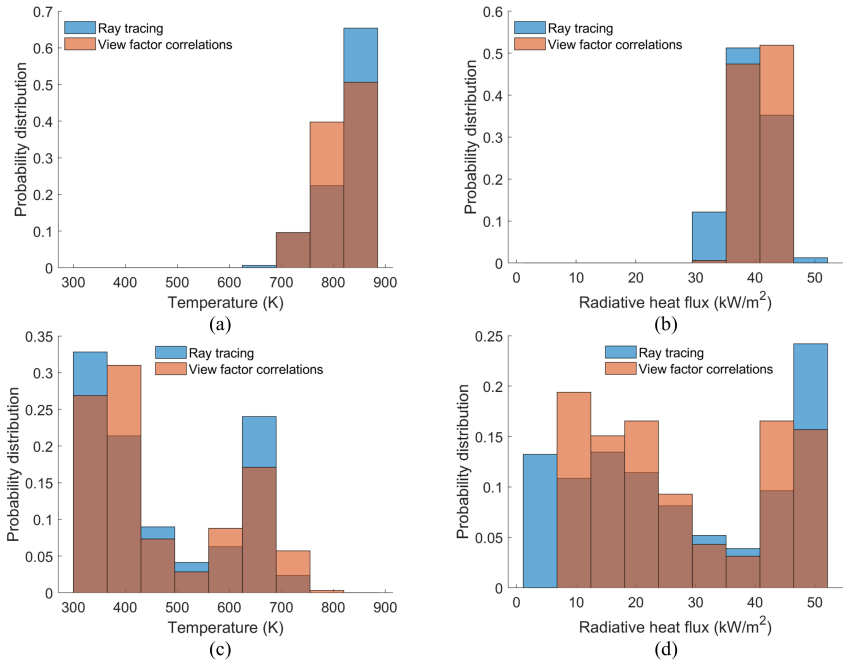


Figure A.2: The radiation model is validated by comparing Monte Carlo ray tracing simulations with our radiative view factor correlations in terms of the probability distribution of particle temperature ((a), (c)) and the probability distribution of net heat flux received by particles ((b), (d)); suspended particle beds are heated for 5 physical seconds at solid volume fractions of 0.02 ((a), (b)) and 0.43 ((c), (d)) respectively.

A.3 Sensitivity Study of Computational Cost and Performance Evaluation Related with Radiation Time Step

A range of radiation-to-flow time step ratios ($\Delta t_{\text{rad}}/\Delta t_{\text{flow}}$) from 1 to 10,000 was selected to evaluate the computational cost and performance as shown in Fig. A.3. The plug flow model with $\phi_{\text{s}} = 0.07$ running for 5 physical seconds is used for this evaluation. With the increase of radiation-to-flow ratio, the computational cost decreases from nearly 2 hours to 2 minutes; while the relative error for the average temperature of all particles in the flow chamber increases up to 0.58%. It is noticeable that when the radiation-to-flow ratio exceeds 1,000, the decrease of computational cost starts to level off and the increase of the computed relative error becomes more significant. Therefore, a radiation time step that equals 1,000 particle flow time step

is considered to retain both low cost and high accuracy for particle flow simulations and implemented in this study.

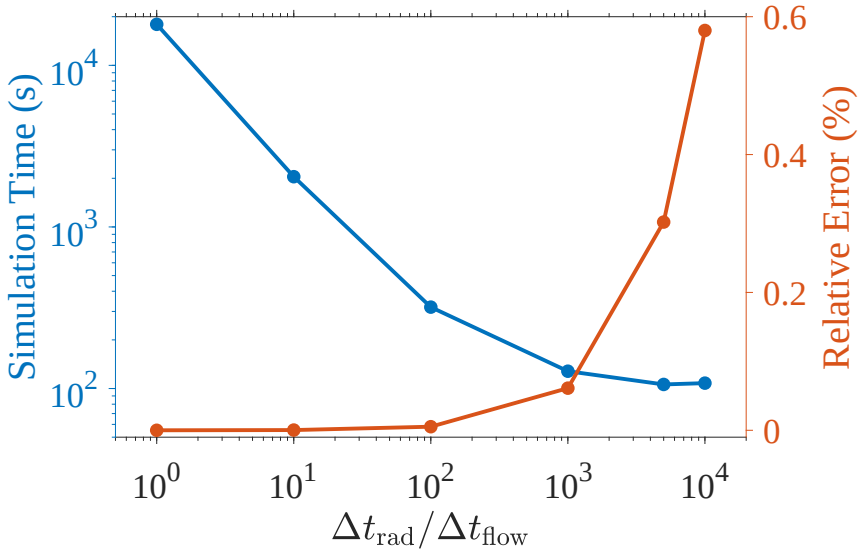


Figure A.3: The computational cost for performing a simulation of plug flow model with $\phi_{\mathrm{s}} = 0.07$ for 5 seconds, and the relative error for the average particle temperatures as an influence of radiation-to-flow time step ratio.

APPENDIX B

Chapter 3: Effects of Spatial Correlations in Particulate Media on Dependent Scattering and Radiative Transport

B.1 *ICS* Calculation Example

An *ICS* calculation example for a two-dimensional (2-D) with Poisson, ordered and clustered distributions are presented in Fig. B.1. A total number of 64 two-dimensional particles with a fixed diameter $d_p = 0.45$ mm were generated inside a square of size 8 mm. To compute the *ICS* value, the 8 mm sized domain was divided into 16 square cells. The mean value and variance for the frequency distribution were calculated for these three spatial distributions of particles. The *ICS* index was computed according to Eq. (3.4). From the results in Fig. B.1, ordered distribution has a negative *ICS* value. Poisson distribution results in $ICS = 0$, indicating complete spatial randomness in particle distribution. Clustered distribution gives a positive *ICS* value.

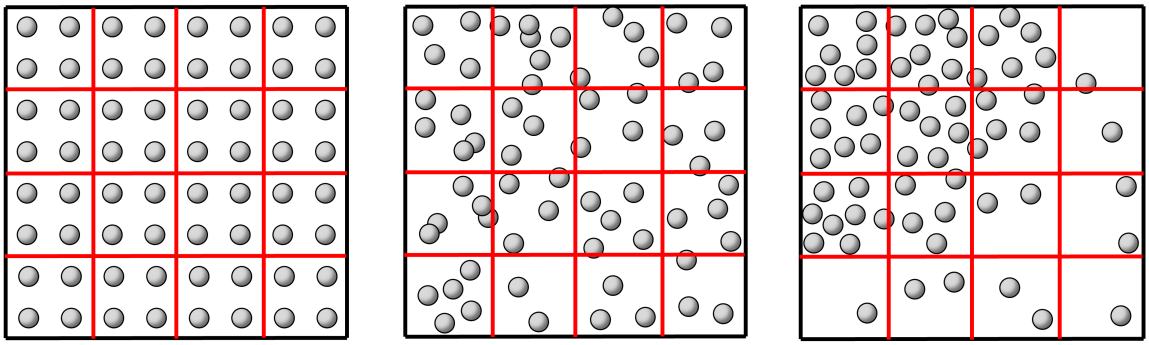


Figure B.1: Two-dimensional (a) ordered, (b) Poissonian, (c) cluster example of quadrat method calculation in a surface of 8 mm × 8 mm with 64 particles with a diameter of 0.45 mm inside, and the area is uniformly divided into 16 quadrat with each size of 2 mm × 2 mm. The red lines indicate the divide of cells in domain. Mean value and variance of the frequency and the calculated ICS value are listed.

B.2 Transmittance versus Optical Thickness for Ordered Beds

Fig. B.2 presents the radiative transmittance as a function of optical thickness specifically for ordered beds with all solid volume fractions ranging $\phi_s = 0.05$–0.50. The results indicate that at $\phi_s = 0.05$–0.35, there is a marginal decrease of transmittance at fixed optical thickness. For higher solid volume fraction ($\phi_s = 0.35$–0.50), transmittance does not continue to decrease with it.

Fig. B.3 shows the tentative fitting results for the ordered beds. Both simple exponential and bi-exponential functions were implemented to fit the MCRT results for the ordered beds. The simple exponential function resulted in deviations up to 95% for transmittance at large optical thicknesses ($\tau > 2$). The bi-exponential function yielded a good fit, which restricted the maximal deviation within 1%. However, there is no physical explanation to justify this bi-exponential function.

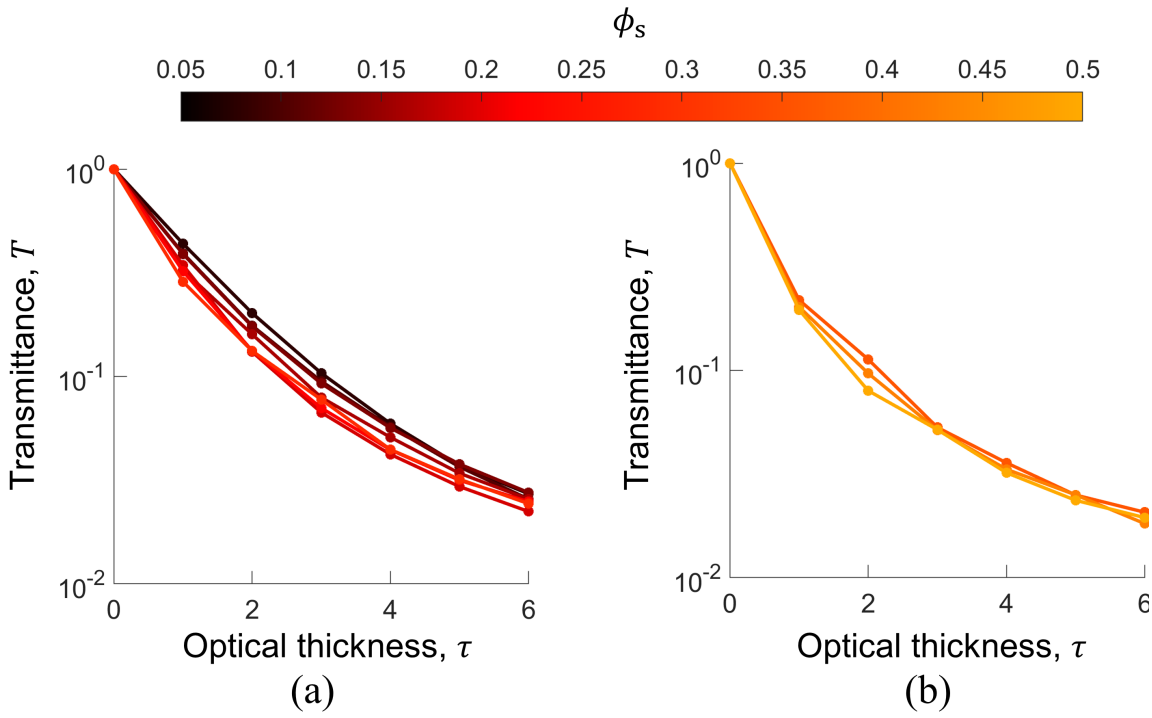


Figure B.2: Transmittance, T, as a function of optical thickness, τ, for ordered bed at solid volume fraction ranging (a) $\phi_s = 0.05$–0.35, and (b) $\phi_s = 0.35$–0.50.

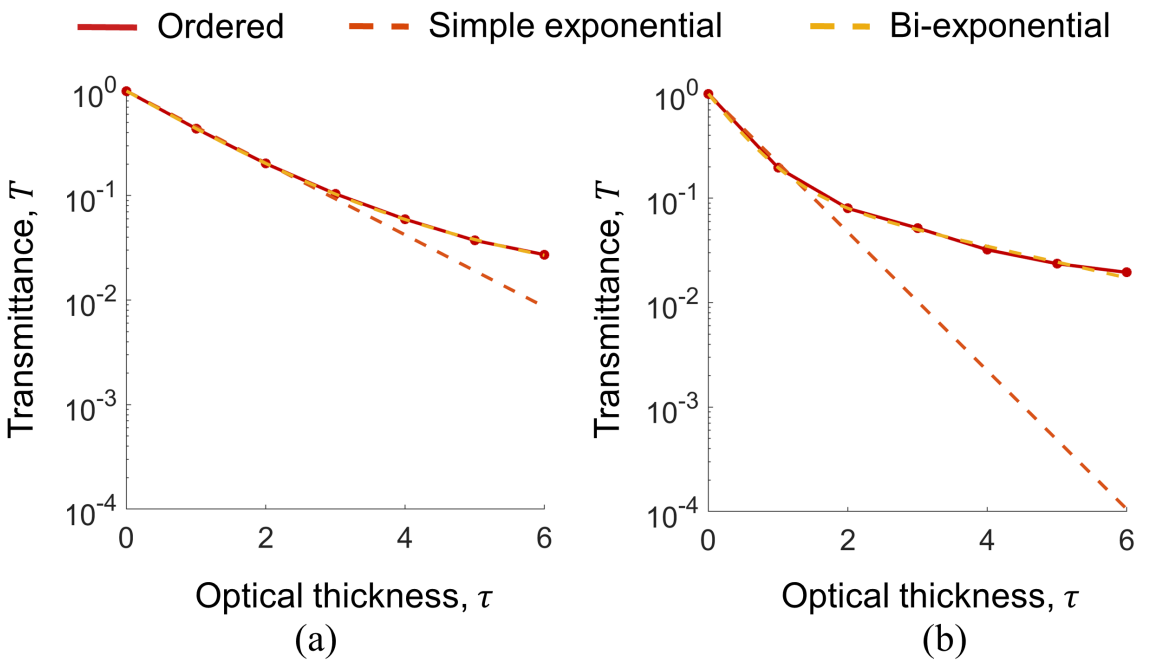


Figure B.3: Transmittance, T, as a function of optical thickness, τ, for ordered bed at solid volume fraction (a) $\phi_s = 0.05$, and (b) $\phi_s = 0.50$. Fitting results of simple exponential and bi-exponential functions (Eqs. (3.12) and (3.13)) are presented with dashed-lines.

B.3 Dependence of Particle Reflectivity on Transmittance

To determine the general relationship between transmittance and optical thickness defined based on the effective extinction, i.e. $\tau^* = \beta z$, where β is the effective extinction coefficient of a medium, we performed path-length ray tracing simulations. We analyzed several cases of particle specular reflectivity values, which are essentially the same as the scattering albedo value for the medium for larger and opaque particles. Path-length simulations were performed using the algorithm shown in Fig. 2.3. The results are compared with a simple exponential decay function, $\exp(-\tau^*)$, as shown in Fig. B.4(a). In all our calculations, we assumed a fixed particle specular reflectivity of 0.7, and for this case (i.e., scattering albedo of $\omega = 0.7$), the average relative error between path length results and the simple exponential decay is 10%, while for $\omega = 0$ and 0.99 the average relative error is at 54% and 83% respectively. Therefore, based on a specific scattering albedo $\omega = 0.7$, the rate of change of $\log(T)$, where, T is radiative transmittance, with optical thickness, τ^*, is nearly 1 and a simple exponential fitting function will be applicable to obtain fitted values for the extinction coefficients.

The relationship between m, which quantifies the rate of change of $\log(T)$ with optical thickness, τ^* (Eq. (B.1)), and the scattering albedo of the medium was determined from the results obtained in Fig. B.4.

$$m = \frac{d(\log(T))}{d\tau} \tag{B.1}$$

By fitting the m values as a function of ω, we obtain a best-fit function, which results in an R^2 value of 0.98 (Eq. (B.2)).

$$m = a\sqrt{1-\omega}, \quad a = 1.416 \tag{B.2}$$

There is precedence to this non-linear dependence of m on ω from the two-flux ap-

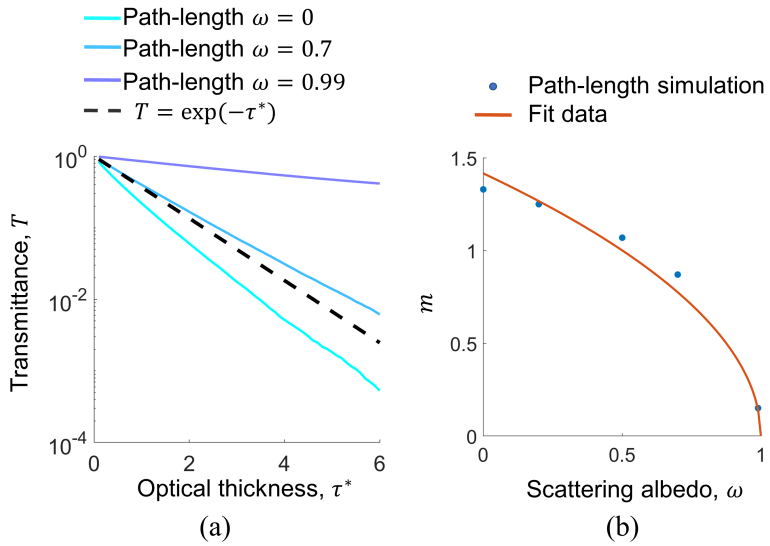


Figure B.4: (a) Path-length ray tracing simulations for media of scattering albedo at $\omega = 0$, 0.7 and 0.99. A simple exponential function is plotted as a comparison with path-length results. (b) m value in Eq. (3.11) computed from path-length simulation as a function of particle reflectivity ρ_p and a fit curve obtained from Eq. (B.1).

proximation for scattering media subjected to diffuse incident flux [110, 133]. Eq. (B.3) shows the closed-form analytical solution to the two-flux approximation of the radiative transport equation in a 1-D, isotropically scattering medium.

$$T = e^{-2\sqrt{1-\omega}\tau} \tag{B.3}$$

The two-flux theory assumes no angular dependence of radiative intensities in the upper and lower hemispheres to arrive at a simplified and tractable pair of differential equations for the radiative transport equation (Eq. (1.1)). To arrive at the closed-form solution for the radiative transmittance as shown in Eq. (B.3), we apply pertinent boundary conditions needed for our simulations, and simplify complex bi-exponential terms that appear in the analytical solutions deduced by Weston et al. [133]. This closed-form solution was also verified by numerically solving the bivariate boundary value problem. For the sake of brevity, these mathematical details have been excluded, but the authors can willingly provide more information to the

interested reader.

B.4 γ–*ICS* Fitting Results with cell size of 0.51 mm

ICS values are strongly affected by the cell size used to determine the frequency distributions. To get the best fit for correlating *ICS* and the scale factors, the cell size was selected between the two limits (0.25 mm $< a_{\text{cell}} <$0.51 mm). The upper limit for a cell size of 0.51 mm is twice the interparticle spacing for a simple cubic packing of the particles in the ordered beds with $\phi_s = 0.5$. Table B.1 presents the calculated *ICS* results under this cell size. Compared with data in Table 3.3, results with a larger cell size have much higher *ICS* values for all cluster beds, while slightly smaller for random beds. Poisson and ordered beds *ICS* values does not change significantly with varied cell sizes.

Fig. A8 represents the γ–*ICS* fitting result under the cell size of 0.51 mm. The scale factors are correlated to the *ICS* values using a cubic polynomial given by Eq. (B.4). The quality of the fitting decreases significantly. The Spearman's test indicates that correlation strength between the scale factor and *ICS* values decreases from 0.99 to 0.96 when excluding the ordered bed points. These results all further reiterate that the fitting quality is higher for cell size equals 0.35 mm than 0.51 mm.

$$\gamma = 0.0012(ICS)^3 + 0.025(ICS)^2 - 0.24(ICS) + 0.86 \tag{B.4}$$

B.5 Additional Results for Angular Distribution for Transmission, $p(\theta_t)$

Except for the fact that the peak value of angular distribution is relatively higher than the one from Fig. 3.6 in the main paper, the general trend is similar for both

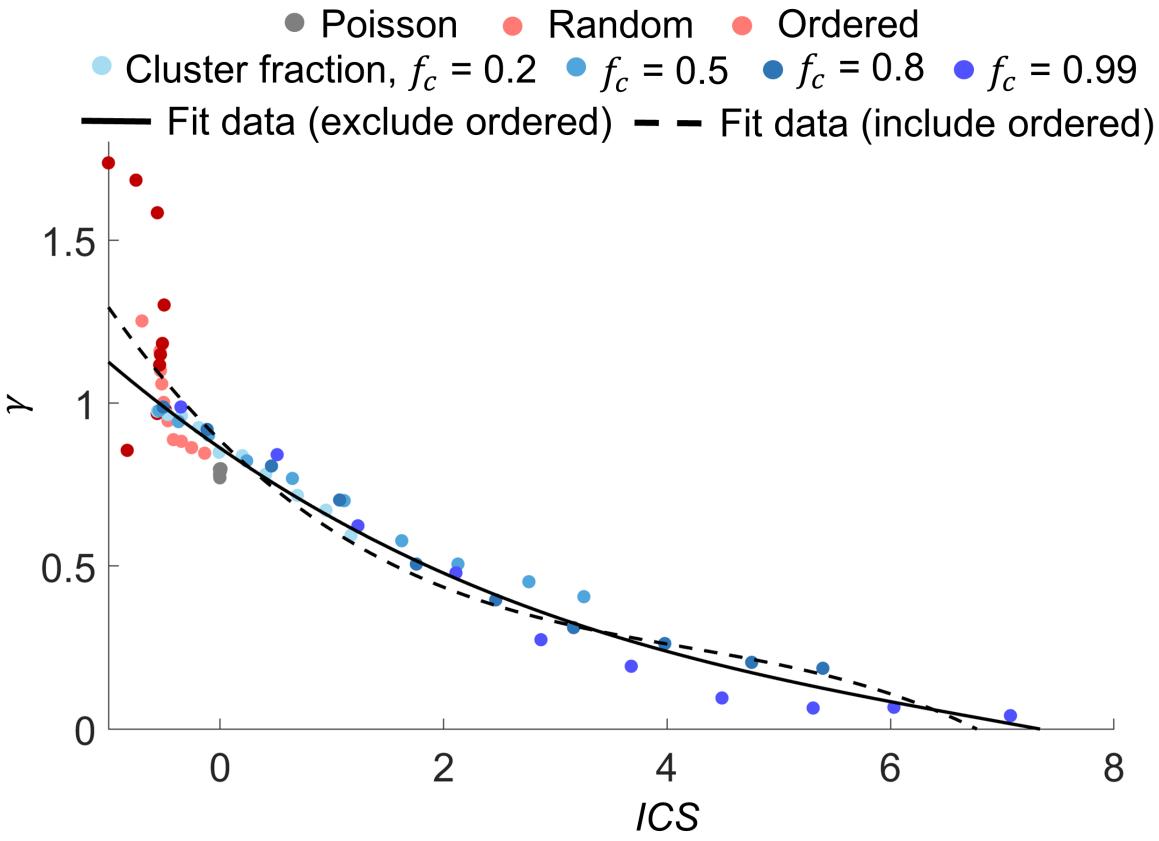


Figure B.5: Scale factor, γ, (ratio of effective extinction coefficient obtained from the ray tracing simulation to the one predicted by independent scattering theory) as a function of the *ICS* values for the Poisson, random, ordered and cluster beds with cluster fractions of 0.2, 0.5, 0.8 and 0.99. The solid and dashed lines are the best-fit, cubic polynomials obtained by excluding and including the data points for the ordered bed respectively.

Table B.1: Computed *ICS* values with a fixed cell size of 0.51 mm for the various spatial distributions and solid volume fractions considered for the packed beds.

Solid Volume Fraction	**Poisson**	**Random**	**Ordered**	**Cluster beds with varying cluster fraction**			
				$f_c = 0.2$	$f_c = 0.5$	$f_c = 0.8$	$f_c = 0.99$
0.05	0.0039	−0.14	−0.83	1.17	3.26	5.39	7.07
0.1	−0.0062	−0.26	−0.56	0.95	2.76	4.76	6.03
0.15	−0.0014	−0.35	−0.49	0.69	2.13	3.98	5.30
0.2	−0.0052	−0.42	−0.53	0.41	1.63	3.16	4.49
0.25	0.0069	−0.47	−0.54	0.20	1.11	2.47	3.68
0.3	0.0015	−0.51	−0.52	−0.01	0.65	1.76	2.87
0.35	−0.0043	−0.52	−0.50	−0.19	0.24	1.07	2.11
0.4	−0.0043	−0.53	−0.56	−0.35	−0.10	0.46	1.23
0.45	−0.0027	−0.54	−0.75	−0.47	−0.37	−0.12	0.51
0.5	0.0001	−0.70	−1.00	−0.56	−0.55	−0.51	−0.35

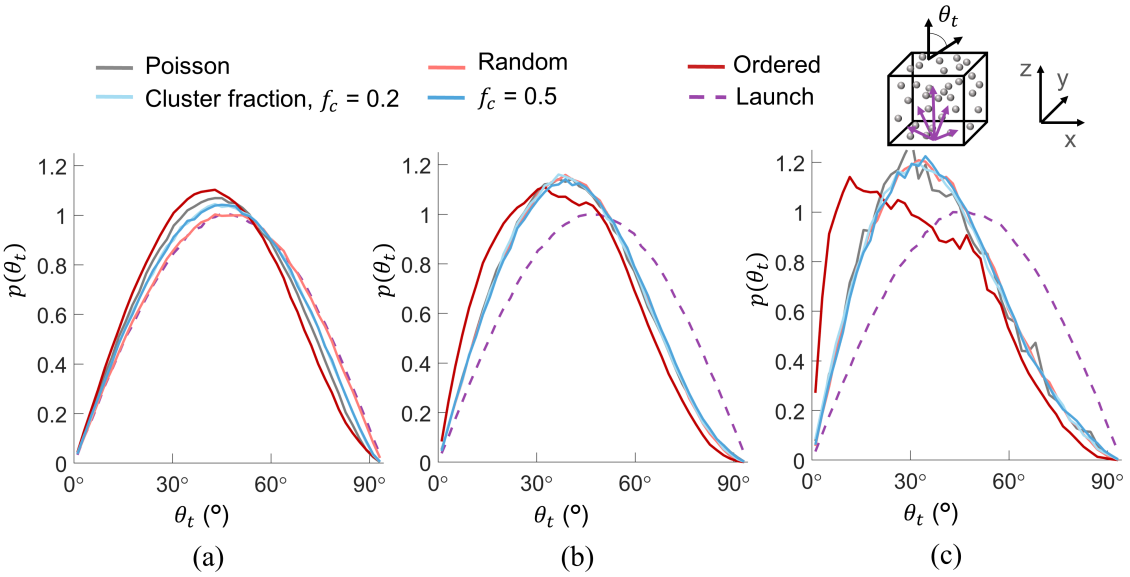


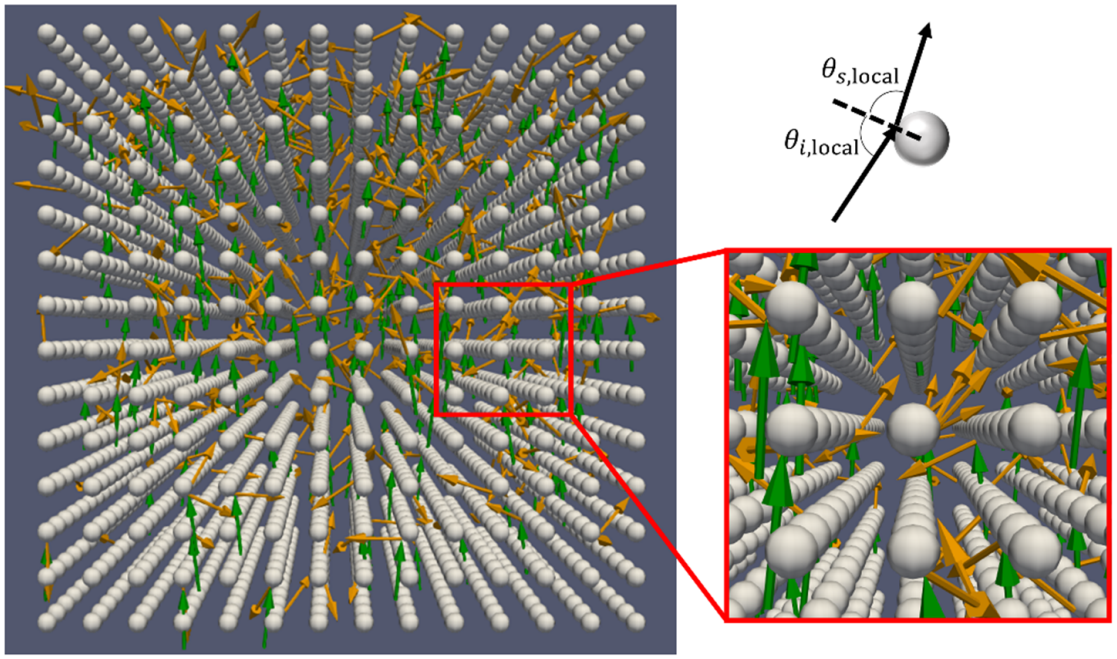
Figure B.6: Probability density function of transmitted angle for Poisson bed, random bed, ordered bed and cluster bed with cluster rate of 0.2 and 0.5 with volume fraction fixed at $\phi_s = 0.20$ and with radiative transmittance of (a) $T = 0.9$, (b) $T = 0.42$ and (c) $T = 0.1$. Ray-tracing modeling domain shown in Fig. 3.1(c,d) with particle diameter of 0.25 mm and particle reflectivity of 0.7 was used to perform collision MCRT simulations. The dashed line is the probability density function of launching angle at the lower surface. The schematic in the legend depicts the diffuse distribution of the launched rays (purple rays at $z = 0$) and the polar angle, θ_t, measured for a transmitted ray to obtain $p(\theta_t)$ as explained in Table 3.2.

solid volume fractions. This is because with higher solid volume fraction, scattering events are more frequency, resulting in more rays getting transmitted at smaller polar angles.

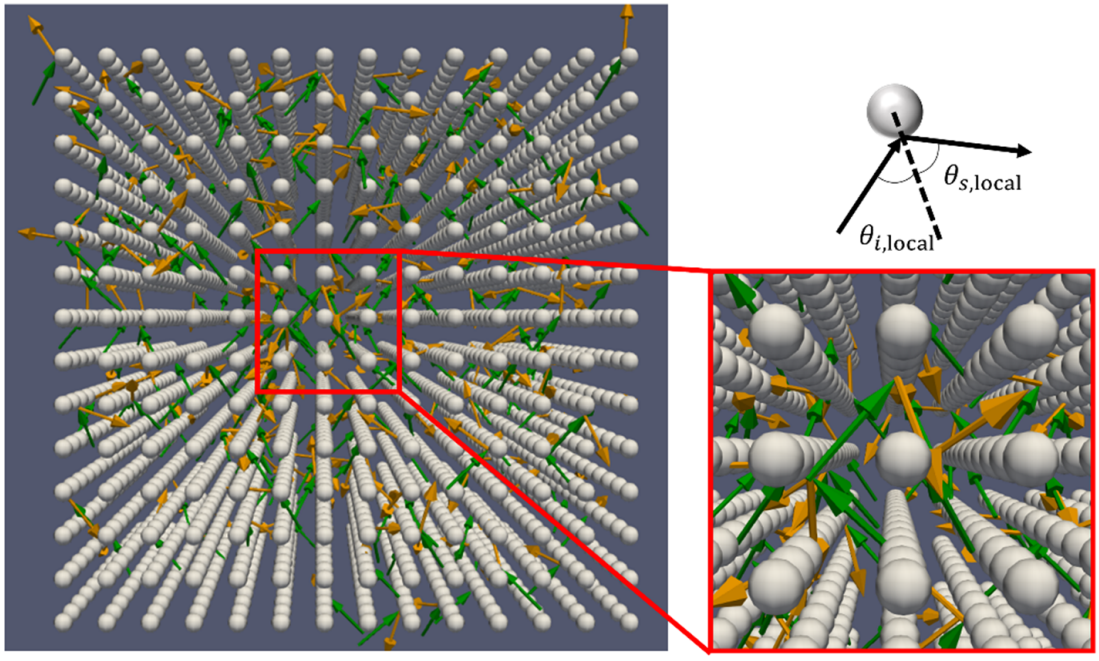
B.6 Additional Results for Scattering Phase Function

Fig. B.7 shows the visualization of scattering in the ordered bed. The results in the main draft (Fig. 3.7) shows that ordered beds exhibit anisotropic scattering. For the case of low solid volume fraction, largest anisotropy in scattering is observed for incident angles that are either closely parallel or antiparallel (i.e., $\theta_i \in [0°, 10°)$ and $[170°, 180°]$), or, when nearly perpendicular ($\theta_i \in [80°, 100°]$) to the z-axis. In Fig. B.7(a), where incident rays are closely parallel with the global z-axis ($\theta_i \in [0°, 10°)$), scattered rays have more forward scattering ($\theta_s \in [0°, 90°)$). For an incident rays ranging in $\theta_i \in [40°, 50°)$ as is shown in Fig. B.7(b), scattered rays have more random distributed orientation, indicating isotropic scattering. The comparison between the zoom-in subplots under these two different incident ranges shows that rays with incident angle, $\theta_i \in [0°, 10°)$, has more forward scattering than the one with $\theta_i \in [40°, 50°)$, which corresponds to the outcome in Fig. 3.7.

Fig. B.8 shows the scattering phase function versus the angle between incident and scattered directions. The results for all beds except the ordered one at high solid volume fraction, indicate isotropic scattering. For the ordered bed at $\phi_s = 0.5$, rays are more likely to be incident on particle surfaces with a large local incident angle, which renders more rays scattered forward. Though it is common in the literature to report scattering phase functions as it depends on the angle between the incident and the scattering ray, this functional form loses information on how scattering occurs as a function of the incident angles. Therefore, in the main paper, we have reported the scattering phase function dependencies on both the incident and the scattered angles, as measured with respect to the z-axis. Both these functions point toward



(a)



(b)

Figure B.7: Visualization of scattering in the ordered beds with solid volume fraction of $\phi_s = 0.05$ considering incident angle, (a) $\theta_i \in [0°, 10°)$, and (b) $\theta_i \in [40°, 50°]$. Incident, θ_i, and scattered, θ_s, polar angles are defined with respect to the global z-axis. The green arrow indicates the incident ray and the orange arrow indicates the scattered ray.

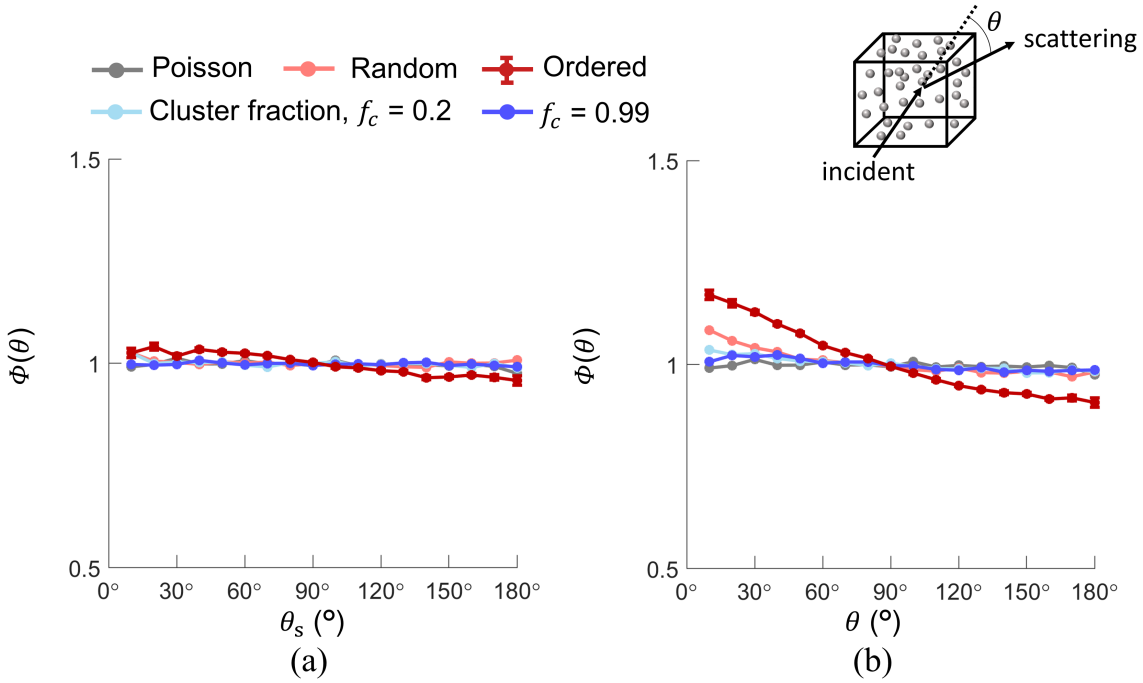


Figure B.8: Scattering phase function, $\Phi^*(\theta^*)$, based on the angle, θ^*, between incident and scattering ray for Poisson, random, ordered and cluster beds with solid volume fractions of (a) $\phi_s = 0.05$ and (b) $\phi_s = 0.5$. Same ray-tracing modeling domain shown in Fig. 3.1(c,d) with particle diameter of 0.25 mm and particle reflectivity of 0.7 was used to obtain the angle between incident and scattered rays. Angle θ^* vary from 0°–180° with statistics obtained for $\Phi^*(\theta^*)$ with a bin size of 10°. The x-axis indicates rays that are scattered with angular intervals for θ^* of [0°,10°),[10°,20°) up to [170°,180°].

increasing anisotropy in the ordered beds with increase in solid volume fraction, with a preference for forward scattering of incident rays in an ordered medium.

APPENDIX C

Chapter 4: Flow Modeling to Characterize Solid Volume Fractions in Gravity-Driven Particle Curtains

C.1 Experimental Setup for Particle Curtain Flow

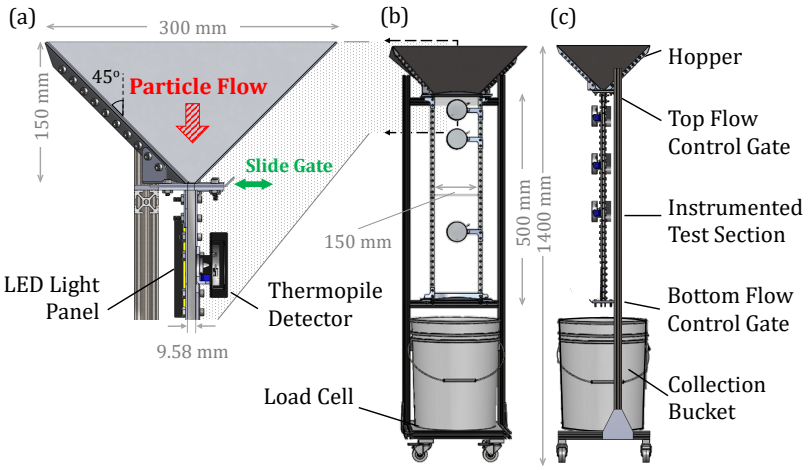


Figure C.1: Lab-scale flow chamber for gravity-driven particle flow experiments. (a) Cross-sectional detail view of the hopper and the top slide gate. (b) Front view of flow chamber. (c) Side view of the flow chamber.

Particle curtain tests were conducted using a laboratory-scale flow chamber (Fig. C.1). The chamber was fabricated from a combination of off-the-shelf and custom-fabricated sheet metal parts. It consists of a frustum-shaped hopper with 45° walls that feeds particles through a 7.5 mm × 150 mm discharge slot into a 9.58 mm × 150 mm × 500 mm channel, which constrains the width of the curtain. Manual slide gates at the top and bottom of the channel allow flow to be controlled, while transparent acrylic windows along its sides allow optical access. A load cell mounted under the collection bucket at the channel base provides mass flow data as a function of time and is used to find the mass flow rate.

Commercially available, highly spherical porcelain particles from Raytech Industries [205] were used for all experiments. These have bulk density of $\rho_p = 2650$ kg/m^3 and were obtained in nominal sizes of 1 mm and 2 mm diameters. Their average size and size distribution differ somewhat from those specified by the manufacturer; the 1 mm particles have an average diameter $d_p = 1.23$ mm and are normally distributed with standard deviation $\sigma_d = 0.1$ mm, while the 2 mm particles have an average diameter $d_p = 2.18$ mm and are normally distributed with $\sigma_d = 0.1$ mm. The average diameter was determined by taking an arithmetic mean of a sample of particle diameters. The size distribution of particles was quantified using image processing techniques. Tests were conducted with small batches of particles at a time, at steady mass flow rates. The flow rates were measured with an iW-8x8-10M-DI-1000U load cell from Loadstar Sensors [206]. The duration of each test was 25 to 35 seconds.

C.2 Sensitivity of DEM results to particle size distributions

Fig. C.2 shows the predicted solid volume fraction as a function of height for a monodisperse particle size distribution compared against the normal size distribution. Note that the critical timestep of the DEM simulation is directly proportional to the minimum particle diameter. Therefore, this critical time step is reduced by 23% for

the monodisperse simulations. The results show that, for both sizes of particles, the difference between predictions computed using the monodisperse and normal distributions at each height is within 5%. This validates the choice of using a uniform particle size obtained from the mean value of the measured size distributions for all subsequent DEM simulations in this study.

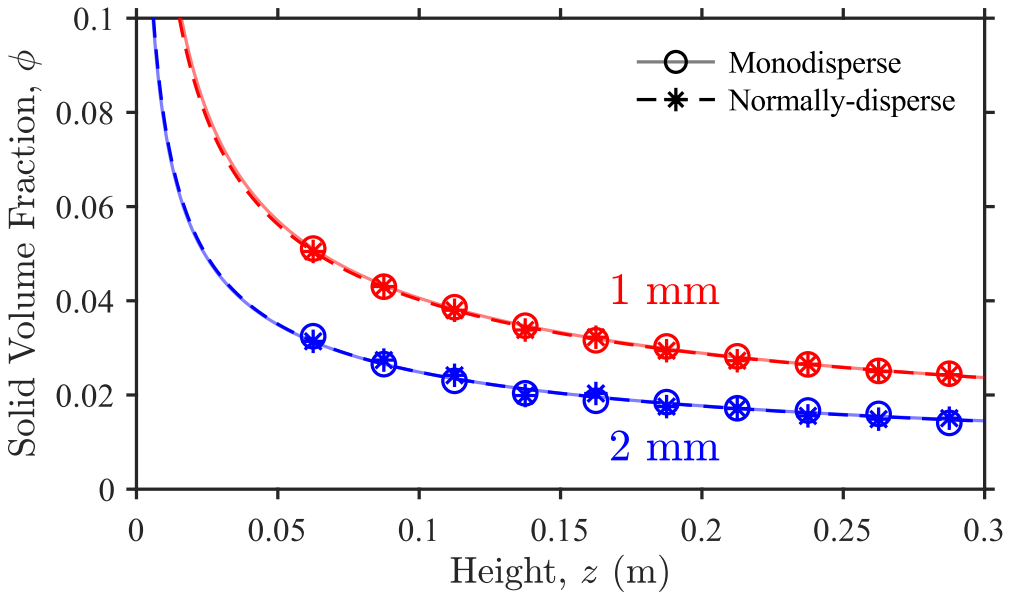


Figure C.2: DEM modeling results for solid volume fraction as a function of height for 1 mm and 2 mm particles with mono- and normally-dispersed size distributions. Plotted lines represent the power law curve fits to data points. In all cases, the monodisperse results show good agreement with the normally-dispersed results.

APPENDIX D

Chapter 5: Conductive and Radiative Heat Transfer Mechanisms Inform Nusselt Number Dependence on Solid Volume Fraction for Granular Flows

D.1 Comparison with Semi-empirical Correlation from Sullivan and Sabersky

Fig. D.1 exhibits the Nusselt number dependence on Péclet number for both moving bed model and plug flow model, compared with the semi-empirical correlation from the previous work of Sullivan & Sabersky [43]. Radiative effects are not considered in the correlation, and only conductive heat transfer is modeled in these simulations. In addition, only mustard seed particles (identical with the material tested in the experiment of Sullivan and Sabersky) are used in this comparison, because the correlation has not yet been confirmed applicable for high-conductivity materials (alumina) [75]. As it is shown from Fig. D.1, the Sullivan and Sabersky's correlation underestimates for the moving beds results with a solid volume fraction

of $\phi_s = 0.55$, and would presumably correspond to a flow with a solid volume fraction between $\phi_s = 0.45$ and $\phi_s = 0.55$. This is because the solid volume fractions measured in Sullivan and Sabersky's experiment are relatively low for a packed flow ($\phi_s = 0.39 - 0.41$). It should be noted that, unlike the Sullivan and Sabersky's correlation, the Nusselt number decreases when Pe_L^* exceeds 600. This plateau and even decrease phenomenon has been captured by the experimental results from Patton et al. and Natarajan et al. [44, 45] after the same modified Péclet number. This comparison further underscores the significance of solid volume fraction on the heat transfer for particle flows.

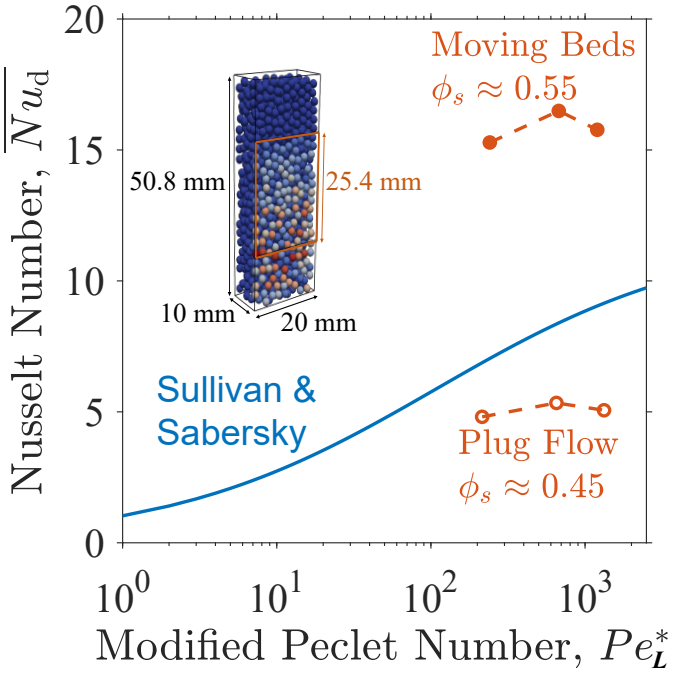


Figure D.1: Nusselt number dependence on Péclet number based on the moving beds ($\phi_s \approx 0.55$) and the plug flow model ($\phi_s \approx 0.45$), and comparison with the semi-empirical correlation from Sullivan and Sabersky's work, where the particles flow through a 20 mm × 10 mm × 50.8 mm channel region with a heating plate in the length of 25.4 mm.

D.2 Particle Size Effect Analysis

To draw insights on the trends of particle size, we conducted further analysis for interpreting conductive heat transfer and radiative heat transfer correspondingly.

Particles are classified as being present in one of two regions — (1) the near-wall region, which includes all particles with their centers located within a width of the particle radius, r_{p}, from the heating walls, and (2) the bulk region, which includes the rest of the particles in the domain (Fig. 5.4(a)). Spatial positions of particles are recorded over a flow time of 1 s (collected from 100 time steps). The total estimated contact area includes the the particle-particle surface area ($\propto N_{\mathrm{bulk}} d_{\mathrm{p}}^2$) in the bulk region and the average contact area between the particles and the walls, which is proportional to the average number of particles in the near-wall region ($\propto N_{\text{near-wall}} d_{\mathrm{p}}^2$). For all solid volume fractions, this total estimated contact area decreases with particle size (Fig. 5.4(b)). This trend correlates with the decreasing conductive heat-transfer coefficients with particle diameter.

To understand the trend better for radiative heat-transfer coefficient with respect to particle size, the view factor matrices used for radiative fluxes calculations are recorded over a flow time of 0.1s (collected from 10 time steps). The averaged wall to all the particles view factors are calculated for different particle sizes (Fig. 5.4(c)). For low solid volume fraction of 0.07, the view factor decreases with particle size as shading effect is minimal for this case and the trend is driven by the beneficial surface area for smaller particle size. For high solid volume fraction of 0.25 and 0.43, the view factor increases and plateaus. This is the competing outcome of beneficial surface area and stronger shading effect for smaller particle size. These view factors determine the radiative fluxes but the radiative heat-transfer coefficients are also affected by conduction. For high solid volume fraction of 0.25 and 0.43 with diameter of 0.4mm, the conduction is strong enough to increase average particle temperature, and therefore decrease temperature difference between walls and particles. This makes

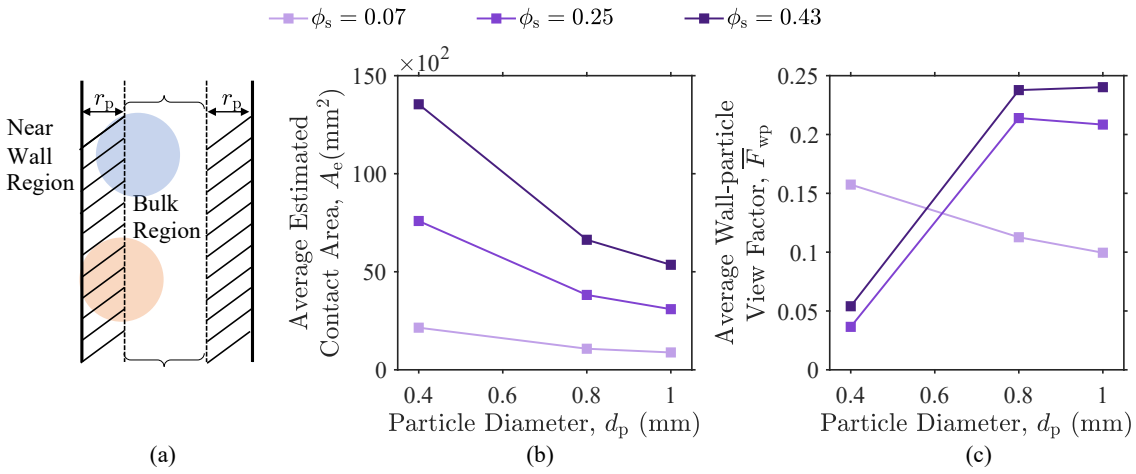


Figure D.2: (a) Schematic for the near-wall region or bulk region; (b)average estimated particle-particle and particle-wall contact area and (c) average wall-particle view factor for different particle diameter.

the radiative heat-transfer coefficient increase, so the heat-transfer coefficients are barely changed with particle size for high solid volume fractions.

Fig. D.2 shows the convoluted influence of particle size, solid volume fraction under the same Péclet number of $Pe_L = 660$ but different mass flow rate. Compared to Fig. 5.4 that is presented under the same mass flow rate, we can conclude that, though absolute values can be different, the trends and interpretations in Sec. 5.3.1 are unchanged.

D.3 Curve-fitting Equations for the Correlation between Nusselt Number and Solid Volume Fraction

The best-fit curves for the overall and radiative Nusselt number as a function of solid volume fraction in Fig. 5.6 are obtained by fitting the plug flow model data, using an exponential and logarithmic dependence for conductive and radiative heat transfer respectively. These two equations both yield R^2 values above 0.99. The fitted equations are shown in Eqs. (D.1) and (D.2) for alumina particles and mustard seeds respectively.

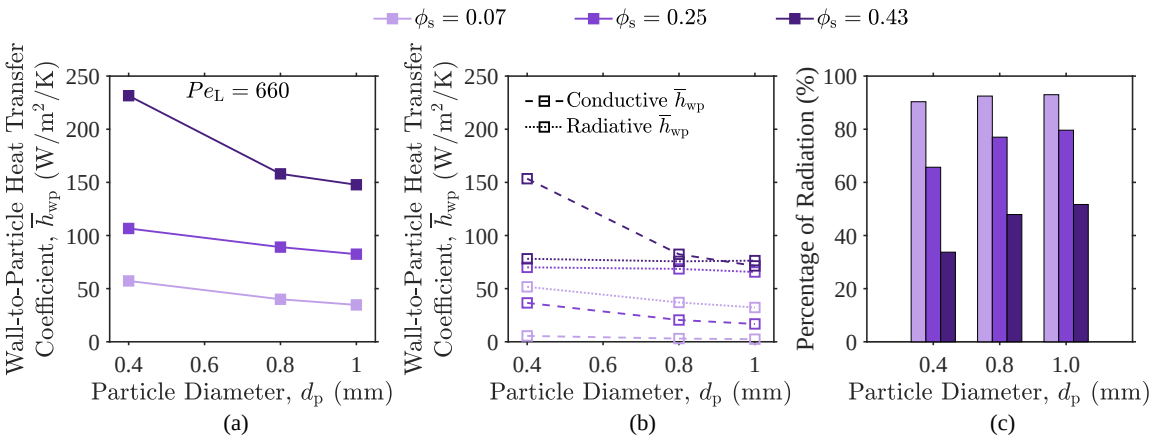


Figure D.3: Coupled effects of particle diameter, d_p, and solid volume fraction, ϕ_s, in the plug flow model ($\phi_s = 0.07, 0.25, 0.43$) at a constant Péclet number of $Pe_L = 660$ on (a) channel-average, wall-to-particle heat-transfer coefficient, $\overline{h}_{wp}$, (b) conductive and radiative heat-transfer coefficients, and (c) the percentage contribution of thermal radiation to the overall heat transfer.

$$\overline{Nu}_{d,\text{Alumina}} = \underbrace{0.11\exp\left(8.15\phi_s\right)}_{\text{Conduction}} + \underbrace{0.39\ln\left(227.80\phi_s\right)}_{\text{Radiation}} \tag{D.1}$$

$$\overline{Nu}_{d,\text{Mustard}} = \overbrace{0.087\exp\left(8.45\phi_s\right)} + \overbrace{1.64\ln\left(72.22\phi_s\right)} \tag{D.2}$$

APPENDIX E

Chapter 6: Discrete Element Modeling for Dense Moving Bed Heat Exchanger Informs Comprehensive New Nusselt-Péclet Number Correlations

E.1 Temperature Profile to Verify Fully Thermal Development

To verify whether the moving bed flow achieves fully thermal development, the non-dimensional temperature gradient, defined in Eq. (E.1), is presented in Fig. E.1.

$$\frac{\partial \theta}{\partial z} = \frac{\partial}{\partial z}\left(\frac{T_{p,0} - T_p(z)}{T_{p,0} - T_w}\right) \tag{E.1}$$

where θ is the non-dimensional temperature, T_w is the wall temperature that is constant at 300 K, $T_{p,0}$ is the inlet temperature of the particles entering the channel, which is at 1,000 K in this study. $T_p(z)$ is the average temperature of particles within a bin size of $\Delta z = 20$ mm along the flow direction at different heights. With the

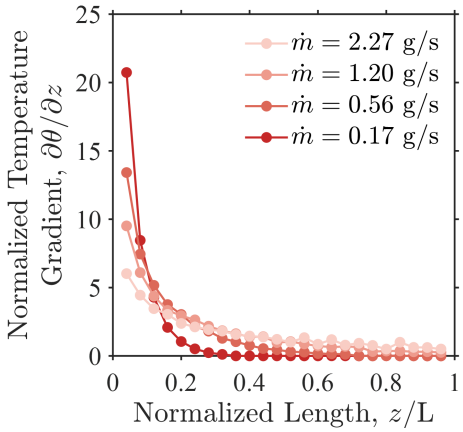


Figure E.1: The non-dimensional temperature gradient along the flow direction, $\partial\theta/\partial z$, as a function of the normalized length, z/L, with average temperatures of particles obtained with a bin size of 20 mm along the z dimension in a channel with $L = 0.5$ m at a mass flow rate of 2.27 g/s.

decrease of mass flow rate, the gradient of the normalized temperature approaches to 0 at a smaller normalized length, indicating the thermal entrance length is shorter. Fig. E.2 illustrates the thermal entrance length obtained from the DEM results with particle sizes varying from 0.4 to 0.6 mm. The thermal entrance length is determined as the height of the position that normalized temperature gradient less than 0.3 ($\partial\theta/\partial z < 0.3$). By comparing with the thermal entrance length given by Muzychka et al. [67], the results generally follow the prediction from the correlation at low flow velocity, with the relative error within 50%. This indicates the experience of predicting heat transfer using continuum assumption is still suitable for discrete particle flow.

E.2 The local profile for velocity

Fig. E.3 demonstrates that the oscillation of the solid volume fraction is strongly correlated to the combined effects of inter-particle collision and friction. This can be validated from the velocity profile (Fig. E.3(a)) obtained from a snapshot of the DEM simulation performed for a moving bed flow with a channel length of L = 0.1

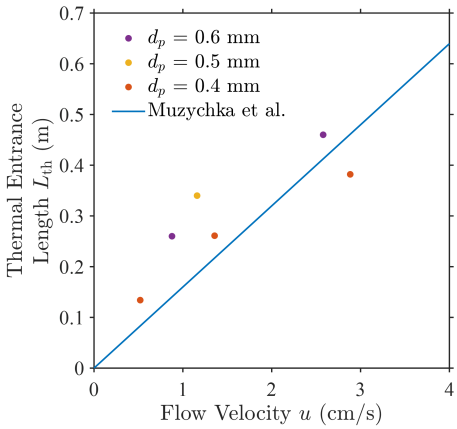


Figure E.2: The thermal entrance length, L_{th}, computed as the position that the $\partial\theta/\partial z < 0.3$, as a function of flow velocity, u, with the particle size varied from 0.4 mm to 0.6 mm; all results are obtained from snapshots that the moving bed flow achieving steady state.

m and a mass flow rate of $\dot{m} = 2.27$ g/s. Unlike a fluid-based plug flow where the velocity remains constant across the entire channel, significant velocity variations are observed at different z positions. Fig. E.3(b) shows the velocity increases along the flow direction and then abruptly drops. This is because the friction effects are not uniform and slow down only a portion of particles. This creates vacancies between particles, which reduces the solid volume fraction (Fig. 6.3(c)). However, the friction forces are insufficient to maintain this state, causing particles to accelerate under gravity until they are stopped by particles at lower heights, allowing the moving bed flow to return to a more densely packed morphology. Fig. E.3(b) shows that at different time, this velocity drop is not fixed at one location but transports to higher position. This behavior is found to be periodic when the channel length is at L = 0.5 m, which is not shown here due to the large aspect ratio.

E.3 Effects of Particle Size on Solid Volume Fraction

Fig. E.4 demonstrates the solid volume fraction decreasing with increasing particle size. The solid volume fraction decreases by 6.5% when the particle diameter increases

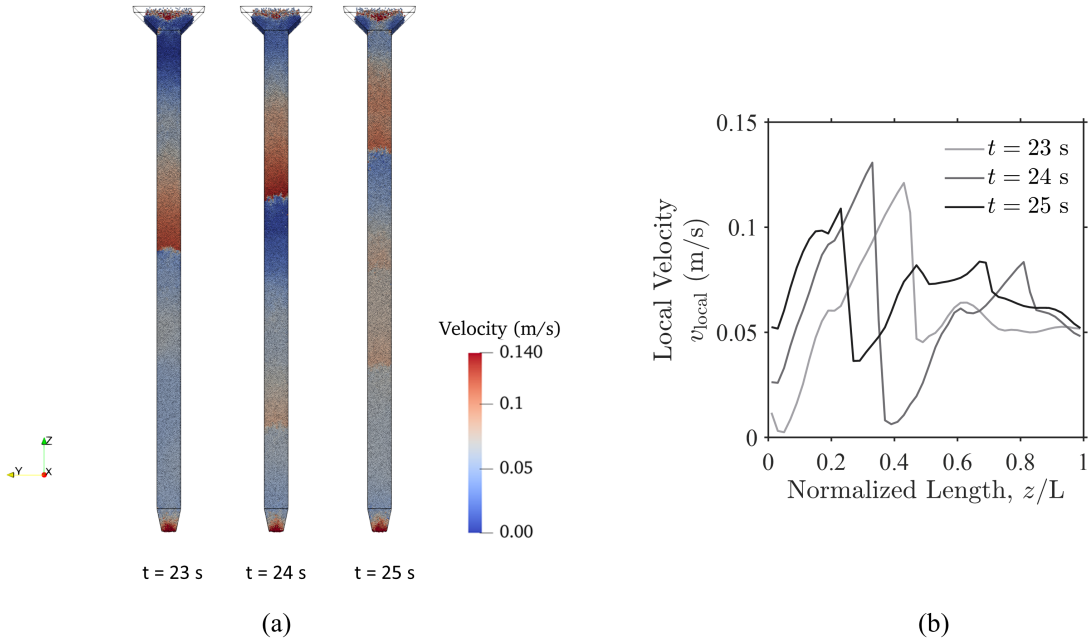


Figure E.3: In a moving bed flow with a channel length of L = 0.1 m and a mass flow rate of $\dot{m} = 2.27$ g/s, (a) the velocity profile obtained from snapshots of the DEM simulation at $t = 23$, 24, 25 s, which is already at a steady state, (b) the local velocity of particles as a function of the normalized length. The local velocity is obtained as the average velocity for particles within a bin size of 1 mm along the z direction.

from 0.3 mm to 0.8 mm, with the corresponding solid volume fraction in the near-wall region reduces by 3.53%. This is because the increase of the particle size results in more voids between the walls and particles, where the solid volume fraction is significantly lower than the one in the bulk region.

E.4 Effects of Rolling Friction on Flow Rate, Solid Volume Fraction and Heat Transfer Coefficient

Compared to static friction coefficient, Fig. E.5 shows that the rolling friction coefficient plays a less significant role in mass flow rate, solid volume fraction and heat transfer coefficient of the moving bed flow. This is because the relative rolling between particles and walls is very rare in a vertical channel setup. Generally, the increase of

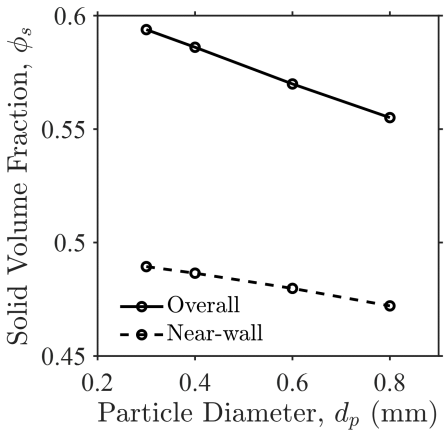


Figure E.4: The solid volume fraction averaged for particles in the entire channel and in the near-wall region, as a function of particle size, ranging from d_p = 0.3–0.8 mm, at a near-constant mass flow rate of $\dot{m} = 2.27 \pm 0.01$ g/s.

rolling friction coefficient for both particle-particle and particle-wall pairs diminishes the mass flow rate. This is consistent with the influence of static friction coefficient that plays as a resistance to the particle flow. However, the increase of particle-wall rolling friction coefficient would improve the packing of particles. This is mostly likely that rolling friction coefficient would help increase the adhesion between particles in the near-wall region and therefore elevate the overall solid volume fraction. This effect also contributes to an improved heat transfer coefficient for elevated particle-wall rolling friction coefficient.

E.5 Comparison with Nusselt Number correlation Based on Effective Thermal Conductivity

Fig. E.6 shows the Nusselt number plot with all thermal conductivity computed using the effective thermal conductivity instead of the bulk thermal conductivity. The effective thermal conductivities are obtained using the ZBS model. In Fig. E.6(a), the deviation between our simulated data and the correlation from the work of Sullivan and Sabersky is still very significant (up to 280%), indicating the dependency of solid

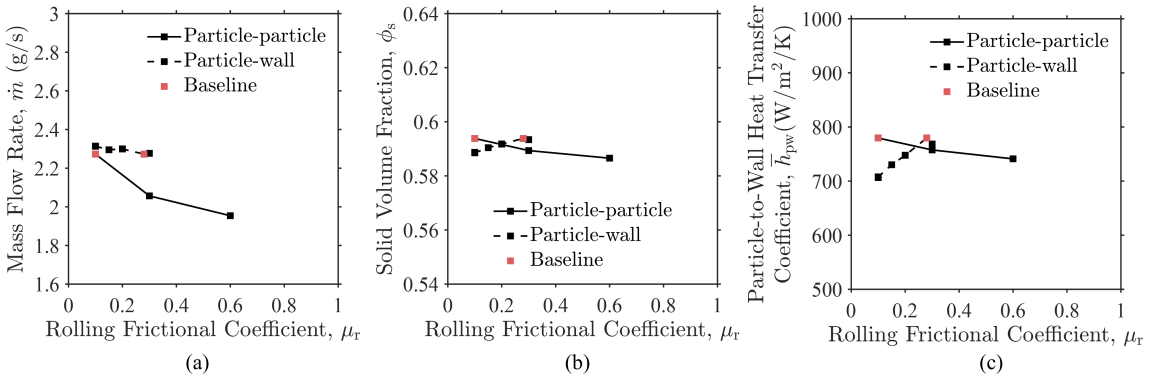


Figure E.5: Effects of the particle-particle and particle-wall, rolling frictional coefficients on (a) mass flow rate, $\dot{m}$, (b) solid volume fraction, ϕ_s, and (c) particle-to-wall heat-transfer coefficient, $\overline{h}_{\mathrm{pw}}$, for a gravity-driven, moving bed, with the rest of parameters fixed as the baseline values in Table 6.1. The identical baseline results are underscored by red dots. The range of the tested static friction coefficient for particle-particle and particle-wall surfaces follows the physical interpretation that $\mu_{\mathrm{r,pp}} < \mu_{\mathrm{s,pp}} = 0.6$ and $\mu_{\mathrm{r,pw}} < \mu_{\mathrm{s,pw}} = 0.3$.

volume fraction is not incorporated in this correlation. The alignment of simulated data with the Graetz number correlation is improved in Fig. E.6(b). This is because the ZBS model implies a similar effective thermal conductivity, ranging from 0.02–0.54 W/m/K, for the tested particle thermal conductivities (0.05–5 W/m/K), which brings more data close to a standard thermal conductivity value of 0.5 W/m/K.

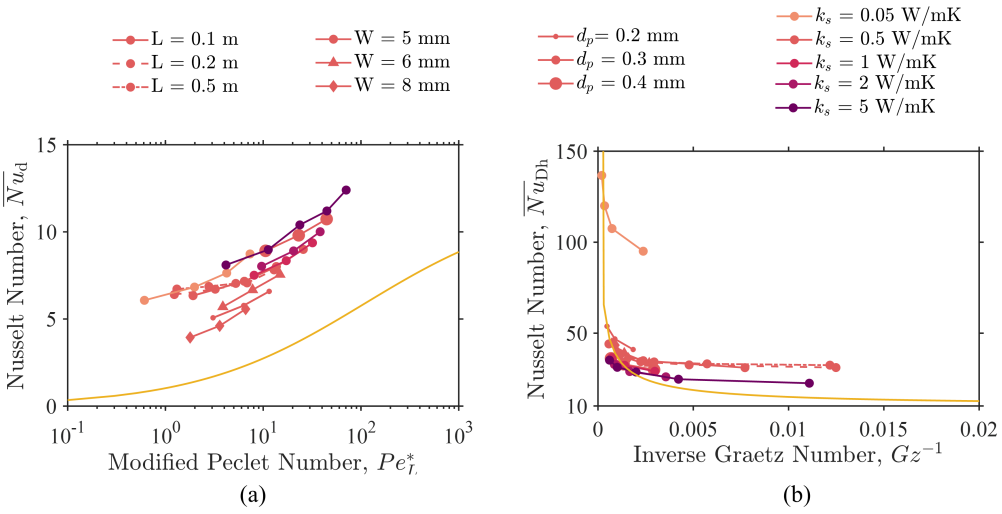


Figure E.6: (a)Particle-diameter-based Nusselt number, $\overline{Nu}_d$, as a function of the modified Péclet number, Pe^*_L, compared with Sullivan and Sabersky's correlation, and (b) the hydraulic-diameter-based Nusselt number, $\overline{Nu}_{D_h}$, as a function of the inverse Graetz number, Gz^{-1}, compared with Muzychka's correlation for plane channel, for the non-dimensional numbers calculated based on the effective thermal conductivity obtained from ZBS model.

BIBLIOGRAPHY

BIBLIOGRAPHY

[1] Oskaras Alšauskas. World energy outlook 2024. *IEA report*, 2024.

[2] Tze-Zhang Ang, Mohamed Salem, Mohamad Kamarol, Himadry Shekhar Das, Mohammad Alhuyi Nazari, and Natarajan Prabaharan. A comprehensive study of renewable energy sources: Classifications, challenges and suggestions. *Energy Strategy Reviews*, 43:100939, 2022.

[3] Geoffrey P. Hammond. Editorial: Towards net-zero 'greenhouse gas' emissions by 2050. *Proceedings of the Institution of Civil Engineers - Energy*, 177(3):95–97, 2024.

[4] Umberto Arena. Process and technological aspects of municipal solid waste gasification. A review. *Waste Management*, 32(4):625–639, 2012.

[5] Jianan Zhang, Yuesen Wang, Valerie L. Muldoon, and Sili Deng. Crude glycerol and glycerol as fuels and fuel additives in combustion applications. *Renewable and Sustainable Energy Reviews*, 159:112206, 2022.

[6] Mark Mehos, Craig Turchi, Judith Vidal, Michael Wagner, Zhiwen Ma, Clifford Ho, William Kolb, Charles Andraka, and Alan Kruizenga. Concentrating solar power Gen3 demonstration roadmap. Technical Report NREL/TP–5500-67464, 1338899, National Renewable Energy Lab (NREL), 2017.

[7] Yang Wang, Shuyu Luo, Lingxiang Yao, Ershun Du, Zhiwen Guan, and Xianyong Xiao. Modeling concentrating solar power plants in power system optimal planning and operation: A comprehensive review. *Sustainable Energy Technologies and Assessments*, 71:103992, 2024.

[8] Dina A. Elalfy, Eid Gouda, Mohamed Fawzi Kotb, Vladimír Bureš, and Bishoy E. Sedhom. Comprehensive review of energy storage systems technologies, objectives, challenges, and future trends. *Energy Strategy Reviews*, 54:101482, 2024.

[9] NREL Options. A modular, cost-effective, build-anywhere particle thermal energy storage technology, 2021.

[10] Rong Guo, Jinhao Bai, Feng Wu, Junwu Wang, Xiaoxun Ma, and Zhiquan Hui. CFD-DEM simulation of wet granular-fluid flows and heat transfer in an integral multi-jet spout-fluidized bed. *Powder Technology*, 403:117384, 2022.

[11] Schwing Technologies. High temperature reactors for gas/solid reactions up to 1100 °C.

[12] Michael F Modest. Chapter 1 - Fundamentals of thermal radiation. In *Radiative Heat Transfer (Third Edition)*, pages 1–30. Academic Press, Boston, 2013.

[13] Michael F Modest. Chapter 12 - Radiative properties of particulate media. In *Radiative Heat Transfer (Third Edition)*, pages 387–439. Academic Press, Boston, 2013.

[14] Subrahmanyan Chandrasekhar. *Radiative Transfer*. Courier Corporation, 2013.

[15] John Howell, M.P. Mengüc, K Daun, and R Siegel. Fundamental radiative transfer relations and approximate solution meth. In *Thermal Radiation Heat Transfer (7th Edition)*, page 46. CRC Press, 2020.

[16] Jelena Mačak, Christoph Goniva, and Stefan Radl. Predictions of the P_1 approximation for radiative heat transfer in heterogeneous granular media. *Particuology*, 82:25–47, 2023.

[17] M. Díaz-Heras, J. I. Córcoles, J. F. Belmonte, and J. A. Almendros-Ibáñez. 3D numerical simulation of a directly irradiated bubbling fluidized bed with SiC particles. *Applied Thermal Engineering*, 190:116812, 2021.

[18] Michael F Modest. Chapter 15 - Approximate solution methods for one-dimensional media. In *Radiative Heat Transfer (Third Edition)*, pages 480–494. Academic Press, Boston, 2013.

[19] Noriaki Wakao and Seiichirō Kagei. *Heat and Mass Transfer in Packed Beds*. Taylor & Francis, 1982.

[20] B. P. Singh and M. Kaviany. Modelling radiative heat transfer in packed beds. *International Journal of Heat and Mass Transfer*, 35(6):1397–1405, 1992.

[21] Rohini Bala Chandran and Jane H. Davidson. Model of transport and chemical kinetics in a solar thermochemical reactor to split carbon dioxide. *Chemical Engineering Science*, 146:302–315, 2016.

[22] B. P. Singh and M. Kaviany. Independent theory versus direct simulation of radiation heat transfer in packed beds. *International Journal of Heat and Mass Transfer*, 34(11):2869–2882, 1991.

[23] Kouichi Kamiuto. Correlated radiative transfer in packed-sphere systems. *Journal of Quantitative Spectroscopy and Radiative Transfer*, 43(1):39–43, 1990.

[24] Jaona Randrianalisoa and Dominique Baillis. Radiative properties of densely packed spheres in semitransparent media: A new geometric optics approach. *Journal of Quantitative Spectroscopy and Radiative Transfer*, 111(10):1372–1388, 2010.

[25] Sophia Haussener and Aldo Steinfeld. Effective heat and mass transport properties of anisotropic porous ceria for solar thermochemical fuel generation. *Materials*, 5(1):192–209, 2012.

[26] R. Coquard, D. Rochais, and D. Baillis. Experimental investigations of the coupled conductive and radiative heat transfer in metallic/ceramic foams. *International Journal of Heat and Mass Transfer*, 52(21):4907–4918, 2009.

[27] C. Y. Zhao, T. J. Lu, and H. P. Hodson. Thermal radiation in ultralight metal foams with open cells. *International Journal of Heat and Mass Transfer*, 47(14):2927–2939, 2004.

[28] R. Arambakam, H. Vahedi Tafreshi, and B. Pourdeyhimi. Dual-scale 3-D approach for modeling radiative heat transfer in fibrous insulations. *International Journal of Heat and Mass Transfer*, 64:1109–1117, 2013.

[29] Rohini Bala Chandran, Robert M. De Smith, and Jane H. Davidson. Model of an integrated solar thermochemical reactor/reticulated ceramic foam heat exchanger for gas-phase heat recovery. *International Journal of Heat and Mass Transfer*, 81:404–414, 2015.

[30] T. J. Hendricks and J. R. Howell. Absorption/scattering coefficients and scattering phase functions in reticulated porous ceramics. *Journal of Heat Transfer*, 118(1):79–87, 1996.

[31] M. Q. Brewster and C. L. Tien. Radiative transfer in packed fluidized beds: Dependent versus independent scattering. *Journal of Heat Transfer*, 104(4):573–579, 1982.

[32] Quinn Brewster. Volume scattering of radiation in packed beds of large, opaque spheres. *Journal of Heat Transfer*, 126(6):1048–1050, 2005.

[33] Asim Kumar Roy Choudhury. Chapter 2 - Object appearance and colour. In *Principles of Colour and Appearance Measurement*, pages 53–102. Woodhead Publishing, 2014.

[34] Tiphaine Galy, Daniel Huang, and Laurent Pilon. Revisiting independent versus dependent scattering regimes in suspensions or aggregates of spherical particles. *Journal of Quantitative Spectroscopy and Radiative Transfer*, 246:106924, 2020.

[35] R. Coquard and D. Baillis. Radiative characteristics of beds of spheres containing an absorbing and scattering medium. *Journal of Thermophysics and Heat Transfer*, 19(2):226–234, 2005.

[36] John C. Chen and Stuart W. Churchill. Radiant heat transfer in packed beds. *AIChE Journal*, 9(1):35–41, 1963.

[37] Ilze Oshina and Janis Spigulis. Beer–Lambert law for optical tissue diagnostics: Current state of the art and the main limitations. *Journal of Biomedical Optics*, 26(10):100901, 2021.

[38] M. Mamouei, K. Budidha, N. Baishya, M. Qassem, and P. A. Kyriacou. An empirical investigation of deviations from the Beer–Lambert law in optical estimation of lactate. *Scientific Reports*, 11(1):13734, 2021.

[39] Jaona Randrianalisoa and Dominique Baillis. Radiative transfer in dispersed media: Comparison between homogeneous phase and multiphase approaches. *Journal of Heat Transfer*, 132(023405), 2009.

[40] A. V. Gusarov. Homogenization of radiation transfer in two-phase media with irregular phase boundaries. *Physical Review B*, 77(14):144201, 2008.

[41] D. Baillis, M. Arduini-Schuster, and J. F. Sacadura. Identification of spectral radiative properties of polyurethane foam from hemispherical and bi-directional transmittance and reflectance measurements. *Journal of Quantitative Spectroscopy and Radiative Transfer*, 73(2):297–306, 2002.

[42] S. P Bhattacharya, T. F Wall, and M Arduini-Schuster. A study on the importance of dependent radiative effects in determining the spectral and total emittance of particulate ash deposits in pulverised fuel fired furnaces. *Chemical Engineering and Processing: Process Intensification*, 36(6):423–432, 1997.

[43] W.N. Sullivan and R.H. Sabersky. Heat transfer to flowing granular media. *International Journal of Heat and Mass Transfer*, 18(1):97–107, 1975.

[44] J.S. Patton, R.H. Sabersky, and C.E. Brennen. Convective heat transfer to rapidly flowing, granular materials. *International Journal of Heat and Mass Transfer*, 29(8):1263–1269, 1986.

[45] V. V. R. Natarajan and M. L. Hunt. Heat transfer in vertical granular flows. *Experimental Heat Transfer*, 10(2):89–107, 1997.

[46] Megan F. Watkins, Yesaswi N. Chilamkurti, and Richard D. Gould. Analytic modeling of heat transfer to vertical dense granular flows. *Journal of Heat Transfer*, 142(2):022103, 2020.

[47] Mengqi Wu, Nan Gui, Xingtuan Yang, Jiyuan Tu, and Shengyao Jiang. Numerical investigation of flow characteristics and packing structure of binary-sized pebble flow in a circulating pebble bed. *Progress in Nuclear Energy*, 150:104312, 2022.

[48] Hao Wu, Nan Gui, Xingtuan Yang, Jiyuan Tu, and Shengyao Jiang. Effect of scale on the modeling of radiation heat transfer in packed pebble beds. *International Journal of Heat and Mass Transfer*, 101:562–569, 2016.

[49] Liuyimei Yang, Qijun Zheng, and Aibing Yu. A continuum model for the segregation of bidisperse particles in a blade mixer. *AIChE Journal*, 68(8):e17734, 2022.

[50] Xiandong Liu, Hai Zhang, Hairui Yang, Yang Zhang, and Junfu Lyu. Validation and evaluation of the CPFD modeling of dense particle flow velocity: Taking particle flow around an obstacle as an example. *Chemical Engineering Journal*, 453:139719, 2023.

[51] Degang Rong and Masayuki Horio. DEM simulation of char combustion in a fluidized bed. *Second International Conference on CFD in the Minerals and Process Industries*, pages 65–70, 1999.

[52] A.B. Morris, S. Pannala, Z. Ma, and C.M. Hrenya. A conductive heat transfer model for particle flows over immersed surfaces. *International Journal of Heat and Mass Transfer*, 89:1277–1289, 2015.

[53] A. B. Morris, S. Pannala, Z. Ma, and C. M. Hrenya. Development of soft-sphere contact models for thermal heat conduction in granular flows. *AIChE Journal*, 62(12):4526–4535, 2016.

[54] A.B. Morris, Z. Ma, S. Pannala, and C.M. Hrenya. Simulations of heat transfer to solid particles flowing through an array of heated tubes. *Solar Energy*, 130:101–115, 2016.

[55] Manogna Adepu, Shaohua Chen, Yang Jiao, Aytekin Gel, and Heather Emady. Wall to particle bed contact conduction heat transfer in a rotary drum using DEM. *Computational Particle Mechanics*, 8(3):589–599, 2021.

[56] Qiang Xie, Zuobing Chen, Qinfu Hou, A.B. Yu, and Runyu Yang. DEM investigation of heat transfer in a drum mixer with lifters. *Powder Technology*, 314:175–181, 2017.

[57] Clara Hartmanshenn, Johannes G. Khinast, Charles D. Papageorgiou, Chris Mitchell, Justin Quon, and Benjamin J. Glasser. Heat transfer of dry granular materials in a bladed mixer: Effect of thermal properties and agitation rate. *AIChE Journal*, 66(4), 2020.

[58] Justin D. Yarrington, Malavika V. Bagepalli, Gokul Pathikonda, Andrew J. Schrader, Zhuomin M. Zhang, Devesh Ranjan, and Peter G. Loutzenhiser. Numerical analyses of high temperature dense, granular flows coupled to high temperature flow property measurements for solar thermal energy storage. *Solar Energy*, 213:350–360, 2021.

[59] Z. Yan, S. K. Wilkinson, E. H. Stitt, and M. Marigo. Discrete element modelling (DEM) input parameters: Understanding their impact on model predictions using statistical analysis. *Computational Particle Mechanics*, 2(3):283–299, 2015.

[60] Zhengbiao Peng, Elham Doroodchi, and Behdad Moghtaderi. Heat transfer modelling in discrete element method (DEM)-based simulations of thermal processes: Theory and model development. *Progress in Energy and Combustion Science*, 79:100847, 2020.

[61] Evan F. Johnson, İlker Tarı, and Derek Baker. Modeling heat exchangers with an open source DEM-based code for granular flows. *Solar Energy*, 228:374–386, 2021.

[62] Johannes Grobbel. *Modeling solar particle receivers with the discrete element method*. Dissertation, Rheinisch-Westfälische Technische Hochschule Aachen, Aachen, 2019.

[63] David Gaviño, Eduardo Cortés, Jesús García, Ignacio Calderón-Vásquez, José Cardemil, Danilo Estay, and Rodrigo Barraza. A discrete element approach to model packed bed thermal storage. *Applied Energy*, 325:119821, 2022.

[64] Zhigang Guo, Shang Zhang, Xing Tian, Jian Yang, and Qiuwang Wang. Numerical investigation of tube oscillation in gravity-driven granular flow with heat transfer by discrete element method. *Energy*, 207:118203, 2022.

[65] W. Van Antwerpen, C.G. Du Toit, and P.G. Rousseau. A review of correlations to model the packing structure and effective thermal conductivity in packed beds of mono-sized spherical particles. *Nuclear Engineering and Design*, 240(7):1803–1818.

[66] Johannes Grobbel, Stefan Brendelberger, Matthias Henninger, Christian Sattler, and Robert Pitz-Paal. Calibration of parameters for DEM simulations of solar particle receivers by bulk experiments and surrogate functions. *Powder Technology*, 364:831–844, 2020.

[67] Y. S. Muzychka, Edmond Walsh, and Pat Walsh. Simple models for laminar thermally developing slug flow in noncircular ducts and channels. *Journal of Heat Transfer*, 132(111702), 2010.

[68] Megan F. Watkins and Richard D. Gould. Experimental characterization of heat transfer to vertical dense granular flows across wide temperature range. *Journal of Heat Transfer*, 141(3):032001, 2019.

[69] Kevin J. Albrecht and Clifford K. Ho. Heat transfer models of moving packed-bed particle-to-sCO_2 heat exchangers. *Journal of Solar Energy Engineering*, 141(3):031006, 2019.

[70] Sarath R. Adapa, Xintong Zhang, Tianshi Feng, Jian Zeng, Ka Man Chung, Kevin J. Albrecht, Clifford K. Ho, Dimitri A. Madden, and Renkun Chen. Heat transfer coefficients of moving particle beds from flow-dependent thermal conductivity and near-wall resistance. *Solar Energy*, 282:112960, 2024.

[71] H. S. Mickley and D. F. Fairbanks. Mechanism of heat transfer to fluidized beds. *AIChE Journal*, 1(3):374–384, 1955.

[72] A. O. O. Denloye and J. S. M. Botterill. Heat transfer in flowing packed beds. *Chemical Engineering Science*, 32(5):461–465, 1977.

[73] Manuk Colakyan. *Moving bed heat transfer and fluidized elutriation.* PhD thesis, Oregon State University, 1984.

[74] Nevenka Obuskovic, Manuk Colakyan, and James G Knudsen. Heat transfer between moving beds of solids and a transverse finned tube. *Heat Transfer Engineering*, 1991.

[75] Gaosheng Wei, Pingrui Huang, Longfei Pan, Liu Cui, Chao Xu, and Xiaoze Du. Experimental, numerical and analytical modeling of heat transfer of gravity driven dense particle flow in vertical heated plates. *International Journal of Heat and Mass Transfer*, 187:122571, 2022.

[76] George Keith Batchelor and R. W. O'Brien. Thermal or electrical conduction through a granular material. *Proceedings of the Royal Society of London. A. Mathematical and Physical Sciences*, 355(1682):313–333, 1977.

[77] G.J. Cheng, A.B. Yu, and P. Zulli. Evaluation of effective thermal conductivity from the structure of a packed bed. *Chemical Engineering Science*, 54(19):4199–4209, 1999.

[78] J Li and D.J Mason. A computational investigation of transient heat transfer in pneumatic transport of granular particles. *Powder Technology*, 112(3):273–282, 2000.

[79] D.J. Gunn. Transfer of heat or mass to particles in fixed and fluidised beds. *International Journal of Heat and Mass Transfer*, 21(4):467–476, 1977.

[80] Kevin J. Albrecht and Clifford K. Ho. Design and operating considerations for a shell-and-plate, moving packed-bed, particle-to-sCO_2 heat exchanger. *Solar Energy*, 178:331–340, 2019.

[81] Zhigang Guo, Zhoutuo Tan, Xing Tian, Zhihong Wu, Tian Wang, Jian Yang, and Qiuwang Wang. Heat transfer prediction of granular flow in moving bed heat exchanger: Characteristics of heat transfer enhancement and dynamic control. *Solar Energy*, 230:1052–1069, 2021.

[82] Peng-Hui Xiao, Ben-Wen Li, and Ya-Song Sun. A model to determine the overall bed-to-wall heat transfer coefficient and its influence factor analysis in moving bed. *International Journal of Heat and Mass Transfer*, 154:119655, 2020.

[83] Nan Gui, Shengyao Jiang, Xingtuan Yang, and Jiyuan Tu. A review of recent study on the characteristics and applications of pebble flows in nuclear engineering. *Experimental and Computational Multiphase Flow*, 4(4):339–349, 2022.

[84] Fenglei Qi and Mark Mba Wright. Particle scale modeling of heat transfer in granular flows in a double screw reactor. *Powder Technology*, 335:18–34, 2018.

[85] Janna Martinek and Zhiwen Ma. Granular flow and heat-transfer study in a near-blackbody enclosed particle receiver. *Journal of Solar Energy Engineering*, 137(5):051008, 2015.

[86] R. J. Braham and A. T. Harris. A complete multi-scale simulation of light absorption within a fluidized bed photoreactor using integrated particle, fluid and photon behaviour models. *Physical Chemistry Chemical Physics*, 15(29):12373, 2013.

[87] Jingjing Chen, Apurv Kumar, Joe Coventry, and Wojciech Lipiński. Heat transfer in directly-irradiated high-temperature solid–gas flows laden with polydisperse particles. *Applied Mathematical Modelling*, 110:698–722, 2022.

[88] Michael F Modest. Chapter 8 - The Monte Carlo method for surface exchange. In *Radiative Heat Transfer (Third Edition)*, pages 247–266. Academic Press, Boston, 2013.

[89] William Strieder. Radiation heat transport in disordered media. *Advances in Water Resources*, 20(2):171–187, 1997.

[90] Michael Oren and Shree K. Nayar. A theory of specular surface geometry. *International Journal of Computer Vision*, 24(2):105–124, 1997.

[91] Haidong Liu, Huaichun Zhou, Dandan Wang, and Yafen Han. Performance comparison of two monte carlo ray-tracing methods for calculating radiative heat transfer. *Journal of Quantitative Spectroscopy and Radiative Transfer*, 256:107305, 2020.

[92] Anton Krieger and Sebastian Wolf. Improving Monte Carlo radiative transfer simulations: A shift of framework. *Astronomy & Astrophysics*, 680:A67, 2023.

[93] Colin Thornton. *Granular Dynamics, Contact Mechanics and Particle System Simulations: A DEM Study*. Springer International Publishing, 2015.

[94] Q Spreiter and M Walter. Classical molecular dynamics simulation with the velocity verlet algorithm at strong external magnetic fields. *Journal of Computational Physics*, 152(1):102–119, 1999.

[95] Christoph Kloss, Christoph Goniva, Alice Hager, Stefan Amberger, and Stefan Pirker. Models, algorithms and validation for opensource DEM and CFD-DEM. *Progress in Computational Fluid Dynamics, an International Journal*, 12(2-3):140–152, 2012.

[96] Alberto Di Renzo and Francesco Paolo Di Maio. An improved integral non-linear model for the contact of particles in distinct element simulations. *Chemical Engineering Science*, 60(5):1303–1312, 2005.

[97] Zhiquan Chen, Xin Tong, and Zhanfu Li. Numerical investigation on the sieving performance of elliptical vibrating screen. 8(9):1151, 2020.

[98] Z.Y. Zhou, A.B. Yu, and P. Zulli. A new computational method for studying heat transfer in fluid bed reactors. *Powder Technology*, 197(1):102–110, 2010.

[99] Michael F. Modest and Sandip Mazumder. Chapter 4 - View factors. In *Radiative Heat Transfer (Fourth Edition)*, pages 127–159. Academic Press, 2022.

[100] G. J. Cheng and A. B. Yu. Particle scale evaluation of the effective thermal conductivity from the structure of a packed bed: Radiation heat transfer. *Industrial & Engineering Chemistry Research*, 52(34):12202–12211, 2013.

[101] Zijie Chen and Rohini Bala Chandran. Radiative view factor correlations in particulate media from ray tracing simulations and data-driven modeling. *International Journal of Heat and Mass Transfer*, 213:124250, 2023.

[102] Hao Wu, Nan Gui, Xingtuan Yang, Jiyuan Tu, and Shengyao Jiang. A matrix model of particle-scale radiative heat transfer in structured and randomly packed pebble bed. *International Journal of Thermal Sciences*, 153:106334.

[103] Evan F. Johnson, İlker Tarı, and Derek Baker. Modeling heat exchangers with an open source DEM-based code for granular flows. *Solar Energy*, 228:374–386, 2021.

[104] Jelena Mačak, Christoph Goniva, and Stefan Radl. Predictions of the P_1 approximation for radiative heat transfer in heterogeneous granular media. *Particuology*, 82:25–47, 2023.

[105] Stefan T. Thynell. Discrete-ordinates method in radiative heat transfer. *International Journal of Engineering Science*, 36(12):1651–1675, 1998.

[106] Pedro J. Coelho. Advances in the discrete ordinates and finite volume methods for the solution of radiative heat transfer problems in participating media. *Journal of Quantitative Spectroscopy and Radiative Transfer*, 145:121–146, 2014.

[107] Bingjia Li, Zijie Chen, and Rohini Bala Chandran. Conductive and radiative heat transfer mechanisms inform Nusselt number dependence on solid volume fraction for granular flows. *Powder Technology*, 440:119737, 2024.

[108] Aidan P. Thompson, H. Metin Aktulga, Richard Berger, Dan S. Bolintineanu, W. Michael Brown, Paul S. Crozier, Axel Kohlmeyer, Stan G. Moore, Trung Dac Nguyen, Ray Shan, Mark J. Stevens, Julien Tranchida, Christian Trott, and Steven J. Plimpton. LAMMPS - a flexible simulation tool for particle-based materials modeling at the atomic, meso, and continuum scales. *Computer Physics Communications*, 271:108171, 2022.

[109] D. A. Zumbrunnen, R. Viskanta, and F. P. Incropera. Heat transfer through granular beds at high temperature. *Wärme - und Stoffübertragung*, 18(4):221–226, 1984.

[110] S. Chandrasekhar. *Radiative transfer*. Dover, 1960.

[111] Bai Song, Anthony Fiorino, Edgar Meyhofer, and Pramod Reddy. Near-field radiative thermal transport: From theory to experiment. *AIP Advances*, 5(5):053503, 2015.

[112] Jaona Randrianalisoa and Dominique Baillis. Radiative transfer in dispersed media: Comparison between homogeneous phase and multiphase approaches. *Journal of Heat Transfer*, 132(023405), 2009.

[113] J. D. Cartigny, Y. Yamada, and C. L. Tien. Radiative transfer with dependent scattering by particles: Part 1—Theoretical investigation. *Journal of Heat Transfer*, 108(3):608–613, 1986.

[114] Y. Yamada, J. D. Cartigny, and C. L. Tien. Radiative transfer with dependent scattering by particles: Part 2—Experimental investigation. *Journal of Heat Transfer*, 108(3):614–618, 1986.

[115] Chang-Lin Tien and B. L. Drolen. Thermal radiation in particulate media with dependent and independent scattering. *Annual Review of Heat Transfer*, 1:1–32, 1987.

[116] Lorenzo Pattelli, Amos Egel, Uli Lemmer, and Diederik S. Wiersma. Role of packing density and spatial correlations in strongly scattering 3D systems. *Optica*, 5(9):1037–1045, 2018.

[117] Victor P. Tishkovets and Elena V. Petrova. Light scattering by densely packed systems of particles: near-field effects. In *Light Scattering Reviews 7: Radiative Transfer and Optical Properties of Atmosphere and Underlying Surface*, pages 3–36. Springer, Berlin, Heidelberg, 2013.

[118] L. M. Zurk, L. Tsang, K. H. Ding, and D. P. Winebrenner. Monte Carlo simulations of the extinction rate of densely packed spheres with clustered and nonclustered geometries. *JOSA A*, 12(8):1772–1781, 1995.

[119] Jaona Randrianalisoa, Sophia Haussener, Dominique Baillis, and Wojciech Lipiński. Radiative characterization of random fibrous media with long cylindrical fibers: Comparison of single- and multi-RTE approaches. *Journal of Quantitative Spectroscopy and Radiative Transfer*, 202:220–232, 2017.

[120] Michael I. Mishchenko. "Independent" and "dependent" scattering by particles in a multi-particle group. *OSA Continuum*, 1(1):243–260, 2018.

[121] Jean Taine and Franck Enguehard. Statistical modelling of radiative transfer within non-Beerian effective phases of macroporous media. *International Journal of Thermal Sciences*, 139:61–78, 2019.

[122] Alexander B. Kostinski. On the extinction of radiation by a homogeneous but spatially correlated random medium. *Journal of the Optical Society of America A*, 18(8):1929–1933, 2001.

[123] Adrian Jarabo, Carlos Aliaga, and Diego Gutierrez. A radiative transfer framework for spatially-correlated materials. *ACM Trans. Graph.*, 37(4):1–13, 2018.

[124] Edward W. Larsen and Richard Vasques. A generalized linear Boltzmann equation for non-classical particle transport. *Journal of Quantitative Spectroscopy and Radiative Transfer*, 112(4):619–631, 2011.

[125] J. K. Eaton and J. R. Fessler. Preferential concentration of particles by turbulence. *International Journal of Multiphase Flow*, 20:169–209, 1994.

[126] M. Krstić. Chapter 9 - Mixing control for jet flows. In *Combustion Processes in Propulsion*, pages 87–96. Butterworth-Heinemann, 2006.

[127] H. K. Pak and P. R. Behringer. Bubbling in vertically vibrated granular materials. *Nature (London)*, 371(6494):231–233, 1994.

[128] R. Brent Rice and Christine M. Hrenya. Characterization of clusters in rapid granular flows. *Physical Review E*, 79(2):021304, 2009.

[129] Noel A. C. Cressie. Spatial point patterns. In *Statistics for Spatial Data*, pages 575–723. John Wiley & Sons, Ltd, 1993.

[130] Andrei Rogers. *Statistical Analysis of Spatial Dispersion: The Quadrat Method*. Pion, 1974.

[131] J. B. Douglas. Clustering and aggregation. *Sankhyā: The Indian Journal of Statistics, Series B (1960-2002)*, 37(4):398–417, 1975.

[132] Ted Chang. Spatial statistics. *Statistical Science*, 19(4):624–635, 2004.

[133] K. C. Weston, A. C. Reynolds, A. Alikhan, and D. W. Drago. Radiative transfer in highly scattering materials - numerical solution and evaluation of approximate analytic solutions, 1974.

[134] Anna Szczepańska. Research design and statistical analysis. *International Statistical Review*, 79(3):491–492, 2011.

[135] Kevin J. Albrecht and Clifford K. Ho. Design and operating considerations for a shell-and-plate, moving packed-bed, particle-to-sCO_2 heat exchanger. *Solar Energy*, 178:331–340, 2019.

[136] Clifford K. Ho, Kevin J. Albrecht, Lindsey Yue, Brantley Mills, Jeremy Sment, Joshua Christian, and Matthew Carlson. Overview and design basis for the Gen 3 Particle Pilot Plant (G3P3). *AIP Conference Proceedings*, 2303:030020, 2020.

[137] Huili Zhang, Hadrien Benoit, Daniel Gauthier, Jan Degrève, Jan Baeyens, Inmaculada Pérez López, Mehrdji Hemati, and Gilles Flamant. Particle circulation loops in solar energy capture and storage: Gas–solid flow and heat transfer considerations. *Applied Energy*, 161:206–224, 2016.

[138] P. A. Cundall and O. D. L. Strack. A discrete numerical model for granular assemblies. *Géotechnique*, 29(1):47–65, 1979.

[139] Florian Fleissner, Timo Gaugele, and Peter Eberhard. Applications of the discrete element method in mechanical engineering. *Multibody System Dynamics*, 18(1):81–94, 2007.

[140] Shuiqing Li, Jeffrey S. Marshall, Guanqing Liu, and Qiang Yao. Adhesive particulate flow: The discrete-element method and its application in energy and environmental engineering. *Progress in Energy and Combustion Science*, 37(6):633–668, 2011.

[141] P. J. Owen and P. W. Cleary. Prediction of screw conveyor performance using the Discrete Element Method (DEM). *Powder Technology*, 193(3):274–288, 2009.

[142] Claudia Hildebrandt, Srikanth R. Gopireddy, Regina Scherließ, and Nora A. Urbanetz. A DEM approach to assess the influence of the paddle wheel shape on force feeding during pharmaceutical tableting. *Advanced Powder Technology*, 31(2):755–769, 2020.

[143] Volodymyr Shatokha. *Iron Ores and Iron Oxide Materials*. IntechOpen, 2018.

[144] Xi Gao, Jia Yu, Liqiang Lu, and William A. Rogers. Coupling particle scale model and SuperDEM-CFD for multiscale simulation of biomass pyrolysis in a packed bed pyrolyzer. *AIChE Journal*, 67(4):e17139, 2021.

[145] Enric Illana Mahiques, Maximilian Brömmer, Siegmar Wirtz, and Viktor Scherer. Simulation of Reacting, Moving Granular Assemblies of Thermally Thick Particles by Discrete Element Method/Computational Fluid Dynamics. *Chemical Engineering & Technology*, 46(7):1317–1332, 2023.

[146] A.K.R. Choudhury. *Principles of Colour and Appearance Measurement: Object Appearance, Colour Perception and Instrumental Measurement*. Elsevier Science, 2014.

[147] F.A. Morrison. *An Introduction to Fluid Mechanics*. Cambridge University Press, 2013.

[148] K. Kesava Rao and Prabhu R. Nott. *An Introduction to Granular Flow*. Cambridge University Press, 2008.

[149] R. M. Nedderman. *Statics and Kinematics of Granular Materials*. Cambridge University Press, 1992.

[150] F. A. L. Dullien. Chapter 3 - pore structure. In *Porous Media: Fluid Transport and Pore Structure*, page 132. Academic Press, 1979.

[151] Christoph Kloss, Christoph Goniva, Alice König, Stefan Amberger, and Stefan Pirker. Models, algorithms and validation for opensource DEM and CFD-DEM. *Progress in Computational Fluid Dynamics*, 12:140–152, 2012.

[152] Theo A. Rulko, Bingjia Li, Brandon Surhigh, J. Michael Mayer, and Rohini Bala Chandran. Optical measurements and flow modeling to characterize solid volume fractions in gravity-driven particle curtains. *Solar Energy*, 264:111989, 2023.

[153] Z. Yan, S. K. Wilkinson, E. H. Stitt, and M. Marigo. Discrete element modelling (DEM) input parameters: understanding their impact on model predictions using statistical analysis. *Computational Particle Mechanics*, 2(3):283–299, 2015.

[154] Jiahui Hao, Yanjie Li, Yu Guo, Hanhui Jin, and Jennifer S. Curtis. The effect of polydispersity on the stresses of cylindrical particle flows. *Powder Technology*, 361:943–956, 2020.

[155] C.J. Coetzee. Review: Calibration of the discrete element method. *Powder Technology*, 310:104–142, 2017.

[156] Johannes Grobbel, Harald Kruggel-Emden, and Robert Pitz-Paal. *Modeling solar particle receivers with the discrete element method*. PhD thesis, Rheinisch-Westfälische Technische Hochschule Aachen, 2020.

[157] Chuyang Chen, Devesh Ranjan, Peter G. Loutzenhiser, and Zhuomin M. Zhang. A numerical study of the spectral radiative properties of packed bed with mixed bauxite and silica spheres. *International Journal of Heat and Mass Transfer*, 207:124025, 2023.

[158] K. C. Weston, Jr Reynolds, A. C., A. Alikhan, and D. W. Drago. Radiative transfer in highly scattering materials - numerical solution and evaluation of approximate analytic solutions. Technical Report 19740021895, The University of Tulsa, OK, 1974.

[159] Clifford K. Ho. A review of high-temperature particle receivers for concentrating solar power. *Applied Thermal Engineering*, 109:958–969, 2016.

[160] Kaijun Jiang, Xiaoze Du, Yanqiang Kong, Chao Xu, and Xing Ju. A comprehensive review on solid particle receivers of concentrated solar power. *Renewable and Sustainable Energy Reviews*, 116:109463, 2019.

[161] Muhammad Imran Khan, Faisal Asfand, and Sami G. Al-Ghamdi. Progress in technology advancements for next generation concentrated solar power using solid particle receivers. *Sustainable Energy Technologies and Assessments*, 54:102813, 2022.

[162] Selvan Bellan, Tatsuya Kodama, Nobuyuki Gokon, and Koji Matsubara. A review on high-temperature thermochemical heat storage: Particle reactors and materials based on solid–gas reactions. *WIREs Energy and Environment*, 11(5):e440, 2022.

[163] Wang Fuqiang, Ma Lanxin, Cheng Ziming, Tan Jianyu, Huang Xing, and Liu Linhua. Radiative heat transfer in solar thermochemical particle reactor: A comprehensive review. *Renewable and Sustainable Energy Reviews*, 73:935–949, 2017.

[164] Jian Zeng, Ka Man Chung, Xintong Zhang, Tianshi Feng, Sarath Adapa, and Renkun Chen. Characterization and understanding of thermal transport in stationary and moving particle beds for concentrating solar power. *Annual Review of Heat Transfer*, 25:117–173, 2022.

[165] Rahman S. Almusafir, Ahmed A. Jasim, and Muthanna H. Al-Dahhan. Review of the fluid dynamics and heat transport phenomena in packed pebble bed nuclear reactors. *Nuclear Science and Engineering*, 197(6):1001–1037, 2023.

[166] Bin Li, Nan Gui, Hao Wu, Xingtuan Yang, Jiyuan Tu, and Shengyao Jiang. Sub-cell radiation-conduction (SCRC) model in densely packed beds of monosized pebbles for htgr under vacuum condition. *International Journal of Heat and Mass Transfer*, 199:123445, 2022.

[167] Hengjun Gai, Peiyi Yang, Qiang Zhang, Mengqi Lin, Hongbing Song, Meng Xiao, Tingting Huang, and Quanhong Zhu. Dual-dense gas-solid circulating fluidized bed reactor. *Fuel*, 337:126872, 2023.

[168] Hamada M. Abdelmotalib, Mahmoud A.M. Youssef, Ali A. Hassan, Suk Bum Youn, and Ik-Tae Im. Heat transfer process in gas–solid fluidized bed combustors: A review. *International Journal of Heat and Mass Transfer*, 89:567–575, 2015.

[169] Hosanna Uwitonze, Ayeon Kim, Heehyang Kim, Boris Brigljević, Hoang Vu Ly, Seung-Soo Kim, Mukesh Upadhyay, and Hankwon Lim. CFD simulation of hydrodynamics and heat transfer characteristics in gas–solid circulating fluidized bed riser under fast pyrolysis flow condition. *Applied Thermal Engineering*, 212:118555, 2022.

[170] Lei Guo and Jesse Capecelatro. The role of clusters on heat transfer in sedimenting gas-solid flows. *International Journal of Heat and Mass Transfer*, 132:1217–1230, 2019.

[171] Bo Leckner. Fluidization characteristics of circulating fluidized bed boilers. *Chemie Ingenieur Technik*, 95(1-2):32–39, 2022.

[172] Charles S. Campbell and Christopher E. Brennen. Computer simulation of granular shear flows. *Journal of Fluid Mechanics*, 151(1):167–188, 2006.

[173] Yupu Yu, Fuliang Nie, Fengwu Bai, and Zhifeng Wang. Theoretical and experimental investigation on heating moving packed beds in a single tube with constant wall temperature. *International Journal of Heat and Mass Transfer*, 180:121725, 2021.

[174] Jingjing Chen, Apurv Kumar, Joe Coventry, Jin-Soo Kim, and Wojciech Lipiński. Numerical modelling of radiative heat transfer in a polydispersion of ceramic particles under direct high-flux solar irradiation. *Journal of Quantitative Spectroscopy and Radiative Transfer*, 278:108008, 2022.

[175] Baokun Liu, Junming Zhao, Linhua Liu, and A.V. Gusarov. Analytical relation of radiation distribution function in random particulate systems. *International Communications in Heat and Mass Transfer*, 141:106555, 2023.

[176] Apurv Kumar, Jin-Soo Kim, and Wojciech Lipiński. Radiation absorption in a particle curtain exposed to direct high-flux solar irradiation. *Journal of Solar Energy Engineering*, 140(6):061007, 2018.

[177] Liang-Shih Fan and Fanxing Li. Chemical looping technology and its fossil energy conversion applications. *Industrial & Engineering Chemistry Research*, 49(21):10200–10211, 2010.

[178] Chao Fan, Xin-Lin Xia, Wei Du, Chuang Sun, and Yang Li. Numerical investigations of the coupled conductive-radiative heat transfer in alumina ceramics. *International Communications in Heat and Mass Transfer*, 135:106097, 2022.

[179] Wei Zhao, Yuanping Cheng, Pinkun Guo, Kan Jin, Qingyi Tu, and Haifeng Wang. An analysis of the gas-solid plug flow formation: New insights into the coal failure process during coal and gas outbursts. *Powder Technology*, 305:39–47, 2017.

[180] Jiahe Shen, Chenglong Jin, Jianming Yuan, Yuyang Cai, and Craig Wheeler. Experimental and numerical analysis of hopper dust suppression during discharge of free falling bulk solids. *Powder Technology*, 415:118108, 2023.

[181] R G Munro. Evaluated material properties for a sintered alpha-alumina. *Journal of the American Ceramic Society*, 80(8):1919–1928, 1997.

[182] C.M. Sorace, M.Y. Louge, M.D. Crozier, and V.H.C. Law. High apparent adhesion energy in the breakdown of normal restitution for binary impacts of small spheres at low speed. *Mechanics Research Communications*, 36(3):364–368, 2009.

[183] Matthew Sandlin and S.I. Abdel-Khalik. A study of granular flow through horizontal wire mesh screens for concentrated solar power particle heating receiver applications – Part I: Experimental studies and numerical model development. *Solar Energy*, 169:1–10, 2018.

[184] C.J. Coetzee. Review: Calibration of the discrete element method. *Powder Technology*, 310:104–142, 2017.

[185] N. G. Deen and J. A. M. Kuipers. Direct Numerical Simulation (DNS) of mass, momentum and heat transfer in dense fluid-particle systems. *Current Opinion in Chemical Engineering*, 5:84–89, 2014.

[186] Gilles Flamant, Benjamin Grange, John Wheeldon, Frédéric Siros, Benoît Valentin, Françoise Bataille, Huili Zhang, Yimin Deng, and Jan Baeyens. Opportunities and challenges in using particle circulation loops for concentrated solar power applications. *Progress in Energy and Combustion Science*, 94:101056, 2023.

[187] Sajjad Mahmoudinezhad, Meisam Sadi, Hamed Ghiasirad, and Ahmad Arabkoohsar. A comprehensive review on the current technologies and recent developments in high-temperature heat exchangers. *Renewable and Sustainable Energy Reviews*, 183:113467, 2023.

[188] Congcong Wu, Haitao Yang, Xiaohei He, Chaoquan Hu, Le Yang, and Hongtao Li. Principle, development, application design and prospect of fluidized bed heat exchange technology: Comprehensive review. *Renewable and Sustainable Energy Reviews*, 157:112023, 2022.

[189] Panagiotis Avrampos and George-Christopher Vosniakos. A review of powder deposition in additive manufacturing by powder bed fusion. *Journal of Manufacturing Processes*, 74:332–352, 2022.

[190] Erlei Li, Zongyan Zhou, Lin Wang, Ruiping Zou, and Aibing Yu. Particle scale modelling of powder recoating and melt pool dynamics in laser powder bed fusion additive manufacturing: A review. *Powder Technology*, 409:117789, 2022.

[191] Guanxiong Miao, Wenchao Du, Zhijian Pei, and Chao Ma. A literature review on powder spreading in additive manufacturing. *Additive Manufacturing*, 58:103029, 2022.

[192] Selvan Bellan, Tatsuya Kodama, Nobuyuki Gokon, and Koji Matsubara. A review on high-temperature thermochemical heat storage: Particle reactors and materials based on solid–gas reactions. *WIREs Energy and Environment*, 11(5):e440.

[193] Alfonso J. Carrillo and José Manuel Serra. Recent progress on redox materials for high-temperature thermochemical heat storage. *Advanced Energy and Sustainability Research*, 6(4):2400317, 2025.

[194] Anti Kur, Jo Darkwa, John Calautit, Rabah Boukhanouf, and Mark Worall. Solid–gas thermochemical energy storage materials and reactors for low to high-temperature applications: A concise review. *Energies*, 16(2):756, 2023.

[195] L. F. Marie, S. Landini, D. Bae, V. Francia, and T. S. O'Donovan. Advances in thermochemical energy storage and fluidised beds for domestic heat. *Journal of Energy Storage*, 53:105242, 2022.

[196] Sarah Roger-Lund, Jo Darkwa, Mark Worall, John Calautit, and Rabah Boukhanouf. A review of thermochemical energy storage systems for district heating in the UK. *Energies*, 17(14), 2024.

[197] Marc T. Dunham and Brian D. Iverson. High-efficiency thermodynamic power cycles for concentrated solar power systems. *Renewable and Sustainable Energy Reviews*, 30:758–770, 2014.

[198] Christos N. Markides. Low-concentration solar-power systems based on organic rankine cycles for distributed-scale applications: Overview and further developments. *Frontiers in Energy Research*, 3:1–16, 2015.

[199] Ka Man Chung, Jian Zeng, Sarath Reddy Adapa, Tianshi Feng, Malavika V. Bagepalli, Peter G. Loutzenhiser, Kevin J. Albrecht, Clifford K. Ho, and Renkun Chen. Measurement and analysis of thermal conductivity of ceramic particle beds for solar thermal energy storage. *Solar Energy Materials and Solar Cells*, 230:111271, 2021.

[200] J. K. Spelt, C. E. Brennen, and R. H. Sabersky. Heat transfer to flowing granular material. *International Journal of Heat and Mass Transfer*, 25(6):791–796, 1982.

[201] Hojin Ahn. *Experimental and Analytical Investigations of Granular Materials: Shear Flow and Convective Heat Transfer*. PhD thesis, California Institute of Technology, 1989.

[202] V. V. R. Natarajan and M. L. Hunt. Kinetic theory analysis of heat transfer in granular flows. *International Journal of Heat and Mass Transfer*, 41(13):1929–1944, 1998.

[203] Kevin J. Albrecht and Clifford K. Ho. High-temperature flow testing and heat transfer for a moving packed-bed particle/sCO_2 heat exchanger. *AIP Conference Proceedings*, 2033(1):040003, 2018.

[204] J. Michael Mayer, Noah Walters, Kevin J. Albrecht, Dimitri A. Madden, and Rohini Bala Chandran. Experimental characterization of heat transfer coefficients in a moving-bed shell-and-plate heat exchanger with non-contact temperature measurements. *International Journal of Heat and Mass Transfer*, 242:126819, 2025.

[205] Lyman Products: Raytech Division. *Safety Data Sheet: Porcelain Balls Finishing Media*, 2019.

[206] LoadStar Sensors. *iWeigh USB Scale*, 2014.